

Spin Crossover Complexes: increasing cooperativity and adding fluorescence through extension of the π -system

Dissertation

Zur Erlangerung des akademischen Grades eines
Doktors der Naturwissenschaften (Dr. rer. nat.) im Promotionsprogramm
Materialchemie und Katalyse an der Bayreuther Graduiertenschule für Mathematik und
Naturwissenschaften (BayNAT)

vorgelegt von
M. Sc. Charles Lochenie
geboren am 22. Juli 1989 in Wolluwé-St-Lambert (BE)

Bayreuth 2016

This doctoral thesis was prepared at the department of Inorganic Chemistry II at the University of Bayreuth from October 2012 until June 2016 and was supervised by Prof. Dr. Birgit Weber.

This is a full reprint of the dissertation submitted to obtain the academic degree of Doctor of Natural Sciences (Dr. rer. nat.) and approved by the Bayreuth Graduate School of Mathematical and Natural Sciences (BayNAT) of the University of Bayreuth.

Thesis submitted: 22.07.2016

Date of defence: 18.11.2016

Acting director: Prof. Dr. Stephan Kümmel

Doctoral committee:

Prof. Dr. Birgit Weber (1st reviewer)

Prof. Dr. Katja Heinze (2nd reviewer)

Prof. Dr. Frank Hahn (chairman)

Prof. Dr. Hans-Werner Schmidt

By convention sweet is sweet, bitter is bitter, hot is hot, cold is cold, color is color; but in truth there are only atoms and the void.

— Democritus

Abbreviations

bipy	bis-pyridine
bpea	1,2-bis(4-pyridyl)ethane
bpee	1,2-bis(4-pyridyl)ethene
bppa	1,3-bis(4-pyridyl)propane
CHCl ₃	trichloromethane
CISSS	Coordination Induced Spin State Switch
χ_{MT}	Molar Magnetic Susceptibility
δ (Mössbauer)	Isomeric Shift
δ (NMR)	Chemical Shift
ΔE_Q	Quadrupole Splitting
dansyl	3-(dansylamido)propyltrimethoxysilane
DEI	Direct Electron Ionisation
dmap	4-(dimethylamino)pyridine
DMF	<i>N, N'</i> -Dimethylformamid
dpp	2,6-di(pyrazol-1-yl)pyridine
DSC	Differential Scanning Calorimetry
EPR	Electron Paramagnetic Resonance
ESI	Electrospray Ionisation
Et	Ethyl
EtOH	Ethanol
γ_{HS}	HS fraction
$\Gamma/2$	Half Width at Half Maximum
Him	1 <i>H</i> -Imidazole
HS	High Spin
IC	Internal Conversion
IR	Infra-red
ISC	Inter-system Crossing
LD-LISSC	Ligand-Driven Light Induced Spin State Change
LIESST	Light Induced Excited Spin State Trapping
LS	Low Spin
mCi	milli Curie
Me	Methyl
MeOH	Methanol
MRI	Magnetic Resonance Imaging
MS	Mass Spectrometer
μ_B	Bohr Magnetron
μ_{eff}	Effective Magnetic Moment
μ_{SO}	Spin-Only Magnetic Moment
NMR	Nuclear Magnetic Resonance
NP	Nanoparticle
PCA	1-pyrenecarboxaldehyde

Ph	Phenyl
phpy	4-phenylpyridine
pina	<i>N</i> -(pyrid-4-yl)isonicotinamide
PL	Photoluminescence
py	pyridine
RhB	Rhodamine B
RT	Room Temperature
<i>S</i>	Spin Number
SCO	Spin Crossover
SEM	Scanning Electron Microscopy
SQUID	Superconducting QUantum Interference Device
ST	Spin Transition
$T_{\frac{1}{2}}$	Spin Transition Temperature
terpy	terpyridine
TGA	Thermogravimetric Analysis
THF	Tetrahydrofuran
trz	1,2,4-triazole
UV-Vis	Ultraviolet-visible
vs.	<i>versus</i>

Table of Contents

1. Abstract/Zusammenfassung	1
2. Introduction	5
3. Overview	29
4. Large Thermal Hysteresis for Iron(II) Spin Crossover Complexes with <i>N</i> -(Pyrid-4-yl)isonicotinamide.	45
5. Iron(II) spin crossover complexes with diaminoanthracene-based Schiff base-like ligands: mononuclear complexes.	74
6. Iron(II) spin crossover complexes with diaminoanthracene-based Schiff base-like ligands: 1D coordination polymers.	108
7. Modulation of the ligand-based fluorescence of 3d metal complexes upon spin state change.	144
8. Synthesis and analysis of the optical properties of a phenanthroline-derived Schiff base-like Ru(II)-Ni(II) complex	172
9. Spin crossover iron(II) coordination polymer with fluorescent properties: correlation between emission properties and spin state.	190
10. List of Publications	217
11. Acknowledgement	222
12. Declaration	224

1. Abstract/Zusammenfassung

The aim of this work was to gain Fe(II) SCO complexes featuring cooperative STs (abrupt, with thermal hysteresis) by trying to build a network of short contacts (hydrogen bonds, π -interactions) in the crystal packing of the complexes in a crystal engineering way. Firstly, the bridging ligand **pina** was used in combination with an Fe(II) Schiff base-like complex to build SCO coordination polymers. The **pina** ligand is known to build hydrogels, so it was used in order to build a hydrogen bond network within the crystal lattice. In total, seven different solvates of the same **pina** coordination polymer were obtained when different solvents were used, some presenting remarkable SCO properties i.e. the sample $([\text{FeL1}(\text{pina})] \cdot x \text{ MeOH}/\text{H}_2\text{O})_n$ shows a 92 K wide hysteresis, which is, to the best of my knowledge, the largest hysteresis reported for Fe(II) SCO complexes. The crystal structure of the sample $([\text{FeL1}(\text{pina})] \cdot 2 \text{ MeOH})_n$ revealed that the **pina** ligand is indeed building a dense hydrogen bond network which is responsible for the cooperative ST observed.

Although SCO complexes with increased cooperativity were obtained by using the **pina** ligand, all synthesised compounds contain non-coordinating solvent molecules, making the SCO properties change upon solvent loss. In order to avoid dependency on the solvent content, the ligand design was re-oriented to favour π -interactions. New equatorial Schiff base-like ligands bearing a naphthalene substituent were synthesised and converted into mononuclear Fe(II) SCO complexes and coordination polymers. From the five mononuclear SCO complexes, the crystal structure of three could be determined, and enables a deep understanding of the structure-magnetic properties relationship i.e. the sample $[\text{FeL4}(\text{py})_2] \cdot \text{py}$ presents a two-step ST ($T_1 = 80 \text{ K}$, $T_2 = 150 \text{ K}$) which finds its origin in the bi-layered crystal structure with two inequivalent Fe(II) centres. Structure-defining C–H $\cdots\pi$ and C–H $\cdots\text{O}$ interactions were found to build an intricate network in all crys-

tal structures. For the coordination polymers, different bridging ligands were used (**bipy**, **bpea**, **bpee**, **bppa**) in order to further increase the cooperativity. The six new SCO coordination polymers present improved SCO properties in comparison to the corresponding mononuclear complexes, and the already reported coordination polymers bearing a benzene group. For example, the samples $([\text{FeL3}(\text{bpea})]\cdot\text{MeOH})_n$ and $([\text{FeL3}(\text{bpee})]\cdot\text{MeOH})_n$ show both a wide thermal hysteresis (23 K and 47 K, respectively). As no crystal structures were obtained, it can only be presumed that C–H $\cdots\pi$ and C–H $\cdots\text{O}$ interactions in combination with the building of 1D chains is responsible for the improved SCO properties.

The π -system of the ligand was then further extended from a naphthalene-ring to a phenazine-ring. The new Schiff base-like ligand showed luminescent properties and the focus of the research was then to investigate the possible interactions between the spin state of the included metal centre and the emission properties. The Ni(II) complex showed that it was possible to turn on/off the luminescence of the ligand upon Coordination Induced Spin State Switch (CISSS), between a luminescence diamagnetic square planar geometry and a non-luminescent paramagnetic square pyramidal geometry. Time-resolved fluorescence spectroscopy measurements revealed a non-radiative energy transfer taking place between the fluorophore and the paramagnetic metal centre. From this point, in order to gain a better understanding of the phenomenon, the phenazine fluorophore was exchanged for a phenanthrene-quinoxaline or a $[\text{Ru}(\text{bipy})_2]^{2+}$ block. In both cases, no influence of the spin state on the emission properties were observed. Finally, an Fe(II) metal centre was included in the phenazine ligand, and converted into the SCO coordination polymer $[\text{FeL1}(\text{bipy})]_n$. The obtained compound presents a wide hysteresis above room temperature ($T_{\frac{1}{2}} \uparrow = 371 \text{ K}$, $T_{\frac{1}{2}} \downarrow = 323 \text{ K}$), which was characterised by SQUID, DSC, and X-ray powder diffraction. The measurement of the emission properties in the solid state shows a dual emission (λ_1 , λ_2) for which the ratio λ_1/λ_2 is depending on the spin state of the metal centre. This unprecedented luminescent Fe(II) SCO coordination polymer opens a wide new research field and new possibilities for applications in the domain of sensors and memory devices.

Das Ziel dieser Arbeit war es, durch die Ausbildung von intermolekularen Wechselwirkungen (Wasserstoffbrückenbindungen, π -Wechselwirkungen) zwischen den Komplexen in einem "crystal engineering" Ansatz, Fe(II) Komplexe zu erhalten, die kooperative SCO (abrupt, mit thermischer Hysterese) zeigen. Zunächst wurde der verbrückende Ligand **pina** genutzt um, in Kombination mit einem Fe(II) Schiff Base ähnlichen Komplex, SCO Koordinationspolymere zu erhalten. Der **pina** Ligand ist bekannt dafür, Hydrogele zu bilden, und wurde daher benutzt, um ein Wasserstoffbrückenbindungsnetzwerk innerhalb der Kristallpackung aufzubauen. Insgesamt wurden, durch den Einsatz verschiedener Lösemittel, sieben verschiedene Solvate des gleichen **pina** Koordinationspolymers erhalten. Einige zeigen bemerkenswerte SCO Eigenschaften, z.B. zeigt die Probe $([\text{FeL1}(\text{pina})] \cdot x \text{ MeOH}/\text{H}_2\text{O})_n$ eine 92 K breite Hysterese, welche, nach meinem Wissen, die größte bekannte Hysterese für einen Fe(II) SCO Komplex ist. Die Kristallstruktur der Probe $([\text{FeL1}(\text{pina})] \cdot 2 \text{ MeOH})_n$ zeigte, dass der **pina** Ligand tatsächlich ein dichtes Wasserstoffbrückenbindungsnetzwerk bildet, welches für den beobachteten, kooperativen SCO verantwortlich ist.

Obwohl SCO Komplexe mit erhöhter Kooperativität durch die Benutzung des **pina** Liganden erhalten wurden, enthalten alle synthetisierten Verbindungen unkoordinierende Lösungsmittelmoleküle, weshalb sich die SCO Eigenschaften durch Verlust des Lösungsmittels verändern. Um eine Abhängigkeit des Lösungsmittelanteils zu verhindern, wurde das Liganddesign umorientiert, um π -Wechselwirkungen zu favorisieren. Neue äquatoriale Schiff Base ähnliche Liganden mit einem Naphthalenrückrad wurden synthetisiert und zu einkernigen Fe(II) SCO Komplexen und Koordinationspolymeren umgesetzt. Von den fünf einkernigen SCO Komplexen konnte von dreien die Kristallstruktur bestimmt werden, und diese ermöglichen ein tieferes Verständnis der Struktur-Eigenschafts Beziehungen, z.B. zeigt die Probe $[\text{FeL4}(\text{py})_2] \cdot \text{py}$ einen zweistufigen SCO ($T_1 = 80 \text{ K}$, $T_2 = 150 \text{ K}$), welcher seinen Ursprung in einer zweilagigen Kristallstruktur mit zwei unabhängigen Fe(II) Zentren hat. Strukturbestimmende C-H \cdots π und C-H \cdots O Wechselwirkungen bilden ein kompliziertes Netzwerk in allen Kristallstrukturen. Um die Kooperativität weiter zu erhöhen wurden verschiedene, verbrückende Liganden (**bipy**, **bpea**, **bpee**, **bppa**) für die Synthese von Koordinationspolymeren genutzt. Die sechs neuen SCO Ko-

ordinationspolymere zeigen im Vergleich mit den dazugehörigen einkernigen Komplexen, und den bereits bekannten Koordinationspolymeren mit einem Benzenring, verbesserte SCO Eigenschaften. Zum Beispiel zeigen die beiden Proben $([\text{FeL3}(\text{bpea})]\cdot\text{MeOH})_n$ und $([\text{FeL3}(\text{bpee})]\cdot\text{MeOH})_n$ eine breite thermische Hysterese (23 K und 47 K). Da keine Kristallstrukturen erhalten wurden, kann nur angenommen werden, dass C–H $\cdots\pi$ und C–H \cdots O Wechselwirkungen in Kombination mit der Ausbildung von 1D Ketten für die verbesserten SCO Eigenschaften verantwortlich sind.

Das π -System des Liganden wurde dann von einem Naphthalenring zu einem Phenazinring weiter ausgebaut. Der neuer Schiff Base ähnliche Ligand zeigte lumineszente Eigenschaften, und rückt nun den Fokus der Forschung auf die Untersuchung von Wechselwirkungen zwischen dem Spinzustand des Metallzentrums und den Emissionseigenschaften. Der entsprechende Ni(II) Komplex zeigt, dass es möglich ist, die Lumineszenz des Liganden mittels eines *Coordination Induced Spin State Switches* (CISSS), zwischen einer lumineszenten, diamagnetischen, quadratisch planaren Koordinationsgeometrie und einer nicht-lumineszenten, paramagnetischen, quadratisch pyramidalen Geometrie ein- und auszuschalten. Zeitaufgelöste Fluoreszenzspektroskopie Messungen zeigen, dass ein strahlungsfreier Energietransfer zwischen dem Fluorophor und dem paramagnetischen Metallzentrum stattfindet. Von diesem Punkt an, um ein besseres Verständnis des Phänomens zu bekommen, wurde das Phenazin Fluorophor gegen einen Phenanthren-quinoxalin oder einen $[\text{Ru}(\text{bipy})_2]^{2+}$ Block ausgetauscht. In beiden Fällen wurde kein Einfluss des Spinzustands auf die Emissionseigenschaften beobachtet. Letztendlich wurde der Fe(II) Komplex des Phenazinliganden hergestellt und zu dem SCO Koordinationspolymer $[\text{FeL1}(\text{bipy})]_n$ umgesetzt. Die dabei erhaltene Verbindung zeigt eine breite Hysterese oberhalb von Raumtemperatur ($T_{\frac{1}{2}} \uparrow = 371 \text{ K}$, $T_{\frac{1}{2}} \downarrow = 323 \text{ K}$), welche mittels SQUID, DSC, und Röntgen-Pulverdiffraktometrie charakterisiert wurde. Die Messungen der Emissionseigenschaften im Feststoff zeigen eine duale Emission (λ_1 , λ_2), für welche das Verhältnis λ_1/λ_2 von dem Spinzustand des Metallzentrums abhängt. Dieses bisher beispiellose Fe(II) SCO Koordinationspolymer eröffnet ein weites Feld für neue Forschung und neue Anwendungsmöglichkeiten in Bereichen der Sensorik und Datenspeicherung.

2. Introduction

2.1 The Spin Crossover Phenomenon

In 1931, *Cambi et al.* reported a series of N,N' -alkyl-dithiocarbamate iron(III) complexes for which the magnetisation does not follow the Curie law.^[1] The unusual magnetic behaviour was further investigated and *Cambi et al.* determined firstly that the type of the alkyl substituent influences the behaviour, secondly that the complexes have upper and lower magnetisation limits corresponding to $S = \frac{5}{2}$ and $S = \frac{1}{2}$, and finally came across the observation that two isomers of the same complex do not present the same magnetic behaviour (see Figure 2.1).^[2] It is only through the development of the *Crystal Field Theory* by Hans Bethe^[3] and John H. Van Vleck^[4] in the 30s, and its later use by coordination chemists in the 50s^[5] that this firstly described "unusual magnetic behaviour" is understood today as the Spin Crossover (SCO) Phenomenon.

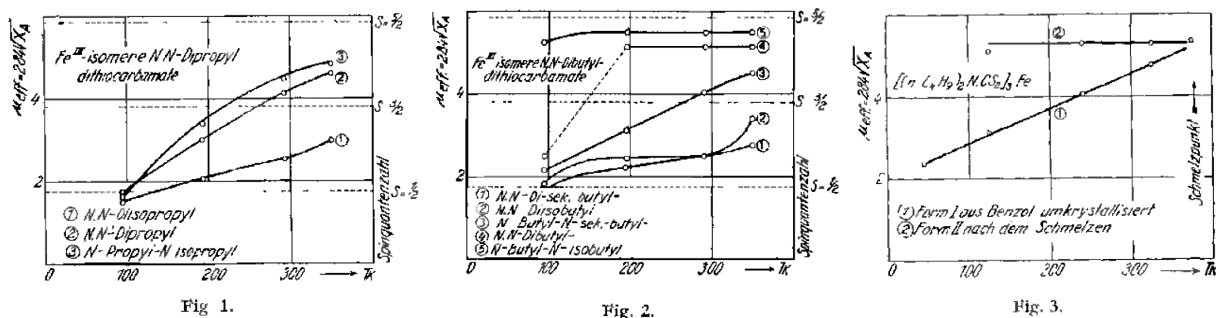


Figure 2.1: "Unusual magnetic behaviour" of a series of N,N' -alkyl-dithiocarbamate iron(III) complexes reported by *Cambi et al.*^[2]

When a transition metal ion with a $3d^4-3d^7$ electronic configuration is the centre of an octahedral complex, the splitting of the d orbitals into the two levels t_{2g} and e_g allow two possible spin states: a high spin (HS) state for which the first rule of Hund is respected

(maximisation of S), and a low spin (LS) state which breaks Hund's rules (depicted in Figure 2.2 in the case of a $3d^6$ metal ion). Most complexes have a defined state, either HS when the total spin pairing energy P is significantly larger than the crystal field strength Δ_O (i.e. $[\text{Fe}(\text{H}_2\text{O})_6]^{2+}$), or LS when $P \ll \Delta_O$ (i.e. $[\text{Fe}(\text{CN})_6]^{4-}$). When P is in the same order of magnitude as Δ_O , SCO is possible, and the complex can switch between the HS and LS states, classically upon physical stimuli such as temperature change, pressure application, or light irradiation.^[6-8]

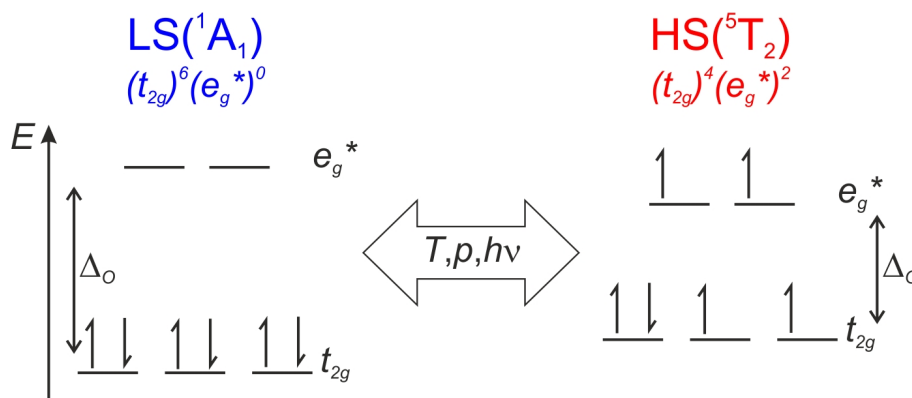


Figure 2.2: Schematic representation of the HS and LS state of a $3d^6$ metal ion in an octahedral coordination sphere.

Up to day, SCO has been reported for Cr(II),^[9-14] Mn(II),^[15] Mn(III),^[16,17] Fe(III),^[1,2,7,18] Co(II),^[7,19,20] and Co(III) complexes^[21,22], however Fe(II) SCO complexes^[6,7] attract the most attention as they switch between a paramagnetic HS state ($S = 2$) and a diamagnetic LS state ($S = 0$) and are most frequently observed. Upon SCO, not only the magnetic properties of the Fe(II) centre changes, but also the electronic properties (i.e. colour) as the HS and the LS state have different electronic ground states (respectively 5T_2 and 1A_1). As consequence of the population of the e_g^* antibonding orbitals in the HS state, the volume of the Fe(II) centre increases when transiting from the LS to HS state, which can be observed on the metal-ligand distances which undergo an elongation of ≈ 0.2 Å.^[23] This elongation has further consequences on the vibrational modes of the molecule. Those changes are often represented either in a Tanabe-Tsugano diagram as function of the crystal field strength Δ_O or in a Jablonski diagram as function of the metal-ligand distance r_{ML} (see Figure 2.3). All those changes offer a wide variety of methods to follow

SCO, as the magnetic changes can be followed with a SQUID magnetometer, a NMR or an EPR spectrometer; the electronic changes can be measured using absorption spectroscopy or diffuse reflectance spectroscopy; and the structural and vibrational changes can be measured with X-ray diffraction (on single crystal and/or on powder), IR spectroscopy, Raman spectroscopy, and ^{57}Fe Mössbauer spectroscopy. Finally a spin crossover complex will take or release energy (heat) upon spin transition (ST) which can be detected with calorimetric measurement (DSC).

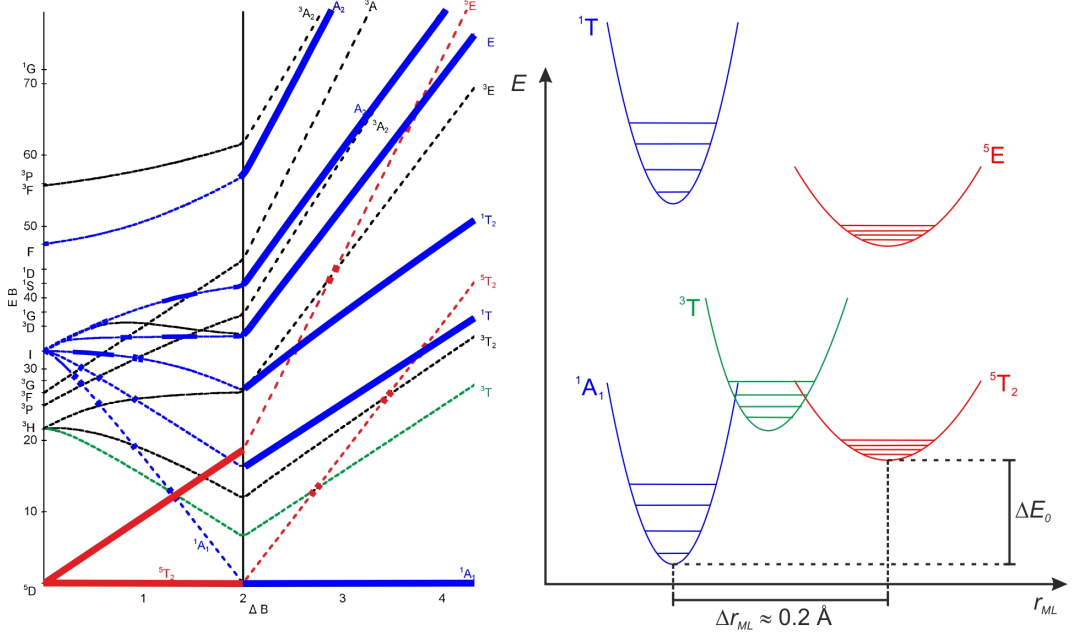


Figure 2.3: Tanabe-Tsugano diagram for a $3d^6$ metal ion^[24] (left) and Jablonski diagram (right). LS state is represented in blue, HS state in red.

2.1.1 Thermal SCO

The driving force for a temperature-stimulated spin transition lies in the thermodynamics. If the spin transition is set as a LS to HS reaction:



The reaction will take place if the free enthalpy ΔG is negative:

$$\Delta G = \Delta H - T\Delta S \quad (2.2)$$

$$\text{if } \Delta G < 0 \tag{2.3}$$

$$\text{then } \Delta H < T\Delta S \tag{2.4}$$

The enthalpy of the HS state (H_{HS}) is higher than the enthalpy of the LS state (H_{LS}) because the latter one is stabilised through the complete population of the t_{2g} orbitals. Therefore, in this reaction, ΔH is positive. The entropy of the HS state (S_{HS}) is bigger than the entropy of the LS state (S_{LS}), because of the greater disorder of the electron distribution in the orbitals in the HS state. Therefore, ΔS is also positive. Then the equation 2.4 can be fulfilled when the temperature T is high enough, that the product $T\Delta S$ can overcome the enthalpy term ΔH . At the equilibrium point $LS \rightleftharpoons HS$, the free enthalpy ΔG is zero, and the temperature of the equilibrium ($T_{\frac{1}{2}}$) is defined as:

$$T_{\frac{1}{2}} = \frac{\Delta H}{\Delta S} \tag{2.5}$$

2.1.2 Light Induced Excited Spin State Trapping

The SCO phenomenon can be triggered with light irradiation, this process is called the *Light Induced Excited Spin State Trapping* (LIESST) effect.^[6,25] At very low temperature, a SCO complex in its LS state is irradiated (usually with green light) and it leaves its ground state 1A_1 for an excited state (i.e. 1T). Upon relaxation, a first intersystem crossing (ISC) can occur, and the complex is now in an intermediate triplet state 3T . Now the complex can either relax towards its original ground state 1A_1 , or relax towards a metastable HS state 5T_2 . Once in the metastable HS state, at very low temperature, the molecule is then trapped at the bottom of the potential well and cannot overcome the energy barrier towards the LS ground state (see Figure 2.4). Upon warming, the trapped molecule will ascend in the potential well and finally relax towards its LS state. The reverse process is also possible, the trapping of a metastable LS state at very low temperature (reverse-LIESST), but then usually the irradiation light used is red. The colour of the irradiation wavelength come from the energy of the respective metal-centred transitions.

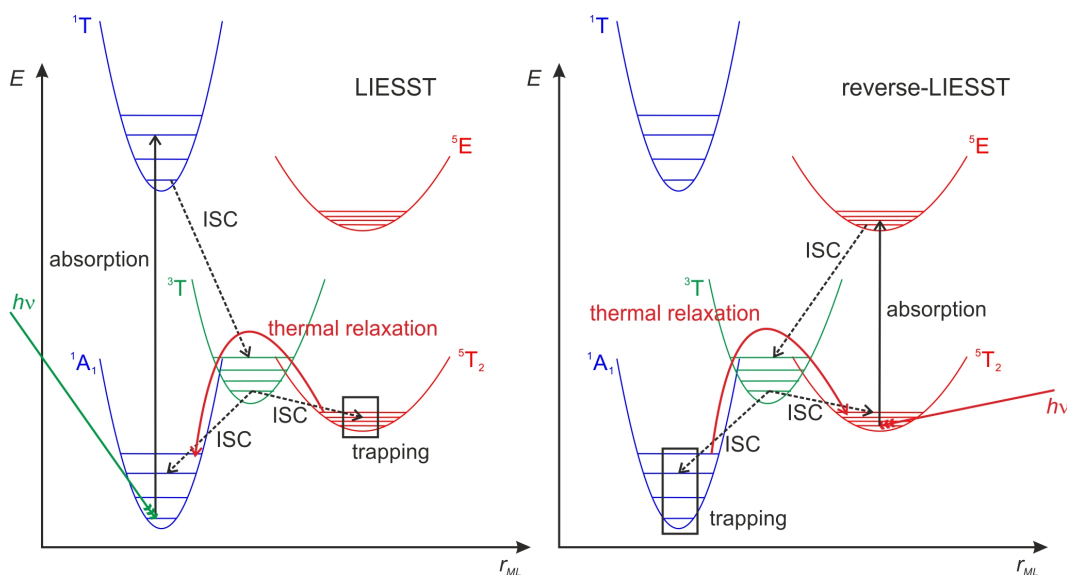


Figure 2.4: Jablonski diagram representing the LIESST (left) and reverse-LIESST (right) effects. Thermal relaxation happens at high temperature.

Technically, a LIESST experiment is carried out this way: firstly the sample is cooled down to 10 K; secondly the sample is irradiated, and excited into its metastable HS state; finally the sample is slowly warmed up and relaxes toward the LS state. The $T(LIESST)$ is then measured, which is the temperature at which half of the molecules have relaxed. A relationship between $T(LIESST)$ and $T_{\frac{1}{2}}$ has been theoretically and empirically established:^[25,26]

$$T(LIESST) = T_0 - 0.3T_{\frac{1}{2}} \quad (2.6)$$

where T_0 is the extrapolated $T(LIESST)$ when $T_{\frac{1}{2}} \rightarrow 0$. It has been found that T_0 is depending on the denticity of the ligand coordinating the SCO metal centre (see Figure 2.5).

2.1.3 SCO in the solid state: cooperativity and hysteresis

SCO can be observed in solution as well as in the solid state, however one system does not necessarily exhibit ST in both phases. In solution, interactions between the SCO centres are negligible, and the spin transition follows a temperature-dependent Boltzmann distribution, in other words: a gradual ST (see Figure 2.6). In the solid state, some

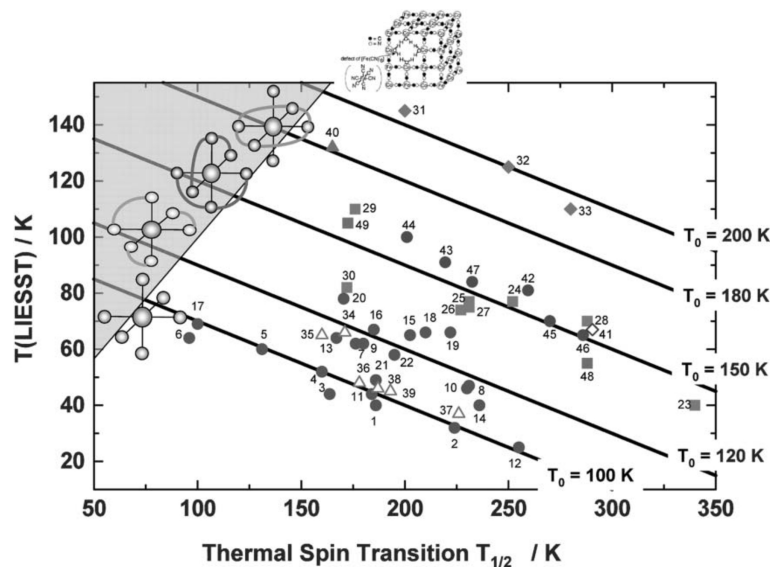


Figure 2.5: Variation of $T(LIESST)$ versus $T_{\frac{1}{2}}$ for spin crossover compounds. The region in gray is meaningless as the $T(LIESST)$ temperature has to be inferior or at least equal to $T_{\frac{1}{2}}$.^[25]

systems also present gradual SCO,^[27] however abrupt STs are also observed, where an electron-phonon coupling between the transiting molecules leads to a cooperative ST.^[28] One model developed by *Spiering et al.*^[29–31] describes the cooperative phenomenon using elastic interactions with at its basis the metal-ligand distance change upon ST. It is proposed that such a change at point defects of a solid will lead to an internal pressure which is then propagated through the crystal lattice via phonon interactions, speeding up the ST process for the other SCO centres. This model was experimentally confirmed through the study of dilution effects for the SCO coordination polymer $[\text{Fe}_x\text{Zn}_{1-x}(\text{ptz})_6](\text{BF}_4)_2$ ($0.1 \leq x \leq 1$) (ptz = 1-propyltetrazole).^[32] Such cooperative SCO can be transmitted through the crystal lattice by many means: the formation of coordination polymers, or metal-organic frameworks can lead to cooperative SCO, but long range interactions can also lead to abrupt STs when the spin centres interact with each other through hydrogen bonds, π -interactions, or Van der Waals interactions. For example, the mononuclear complex $[\text{FeL}(\text{Him})_2]$ ^[33] presents abrupt ST with a 70 K-wide hysteresis, and it was revealed that the dense hydrogen bond network of the crystal lattice was responsible for the cooperative SCO.^[34]

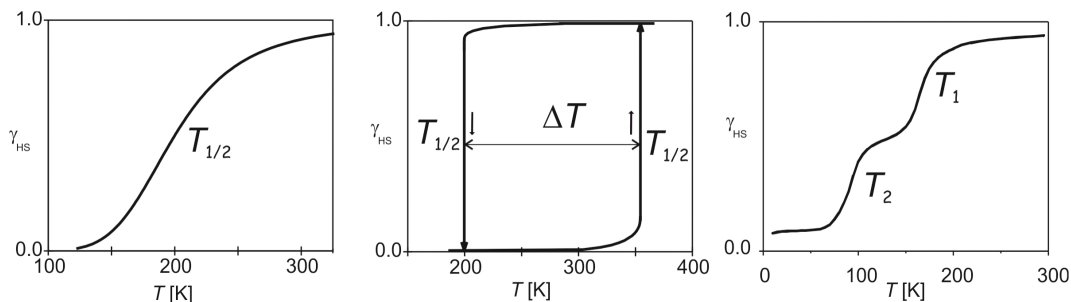


Figure 2.6: Different types of SCO: gradual (left), abrupt with hysteresis (centre), stepwise (right).

Some STs present another effect of high interest: a thermal hysteresis, also known as memory effect. A thermal hysteresis appears when the HS to LS and LS to HS transition do not happen at the same temperature ($T_{\frac{1}{2}\uparrow} \neq T_{\frac{1}{2}\downarrow}$). A simple way to explain this phenomenon is to consider that upon ST, the SCO molecules stabilise their newly acquired spin state through structural changes i.e. crystallographic phase transition, formation or breaking of short contacts. This stabilisation may happen upon HS to LS ST, LS to HS ST, or upon both STs (see Figure 2.7). The mononuclear complex $[\text{FeL}(\text{Him})_2]$ ^[33] exemplifies this phenomenon: in the crystal packing, very specific hydrogen bonds connect *1H*-imidazole with the first coordination sphere of the Fe(II) centre ($\text{Fe}-\text{O}\cdots\text{H}-\text{N}$). Upon HS to LS ST, the metal-ligand distance decreases, and therefore the hydrogen bond length increases, decreasing its electron pulling effect ($\text{Fe}-\text{O}\cdots\cdots\text{H}-\text{N}$). As the hydrogen bond connects directly to the first coordination sphere, this elongation upon SCO has a drastic influence on the crystal field strength, and leads to the 70 K-wide hysteresis. As well as for cooperativity, such interactions can be induced by hydrogen bonds,^[34] π -interactions,^[35] and Van der Waals interactions.^[20,36] It was proposed by Halcrow that not only the volume change upon SCO can be responsible for a thermal hysteresis, but any structural changes upon SCO in general, e.g. rotation of a ligand from LS to HS.^[37]

2.1.4 Applications

Many potential applications were already proposed for SCO complexes, or SCO composite materials, but they are depending on the type of ST. Abrupt ST with hysteresis are particularly indicated for applications in the domain of memory devices and displays, as

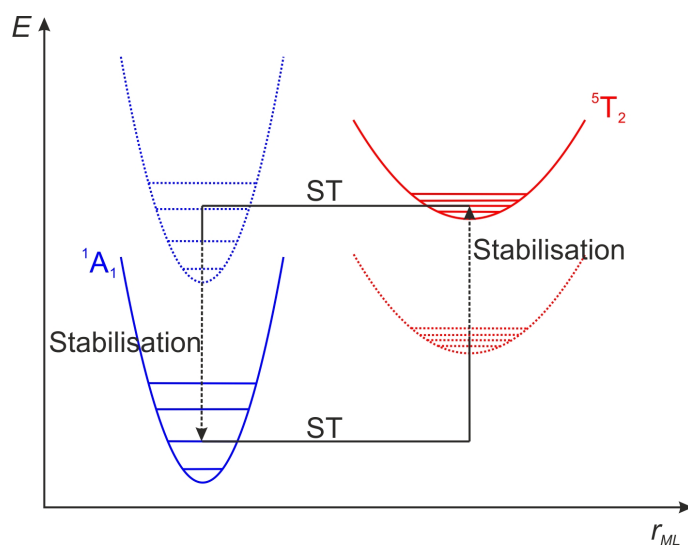


Figure 2.7: Jablonski diagram depicting the structural stabilisation(s) responsible for hysteresis phenomenon.

in the bistable domain, the SCO material can exist in the LS or the HS state at the same temperature. If one uses the LS state as a 0 and the HS as a 1, the SCO material becomes a memory device (see Figure 2.8).^[38,39] A perfect SCO material would exhibit a stable 100 K-wide hysteresis around room temperature. Another application domain is sensorics: a SCO material exhibiting a gradual SCO can be used as thermometer over the temperature span of the transition.^[40] Irreversible spin crossover complexes have recently been commercialised by *Olikrom*, and will be used by *Airbus* as paint for critical parts of the planes, in order to detect any pressure or temperature changes happening in-flight.^[41] Finally SCO complexes are proposed as MRI contrast agents.^[42]

2.1.5 Coordination Induced Spin State Switch

The spin state of Ni(II) complexes can also be switched, however not with a physical stimulus, but with a chemical stimulus. A diamagnetic ($S = 0$) square planar Ni(II) complex turns into a paramagnetic ($S = 1$) square pyramidal/octahedral complex upon coordination of (solvent) molecule(s) (see Figure 2.9). The *Coordination Induced Spin State Switch* (CISSS), then often observed in solution, is chemically induced and can be investigated with SQUID magnetometry, UV-Vis spectroscopy, NMR Spectroscopy (Evans method), often in function of the concentration of ligating molecules. A well

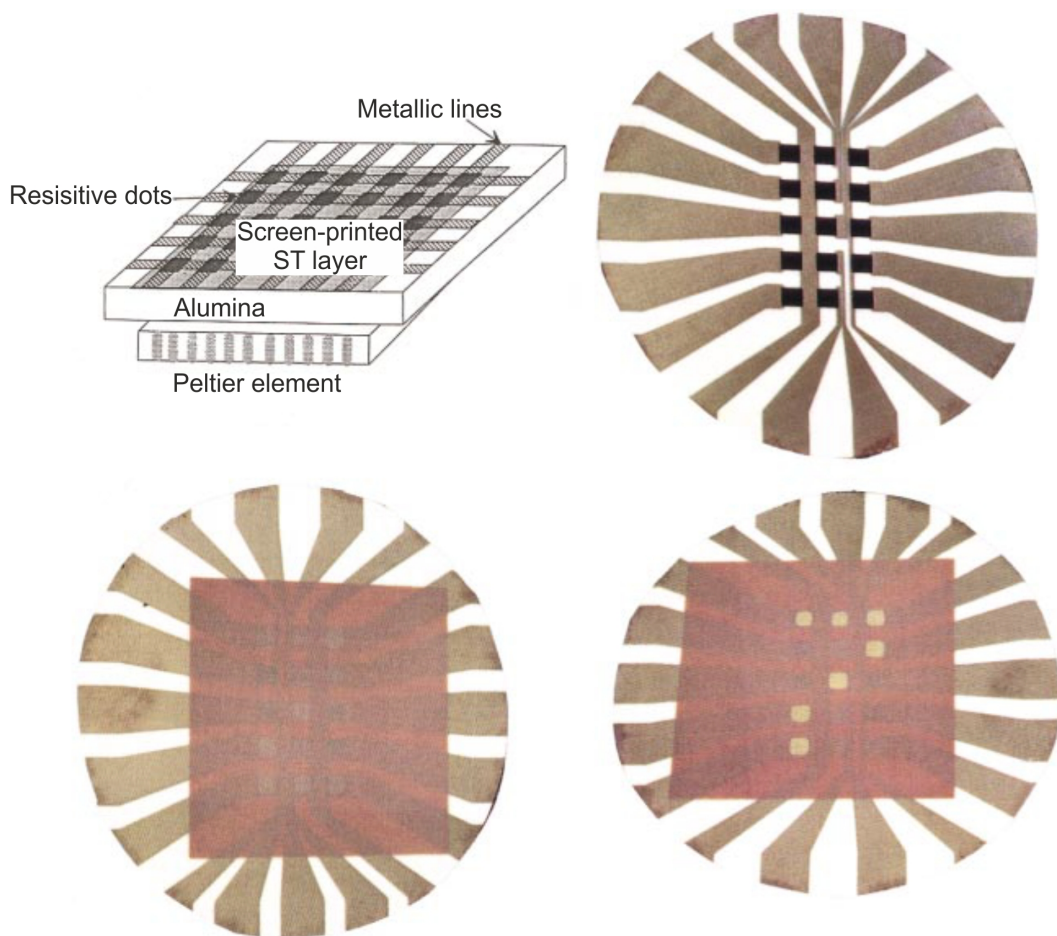


Figure 2.8: Schematics of a screen-printed ST-based display (top left), alumina support with resistive dots (top right), alumina support with the screen-printed ST-based material (bottom left), and information written on the display (the ST-based material goes from purple (LS state) to white (HS state) upon heating).^[38,39]

known system for this phenomenon was developed by *Herges et al.*, and consists of a Ni(II) porphyrin complex with perfluorinated aromatic substituents.^[43] The system in solution exhibits CISSS when in contact with pyridine-based molecules. The system was then modified to bear an azopyridine arm whose N=N double bond can be photoswitched reversibly from *trans* to *cis* configuration. In the *cis* configuration, the nitrogen atom of the pyridine is close enough to the Ni(II) centre to coordinate and induce spin state switch (see Figure 2.10).^[44,45] The chemical stimulus to induce CISSS is then photo-stimulated, and the phenomenon becomes a *Ligand-Driven Light Induced Spin State Change* (LDLISSC). This system was lately modified to be soluble in water, and was proposed as MRI contrast agent.^[46]

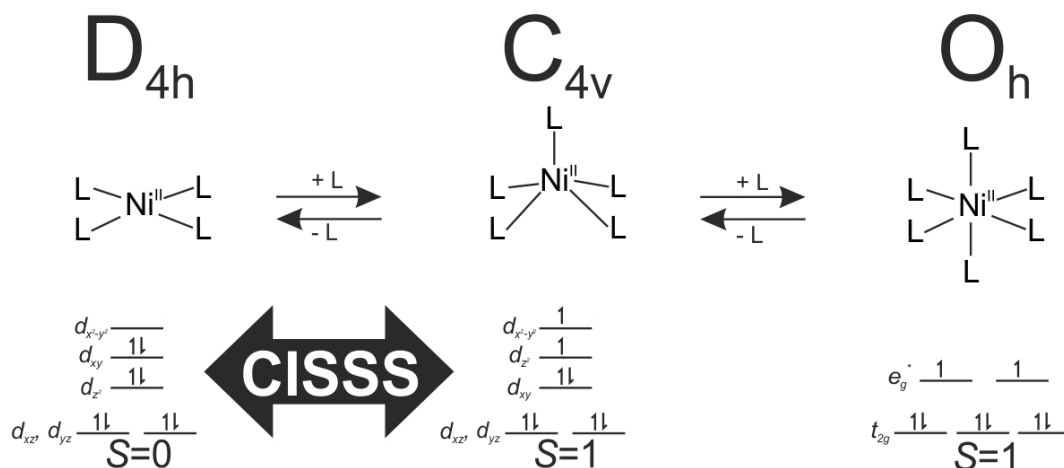


Figure 2.9: Scheme of the different spin states of a Ni(II) complex depending on its coordination sphere.

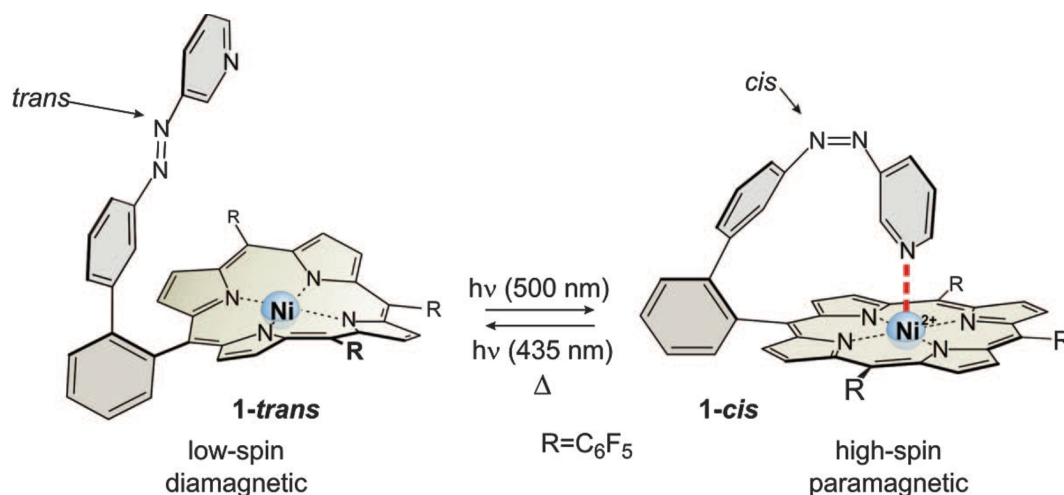


Figure 2.10: Reversible light-induced magnetic switching of azopyridine-functionalised Ni(II) porphyrin complex.^[45]

2.2 SCO and Luminescence

In the last years, part of the research in the domain of SCO complexes was directed at synthesising, characterising, and understanding multifunctional systems where a SCO function is coupled with another feature, i.e. liquid crystallinity,^[47] conductivity,^[48] magnetic ordering,^[48] or luminescence.^[49] Considering this thesis, the coupling between SCO and luminescent properties is of particular interest. In literature, two main strategies are used to couple those two features: the first is to create a composite material made of a

SCO complex and a luminescent material; the second is to covalently bind a fluorophore to a SCO complex at the molecular level. In the next sections, a short introduction to photoluminescence will be given, as well as some relevant examples for both strategies.

2.2.1 Photoluminescence

Photoluminescence is defined as the spontaneous emission of radiation from an electronically excited species or from a vibrationally excited species not in thermal equilibrium with its environment, arising from direct photoexcitation of the emitting species.^[50] With the right irradiation, a luminescent species will absorb the photon and go from its ground state S_0 to its excited state S_1 . In its excited state, the species can relax towards its ground state by emitting light (*fluorescence*), or through an internal conversion (IC, non-radiative). IC can be seen as relaxation through vibrations or collisions with other molecules. Some systems, instead of relaxing back to the ground state, undergo an inter-system crossing (ISC) towards the triplet state T_1 . From this excited state T_1 , the system can either relax by emitting light (*phosphorescence*), or through an IC. The phosphorescent emission is a forbidden transition as it goes from a triplet state to a singlet state. Therefore the lifetime of the phosphorescent excited states are generally longer.^[51] As the phosphorescent excited state is a triplet state, molecular oxygen in its triplet ground state will quench phosphorescent emission. In Figure 2.11, the different transitions are illustrated in a Jablonski diagram, and the corresponding characteristic times are given.

Fluorescence and phosphorescence are extremely sensitive phenomena, particularly to the environment of the emitting species. Parameters such as temperature, the viscosity or dielectric constant of the used solvent, or the type of the solvent used can have drastic influences on the position, shape, and intensity of the emission feature.^[51] Structural changes can also influence the emission properties of a molecule: for example, the monoanion and dianion of the well-known fluorescein are fluorescent, however the neutral and protonated forms are non-emitting.^[52] On this basis, a major environmental or structural change such as a SCO must have an influence on neighbouring fluorophores.

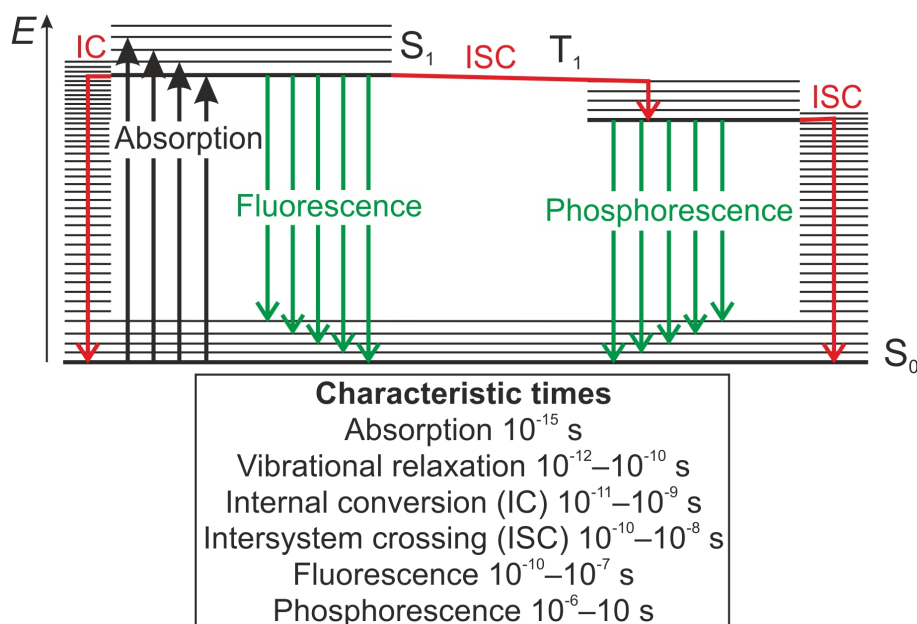


Figure 2.11: Jablonski diagram of the different phenomena involved in photoluminescence. Black arrows represent radiative excitation (absorption), green arrows radiative de-excitation processes, and red arrows non-radiative processes. Characteristic times taken from *Valeur et al.*^[51]

2.2.2 Luminescent SCO composite materials

Electroluminescent thin films doped with a SCO complex

In 2008, *Matsuda et al.* reported the fabrication of a temperature-dependent electroluminescent device based on a thin film of the SCO complex $[\text{Fe}(\text{dpp})_2](\text{BF}_4)_2$ doped with Chlorophyll *a* (dpp = 2,6-di(pyrazol-1-yl)pyridine) (depicted in Figure 2.12).^[53–55] The SCO complex $[\text{Fe}(\text{dpp})_2](\text{BF}_4)_2$ itself presents an abrupt SCO at $T_{\frac{1}{2}} = 259$ K.^[56] It was demonstrated that the thin film Chlorophyll *a*: $[\text{Fe}(\text{dpp})_2](\text{BF}_4)_2$ in its HS state is electroluminescent, but not in the LS state. When the doping material was changed to Nile Red (9-diethylamino-5-benzo[α]phenoxazinone), the thin film was then always electroluminescent regardless of the spin state. The authors concluded that the on/off switching is due to a change of the molecular orbital level of the complex $[\text{Fe}(\text{dpp})_2](\text{BF}_4)_2$ upon ST.

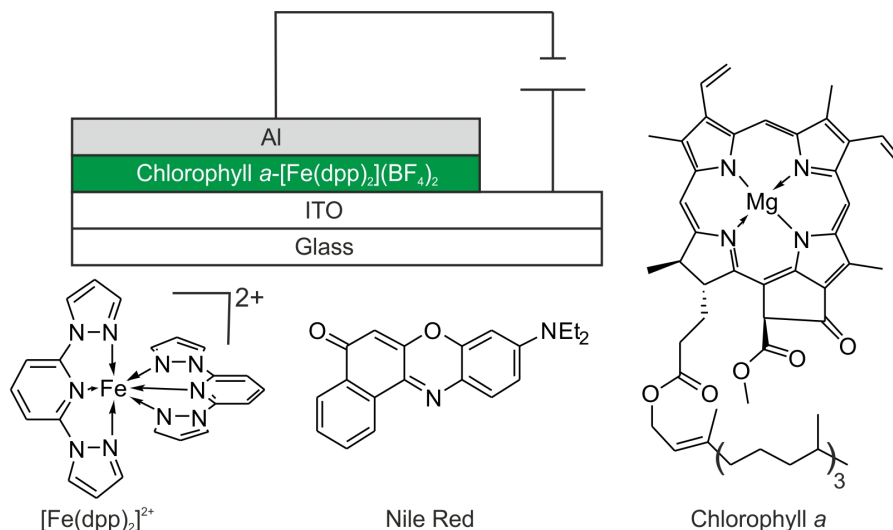


Figure 2.12: The fabricated electrochromic device fabricated by *Matsuda et al.*,^[54] and chemical structure of [Fe(dpp)₂]²⁺ (left), Nile Red (middle), and Chlorophyll *a* (right).

SCO-core-luminescent-shell nanoparticles

In 2011, *Colacio et al.* reported the synthesis of core-shell nanoparticles (NPs) for which the core is made of the complex [Fe_(1-x)Zn_x(Htrz)₂(trz)](BF₄)₂ ($x = 0, 0.2, 0.5$) (trz = 1,2,4-triazole), and the shell is a silica layer on which is grafted the organic fluorophore 3-(dansylamido)propyltrimethoxysilane (**dansyl**) (see Figure 2.13). The SCO core exhibits an hysteresis with varying $T_{\frac{1}{2}\uparrow}$ and $T_{\frac{1}{2}\downarrow}$ in function of the Fe:Zn ratio. Fluorescence spectroscopy showed that the emission properties of the NPs are strongly dependent on their spin state, and that the HS state is emitting up to three times more than the LS state. Absorption spectra in the HS and the LS states revealed an overlap of the $^1A_1 \rightarrow ^1T$ transition of the LS state with the emission peak of the **dansyl** group, quenching the emission of the NPs.^[57]

Co-crystallisation of SCO complexes with a luminescent partner

In this section, two examples of SCO material where a fluorescent dye was co-crystallised with a SCO complex will be presented. A first example with a SCO complex of the triazole family was reported by *Matsukiwono et al.*: an Fe(II) 1,2,4-triazole chain bearing a lipophilic rest (4-C₁₂H₂₅OC₃H₆-trz) was crystallised with the fluorescing 1-pyrenesulfonate counter-anion (see Figure 2.14). The authors observed the same effect as for the latter

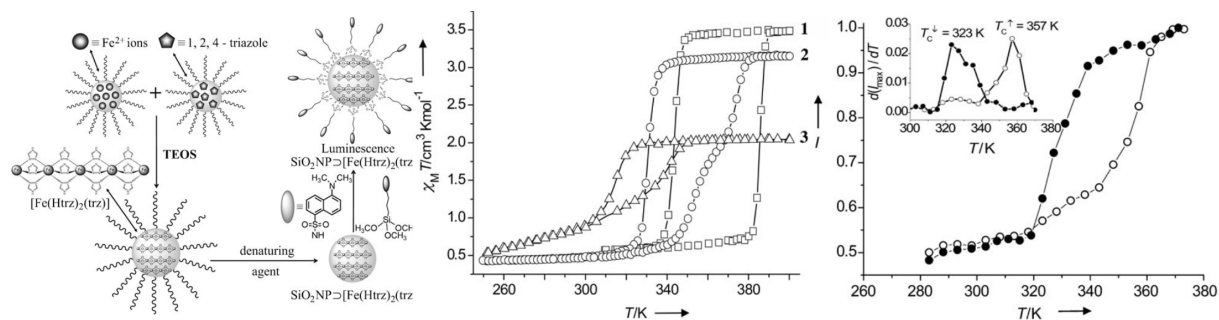


Figure 2.13: Synthesis scheme of the SCO-core-luminescent-shell nanoparticles (left); Magnetic measurement of **dansyl**-SiO₂NP \supset [Fe_(1-x)Zn_x(Htrz)₂(trz)](BF₄)₂ (**1**: $x = 1$; **2**: $x = 0.2$; **3**: $x = 0.5$) (middle); Thermal variation of the fluorescence intensity at 495 nm upon heating (open circles) and cooling (closed circles) (right).^[57]

SCO-core-luminescent-shell NPs: the fluorescence of the counter-anion is quenched in the LS state due to overlap of the emission peak with the $^1A_1 \rightarrow ^1T$ transition.^[58]

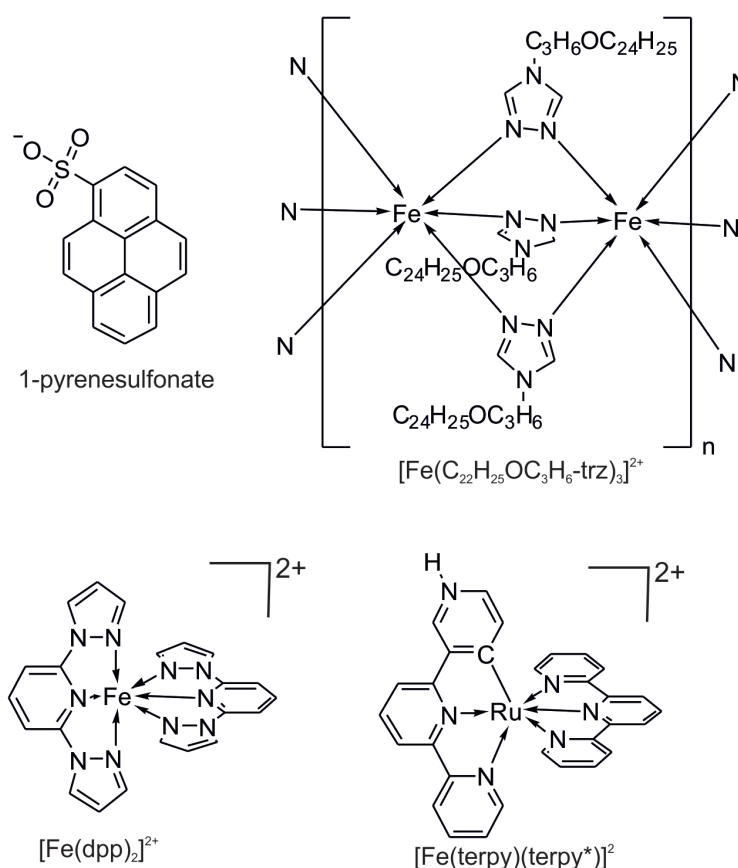


Figure 2.14: Chemical structure of the different SCO complexes and fluorophores used for the creation of co-crystallised materials.

A second example was reported by *Halcrow et al.* in 2015: different solid solutions of the SCO complex $[\text{Fe}(\text{dpp})_2](\text{BF}_4)_2$ and the phosphorescent complex $[\text{Ru}(\text{terpy})(\text{terpy}^*)](\text{BF}_4)_2$ were prepared by co-crystallisation of both complexes. After demonstrating that only co-crystals were obtained, the magnetic properties were investigated. The co-crystals exhibit all SCO, however the authors could not observe any emission upon irradiation in the solid state, regardless of the spin state of the Fe(II) complex.^[59]

2.2.3 Luminescent SCO complexes

The second strategy to couple luminescence and SCO is to covalently bind a fluorophore with a SCO complex. A first example from the triazole family: *Garcia et al.* reported the synthesis of a dinuclear Fe(II) complex (see Figure 2.15) where the triazoles have for substituent on the fourth position a salicylidene fluorescing group, presenting an abrupt ST at 150 K. The dinuclear complex exhibits one emission feature at $\lambda = 394$ nm in the LS state, however in the HS state the dinuclear features two emission peaks: one is the emission feature of the LS state shifted to 414 nm, and a new peak at 510 nm. It also seems that the evolution of the intensity of the emission features with temperature is irregular in the region of the ST, however it was not discussed by the authors. The correlation between the emission wavelength and the magnetic properties, as well as the crystal structure of the dinuclear complex, and the emission spectra at different temperatures are shown in Figure 2.15.^[60]

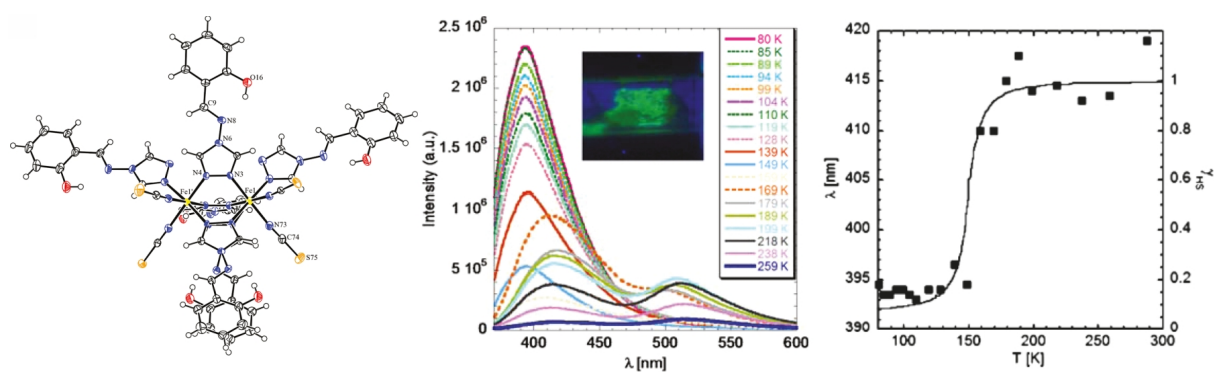


Figure 2.15: Crystal structure of the fluorescing Fe(II) dinuclear complex (left), emission spectra at different temperature (middle), and correlation between the emission wavelength and the magnetic properties (right).^[60]

Another luminescent example from the triazole family was reported by *Wang et al.*. The fluorophores 1-pyrenecarboxaldehyde (PCA) and Rhodamine B (RhB) were grafted on a Fe(II) aminotriazole coordination polymer. The grafted polymers exhibit a rather gradual SCO with a relatively small 10 K hysteresis between 200 and 300 K. The evolution of the fluorescence intensity is irregular regards to temperature in the region of the SCO, and allows to follow the spin crossover through measurement of the emission properties. In Figure 2.16, the chemical structure of the coordination polymer is depicted, as well as the plots of the evolution of the intensity of the fluorescence and the first-order derivative of the magnetic susceptibility temperature product *vs.* temperature.^[61] There are also examples where a fluorophore was attached to a SCO complex, however no coupling or correlation between the spin state and the emission properties were observed.^[62,63]

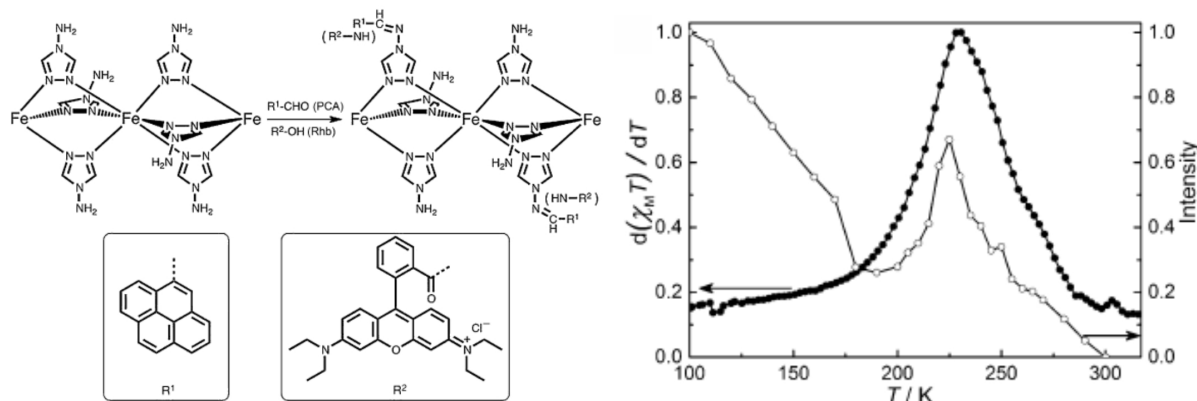


Figure 2.16: Synthesis pathway of RhB- and PCA-grafted Fe(II) triazole coordination polymers (left) and evolution of the intensity of the fluorescence and the first-order derivative of the magnetic susceptibility temperature product *vs.* temperature.^[61]

2.3 Ligand System

The complexes presented in this work are all based on tetradentate Schiff base-like ligands reported by *Jäger et al.* in 1966.^[64] When deprotonated, the two chelate cycles can easily bind to a metal centre i.e. V(IV),^[65] Fe(II),^[33,34,66–92] Fe(III),^[66,68,77,93] Co(II),^[94] Ni(II),^[64,95] Cu(II),^[64,65,95,96] Zn(II).^[97] It was quickly observed that some Fe(II) complexes with the N₄O₂ coordination sphere present SCO.^[67] The Schiff base-like ligand is optimal for the synthesis of SCO complexes as its carbonyl- substituents allow a fine

tuning of the crystal field strength. Moreover, the obtained complexes are neutral, which leaves any counter-anion effects out of the picture. As explained in Section 2.1.3, short- and long-range interactions between the spin centres are needed to obtain cooperative SCO. Therefore the starting Schiff base-like ligand was modified to bear different groups on the phenyl-ring in order to induce the formation of specific interactions in a crystal engineering way.

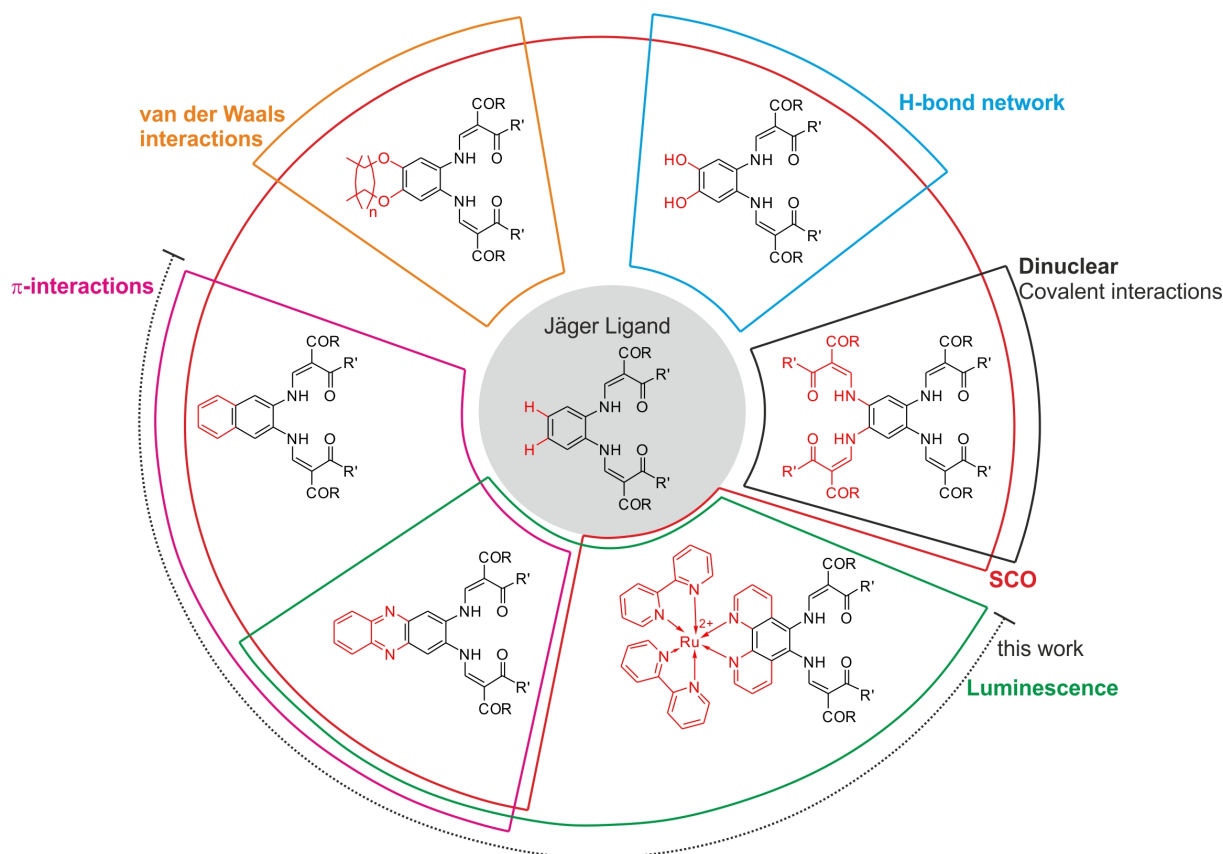


Figure 2.17: The Schiff base-like ligands and their different modifications.

The addition of two supplementary chelate arms allowed the synthesis of dinuclear complexes, and of ladder-like coordination polymers, which showed more cooperative SCO.^[78,79,86,98–100] In an effort to induce hydrogen bond network through the solid lattice, hydroxy-groups were added to the complex. This was successful and SCO coordination polymers with intricate hydrogen bond networks were obtained.^[101–103] However, one drawback of inducing hydrogen bond network is the rather high probability to include solvent molecules in the crystal structure, which can make the SCO properties unstable

upon loss of those solvent molecules. One can also induce lipid layer-like structures by exchanging the hydroxy- for alkoxy-groups, with different alkyl chain lengths. It was reported that cooperative SCOs are obtained when the lipid layer-like structure is obtained, which happens to be triggered by the ratio of the length of the alkyl chains regards to the dimension of the Fe(II) complex head. The complicated relationships between structure, phase transitions, and SCO properties are still being investigated.^[27,36,104,105] In this work, the ligand design focused on favouring π -interactions between spin centres. The π -system of the Schiff base-like ligand was then extended first to a naphthalene^[106,107], and then to a phenazine^[108]. The latter system exhibits fluorescence and a particular care was given to the investigation of the possible coupling between SCO and luminescence. In this aim, the ligand system was once more modified to bear a phosphorescent Ru(II) complex. In Figure 2.17, the Schiff base-like ligand and its different modifications are presented.

References

- [1] L. Cambi, L. Szegö, *Ber. dtsh. Chem. Ges. A/B* **1931**, *64*, 2591–2598.
- [2] L. Cambi, L. Malatesta, *Ber. dtsh. Chem. Ges. A/B* **1937**, *70*, 2067–2078.
- [3] H. Bethe, *Ann. Phys.* **1929**, *3*, 135–206.
- [4] J. H. Van Vleck, *J. Chem. Phys.* **1935**, *3*, 803–813.
- [5] C. J. Ballhausen, *J. Chem. Educ.* **1979**, *56*, 194–197, 215–218, 357–361.
- [6] P. Gülich, H. Goodwin, *Spin Crossover in Transition Metal Compounds I-III*, Springer, Berlin, DE, **2004**.
- [7] M. Halcrow, *Spin-Crossover Materials*, John Wiley & Sons Ltd., Chichester, UK, **2013**.
- [8] P. Gülich, A. Hauser, H. Spiering, *Angew. Chem. Int. Ed.* **1994**, *33*, 2024–2054.
- [9] D. M. Halepoto, D. G. L. Holt, L. F. Larkworthy, G. J. Leigh, D. C. Povey, G. W. Smith, *J. Chem. Soc., Chem. Commun.* **1989**, 1322–1323.
- [10] D. M. Halepoto, D. G. L. Holt, L. F. Larkworthy, D. C. Povey, G. W. Smith, *Polyhedron* **1989**, *8*, 1821–1822.
- [11] M. Sorai, Y. Yumoto, D. M. Halepoto, L. F. Larkworthy, *J. Phys. Chem. Solids* **1993**, *54*, 421–430.
- [12] P. Gülich, A. B. Gaspar, V. Ksenofontov, Y. Garcia, *J. Phys.: Condens. Matter* **2004**, *16*, S1087–S1108.
- [13] A. K. Hughes, V. J. Murphy, D. O’Hare, *J. Chem. Soc., Chem. Commun.* **1994**, 163–164.
- [14] H. Sitzmann, M. Schär, E. Dormann, M. Kelemen, *Z. Anorg. Allg. Chem.* **1997**, *623*, 1850–1852.
- [15] F. Franceschi, J. Hesschenbrouck, E. Solari, C. Floriani, N. Re, C. Rizzoli, A. Chiesi-Villa, *J. Chem. Soc., Dalton Trans.* **2000**, 593–604.
- [16] P. G. Sim, E. Sinn, *J. Am. Chem. Soc.* **1981**, *103*, 241–243.
- [17] L. Kaustov, M. E. Tal, A. I. Shames, Z. Gross, *Inorg. Chem.* **1997**, *36*, 3503–3511.
- [18] P. J. van Koningbruggen, Y. Maeda, H. Oshio, *Spin Crossover in Transition Metal Compounds I-III*, Berlin, DE, **2004**.
- [19] H. A. Goodwin, *Spin Crossover in Transition Metal Compounds I-III*, Springer, Berlin, DE, **2004**.

-
- [20] S. Hayami, Y. Komatsu, T. Shimizu, H. Kamihata, Y. H. Lee, *Coord. Chem. Rev.* **2011**, *255*, 1981–1990.
- [21] P. Gütllich, B. R. McGarvey, Kläui, *Inorg. Chem.* **1980**, *19*, 3704–3706.
- [22] W. Eberspach, N. El Murr, W. Kläui, *Ang. Chem. Int. Ed.* **2003**, *21*, 915–916.
- [23] P. Guionneau, M. Marchivie, G. Bravic, J.-F. Létard, D. Chasseau, *Spin Crossover in Transition Metal Compounds I-III*, Springer, Berlin, DE, **2004**.
- [24] J. E. Huheey, E. A. Keiter, R. L. Keiter, *Inorganic Chemistry*, HarperCollinsCollegePublishers, New York, USA, **1993**.
- [25] J.-F. Létard, *J. Mater. Chem.* **2006**, *16*, 2550–2559.
- [26] A. Hauser, C. Enachescu, M. L. Daku, A. Vargas, N. Amstutz, *Coord. Chem. Rev.* **2006**, *250*, 1642–1652.
- [27] S. Schlamp, K. Dankhoff, B. Weber, *New J. Chem.* **2014**, *38*, 1965–1972.
- [28] P. Gütllich, Y. Garcia, H. A. Goodwin, *Chem. Soc. Rev.* **2000**, *29*, 419–427.
- [29] H. Spiering, E. Meissner, H. Köppen, E. W. Müller, P. Gütllich, *Chem. Phys.* **1982**, *68*, 65–71.
- [30] N. Willenbacher, H. Spiering, *J. Phys. C: Solid State Phys.* **1988**, *21*, 1423–1439.
- [31] H. Spiering, N. Willenbacherr, *J. Phys.: Condens. Matter* **1989**, *1*, 10089–10105.
- [32] A. Hauser, P. Gütllich, H. Spiering, *Inorg. Chem.* **1986**, *25*, 4245–4248.
- [33] B. Weber, W. Bauer, J. Obel, *Angew. Chem. Int. Ed.* **2008**, *47*, 10098–10101.
- [34] B. Weber, W. Bauer, T. Pfaffeneder, M. M. Dîrtu, A. D. Naik, A. Rotaru, Y. Garcia, *Eur. J. Inorg. Chem.* **2011**, 3193–3206.
- [35] J. A. Real, A. B. Gaspar, V. Niel, M. C. Muñoz, *Coord. Chem. Rev.* **2003**, *236*, 121–141.
- [36] S. Schlamp, B. Weber, A. D. Naik, Y. Garcia, *Chem. Commun.* **2011**, *47*, 7152–7154.
- [37] M. A. Halcrow, *Coord. Chem. Rev.* **2009**, *253*, 2493–2514.
- [38] O. Kahn, *Science* **1998**, *279*, 44–48.
- [39] O. Kahn, C. Jay, J. Krober, R. Claude, F. Groliere, *EP0666561*, **1995**.
- [40] J. Linares, E. Codjovi, Y. Garcia, *Sensors* **2012**, *12*, 4492–4479.
-

-
- [41] <http://www.euronews.com/2015/07/16/chameleon-smartpaint-that-reacts-to-temperature-light-and-pressure/>, accessed on the 30/05/16.
- [42] R. N. Muller, L. V. Elst, S. Laurent, *J. Am. Chem. Soc.* **2003**, *125*, 8405–8407.
- [43] S. Thies, C. Bornholdt, F. Köhler, F. D. Sönnichsen, C. Näther, F. Tuczek, R. Herges, *Chem. Eur. J.* **2010**, *16*, 10074–10083.
- [44] S. Thies, H. Sell, C. Schütt, C. Bornholdt, C. Näther, F. Tuczek, R. Herges, *J. Am. Chem. Soc.* **2011**, *133*, 16243–16250.
- [45] S. Venkataramani, U. Jana, M. Dommaschk, F. D. Sönnichsen, F. Tuczek, R. Herges, *Science* **2011**, *331*, 445–448.
- [46] M. Dommaschk, F. Gutzeit, S. Boretius, R. Haag, R. Herges, *Chem. Commun.* **2014**, *50*, 12476–12478.
- [47] S. Hayami, *Spin-Crossover Materials*, John Wiley & Sons Ltd., Chichester, UK, **2013**.
- [48] O. Sato, Z.-Y. Li, S. Kang, S. Kanegawa, *Spin-Crossover Materials*, John Wiley & Sons Ltd., Chichester, UK, **2013**.
- [49] H. J. Sheperd, C. M. Quintero, G. Molnár, L. Salmon, A. Bousseksou, *Spin-Crossover Materials*, John Wiley & Sons Ltd., Chichester, UK, **2013**.
- [50] S. E. Braslavsky, *Pure Appl. Chem.* **2007**, *79*, 293–465.
- [51] B. Valeur, M. N. Berberan-Santos, *Molecular Fluorescence. Principles and applications*, Wiley-VCH, Weinheim, DE, **2013**.
- [52] R. Sjöback, J. Nygren, M. Kubista, *Spectroch. Acta A* **1995**, *51*, L7–L21.
- [53] M. Matsuda, H. Isozaki, H. Tajima, *Chem. Lett.* **2008**, *37*, 374–375.
- [54] M. Matsuda, H. Isozaki, H. Tajima, *Thin Solid Films* **2008**, *517*, 1465–1467.
- [55] M. Matsuda, K. Kiyoshima, R. Uchida, N. Kinoshita, H. Tajima, *Thin Solid Films* **2013**, *531*, 451–453.
- [56] J. M. Holland, J. A. McAllister, C. A. Kilner, M. Thornton-Pett, A. J. Bridgeman, M. A. Halcrow, *J. Chem. Soc., Dalton Trans.* **2002**, 548–554.
- [57] S. Titos-Padilla, J. M. Herrera, X.-W. Chen, J. J. Delgado, E. Colacio, *Angew. Chem. Int. Ed.* **2011**, *50*, 3290–3293.
-

-
- [58] H. Matsukizono, K. Kuroiwa, N. Kimizuka, *Chem. Lett.* **2008**, *37*, 446–447.
- [59] L. J. Kershaw Cook, M. A. Halcrow, *Polyhedron* **2015**, *87*, 91–97.
- [60] Y. Garcia, F. Robert, A. D. Naik, G. Zhou, B. Tinant, K. Robeyns, S. Michotte, L. Piriaux, *J. Am. Chem. Soc.* **2011**, *133*, 15850–15853.
- [61] C.-F. Wang, R.-F. Li, X.-Y. Chen, R.-J. Wei, L.-S. Zheng, J. Tao, *Angew. Chem. Int. Ed.* **2015**, *54*, 1574–1577.
- [62] M. Hasegawa, F. Renz, T. Hara, Y. Kikuchi, Y. Fukuda, J. Okubo, T. Hoshi, W. Linert, *Chem. Phys.* **2002**, *277*, 21–30.
- [63] A. Santoro, L. J. Kershaw Cook, R. Kulmaczewski, S. A. Barrett, O. Cespedes, M. A. Halcrow, *Inorg. Chem.* **2015**, *54*, 682–693.
- [64] L. Wolf, E.-G. Jäger, *Z. Anorg. Allg. Chem.* **1966**, *346*, 76–91.
- [65] B. Weber, J. Obel, L. R. Lorenz, W. Bauer, L. Carrella, E. Rentschler, *Eur. J. Inorg. Chem.* **2009**, 5535–5540.
- [66] B. R. Müller, G. Leibelng, E.-G. Jäger, *Mol. Cryst. Liq. Cryst. Sci. Technol., Sect. A* **1999**, *334*, 389–394.
- [67] B. R. Müller, G. Leibelng, E.-G. Jäger, *Chem. Phys. Lett.* **2000**, *319*, 368–374.
- [68] B. Weber, H. Görls, M. Rudolph, E.-G. Jäger, *Inorg. Chim. Acta* **2002**, *337*, 247–265.
- [69] B. Weber, R. Tandon, D. Himsl, *Z. Anorg. Allg. Chem.* **2007**, *633*, 1159–1162.
- [70] B. Weber, F. A. Walker, *Inorg. Chem.* **2007**, *46*, 6794–6803.
- [71] B. Weber, E. S. Kaps, K. Achterhold, F. G. Parak, *Inorg. Chem.* **2008**, *47*, 10779–10787.
- [72] B. Weber, E. S. Kaps, C. Desplanches, J.-F. Létard, *Eur. J. Inorg. Chem.* **2008**, 2963–2966.
- [73] B. Weber, E. S. Kaps, C. Desplanches, J.-F. Létard, *Eur. J. Inorg. Chem.* **2008**, 4891–4898.
- [74] B. Weber, C. Carbonera, C. Desplanches, J.-F. Létard, *Eur. J. Inorg. Chem.* **2008**, 1589–1598.
- [75] B. Weber, E. S. Kaps, J. Obel, W. Bauer, *Z. Anorg. Allg. Chem.* **2008**, *636*, 1421–1426.
- [76] W. Bauer, B. Weber, *Acta Cryst. C* **2008**, *64*, m237–m239.
- [77] B. Weber, E.-G. Jäger, *Eur. J. Inorg. Chem.* **2009**, 465–477.
- [78] B. Weber, *Coord. Chem. Rev.* **2009**, *253*, 2432–2449.
-

-
- [79] W. Bauer, B. Weber, *Inorg. Chim. Acta* **2009**, *362*, 2341–2346.
- [80] S. Thallmair, W. Bauer, B. Weber, *Polyhedron* **2009**, *28*, 1796–1801.
- [81] T. M. Pfaffeneder, W. Bauer, B. Weber, *Z. Anorg. Allg. Chem.* **2010**, *636*, 183–187.
- [82] T. M. Pfaffeneder, S. Thallmair, W. Bauer, B. Weber, *New J. Chem.* **2011**, *35*, 691–700.
- [83] W. Bauer, W. Scherer, S. Altmannshofer, B. Weber, *Eur. J. Inorg. Chem.* **2011**, 2803–2818.
- [84] W. Bauer, T. Pfaffeneder, K. Achterhold, B. Weber, *Eur. J. Inorg. Chem.* **2011**, 3183–3192.
- [85] C. Lochenie, W. Bauer, S. Schlamp, P. Thoma, B. Weber, *Z. Anorg. Allg. Chem.* **2012**, *638*, 98–102.
- [86] W. Bauer, S. Schlamp, B. Weber, *Chem. Commun.* **2012**, *48*, 10222–10224.
- [87] S. Schlamp, J. Schulten, R. Betz, T. Bauch, A. V. Mudring, B. Weber, *Z. Anorg. Allg. Chem.* **2012**, *638*, 1093–1102.
- [88] R. Nowak, W. Bauer, T. Ossiander, B. Weber, *Eur. J. Inorg. Chem.* **2013**, 975–983.
- [89] C. Baldé, W. Bauer, E. Kaps, S. Neville, C. Desplanches, G. Chastanet, B. Weber, J.-F. Létard, *Eur. J. Inorg. Chem.* **2013**, 2744–2750.
- [90] C. Lochenie, W. Bauer, A. P. Railliet, S. Schlamp, Y. Garcia, B. Weber, *Inorg. Chem.* **2014**, *53*, 11563–11572.
- [91] S. Schlamp, C. Lochenie, T. Bauer, R. Kempe, B. Weber, *Eur. J. Inorg. Chem.* **2015**, 408–413.
- [92] S. Schönfeld, C. Lochenie, P. Thoma, B. Weber, *CrystEngComm* **2015**, *17*, 5389–5395.
- [93] B. R. Müller, G. Leibelng, E.-G. Jäger, *J. Mag. Mag. Mat.* **2002**, *246*, 283–289.
- [94] E.-G. Jäger, P. Renner, *Z. Chem.* **1978**, *18*, 193.
- [95] C. Lochenie, S. Schlamp, A. P. Railliet, K. Robeyns, B. Weber, Y. Garcia, *CrystEngComm* **2014**, *16*, 6213–6218.
- [96] K. Dankhoff, C. Lochenie, F. Puchtler, B. Weber, *Eur. J. Inorg. Chem.* **2016**, 2136–2143.
- [97] B. Weber, private communication.
- [98] B. Weber, E. Kaps, *Heteroatom Chem.* **2005**, *16*, 391–397.
- [99] B. Weber, J. Obel, D. Henner-Vasquez, W. Bauer, *Eur. J. Inorg. Chem.* **2009**, 5527–5534.
-

- [100] B. Weber, E.-G. Jäger, *Z. Anorg. Allg. Chem.* **2009**, *635*, 130–133.
- [101] B. Weber, J. Obel, *Z. Anorg. Allg. Chem.* **2009**, *635*, 2474–2479.
- [102] B. Weber, J. Obel, D. Henner-Vásquez, W. Bauer, *Eur. J. Inorg. Chem.* **2009**, 5527–5534.
- [103] W. Bauer, C. Lochenie, B. Weber, *Dalton Trans.* **2014**, *43*, 1990–1999.
- [104] S. Schlamp, P. Thoma, B. Weber, *Eur. J. Inorg. Chem.* **2012**, 2759–2768.
- [105] S. Schlamp, P. Thoma, B. Weber, *Chem. Eur. J.* **2014**, *20*, 6462–6473.
- [106] C. Lochenie, J. Heinz, W. Milius, B. Weber, *Dalton Trans.* **2015**, *44*, 18065–18077.
- [107] C. Lochenie, A. Gebauer, O. Klimm, F. Puchtler, B. Weber, *New J. Chem.* **2016**, *40*, 4687–4695.
- [108] C. Lochenie, K. G. Wagner, M. Karg, B. Weber, *J. Mater. Chem. C* **2015**, *3*, 7925–7935.

3. Overview

This thesis comprises six publications, which are presented in Chapters 4–9. The individual contributions to joint publications are pointed out in Section 3.2.

3.1 Synopsis

This work started with the motivation to obtain, characterise, and analyse SCO complexes exhibiting cooperative STs, if possible with hysteresis. It is known that cooperative STs are favoured by the presence of long-range interactions (van der Waals interactions, π -interactions, or hydrogen bonds) between the SCO centres within the crystal lattice, thus the idea to try to induce the formation of a hydrogen bond network between the chains of a SCO coordination polymer arose. For this purpose, the **pina** (*N*-(Pyrid-4-yl)isonicotinamide) was selected as bridging ligand, as the **pina** itself is reported to form hydrogels.

In Chapter 4, a series of 1D SCO coordination polymers made of **pina** as bridging ligand, and an Fe(II)-containing Schiff base-like ligand is presented. The particularity of this series is that all compounds only differs in the nature and/or amount of non-coordinating solvent molecules included in the crystal lattice. Methanol, ethanol, DMF, THF, and mixture of water and methanol were used in the synthesis process. In the case of methanol, different synthesis processes were tried (reflux condition and slow diffusion setup). The samples with 0.5 MeOH, 0.5 EtOH, and 2 H₂O included in the lattice, all obtained from reflux conditions in the corresponding solvent, to the exception of the 2 H₂O which was obtained from using THF without previously drying it, are all pure HS complexes. A comparison of the X-ray powder diffractograms revealed that all three samples have the same pattern, and consequently the same structure.

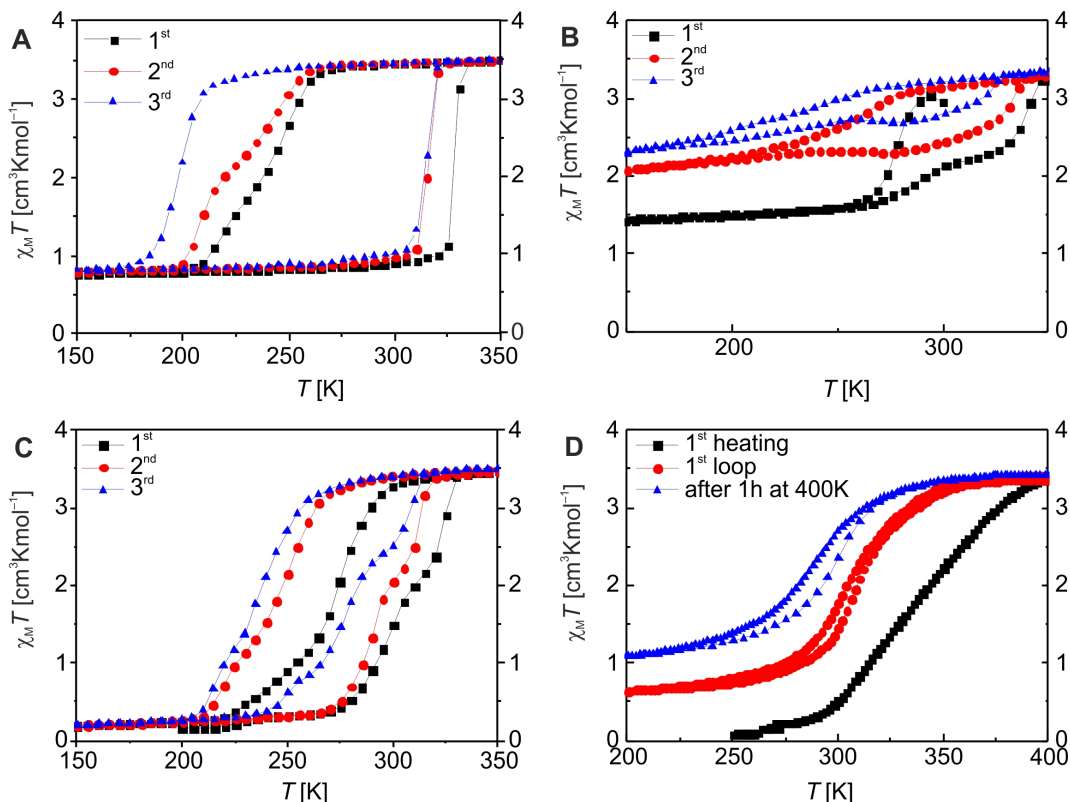


Figure 3.1: Magnetic properties of the different solvates of the pina coordination polymer: $([\text{FeL1}(\text{pina})] \cdot x \text{ MeOH}/\text{H}_2\text{O})_n$ (A), $([\text{FeL1}(\text{pina})] \cdot 0.5 \text{ MeOH} \cdot 0.5 \text{ H}_2\text{O})_n$ (B), $([\text{FeL1}(\text{pina})] \cdot 2 \text{ MeOH})_n$ (C), and $([\text{FeL1}(\text{pina})] \cdot \text{DMF})_n$ (D). For more detailed information, see Chapter 4.

A sample with 2 MeOH included in the crystal lattice could be obtained from a liquid-liquid slow diffusion setup as monocrystal and the X-ray structure could be determined. The structure revealed the formation of the aimed hydrogen bond linking the 1D chains of the coordination polymers, directly through a short contact between the peptide hydrogen of the pina and the carbonyl-group of the Schiff base-like ligand of a neighbouring chain, and indirectly through a methanol molecule which acts as acceptor and donor between chains, leading to the formation of a 2D network through the crystal lattice. The corresponding magnetic properties reveals first a 34 K wide hysteresis ($T_{\frac{1}{2}\uparrow} = 306 \text{ K}$, $T_{\frac{1}{2}\downarrow} = 272 \text{ K}$), which gets broader (45 K) and shifts to lower temperature once the solvent is removed of the sample ($T_{\frac{1}{2}\uparrow} = 281 \text{ K}$, $T_{\frac{1}{2}\downarrow} = 236 \text{ K}$). Another sample with 1 DMF molecule included presents a very gradual ST ($T_{\frac{1}{2}} = 335 \text{ K}$), which once again changes upon solvent loss, and then presents a 10 K wide hysteresis at lower temperature ($T_{\frac{1}{2}\downarrow} = 288 \text{ K}$, $T_{\frac{1}{2}\uparrow} = 298 \text{ K}$).

A sample with an unknown amount of methanol and water molecules ($x\text{MeOH}/\text{H}_2\text{O}$) presents a huge hysteresis of 88 K ($T_{\frac{1}{2}\downarrow} = 240$ K, $T_{\frac{1}{2}\uparrow} = 328$ K), which is stable upon cycling. The "unknown" amount has for origin the use of a not completely dry **pina** ligand in the synthesis. Indeed the **pina** ligand is very hygroscopic and much effort has to be given to keep it dry. Attempts to reproduce this sample in a controlled manner by using mixture of methanol and water were then unsuccessful. However another interesting phase was obtained, with 0.5 MeOH and 0.5 H₂O included in the crystal lattice. This compound presents unstable SCO properties. Every time it goes from LS to HS transition at $T_{\frac{1}{2}\uparrow} = 321$ K, a larger HS fraction is measured in the subsequent HS to LS transition at $T_{\frac{1}{2}\downarrow} = 275$ K. A detailed DSC and Mössbauer study revealed that supplementary phase transition are happening before/after each STs. In the end, this series of compounds still shows that remarkable SCO properties were obtained by combining hydrogen bond network and a polymeric structure. However, the inclusion of solvent molecule in the crystal lattice makes the SCO properties, regardless of how good they are, rather unattractive for potential applications, unless these applications requires irreversible changes of the SCO properties upon heating. In Figure 3.1, the magnetic properties of the different solvates of the **pina** coordination polymer are presented.

In a next step, the Schiff base-like ligand was altered to bear a naphthalene backbone, with the aim to induce π -interactions in the crystal lattice. This was motivated by the fact that most of the solvents used for the synthesis of our SCO complexes do not have a π -system, which could maybe hinder the solvent influence observed on the **pina** samples. In Chapter 5, the synthesis of the new naphthalene-based Schiff base-like ligands is presented, as well as the precursor Fe(II) complexes. A first difference with the original phenylene-based Schiff base-like ligands is that two of the precursor Fe(II) complexes did not precipitates as expected with methanol coordinating the axial positions. Instead, they form a 2D network, where the carbonyl substituents of the ligand act as axial ligand of neighbouring Fe(II) centres. Then those precursor Fe(II) complexes were converted into SCO complexes by adding/substituting a *N*-donor ligand on the axial positions (pyridine, 4-phenylpyridine, and 4-(dimethylamino)pyridine).

From the resulting ten mononuclear complexes, five exhibit SCO, whereas the remainders stay HS. The compound $[\text{FeL4}(\text{py})_2]\cdot\text{py}$ displays an incomplete two-step transition at low temperature ($T_1 = 150$ K, $T_2 = 80$ K). The crystal structure could be determined and has two inequivalent Fe(II) centres in the asymmetric unit, as well as non-coordinating pyridine. The crystal lattice explains well the magnetic properties as the two inequivalent Fe(II) complexes are forming layers perpendicular to the a axis, the layers being separated by non-coordinating pyridine molecules. Intricate face-to-edge π -interactions and C–H \cdots O short contacts link the complexes with each others within a layer. The samples $[\text{FeL3}(\text{py})_2]\cdot\text{py}$, $[\text{FeL1}(\text{phpy})_2]$, and $[\text{FeL4}(\text{phpy})_2]$ all present abrupt cooperative ST, and the two latter compounds exhibit also a 10 K wide hysteresis. The crystal structure of $[\text{FeL3}(\text{py})_2]\cdot\text{py}$ could be determined in both LS and HS states. The complexes are forming 1D chains through face-to-edge π -interactions between axial pyridine ligands and the naphthalene rings. Moreover, those 1D chains are then connected with one other through C–H \cdots O short contacts. The crystal structure of $[\text{FeL1}(\text{phpy})_2]$ has a similar packing, except that in this case the 1D chains are formed through C=O $\cdots\pi$ -interactions between the ester substituents and the naphthalene rings. Finally the sample $[\text{FeL1}(\text{dmap})_2]$ presents a two-step SCO, however no crystal structure could be determined. A Mössbauer spectrum presents an asymmetric doublet for Fe(II) HS, as well as broad peaks, indication of that two inequivalent Fe(II) centres are in the compound. All those SCO complexes shows that π -interactions can be induced in the crystal packing through introduction of the naphthalene rings, and increases the cooperativity of the obtained SCO properties. In Figure 3.2, the crystal packing of $[\text{FeL3}(\text{py})_2]\cdot\text{py}$ (top), $[\text{FeL1}(\text{phpy})_2]$ (middle), and $[\text{FeL4}(\text{phpy})_2]$ (bottom) are presented.

With the aim to further increase the cooperativity, the new naphthalene-based Schiff base-like ligand were then used to synthesise Fe(II) 1D coordination polymers with the bridging ligands **bipy** (4,4'-bipyridine), **bpea** (1,2-bis(pyrid-4-yl)ethane), **bpee** (1,2-bis(pyrid-4-yl)ethene), and **bppa** (1,3-bis(pyrid-4-yl)propane) (See Chapter 6). Of the sixteen obtained complexes, six complexes are SCO active, the rest stays HS or LS over the investigated temperature range. As no crystal structures could be determined, the SCO complexes were investigated not only with SQUID magnetometry, but also with

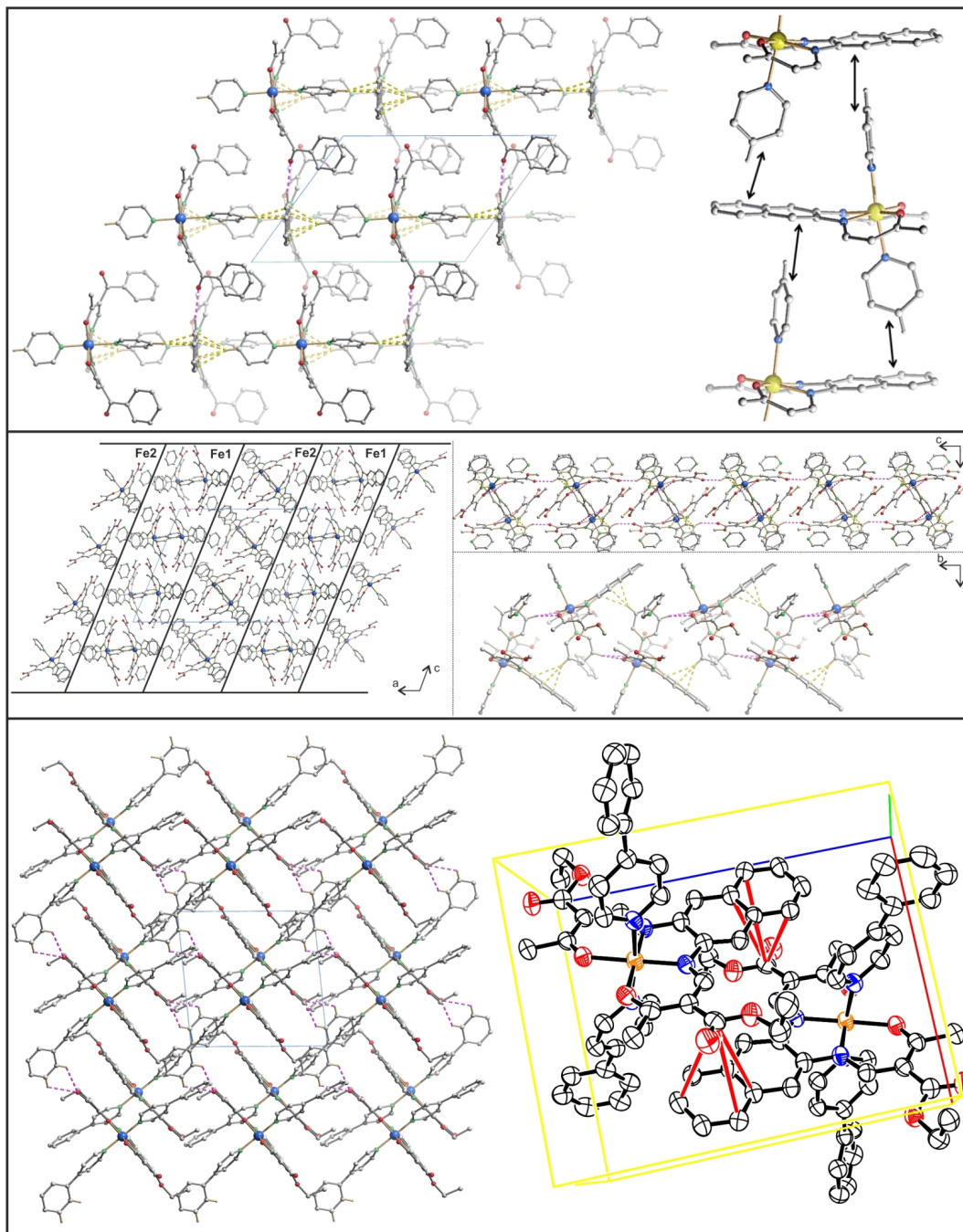


Figure 3.2: The different short contacts observed in the crystal packing of $[\text{FeL3}(\text{py})_2]\cdot\text{py}$ (top), $[\text{FeL1}(\text{phpy})_2]$ (middle), and $[\text{FeL4}(\text{phpy})_2]$ (bottom). For more detailed information, see Chapter 5.

DSC, X-ray powder diffraction, and Mössbauer spectroscopy. The two most interesting samples are $([\text{FeL3}(\text{bpea})]\cdot\text{MeOH})_n$ and $([\text{FeL3}(\text{bpee})]\cdot\text{MeOH})_n$ as they both present SCO with an hysteresis width of 28 K ($T_{\frac{1}{2}\uparrow} = 223$ K, $T_{\frac{1}{2}\downarrow} = 195$ K) and 40 K ($T_{\frac{1}{2}\uparrow} = 210$ K, $T_{\frac{1}{2}\downarrow} = 250$ K), respectively. Both samples presents similar powder diffrac-

tograms as well as similar Mössbauer spectra, which is a hint that both coordination polymers have the same crystal packing. The difference between the two coordination polymers arise only from the substitution of the single bond of the **bpea** ligand for a double bond in the **bpee** ligand. The **bpee** ligand is then more rigid than the **bpea** ligand, which leads to a better propagation of the ST through the crystal lattice, and indeed it was observed that $([\text{FeL3}(\text{bpee})]\cdot\text{MeOH})_n$ exhibits a larger hysteresis than $([\text{FeL3}(\text{bpea})]\cdot\text{MeOH})_n$. Another characteristic is that the ligand **bpee** is a slightly worse *N*-donor than **bpea**, because of the electron-pulling effect of the double bond. As consequence, the HS state of sample $([\text{FeL3}(\text{bpee})]\cdot\text{MeOH})_n$ is slightly more stabilised, and the STs happen at higher temperatures than for $([\text{FeL3}(\text{bpea})]\cdot\text{MeOH})_n$. The only big difference between the two coordination polymers is the calorimetric response of the samples upon SCO. The sample $([\text{FeL3}(\text{bpee})]\cdot\text{MeOH})_n$ present an unusual asymmetric response, as upon warming, the LS to HS DSC peak is intense ($\Delta H \uparrow = 10.2(12)$ kJ·mol⁻¹), and upon cooling the HS to LS DSC peak is rather small ($\Delta H \downarrow = 2.7(9)$ kJ·mol⁻¹). Usually the enthalpy values of both STs are of the same magnitude, what could be the reason for this unusual behaviour could be the presence of an endothermic transition upon cooling and upon heating, which overlap with the STs. Interestingly, the mononuclear complex $[\text{FeL3}(\text{py})_2]\cdot\text{py}$ (Chapter 5) already showed cooperativity with an abrupt ST, and the aim of increasing further the cooperativity, the coordination polymers were synthesised. We can see here with the two compounds $([\text{FeL3}(\text{bpea})]\cdot\text{MeOH})_n$ and $([\text{FeL3}(\text{bpee})]\cdot\text{MeOH})_n$, that the aim was reached as they both display increased cooperativity. Another aim was to avoid solvent influence on the SCO properties, and was partially reached. Albeit a majority of the synthesised SCO coordination polymers contain non-coordinating solvent molecules, only a very low influence on the SCO properties was observed upon solvent loss. In Figure 3.3, the magnetic properties of $[\text{FeL3}(\text{py})_2]\cdot\text{py}$, $([\text{FeL3}(\text{bpea})]\cdot\text{MeOH})_n$, and $([\text{FeL3}(\text{bpee})]\cdot\text{MeOH})_n$ are presented.

In all crystal structures of SCO complexes with the naphthalene-derived Schiff base-like ligand, only face-to-edge π -interactions were observed, probably because the naphthalene group is too short to build face-to-face π -interactions. However, we were interested in building face-to-face π -interactions and see if the cooperativity further increases, and

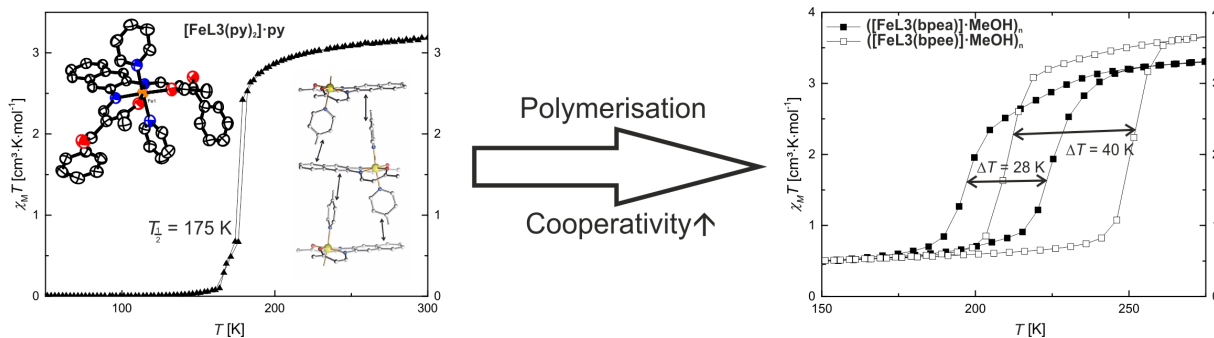


Figure 3.3: Magnetic properties of $[\text{FeL3}(\text{py})_2]\cdot\text{py}$, $([\text{FeL3}(\text{bpea})]\cdot\text{MeOH})_n$, and $([\text{FeL3}(\text{bpee})]\cdot\text{MeOH})_n$. For more detailed information, see Chapter 5 and 6.

therefore the phenazine system was chosen to replace the naphthalene group in the ligand structure. It was quickly observed that the new phenazine-derived Schiff base-like ligands are luminescent. The first interesting study to make was to investigate the influence of the complexation of a paramagnetic or diamagnetic metal centre on the emission properties. Ni(II), Cu(II), and Zn(II) were selected because Cu(II) is paramagnetic and Zn(II) is diamagnetic independently of the coordination sphere, and Ni(II) can be switched from diamagnetic to paramagnetic when changing coordination geometry. The latter phenomenon is called *Coordination Induced Spin State Switch* (CISSS) and has been subject to intensive research in the SCO community for the last years. The CISSS phenomenon is very similar to the SCO phenomenon, but it requires a chemical stimuli instead of a physical stimuli. In Chapter 7, the absorption and emission properties, as well as the influence of the spin state of the metal centre on those properties are reported. The study was done in two solvents: trichloromethane and pyridine. In trichloromethane, the solved complexes adopt a square planar geometry, which leads to a diamagnetic ($S = 0$) Ni(II) complex. In contrast, the Ni(II) complex solved in pyridine adopts a square pyramidal or an octahedral geometry, as pyridine molecules coordinate the axial positions, and the complex is paramagnetic ($S = 1$). The Cu(II) complexes are paramagnetic ($S = \frac{1}{2}$) and the Zn(II) complexes diamagnetic ($S = 0$) regardless of the solvent. It was observed that all complex solutions with a diamagnetic metal centre (Zn(II), Ni(II) in trichloromethane) were still luminescent, and that the complex solutions with a paramagnetic metal centre (Cu(II), Ni(II) in pyridine) do not exhibit fluorescence. The crystal structure of the Ni(II) and Cu(II) complexes revealed that the phenazine group is coplanar with the coordination

plane of the metal centre, meaning that the metal centre is part of the π -system of the ligand. Further time-resolved fluorescence spectroscopy measurement showed that the lifetime of the emission drastically drops when the Ni(II) centre goes from its diamagnetic to its paramagnetic spin state. This observation, in combination with the structural data, leads to the conclusion that a non-radiative energy transfer takes place between the fluorophore and the metal centre when the latter one is in a paramagnetic spin state. To be more precise, a Dexter electron transfer (DET) is presumed to take place. In Figure 3.4, the structure of the Ni(II) complex, as well as the optical measurement showing the loss of the emission properties upon CISSS are presented.

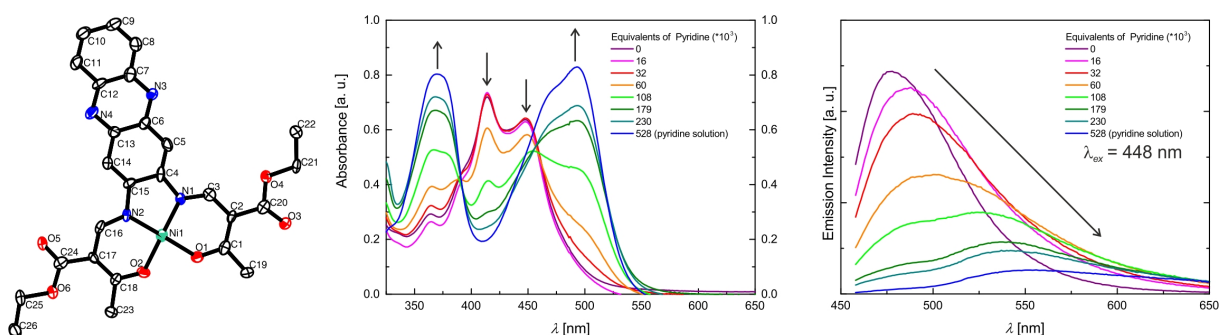


Figure 3.4: Crystal structure of the phenazine-derived Ni(II) complex (left), absorption (centre) and emission (right) spectra of the Ni(II) complex upon CISSS. For more detailed information, see Chapter 7.

In order to confirm/infirm the DET, two experimental investigations can be done: either exchanging the phenazine-group for another fluorophore, or exchanging the Ni(II) centre for another metal centre that can also switch spin state i.e. Fe(II). The exchange of the fluorophore was done by synthesising a phenanthrene-quinoxaline Schiff base-like ligand. The ligand and the corresponding Ni(II), Cu(II), and Zn(II) complexes are presented in Chapter 7. The Ni(II) complex is luminescent but the spin state of the metal centre does not influence the emission properties of the complex. This hint rather confirms the DET, but to be sure a third fluorophore was tried: a Ru(II) polypyridine complex was used. A phenanthroline-derived Schiff base-like ligand was synthesised, which coordinates a $[\text{Ru(II)}(\text{bipy})_2]^{2+}$ block on the phenanthroline side, and a Ni(II) metal centre is then incorporated in the chelate-cycles. This is the first synthesis of such bimetallic complex. The emission properties of the Ru(II) metallaligand were then investigated in water and

pyridine, with and without Ni(II) centre. Here again, the spin state of the Ni(II) complex seems to have no influence on the emission properties of the fluorophore. An analysis of the crystal structure of the bimetallic complex showed that, unlike the phenazine-derivative, the Ni(II) centre is not part of the π -system of the fluorophore, as a steric hindrance forbids the chelate cycles to be in the same plane as the phenanthroline, which forbids any DET between the fluorophore and the Ni(II) centre. Nevertheless, the new bimetallic complex could be modified to avoid this steric hindrance in a future work. The synthesis, crystal structure, and optical properties of the bimetallic Ru(II)-Ni(II) complex are described in Chapter 8.

In a further step, the Ni(II) centre from the phenazine-derived complex was exchanged for an Fe(II) centre. The aim was to observe if the emission properties of the phenazine-fluorophore could also be influenced by the spin state of an Fe(II) SCO complex. Therefore a coordination polymer with bipy (4,4'-bipyridine) as bridging ligand was synthesised, and present a wide thermal hysteresis of 48 K above room temperature ($T_{\frac{1}{2}\uparrow} = 371$ K and $T_{\frac{1}{2}\downarrow} = 323$ K) (See Figure 3.5). The SCO properties were also characterised with DSC and powder X-ray diffraction, and both analyses show that a major structural change happens upon SCO, which is causing the wide hysteresis. No single crystal suitable for X-ray analysis could be grown, however the structure of the corresponding dimer could be determined (See Figure 3.5). The dimer could then be obtained as bulk material through fine tuning of the reaction conditions. The emission properties of both coordination polymer and dimer in the solid state were measured in regard to temperature. The first observation is that both compounds show dual emission (λ_1, λ_2) upon photoexcitation. The dimer has an intense peak at $\lambda_2 = 686$ nm, and a smaller feature at $\lambda_1 = 550$ nm, and the ratio between both peaks is constant when changing the temperature. The coordination polymer, however, shows at room temperature an enhanced peak at $\lambda_1 = 550$ nm, and a relatively smaller peak at $\lambda_2 = 673$ nm. Upon SCO, the ratio of the two peaks change, as in the HS state, both peaks are almost equal in intensity. The evolution of the ratio λ_1/λ_2 with temperature, as well as the SQUID data is shown in Figure 3.5. Dual emission means that two different relaxation processes occur, with different electronic origins. We made the hypothesis, based on our knowledge on the corresponding Ni(II)

complexes, that one process is a ligand-centred relaxation (λ_1), and the other process is a metal-centred relaxation after an electron exchange between ligand-based and metal-based orbitals (λ_2). The later process is only possible when the Fe(II) complex is in its HS state, as the electron exchange is favoured by the presence of unpaired electrons in the metal-centred orbitals. The synthesis, characterisation, and analyses of the magnetic and emission properties of both dimer and SCO coordination polymer are presented in Chapter 9.

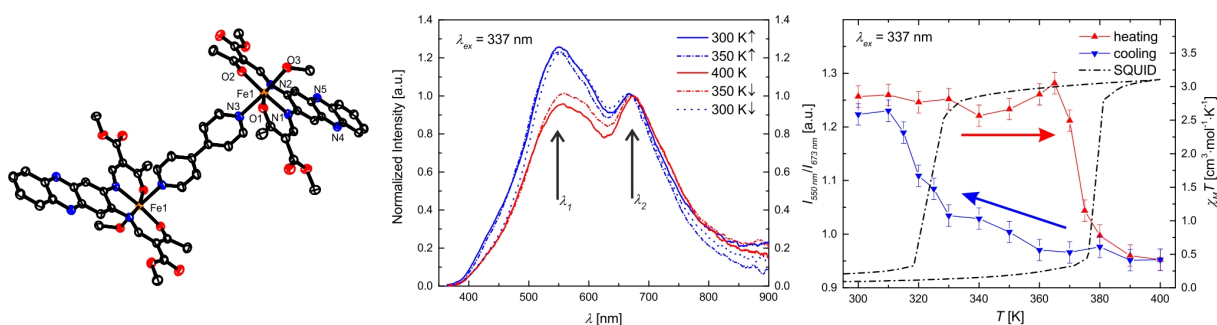


Figure 3.5: Crystal structure of the phenazine-derived Fe(II) luminescent dimer (left), emission spectra at different temperatures of the phenazine-derived Fe(II) luminescent SCO coordination polymer (centre), ratio λ_1/λ_2 vs. temperature as well as the magnetic properties (right). For more detailed information, see Chapter 9.

The original aim of this work was to obtain SCO complexes exhibiting cooperative transitions by creating short- and long-range interactions in the crystal packing. First the pina bridging ligand was used to build an hydrogen bond network within the crystal lattice, and SCO coordination polymers displaying wide thermal hysteresis were obtained. In a second step, the equatorial Schiff base-like ligand was modified to bear an extended π -system, and the gained mononuclear complexes and coordination polymers present enhanced SCO properties. A structural analysis revealed that $C-H \cdots \pi$ and $C-H \cdots O$ interactions were present between the complexes in the crystal lattice, and therefore responsible for the enhanced SCO properties. Then the π -system was further extended to the phenazine system, in order to maybe favour face-to-face π -interaction, but as the new ligand displays luminescent properties, the aim was shifted to the study of the interactions between the metal centre and the emission properties, specially to the effect of a spin state change.

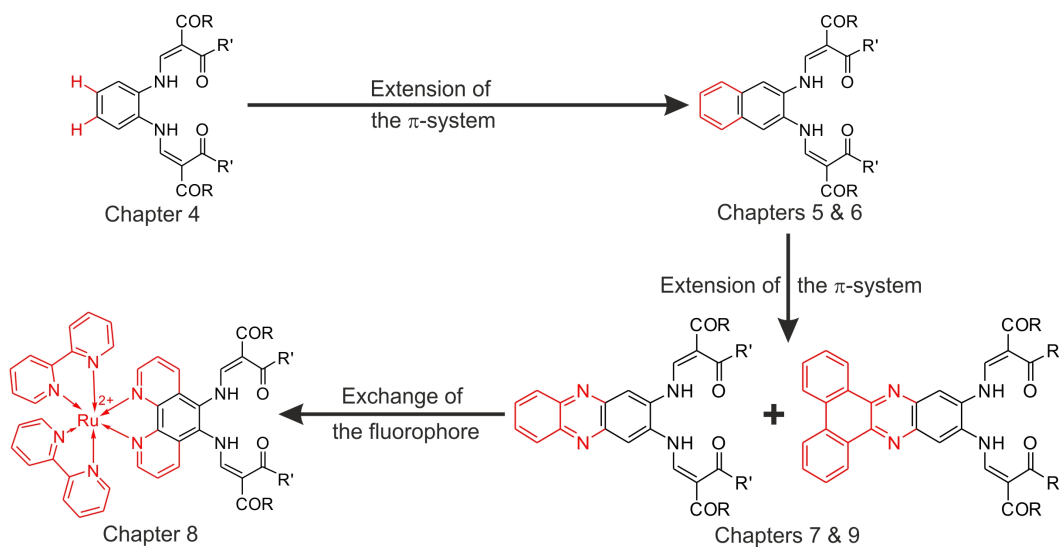


Figure 3.6: Overview of the different equatorial ligands used or designed in this work, with the corresponding chapter(s).

As it was revealed that in the case of the Ni(II) complex, the fluorescence could be turned on/off through Coordination Induced Spin State Switch, where the square planar diamagnetic Ni(II) complex is emitting, and after coordination of pyridine, the square pyramidal/octahedral paramagnetic Ni(II) complex is not emitting any more. In a next step, the exchange of the fluorophore for a phenanthrene-quinoxaline or a $[\text{Ru(II)(bipy)}_2]^{2+}$ was done, however no control on the emission properties through spin state change could be observed. In a last step, the Ni(II) metal centre was exchanged for an Fe(II) centre, which when converted into a coordination polymer with bipy, becomes SCO active and displays a wide hysteresis above room temperature. Here again, the emission properties are influenced from the spin state of the Fe(II) centre. To sum up, this work shows that through thoughtful design of the equatorial ligand (See Figure 3.6), not only the SCO properties can be improved, but a new function, luminescence, can be added. The new multifunctional compounds, where the spin state, and therefore the SCO properties, are influencing the luminescence properties, open a wide research field, as well as new potential applications in the domain of sensors.

3.2 Individual Contributions to Joint Publications

The results presented in this thesis were obtained in collaboration with others and are published, accepted, or are to be submitted as indicated below. In the following, the contributions of all co-authors to the publications are specified. The asterisk denotes the corresponding authors.

Chapter 4

This work was published in Inorganic Chemistry (*Inorg. Chem.* **2014**, *53*, 11563–11572) with the title:

”Large Thermal Hysteresis for Iron(II) Spin Crossover Complexes with *N*-(Pyrid-4-yl)isonicotinamide.”

Charles Lochenie, Wolfgang Bauer, Antoine P. Railliet, Stephan Schlamp, Yann Garcia, Birgit Weber*.

I synthesised and characterised all complexes and ligands presented in this work; carried out a part of the magnetic measurements and wrote the experimental section, result section and the conclusion. The crystal structure was obtained and solved by Wolfgang Bauer. Stephan Schlamp carried out part of the magnetic measurements. The Mössbauer and DSC studies were carried out by myself under the supervision of Antoine P. Railliet and Yann Garcia at the Université catholique de Louvain (BE). Birgit Weber supervised this work, contributed to the interpretation of the results, wrote the introduction, and was involved in scientific discussions and correction of the manuscript.

Chapter 5

This work was published in Dalton Transactions (*Dalton Trans.* **2015**, *44*, 18065–18077) with the title:

”Iron(II) spin crossover complexes with diamidonaphthalene-based Schiff base-like ligands: mononuclear complexes.”

Charles Lochenie, Julia Heinz, Wolfgang Milius, Birgit Weber*.

I established the ligand system, wrote the publication, carried out the magnetic measurements, measured and solved all crystal structures, and performed the Mössbauer measurements. The synthesis and characterisation of the ligands and complexes was undergone by myself or by Julia Heinz under my supervision during her Bachelor thesis. Wolfgang Milius carried out the X-ray powder diffraction measurements. Birgit Weber supervised this work, was involved in the scientific discussions, and corrected the manuscript.

Chapter 6

This work was published in New Journal of Chemistry (*New J. Chem.* **2016**, *40*, 4687–4695) with the title:

”Iron(II) spin crossover complexes with diamidonaphthalene-based Schiff base-like ligands: 1D coordination polymers.”

Charles Lochenie, Andreas Gebauer, Ottokar Klimm, Florian Puchtler, Birgit Weber*.

I established the ligand system, wrote the publication, carried out the magnetic measurements, treated and interpreted the DSC measurements, and carried out the Mössbauer study. All ligands and complexes were synthesised and characterised by myself or by Andreas Gebauer under my supervision during his Bachelor thesis. Ottokar Klimm took the SEM pictures. Florian Puchtler carried out the X-ray powder diffraction measurements. Birgit Weber supervised this work, was involved in the scientific discussions, and corrected the manuscript.

Chapter 7

This work was published in Journal of Material Chemistry C (*J. Mater. Chem. C* **2015**, *3*, 7925–7935) with the title:

”Modulation of the ligand-based fluorescence of 3d metal complexes upon spin state change.”

Charles Lochenie, Kristina G. Wagner, Matthias Karg*, Birgit Weber*.

I established the ligand system, wrote the publication, synthesised and characterised all ligands and complexes presented, measured and solved all crystal structures, carried out the absorption spectroscopy measurements. The emission spectroscopy measurements were performed by myself and Kristina G. Wagner. The fits of the decay curves were done by Kristina G. Wagner. Matthias Karg and Birgit Weber supervised this work, were involved in the scientific discussions, and corrected the manuscript.

Chapter 8

This work is to be submitted with the title:

”Synthesis and analysis of the optical properties of a phenanthroline-derived Schiff base-like Ru(II)-Ni(II) complex”

Hannah Kurz, Charles Lochenie, Kristina G. Wagner, Matthias Karg, Birgit Weber*.

Hannah Kurz under my supervision during her Bachelor thesis synthesised and characterised all ligands and complexes, performed the absorption spectroscopy measurements, and wrote a part of the publication. I measured and solved the crystal structures, carried out the emission spectroscopy measurements, and wrote a part of the publication. The fits of the decay curves were done by Kristina G. Wagner. Matthias Karg and Birgit Weber supervised this work, were involved in the scientific discussions, and corrected the manuscript.

Chapter 9

This work is to be submitted with the title:

”Spin crossover iron(II) coordination polymer with fluorescent properties: correlation between emission properties and spin state.”

Charles Lochenie, Bernadette Maier, Konstantin Schötz, Fabian Panzer, Florian Puchtler, Anna Köhler, Birgit Weber*.

I established the ligand system, wrote the publication, measured and solved all crystal structures, carried out the magnetic measurements, and treated and interpreted the DSC measurements. All ligands and complexes were synthesised and characterised by myself or by Bernadette Maier under my supervision during a practical course. The fluorescence spectroscopy measurements were carried out by Konstantin Schötz and Fabian Panzer. Florian Puchtler carried out the X-ray powder diffraction measurements. Anna Köhler and Birgit Weber supervised this work, were involved in the scientific discussions, and corrected the manuscript.

4. Large Thermal Hysteresis for Iron(II) Spin Cross-over Complexes with *N*-(Pyrid-4-yl)isonicotinamide.

Charles Lochenie,^{a,b} Wolfgang Bauer,^a Antoine P. Railliet,^b
Stephan Schlamp,^a Yann Garcia,^{*,b} and Birgit Weber^{*,a}

^aInorganic Chemistry II, Universität Bayreuth, Universitätstrasse 30, NW I,
95440 Bayreuth, Germany.

^bInstitute of Condensed Matter and Nanosciences, Molecules, Solids and Reactivity
(IMCN/MOST), Université Catholique de Louvain, Place Louis Pasteur 1, 1348 Louvain-la-Neuve, Belgium.

Published in *Inorg. Chem.* **2014**, *53*, 11563–11572.

Reproduced with the permission of the American Chemical Society.

Abstract

A new series of iron(II) 1D coordination polymers with the general formula [FeL1(pina)]·*x*solvent with L1 being a tetradentate N₂O₂²⁻ coordinating Schiff base-like ligand [[(3,3'-[1,2-phenylenebis-(iminomethylidene)]bis(2,4-pentanedionato)(2-)-*N,N',O²,O²'*], and pina being a bridging axial ligand *N*-(pyrid-4-yl)isonicotinamide, are discussed. The X-ray crystal structure of [FeL1(pina)]·2MeOH was solved for the low-spin state. The compound crystallizes in the monoclinic space group *P21/c*, and the analysis of the crystal packing reveals the formation of a hydrogen bond network where additional methanol

molecules are included. Different magnetic properties are observed for the seven samples analyzed, depending on the nature of the included solvent molecules. The widest hysteresis loop is observed for a fine crystalline sample of composition $[\text{FeL1}(\text{pina})] \cdot x\text{H}_2\text{O}/\text{MeOH}$. The 88 K wide thermal hysteresis loop ($T_{\frac{1}{2}\uparrow} = 328$ K and $T_{\frac{1}{2}\downarrow} = 240$ K) is centered around room temperature and can be repeated without a loss of the spin transition properties. For the single crystals of $[\text{FeL1}(\text{pina})] \cdot 2\text{MeOH}$, a 51 K wide hysteresis loop is observed ($T_{\frac{1}{2}\uparrow} = 296$ K and $T_{\frac{1}{2}\downarrow} = 245$ K) that is also stable for several cycles. For a powder sample of $[\text{FeL1}(\text{pina})] \cdot 0.5\text{H}_2\text{O} \cdot 0.5\text{MeOH}$ a cooperative spin transition with a 46 K wide hysteresis loop around room temperature is observed ($T_{\frac{1}{2}\uparrow} = 321$ K and $T_{\frac{1}{2}\downarrow} = 275$ K). This compound was further investigated using Mössbauer spectroscopy and DSC. Both methods reveal that, in the cooling mode, the spin transition is accompanied by a phase transition while in the heating mode a loss of the included methanol is observed that leads to a loss of the spin transition properties. These results show that the pina ligand was used successfully in a crystal engineering-like approach to generate 1D coordination polymers and improve their spin crossover properties.

4.1 Introduction

Iron(II) spin crossover (SCO) complexes belong to a fascinating class of materials that can be switched between the paramagnetic high-spin state (HS, $S = 2$) and the diamagnetic low-spin state (LS, $S = 0$) by physical stimuli such as temperature, pressure, or light.^[1–17] This transition causes electronic, structural, vibrational, and magnetic changes that can be monitored by many different physical methods such as ^{57}Fe Mössbauer spectroscopy or detected visually due to a color change associated with thermochromism, in many cases. Since their discovery in 1931 by *Cambi et al.*,^[18,19] SCO complexes never cease to attract interest due to the numerous potential applications as memory devices, displays,^[20–22] or sensors.^[23] The possibility to form micro- and nanoparticles,^[24–26] gels,^[27] or liquid-crystalline materials,^[28] reinforced the interest in SCO materials.^[29–31] Of the different types of spin transitions (gradual, stepwise, incomplete),^[3] SCO complexes exhibiting thermal hysteresis are particularly suited for the mentioned applications. Up to now, the largest hysteresis is a 70 K wide loop for a complex with a Schiff base-like lig-

and imidazole as ligands.^[32] It was demonstrated that the crystal packing, especially hydrogen bond network,^[33,34] but also structural changes upon spin transition,^[35] have a huge influence on the SCO properties of these complexes. We seek to systematically improve the SCO properties of our complexes thanks to crystal engineering to obtain wide and stable hysteresis loops around room temperature. One strategy was to modify the equatorial Schiff base-like ligand through the introduction of additional hydroxyl groups in the outer periphery to optimize the preconditions for the observation of hydrogen bond networks. This strategy was not successful for mononuclear complexes with pyridine or 4-dimethylaminopyridine as axial ligand.^[36] However, for the corresponding 1D coordination polymers with bridging axial ligands as 4,4'-bipyridine or bis(4-pyridyl)ethene, an increased occurrence of thermal hysteresis loops was observed.^[37]

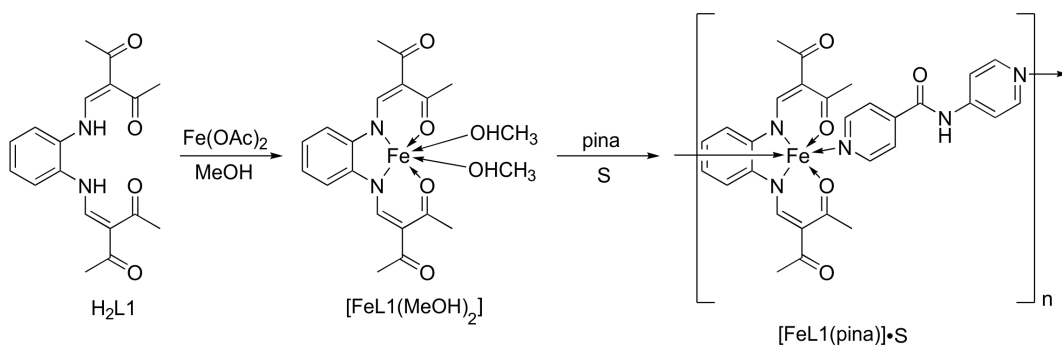
In this work we present an alternative approach to improve the hydrogen network between the polymer chains of Schiff base-like iron(II) SCO complexes. The objective was to build the hydrogen bond network through the crystal packing by using the pina ligand, which itself is known to make a hydrogel.^[38] For this, iron(II) complexes made of a Schiff base-like equatorial ligand and a bridging *N*-(pyrid-4-yl)-isonicotinamide (pina) axial ligand were synthesized. It has recently been shown that the solvent or the method of synthesis can have a crucial influence on SCO complexes of this ligand family^[39] and of other SCO systems.^[40,41] Therefore, complex [FeL1(pina)] (**1**) was synthesized in various solvents using three different methods. Seven phases that vary in the amount of solvent included in the crystal packing were obtained. All samples were investigated by SQUID magnetometry, the most interesting samples being investigated further using Mössbauer spectroscopy, DSC measurements, and single crystal X-ray diffraction, when appropriate.

4.2 Experimental Section

Synthesis. All reagents were of reagent grade and used without further purification. MeOH and EtOH were purified by distillation under argon,^[42] DMF was dried on molecular sieves and degassed, and THF and water were degassed. All syntheses were carried out under argon using Schlenk tube techniques. IR spectra were recorded on a Shimadzu

FTIR-84005 spectrometer using KBr discs at room temperature. CHN analyses were performed at MEDAC Ltd. (U.K.). Mass spectra were recorded with a Jeol MS-700 device, with DEI+ as ionization method.

The synthesis is performed in two steps starting from iron(II) acetate and a Schiff base-like ligand H_2L1 that are reacted to give a first complex $[FeL1(MeOH)_2]$ that is then converted with pina in the solvent S to give $[FeL1(pina)] \cdot xS$ (Scheme 4.1). The syntheses of the ligand H_2L1 ,^[43] the pina ligand,^[38] iron acetate,^[44] and the complex $[FeL1(MeOH)_2]$ ^[45] have been performed as previously described. All syntheses except that of $1 \cdot xMeOH/H_2O$ were reproduced at least once.



Scheme 4.1: General Structure of the Ligands and Complexes: Abbreviations Used and Synthesis Pathway of the $[FeL1(pina)]$ Complexes.

$[FeL1(pina)] \cdot 0.5 MeOH$ (1·0.5 MeOH). A solution of $[FeL1(MeOH)_2]$ (0.55 g) and pina (1.08 g) in methanol (45 mL) was heated to reflux for 1 h. The formation of a dark violet precipitate was observed in the boiling heat. After cooling and filtration, the precipitate was washed with methanol (2×5 mL) and dried *in vacuo*. Yield: 0.51g, 74%. IR (KBr): $\tilde{\nu} = 3229(w)$ (NH), 1687(m) (CO), 1647(s) (CO), 1560(vs) cm^{-1} (CO). MS (DEI(+), 70 eV) m/z (%): 382 (70) $[FeL1+]$, 199 (97) $[pina+]$, 106 (100). Elemental analysis calcd (found) for $C_{29.5}H_{29}FeN_5O_{5.5}$ (597.15): C 59.3 (59.3), H 4.7 (4.9), N 11.4 (11.7).

$[FeL1(pina)] \cdot xMeOH/H_2O$ (1· $xMeOH/H_2O$). Amorphous black crystals of the composition $1 \cdot xMeOH/H_2O$ were obtained by slow diffusion using a homemade Schlenk of

[FeL1(MeOH)₂] (0.11 g, 0.25 mmol) and pina (0.24 g, later analysis revealed that there were still traces of water in the ligand, for all further approaches the ligand was dried completely) in methanol solution after 2 weeks. Elemental analysis calcd (found) for C₂₉H₂₇FeN₅O₅ (581.40, since the exact solvent composition is unknown, the calculated values correspond to the solvent-free complex): C 59.91 (58.5), H 4.68 (4.9), N 12.05 (11.7).

[FeL1(pina)]·2MeOH (1·2MeOH). Violet crystals of sufficient quality for X-ray analysis were obtained by slow diffusion techniques of [FeL1(MeOH)₂] (0.12 g) and pina (0.27 g) in methanol solution after 1 week. Elemental analysis calcd (found) for C₃₁H₃₅FeN₅O₇ (645.49): C 57.7 (57.4), H 5.5 (5.0), N 10.9 (10.8).

[FeL1(pina)]·0.5 H₂O·0.5 MeOH (1·0.5 H₂O·0.5 MeOH). [FeL1(MeOH)₂] (0.5 g) was dissolved in 20 mL mixture of methanol and water (98:2). Pina (0.22 g) was dissolved in 20 mL of the same mixture. Then the pina solution was added to the [FeL1(MeOH)₂] solution, and the mixture was stirred 2 h at room temperature. A dark purple powder precipitated, and was filtered, washed twice with 5 mL of MeOH, and carefully dried *in vacuo*. Yield: 0.6 g, 95%. IR (KBr): $\tilde{\nu}$ = 3165(b) (OH), 1685(m) (CO), 1593(s) (CO), 1555(vs) cm⁻¹ (CO). TGA on 5.7470 mg at 25 °C: 5.5513 mg at 100 °C (-3.405% -solvent loss, theory -4.12%), 3.8603 mg at 315 °C (-32.835% -decomposition). Elemental analysis calcd (found) for C_{29.5}H₃₀FeN₅O₆ (606.43): C 58.43 (58.4), H 4.99 (4.9), N 11.55 (11.6).

[FeL1(pina)]·0.5 EtOH (1·0.5 EtOH). A solution of [FeL1(MeOH)₂] (0.41 g) and pina (1.85 g) in ethanol (20 mL) was refluxed for 1 h. A dark red powder precipitated, and was filtered, washed twice with 5 mL of EtOH, and carefully dried *in vacuo*. Yield: 0.49 g, 87%. IR (KBr): $\tilde{\nu}$ = 3234(w) (NH), 1678(m) (CO), 1658(s) (CO), 1574(vs) cm⁻¹ (CO). MS (DEI(+), 70 eV) m/z (%): 382 (70) [FeL1+], 199 (97) [pina+], 106 (100). Elemental analysis calcd (found) for C₃₀H₃₀FeN₅O_{5.5} (604.44): C 59.6 (59.3), H 5.0 (4.9), N 11.6 (11.7).

[FeL1(pina)]·DMF (1·DMF) . A solution of [FeL1(MeOH)₂] (0.69 g) and pina (3.1 g) in DMF (20 mL) was refluxed for 1 h. Dark purple crystals appeared after one night

at room temperature, and were filtered, washed twice with 5 mL of DMF, and carefully dried *in vacuo*. Yield: 0.51 g, 52%. IR (KBr): $\tilde{\nu} = 3221(\text{w})$ (NH), 1675(m) (CO), 1646(s) (CO), 1559(vs) cm^{-1} (CO). MS (DEI-(+), 70 eV) m/z (%): 382 (70) [FeL1+], 199 (97) [pina+], 106 (100). TGA on 25.31 mg at 25 °C; 24.75 mg at 200 °C (-3.2% -solvent loss), 13.14 mg at 315 °C (-39.9% -decomposition). Elemental analysis calcd (found) for $\text{C}_{32}\text{H}_{34}\text{FeN}_6\text{O}_6$ (654.49): C 58.7 (58.6), H 5.2 (5.3), N 12.8 (12.8).

[FeL1(pina)]·2 H₂O (1·2 H₂O). [FeL1(MeOH)₂] (0.62 g) was dissolved in 40 mL of THF. Pina (2.7 g) was dissolved in 40 mL of THF. Then, the pina solution was added to the [FeL1(MeOH)₂] solution, and the mixture was stirred overnight at room temperature. A red powder precipitated, and was filtered, washed twice with 5 mL of THF, and carefully dried *in vacuo*. Yield: 0.85 g, quantitative. IR (KBr): $\tilde{\nu} = 3205(\text{w})$ (NH-OH), 1689(m) (CO), 1653(s) (CO), 1547(vs) cm^{-1} (CO). MS (DEI-(+), 70 eV) m/z (%): 382 (70) [FeL1+], 199 (97) [pina+], 106 (100). Elemental analysis calcd (found) for $\text{C}_{29}\text{H}_{31}\text{FeN}_5\text{O}_7$ (617.16): C 56.2 (56.24), H 5.0 (4.9), N 11.3 (10.9).

X-ray Structure Analysis. The intensity data of 1·2MeOH were collected on an Oxford XCalibur diffractometer by using graphite-monochromated Mo K α radiation. The data were corrected for Lorentz and polarization effects. The structure was solved by direct methods (SIR-97)^[46] and refined by full-matrix least-squares techniques against $F_o^2 - F_c^2$ (SHELXL-97).^[47] All hydrogen atoms were calculated in idealized positions with fixed displacement parameters. ORTEP-III^[48] was used for the structure representation, and SCHAKAL-99^[49] to illustrate molecule packing. The crystallographic data are summarized in Table 4.2.

X-ray Powder Diffraction. X-ray powder diffraction data were collected at a STOE StadiP X-ray powder diffractometer in transmission geometry from 5° to 30°(2 Θ). Samples were placed in capillaries, and Cu K α 1 radiation was used for the measurement. Radiation was detected with a Mythen 1K detector.

Magnetic Measurements. Magnetic susceptibility data were collected using a Quantum Design MPMSR-2 or an MPMSXL-5 SQUID magnetometer under an applied field

of 0.5 T over the temperature range 2–400 K in the settle mode. Samples were placed in gelatin capsules held within a plastic straw. Data were corrected for the diamagnetic contributions of the ligands by using tabulated Pascal’s constants and those of the sample holder.

^{57}Fe Mössbauer Spectroscopy. Variable temperature ^{57}Fe Mössbauer measurements were recorded in transmission geometry on a constant-acceleration Wissel spectrometer loaded with a 45 mCi $^{57}\text{Co}(\text{Rh})$ source from Cyclotron Ltd. The sample was sealed in a Teflon holder, and low temperature spectra were recorded using an Optistat Oxford instruments liquid nitrogen cryostat. The spectra were fitted using Recoil 1.05 Mössbauer Analysis Software.^[50] The isomer shift values are given with respect to an α -Fe reference at room temperature.

Thermogravimetric Analyses. Thermogravimetric analyses were carried out on a SDT 2960 Simultaneous DSC-TGA under nitrogen atmosphere using alumina sample holder.

Differential Scanning Calorimetry. Calorimetric measurements sealed in an aluminium sample holder were carried out with a PerkinElmer DSC-7 differential scanning calorimeter at a scan rate of 10 K/min following described procedures.^[51]

4.3 Results and Discussion

4.3.1 Syntheses.

The general synthetic pathway for the synthesis of the $[\text{FeL1}(\text{pina})]$ coordination polymers is given in Scheme 4.1. Three different synthetic modes were used to prepare the complex $[\text{FeL1}(\text{pina})](\mathbf{1})$ and its solvates: (i) The starting materials $[\text{FeL1}(\text{MeOH})_2]$ and pina were mixed in the desired solvent and heated to reflux for 1 h, to afford $\mathbf{1}\cdot 0.5\text{MeOH}$, $\mathbf{1}\cdot 0.5\text{EtOH}$, and $\mathbf{1}\cdot \text{DMF}$. (ii) By slow diffusion, this method used a homemade Schlenk tube setup which was, to a given height, separated into two chambers by a dividing wall.

Table 4.1: Overview of the SCO Behavior, Characteristic $\chi_M T$ Values [$\text{cm}^3 \cdot \text{K} \cdot \text{mol}^{-1}$], HS Residue (γ_{HS}) at 150 K, and $T_{\frac{1}{2}}$ Values [K].

compound	spin state behavior	$\chi_M T$ (350 K)	$\chi_M T$ (150 K)	γ_{HS} (150 K)	$T_{\frac{1}{2}}$ [K]
1·0.5MeOH	HS	3.33	3.24		
1· <i>x</i> MeOH/H ₂ O	hysteresis, 88 K, ^a 92 K ^b	3.49	0.76	0.2	↓240, ↑328 ^a ↓224, ↑316 ^b
1·2MeOH	complete, hysteresis, 34 K, ^a 51 K, ^b 45 K ^c	3.64	0.2	0	↓272, ↑306 ^a ↓245, ↑296 ^b ↓236, ↑281 ^a
1·0.5MeOH ·0.5H ₂ O	incomplete, unstable, hysteresis, 46 K, ^a 65 K, ^b 73 K ^c	3.23	1.41, ^a 2.07, ^b 2.29 ^c	0.40 ^a 0.59 ^b 0.65 ^c	↓275, ↑321 ^a ↓263, ↑328 ^b ↓238, ↑311 ^a
1·0.5EtOH	HS	3.53	3.46		
1·2H ₂ O	HS	3.44	3.35		
1·DMF	solvent release, hysteresis, 4 K, ^b 10 K ^c	3.42	0.08, ^a 0.64, ^b 1.08 ^c	0, ^a 0.19 ^b 0.30 ^c	↑335 ^{a,d} ↓305, ↑309 ^b ↓288, ↑298 ^c

^aMagnetic measurement: loop 1. ^bLoop 2. ^cLoop 3. ^dSpin transition upon solvent release. The exact temperature depends on the scan rate.

(iii) The starting iron complex and the axial ligand were dissolved separately in the desired solvent, and the solutions were then mixed at room temperature.

The syntheses were first carried out in methanol, leading to two different samples, 1·0.5MeOH (reflux condition, powder) and an undefined phase 1·*x*MeOH/H₂O (diffusion setup, fine crystals). Magnetic measurements (see Magnetic Measurements section) revealed that 1·0.5MeOH is a pure HS complex while the sample 1·*x*MeOH/H₂O is showing a spin transition with extremely large hysteresis around room temperature. The spin transition properties and the stability of the sample up to 400 K did raise our interest for this compound. Only a small amount of sample was obtained from the first diffusion setup, and the crystals were not of sufficient quality for single crystal X-ray structure analysis. Therefore, attempts were made to reproduce the synthesis using slow diffusion. Single crystals of sufficient X-ray quality were obtained but with a different composition (1·2MeOH). Magnetic measurements reveal SCO behavior with a hysteresis close to room temperature. The hysteresis loop width, however, is significantly smaller.

Since solvent has a strong influence on the SCO behavior of this system, the synthesis was repeated in different solvents: mixtures of water and methanol, ethanol, tetrahydrofuran (THF), and dimethylformamide (DMF). Mixtures of methanol and water were used to account for remaining water in the very hygroscopic pina ligand. This is the most likely reason for the different outcomes of the first and second diffusion setup. Indeed, in a mixture of a 98:2 ratio of methanol and water, respectively, a new powder sample $1 \cdot 0.5\text{H}_2\text{O} \cdot 0.5\text{MeOH}$ was obtained. Magnetic measurements of this sample show a wide hysteresis around room temperature, that is, however, not complete and unstable. Further syntheses were done with ethanol, THF, and DMF. From the synthesis in ethanol, one pure HS sample $1 \cdot 0.5\text{EtOH}$ was obtained, and from synthesis in THF, a further pure HS sample $1 \cdot 2\text{H}_2\text{O}$. The synthesis in DMF produced an interesting phase $1 \cdot \text{DMF}$ which is undergoing SCO. In Table 4.1, an overview of the synthesized complexes and the characteristic temperatures and $\chi_M T$ values is given. The syntheses of all samples except that of $1 \cdot x\text{MeOH}/\text{H}_2\text{O}$ were reproduced at least once.

4.3.2 X-ray Structure Analysis.

Crystals with the composition $1 \cdot 2\text{MeOH}$ were of sufficient quality for a single crystal X-ray structure analysis, and we were able to solve the structure at 173 K where the complex is in the low-spin state according to the magnetic measurements. The crystal structure of compound $1 \cdot 2\text{MeOH}$ describes the first example for coordination polymer with pina as axial ligand. The crystallographic data are summarized in Table 4.2. Selected bond lengths and angles are shown in Table 4.3. ORTEP drawing of the asymmetric unit is given in Figure 4.2.

Compound $1 \cdot 2\text{MeOH}$ crystallizes in the monoclinic space group $P2_1/c$. The observed bond lengths around the iron center are within the range reported for other octahedral iron(II) complexes made of this ligand type in the LS state.^[7,39,52,53] The average values are $1.90 \text{ \AA}(\text{Fe}-\text{N}_{eq})$, $1.94 \text{ \AA}(\text{Fe}-\text{O}_{eq})$, and $2.01 \text{ \AA}(\text{Fe}-\text{N}_{ax})$. The observed O–Fe–O angle is with 88.9° clearly indicative of LS iron(II).^[7,39,52,53] The axial pina ligand links the iron centers as bridging bidentate ligand. Analysis of the polymeric structures reveals an infinite one-dimensional chain with the base vector $[100]$. The pina ligand is disordered, mainly

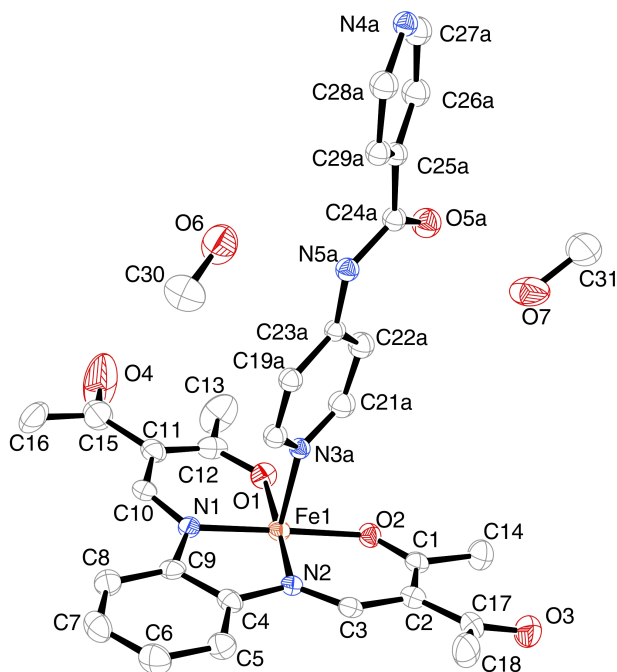


Figure 4.2: ORTEP drawing of the asymmetric unit of 1·2MeOH. Hydrogen atoms and the disorder of the pina ligand have been omitted for clarity. Thermal ellipsoids are shown with a 50% probability.

concerning the asymmetric peptide bond. However, the carbonyl oxygen is pointing at the same direction in both disordered structures. This disorder could be the reason for the small steps/plateaus observed in the magnetic measurements. The asymmetric unit additionally contains two methanol molecules, each bound to the peptide bond through hydrogen bonds. The details for the hydrogen bonds are summarized in Table 4.4 ; an excerpt of the molecule packing is given in Figure 4.3. In one case, the hydroxy group of methanol is the donor group (O7-H7A) and the carbonyl oxygen of the peptide bond the acceptor (O5). In the other case, methanol is the acceptor (O6) of the N-H group of the peptide bond (N5-H5). This solvent molecule moreover participates in a second hydrogen bond between its hydroxy group (O6-H6A) and the carbonyl group (O3) of an adjacent equatorial ligand and, thus, is part of an infinite one-dimensional hydrogen bond chain (base vector [001], Figure 4.3). One further direct short contact is observed between the carbonyl group of the equatorial ligand and the nitrogen of the peptide bond. It should be mentioned that only the axial ligand and substituents of the equatorial ligand are involved in the hydrogen bond network and no participation of the donor oxygen atom

Table 4.2: Crystallographic Data of $[\text{FeL1}(\text{pina})]\cdot 2\text{MeOH}$ ($1\cdot 2\text{MeOH}$).

1·2MeOH	
formula	$\text{C}_{31}\text{H}_{35}\text{FeN}_5\text{O}_7$
M [g·mol ⁻¹]	645.49
cryst syst	monoclinic
space group	$P2_1/c$
a [Å]	13.3304(11)
b [Å]	12.9564(11)
c [Å]	21.5188(15)
α [°]	90
β [°]	127.769
γ [°]	90
V [Å ³]	2937.9(4)
Z	4
ρ [g·cm ⁻³]	1.459
μ [mm ⁻¹]	0.571
cryst size [mm]	0.32 × 0.19 × 0.11
T [K]	173(2)
λ (Mo $K\alpha$) [Å]	0.71073
θ range [°]	4.19–25.38
reflns collected	11924
indep reflns (R_{int})	5286 (0.0391)
params	391
restraints	24
$R(F)$ (all data)	0.0516 (0.0924)
$wR2$	0.1316
$Goof$	0.960

of the equatorial ligand, as for the corresponding mononuclear imidazole complexes, is observed.

4.3.3 Powder X-ray Diffraction

In order to verify that the different samples of **1** assume similar structures, the calculated powder X-ray diffraction pattern of $1\cdot 2\text{MeOH}$ is compared with measured PXRD patterns. The results are given in the Supporting Information, Figure 4.10. Indeed, in the region $2\Theta = 8\text{--}8.5^\circ$ and $2\Theta = 26\text{--}27^\circ$, strong similarities in the diffraction patterns are observed. This can be used as confirmation that in all cases coordination polymers were formed with an approximate distance between the iron centers of 13.5 Å and a distance between the polymer chains in the region of 4 Å. The diffraction pattern of the three pure HS complexes $1\cdot 0.5\text{MeOH}$, $1\cdot 2\text{H}_2\text{O}$, and $1\cdot 0.5\text{EtOH}$ are almost identical. Apparently

Table 4.3: Selected Bond Lengths [\AA] and Angles [$^\circ$] of the Structure of $1 \cdot 2\text{MeOH}$.

compound	Fe-N _{eq}	Fe-O _{eq}	Fe-N _{ax}	O _{eq} -Fe-O _{eq}	N _{ax} -Fe-N _{ax}
1·2MeOH	1.904(3)	1.940(2)	2.026(13) ^a 1.93(3) ^b	88.89(10)	174.4(3) ^{a,c}
	1.898(3)	1.947(2)	2.008(11) ^a 2.05(3) ^b		172.6(8) ^{b,c}

^aRelated to N3A. ^bRelated to N3B; symmetry code. ^c $1 + x, y, z$.

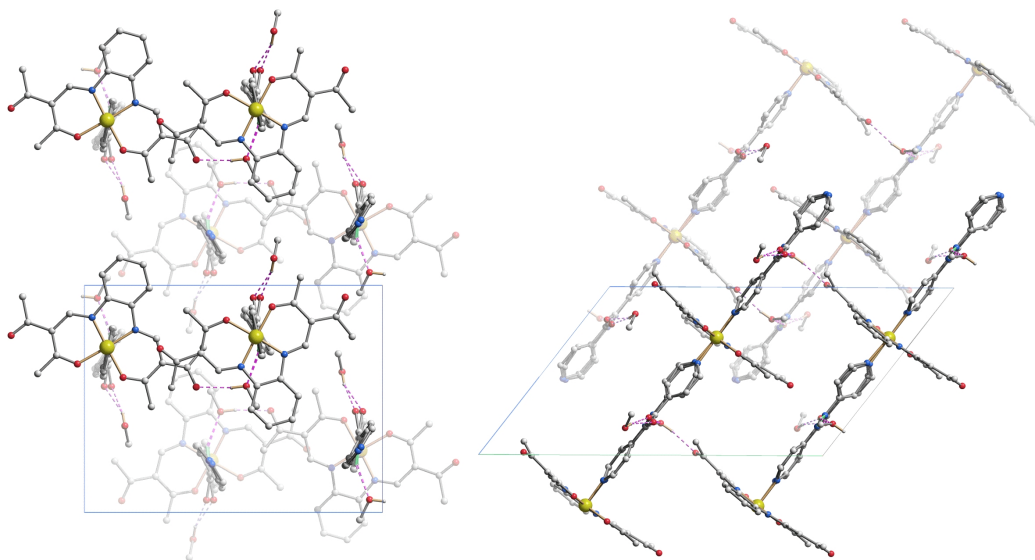


Figure 4.3: Crystal packing of $1 \cdot 2\text{MeOH}$. View along $[100]$ (left) and along $[010]$ (right). Hydrogen atoms are omitted for clarity. The hydrogen bonds are given as dashed lines.

they all precipitate in the same packing pattern independent of the cocrystallized solvent molecules. This assumption is supported further by the fact that the solvent-free sample of $1 \cdot 0.5\text{MeOH}$ (after annealing at $100\text{ }^\circ\text{C}$ for 5 h under vacuum to remove all methanol) shows the same diffraction pattern as before.

The diffraction patterns of the three spin transition samples $1 \cdot \text{DMF}$, $1 \cdot 2\text{MeOH}$, and $1 \cdot 0.5\text{H}_2\text{O} \cdot 0.5\text{MeOH}$ also show some similarities, especially in the regions $2\Theta = 12\text{--}15^\circ$ and $2\Theta = 20\text{--}23^\circ$. There are, however, also some differences in good agreement with the different magnetic properties observed in the magnetic measurements. There are pronounced differences between the diffraction patterns of the pure HS complexes and the SCO complexes.

Table 4.4: Summary of the Intermolecular Hydrogen Bonds of 1·2MeOH with $d(\text{D}\cdots\text{A}) < R(\text{D}) + R(\text{A}) + 0.5 \text{ \AA}$, $d(\text{H}\cdots\text{A}) < R(\text{H}) + R(\text{A}) - 0.12 \text{ \AA}$, $\text{D-H}\cdots\text{A} > 100.0^\circ$

compound	D	H	A	D-H [Å]	H \cdots A [Å]	D \cdots A [Å]	D-H \cdots A [°]
1·2MeOH	N5A	H5A	O6	0.88	2.19	3.008(6)	155
	N5B	H5B	O6	0.88	2.16	2.893(13)	141
	O7	H7A	O5A	0.84	2.09	2.887(7)	159
	O7	H7A	O5B	0.84	1.94	2.771(13)	169
	O6	H6A	O3 ^a	0.84	2.04	2.865(4)	169
	C18	H18A	O7 ^b	0.98	2.58	3.458(7)	149
	C18	H18C	O6 ^c	0.98	2.59	3.327(5)	132
	C20A	H20A	O3 ^b	0.95	2.50	3.217(10)	132

Symmetry codes: ^a $x, -\frac{1}{2} - y, \frac{1}{2} + z$; ^b $-x, \frac{1}{2} + y, -\frac{1}{2} - z$; ^c $x, -\frac{1}{2} - y, -\frac{1}{2} + z$.

4.3.4 Magnetic Measurements.

Of the seven samples investigated, three (1·0.5MeOH, 1·0.5EtOH, 1·2H₂O) are pure HS complexes in the entire temperature range with a $\chi_M T$ product in the range of 3.4 cm³·K·mol⁻¹, typical for HS iron(II). The corresponding plot of the $\chi_M T$ product versus temperature is displayed in the Supporting Information, Figure 4.11. For the other four samples SCO behavior is observed, which is described in the following.

The result from the magnetic measurements (plot of the $\chi_M T$ product vs T) of the undefined sample 1· x MeOH/H₂O is displayed in Figure 4.4. The compound shows a spin transition with a very wide thermal hysteresis around room temperature. At room temperature the $\chi_M T$ product is with 0.89 cm³·K·mol⁻¹, indicative of a sample with the majority of the spins in the LS state. Upon cooling, this value remains constant down to 50 K. Upon heating, the compound remains first in the LS state and undergoes an abrupt spin transition to the HS state above room temperature with $T_{\frac{1}{2}\uparrow} = 328 \text{ K}$. At 350 K, the $\chi_M T$ product is with 3.49 cm³·K·mol⁻¹ in the typical region for HS iron(II) complex. Upon cooling, a relatively gradual spin transition to the low-spin (LS) state is observed with $T_{\frac{1}{2}\downarrow} = 240 \text{ K}$ and a $\chi_M T$ product of 0.79 cm³·K·mol⁻¹ at 150 K. About 20% of the molecules remain in the HS state. This corresponds to an apparent thermal hysteresis of 88 K. The hysteresis is apparent in the sense that solvent molecules are released during the first warming process as first identified for [Fe(hyetrz)₃](3-nitrophenylsulfonate)₂·3H₂O.^[54] After heating to 400 K, a second loop of measurement shows that the transition temperatures are shifted to lower temperatures ($T_{\frac{1}{2}\downarrow} = 224 \text{ K}$ and $T_{\frac{1}{2}\uparrow} = 316 \text{ K}$) and the hysteresis

loop is with 92 K slightly wider. A closer inspection of the curve progression of the second cycle in the cooling mode reveals the formation of a slight plateau in the region of 224 K; thus, a two-step spin transition takes place while a one-step spin transition is observed during heating. The transition temperatures for the two steps are 244 and 209 K. Thus, for the second step the hysteresis width is 107 K. The difference between the first and the second cycles is most likely due to a loss of solvent molecules included in the crystal packing during the heating process. After heating the sample to 400 K for 1 h to remove all solvent, a third cycle was measured. Upon cooling, the transition temperature is again shifted to lower temperatures with $T_{\frac{1}{2}\downarrow} = 199$ K, whereas, upon heating, the transition temperature remains constant ($T_{\frac{1}{2}\uparrow} = 316$ K). A thermal hysteresis loop with a width of 117 K is observed! Due to difficulties with the reproduction of this sample, no further measurements on this material were possible.

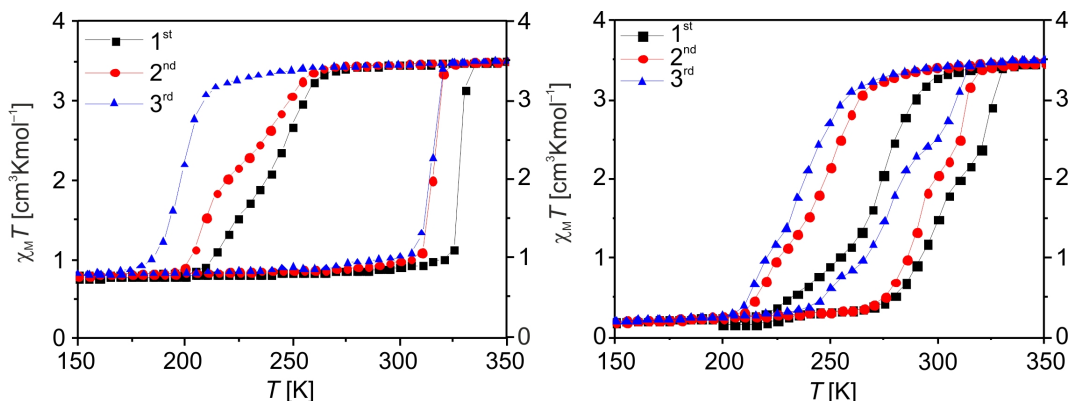


Figure 4.4: Plots of the $\chi_M T$ product versus T for $1 \cdot x\text{MeOH}/\text{H}_2\text{O}$ (left) and $1 \cdot 2\text{MeOH}$ (right). The first loop (black squares) corresponds to measurements starting at room temperature; the sample is not heated above 350 K. Before the second loop (red circles) the sample was shortly heated to 400 K, and before the third loop (blue triangles) the sample was left at 400 K for 1 h to remove all solvent.

Magnetic measurements of $1 \cdot 2\text{MeOH}$, displayed in Figure 4.4, reveal SCO behavior with a hysteresis close to room temperature. The room temperature $\chi_M T$ product of this sample is with $3.39 \text{ cm}^3 \cdot \text{K} \cdot \text{mol}^{-1}$ in the typical region for a HS iron(II) complex. Upon heating to 350 K, it increases to a value of $3.64 \text{ cm}^3 \cdot \text{K} \cdot \text{mol}^{-1}$. Upon cooling, compound $1 \cdot 2\text{MeOH}$ undergoes a spin transition to the LS state with a $T_{\frac{1}{2}\downarrow} = 272$ K and a $\chi_M T$

product of $0.2 \text{ cm}^3\cdot\text{K}\cdot\text{mol}^{-1}$ at 150 K. For this sample the spin transition is complete. Upon heating, the compound undergoes an abrupt spin transition back to HS state with $T_{\frac{1}{2}\uparrow} = 306 \text{ K}$, exhibiting a thermal hysteresis of 34 K. Indications for small steps in the heating and cooling mode are observed. The disorder of the pina ligand observed in the X-ray structure of this complex is most likely the reason for this behavior. Indeed, the pina ligand is asymmetric, having an acidside and an amino-side, which gives the possibility for the iron centers to be coordinated twice to both ends or once to each side. This situation may result in a slight change in the crystal field strength that could be responsible for the small steps. Only the average values are considered for the following discussion. Further loops of measurement (after heating to 400 K for a few minutes and for 1 h to remove the solvent included in the material) show that the hysteresis is shifted to lower temperature once the solvent is lost. Again, this is comparable with the behavior of the first crystalline sample. The loss of the solvent is also accompanied by an increase of the hysteresis width to 51 K for the second cycle and 45 K for the third cycle.

The results of the magnetic measurements of $1\cdot 0.5 \text{ H}_2\text{O}\cdot 0.5\text{MeOH}$ are displayed in Figure 4.5. The room temperature $\chi_M T$ product is with $2.94 \text{ cm}^3\cdot\text{K}\cdot\text{mol}^{-1}$ indicative of an iron(II) complex that is almost completely in the HS state. Upon cooling, the compound undergoes an incomplete spin transition around 275 K, with a remaining $\chi_M T$ product of $1.41 \text{ cm}^3\cdot\text{K}\cdot\text{mol}^{-1}$ at 150 K ($\gamma_{HS} = 0.4$). Upon heating, the $\chi_M T$ product increases first slowly, than more rapidly, until the compound is back in the HS state in a two-step transition with an average $T_{\frac{1}{2}\uparrow} = 321 \text{ K}$, leading formally to a 46 K wide hysteresis. As further cycles are measured, the transition temperatures are shifted to lower temperatures, and an increase of the hysteresis width (up to 73 K for the third cycle) is observed, in agreement with the results of the previously described samples. However, for the sample $1\cdot 0.5\text{H}_2\text{O}\cdot 0.5\text{MeOH}$ a significant increase of the remaining HS fraction is observed. For the third cycle, $\gamma_{HS} = 0.65$, only one-third of the iron centers undergo spin transition. In the Supporting Information, Figure 4.12, the TGA analysis of the sample is given to confirm the solvent loss upon heating.

The sample $1\cdot\text{DMF}$ (Figure 4.5) is at room temperature almost in the LS state. At 250 K the $\chi_M T$ product is with $0.08 \text{ cm}^3\cdot\text{K}\cdot\text{mol}^{-1}$ characteristic for an iron(II) LS complex.

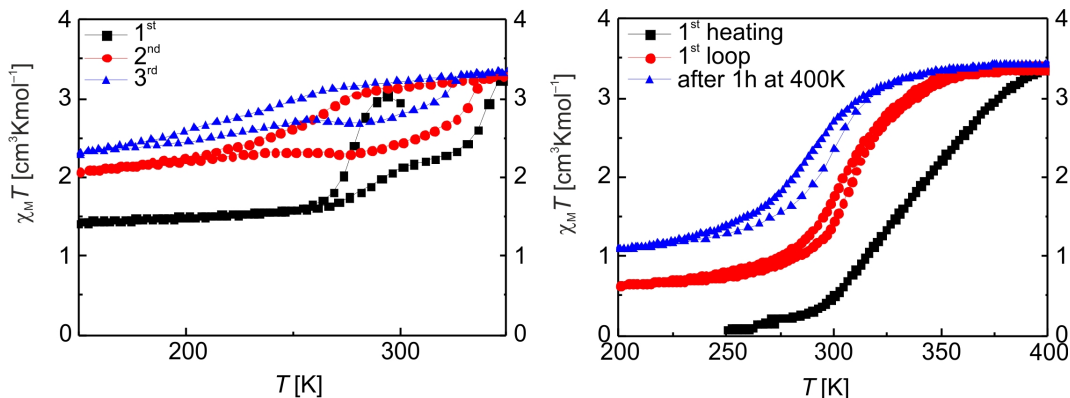


Figure 4.5: Plots of the $\chi_M T$ product versus T for compounds $1 \cdot 0.5\text{H}_2\text{O} \cdot 0.5\text{MeOH}$ (left) and $1 \cdot \text{DMF}$ (right).

Upon heating, solvent loss accompanied by a gradual spin transition starting around 300 K and ending at 400 K is observed. The solvent loss was followed by TGA (see Experimental Section and Supporting Information, Figure 4.12). At 400 K in the HS state a $\chi_M T$ product of $3.35 \text{ cm}^3 \cdot \text{K} \cdot \text{mol}^{-1}$ is obtained. The second cooling/heating cycle reveals a shift of the spin transition to lower temperatures and a small hysteresis of 4 K ($T_{\frac{1}{2}\downarrow} = 305 \text{ K}$, $T_{\frac{1}{2}\uparrow} = 309 \text{ K}$). The $\chi_M T$ product of $0.64 \text{ cm}^3 \cdot \text{K} \cdot \text{mol}^{-1}$ at 150 K indicates that the spin state change is no longer complete but a remaining HS fraction of $\gamma_{HS} = 0.19$ is obtained. The compound was kept 1 h at 400 K in order to remove the included solvent completely. This resulted in a shift of the transition temperature to lower temperatures, an increase of the hysteresis width (10 K, $T_{\frac{1}{2}\downarrow} = 288 \text{ K}$, $T_{\frac{1}{2}\uparrow} = 298 \text{ K}$), and a higher HS fraction ($\chi_M T = 1.08 \text{ cm}^3 \cdot \text{K} \cdot \text{mol}^{-1}$ at 150 K, $\gamma_{HS} = 0.30$).

All samples showing spin transition have in common that the spin transition is shifted to lower temperatures upon solvent loss and a slight increase of the hysteresis width is observed. However, for the first two samples the remaining HS fraction does not change with repeating heating/cooling cycles while for the latter two samples a significant increase for the remaining HS fraction is observed. Apparently, for the powder samples the loss of methanol, water, or DMF molecules causes the formation of defects in the crystal lattice resulting in a loss of the spin transition properties.

4.3.5 Mössbauer Spectroscopy and Thermal Analysis

The compound $1 \cdot 0.5\text{H}_2\text{O} \cdot 0.5\text{MeOH}$ was resynthesized in high amount to allow further investigations of the complex spin transition behavior using differential scanning calorimetry (DSC) and ^{57}Fe Mössbauer spectroscopy. The DSC measurements were done in order to track other phase transitions occurring upon cooling and heating that could explain the unstable ST behavior (Figure 4.6). Upon cooling, a first endothermic transition occurs around 297 K, which is directly followed by a sharper transition at 291 K. One transition corresponds to the incomplete HS to LS transition and the other one to another first order phase transition. Upon warming, one broad exothermic transition is observed with a maximum at 353 K corresponding to the LS to HS state spin transition, with a weak shoulder around the boiling point of methanol ($\simeq 338$ K). Thus, one could assume that the loss of methanol triggers the LS to HS spin state change. Determined values of enthalpy ($\Delta H \downarrow = 33 \text{ kJ} \cdot \text{mol}^{-1}$ and $\Delta H \uparrow = 39 \text{ kJ} \cdot \text{mol}^{-1}$, assuming that two-third of the iron centers switch the spin state) and entropy ($\Delta S \downarrow = 113 \text{ J} \cdot \text{mol}^{-1} \text{K}^{-1}$ and $\Delta S \uparrow = 119 \text{ J} \cdot \text{mol}^{-1} \text{K}^{-1}$) are significantly higher than observed for spin transitions in similar materials^[33] due to the presence of other thermodynamic phenomena occurring at the same time: another phase transition upon cooling, and the methanol vaporization upon heating. Obviously, those phenomena are related to the spin transitions. The small difference of transition temperatures when one compares the DSC results to the SQUID measurement originates from the different measurements modes (sweep for the DSC, settle for the SQUID).

^{57}Fe Mössbauer spectrometry was used to understand the incompleteness of the spin transition of the powder phase $1 \cdot 0.5\text{H}_2\text{O} \cdot 0.5\text{MeOH}$. Mössbauer parameters of all spectra are summarized in the Supporting Information, Table 4.5. Selected spectra are shown in Figure 4.7. A plot of the A_{HS}/A_{tot} versus T is shown in Figure 4.8, assuming equal Debye-Waller factors for the LS and HS ions. The spectrum at 298 K shows two different signals: one quadrupole doublet corresponding to HS iron(II) ions with a large quadrupole splitting ($\delta = 0.92(1) \text{ mm/s}$; $\Delta E_Q = 2.24(1) \text{ mm/s}$; $\Gamma/2 = 0.20(2) \text{ mm/s}$; $A_{HS}/A_{tot} = 93(3)\%$) and another quadrupole doublet corresponding to LS iron(II) ions with a smaller quadrupole splitting ($\delta = 0.38(2) \text{ mm/s}$; $\Delta E_Q = 0.84(4) \text{ mm/s}$; $\Gamma/2 = 0.11(2) \text{ mm/s}$;

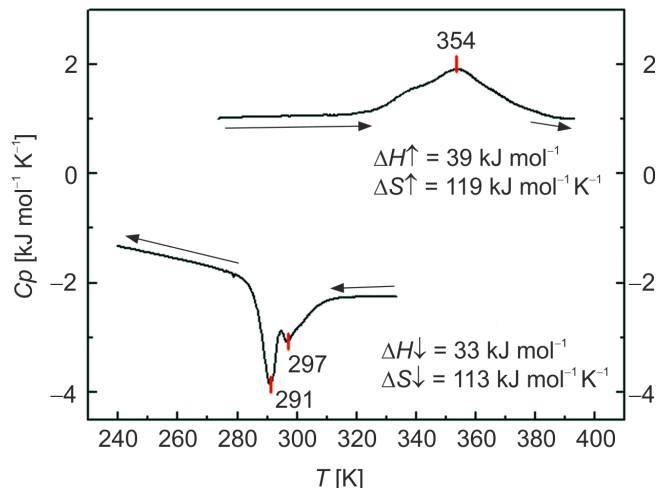


Figure 4.6: DSC measurement of $1 \cdot 0.5\text{H}_2\text{O} \cdot 0.5\text{MeOH}$. Measured enthalpy and entropy values are given in the cooling and warming modes (5 K/min). The values were corrected by a factor 1.5 as only two-third of the iron centers are involved in the spin transition as indicated by Mössbauer spectroscopy and magnetic measurements.

A_{LS}/A_{tot} 7(3)%). The hyperfine parameters are similar to reported ones for 1D chains of complexes with similar ligand system.^[55] In the following, the Mössbauer spectra were first recorded upon cooling down to 78 K, then upon warming up to 348 K. Upon cooling, the compound undergoes an incomplete spin transition with a $T_{\frac{1}{2}\downarrow} = 280$ K, with a remaining HS area of 30% at 78 K. The transition temperature is in good agreement with the results from the magnetic measurements (275 K); however, the spin transition is more complete. This can be explained because the Mössbauer measurements are done in closed Teflon capsules at ambient pressure. In contrast to this in the SQUID magnetometer the sample is in constant vacuum. The results of the SQUID measurements on this sample show that upon solvent loss the spin transition is less complete. Upon warming, the HS fraction remains constant up to 298 K. Above 298 K, the LS to HS conversion starts, that is, however, not complete at 348 K.

The spectrum at 298 K after the first cooling shows a different population of the two iron(II) states compared to the first spectrum at 298 K. Thus, clear evidence for the room temperature bistability is obtained. The sample was further heated up to 348 K, showing an increase of the HS fraction at higher temperatures. The analysis of isomer shift δ , quadrupole splitting ΔE_Q , and half line width $\Gamma/2$ with respect to the temperature

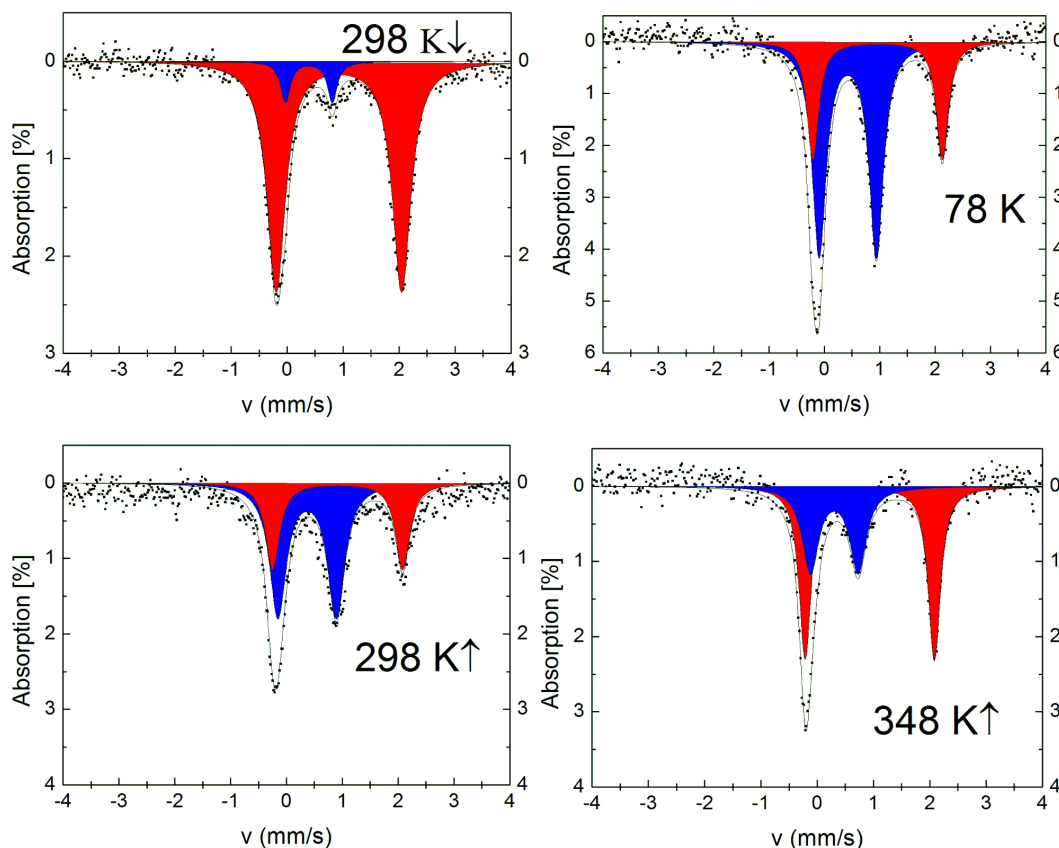


Figure 4.7: Selected Mössbauer spectra of $1 \cdot 0.5\text{H}_2\text{O} \cdot 0.5\text{MeOH}$. HS Fe^{II} signal is depicted in red, LS Fe^{II} in blue. Measurement temperatures are indicated on the spectra.

reveals that all parameters show some modifications upon cooling between 272 and 232 K. Especially, the line width suddenly raises to high values (at 252 K, $\Gamma/2 = 0.28(3)$ mm/s for the HS state and $0.34(3)$ mm/s for the LS state). The plots of the Mössbauer parameters versus T are shown in Figure 4.9. This sudden jump, which is occurring right after the spin transition around 250 K upon cooling, is attributed to a phase transition. This is in good agreement with the results from the DSC measurements that a phase transition is occurring during the HS to LS spin transition. Mössbauer spectroscopy therefore allows attributing the DSC peak at 297 K (Figure 4.6) to the spin transition and the sharper peak at 291 K to the phase transition. However, the exact nature of the phase transition (changes in the hydrogen bond network, reorientation of the ligand) is yet to be determined. The results support the tendency that wide hysteresis loops are observed, when the spin transition is accompanied by pronounced structural changes.^[35]

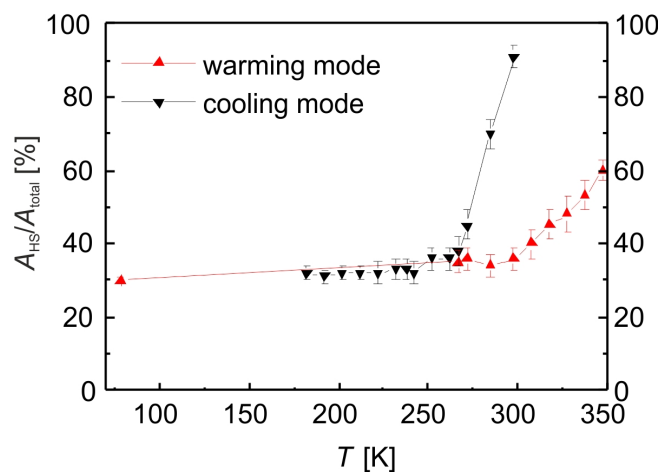


Figure 4.8: A_{HS}/A_{tot} [%] versus T [K] plot of the Mössbauer spectra measured on the compound $1 \cdot 0.5H_2O \cdot 0.5MeOH$.

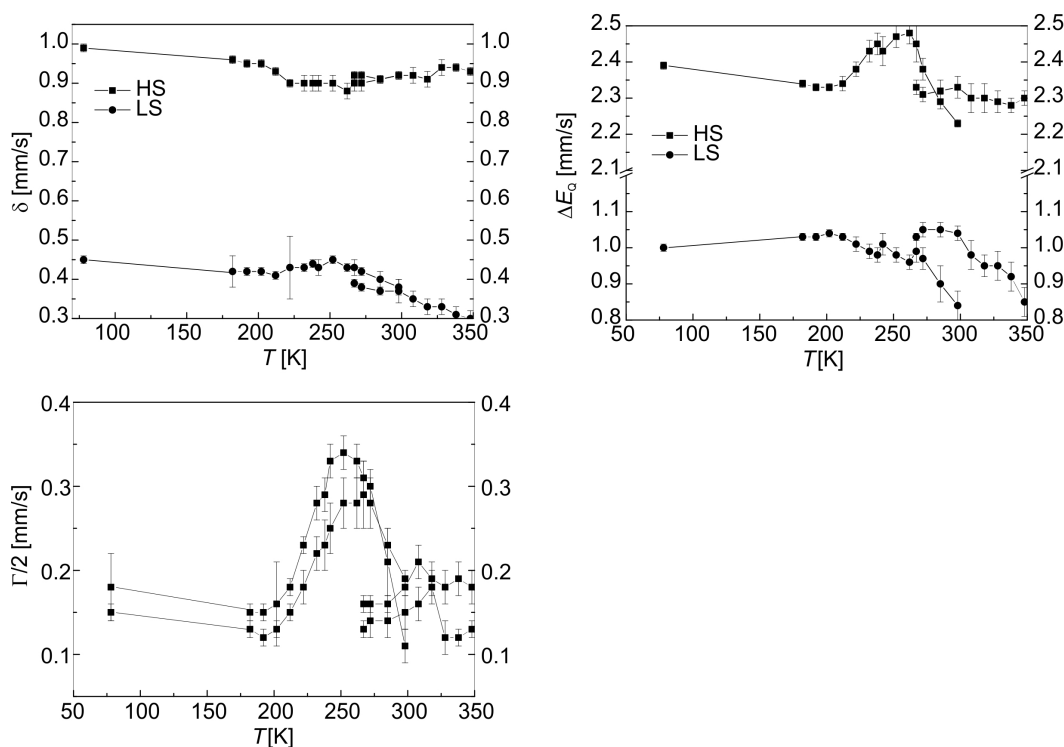


Figure 4.9: Plots of the isomer shift δ , quadrupole splitting ΔE_Q , and half line width $\Gamma/2$ vs T for both HS and LS signals of compound $1 \cdot 0.5H_2O \cdot 0.5MeOH$

One further piece of important information from Mössbauer spectroscopy is that only one iron site is observed for the HS and the LS state. This implies that the coordination spheres of the iron centers are not changed after the phase transition or the loss of solvent. Therefore, the phase transition could be a rearrangement of the hydrogen bond network,

as it was already discussed for similar systems.^[12] Another possibility would be changes in the orientation of the ligand, e.g., the rotation of the axial ligand from eclipsed to staggered.

For compound $\mathbf{1}\cdot 0.5\text{H}_2\text{O}\cdot 0.5\text{MeOH}$, the unstable character of the SCO is most likely due to the loss of methanol during the LS to HS spin transition. On the basis of the powder diffraction pattern of $\mathbf{1}\cdot 0.5\text{H}_2\text{O}\cdot 0.5\text{MeOH}$ (partially dried sample) it is difficult to say if the solvent-free sample is identical to the annealed sample $\mathbf{1}$ obtained from the pure HS complexes or if another pure HS phase is obtained.

4.4 Conclusion

We hereby reported the synthesis of seven solvates of the coordination polymer $[\text{FeL1}(\text{pina})](\mathbf{1})$ showing either spin crossover or being HS depending on the type of solvent used. Compound $\mathbf{1}\cdot x\text{H}_2\text{O}/\text{MeOH}$, obtained as crystals, shows a very wide hysteresis of 88 K. Attempts to repeat the synthesis of those crystals led to new compound $\mathbf{1}\cdot 2\text{MeOH}$, presenting a wide hysteresis of up to 51 K around room temperature. The crystal structure of $\mathbf{1}\cdot 2\text{MeOH}$ was determined, showing 1D coordination polymers linked together by an hydrogen bond network, therefore creating a 2D network through the crystal packing. Thus, the pina ligand was used successfully in a crystal engineering-like approach to improve the spin transition properties of the iron(II) coordination polymers with regard to the observation of thermal hysteresis loops. The thermal hystereses are wider than those observed for related complexes with rigid ligands as 4,4'-bipyridine^[56] or with modified equatorial ligands.^[37] From other methods of synthesis, the compound $\mathbf{1}\cdot 0.5\text{H}_2\text{O}\cdot 0.5\text{MeOH}$ was obtained. This latter sample shows also a wide hysteresis loop of 46 K around room temperature. However, this compound is not stable upon heating, being turned into an HS compound $\mathbf{1}\cdot x\text{H}_2\text{O}$ upon loss of methanol. The compound $\mathbf{1}\cdot 0.5\text{H}_2\text{O}\cdot 0.5\text{MeOH}$ was analyzed with DSC and Mössbauer spectroscopy. Finally, the compound $\mathbf{1}\cdot \text{DMF}$ was obtained from synthesis in DMF. This latter compound shows a gradual spin crossover, but once the solvent is removed under vacuum, it shows a hysteresis of 10 K around room temperature. All the reported compounds show that their spin crossover properties

strongly depend on the included solvent molecules and are most likely driven by the intermolecular interactions through a hydrogen bond network, as expected by choosing the pina ligand for synthesis of coordination polymers. This work confirms our concept that hydrogen bonds have the optimal balance between elasticity and rigidity to communicate the structural changes upon spin transition from one molecule to another. With the concept of Halcrow,^[35] pronounced structural changes are necessary for the observation of ferroelastic properties (hysteresis^[57]) in spin crossover materials. The combination of equatorial and axial ligands might be especially suited to allow such changes. Next to changes in the hydrogen bond network, e.g. a rotation of the axial ligand is possible. Further work is ongoing in the synthesis of derivatives of the pina ligand in order to form even stronger hydrogen bond networks.

Author Information

Corresponding Authors

*E-mail: yann.garcia@uclouvain.be.

*E-mail: weber@uni-bayreuth.de.

Author Contributions

The manuscript was written through contributions of all authors. All authors have given approval to the final version of the manuscript.

Notes

The authors declare no competing financial interest.

Acknowledgments

We thank Florian Puchtler (University of Bayreuth) for the collection of powder diffraction data. Further, we thank the Fonds National de la Recherche Scientifique-FNRS and the COST action CM1305, as well as GFSM for allowing C.L. and A.P.R. to attend GFSM 2012. Support from the University of Bayreuth, the Deutsche Forschungsgemeinschaft (WE 3546_4-1 and SFB 840/A10), and the Fonds der Chemischen Industrie is gratefully acknowledged.

4.5 Supporting Information

Figure 4.10: Top: Powder X-ray diffraction pattern of the samples discussed in this work. The red line is the calculated diffraction pattern of the single crystals of 1·2 MeOH. Bottom: comparison of the powder X-ray diffraction pattern of sample 1·0.5 MeOH and the annealed sample 1·0.5 MeOH.

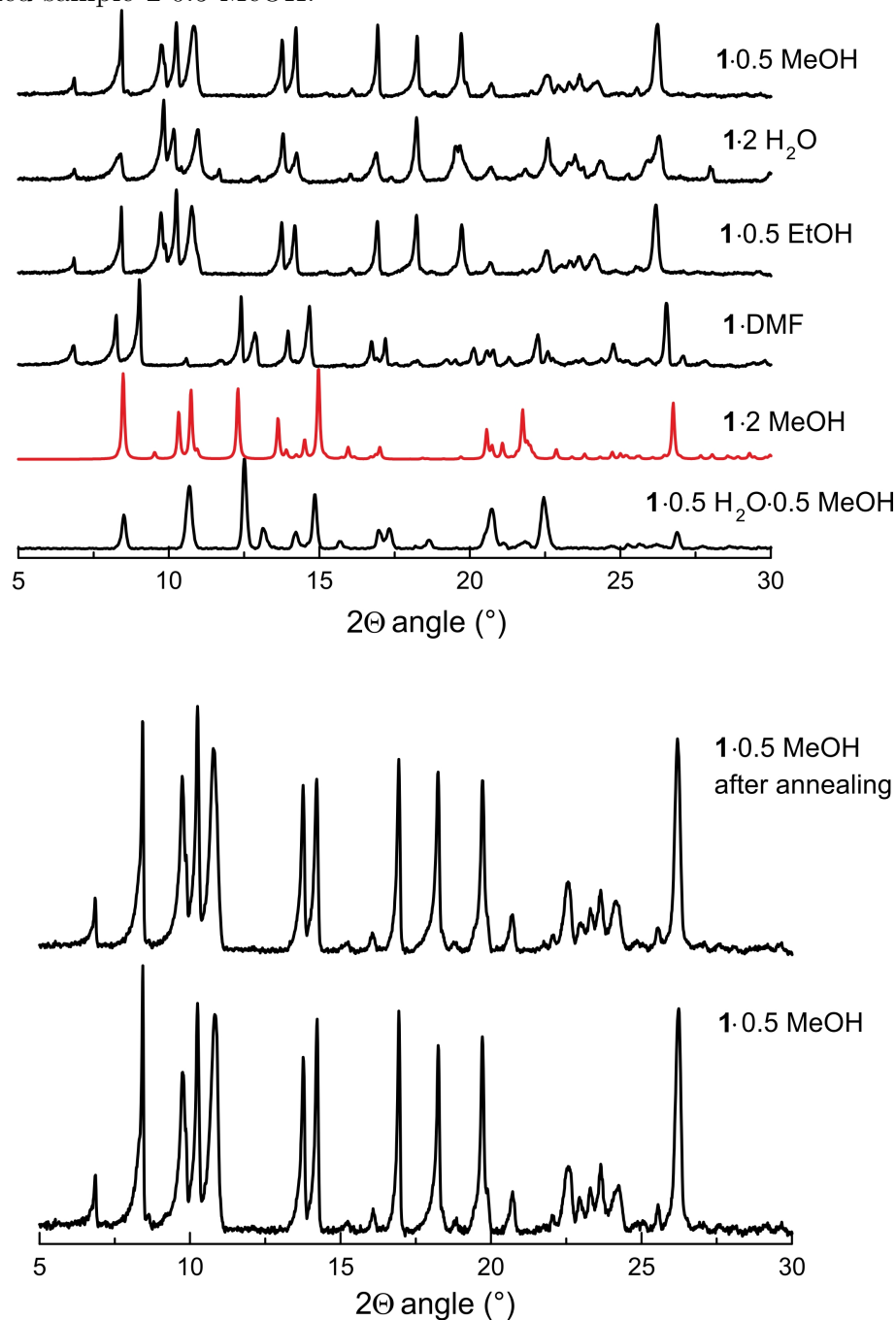


Table 4.5: Mössbauer parameters of $[\text{FeL1}(\text{pina})]\cdot 0.5 \text{H}_2\text{O}\cdot 0.5 \text{MeOH}$ (**1·0.5 H₂O·0.5 MeOH**).

T (K)	Attribution	δ (mm/s)	ΔE_Q (mm/s)	$\Gamma/2$ (mm/s)	Area/total area
298↓	HS Fe(II)	0.92(1)	2.23(1)	0.19(1)	91(3)%
	LS Fe(II)	0.38(2)	0.84(4)	0.11(2)	9(3)%
285↓	HS Fe(II)	0.91(1)	2.29(2)	0.23(2)	70(4)%
	LS Fe(II)	0.40(2)	0.90(5)	0.21(4)	30(4)%
272↓	HS Fe(II)	0.90(2)	2.38(3)	0.28(3)	45(4)%
	LS Fe(II)	0.42(1)	0.97(3)	0.30(2)	55(4)%
267↓	HS Fe(II)	0.90(2)	2.45(5)	0.29(4)	38(4)%
	LS Fe(II)	0.43(2)	0.99(3)	0.31(2)	62(4)%
262↓	HS Fe(II)	0.88(2)	2.48(3)	0.28(3)	36(3)%
	LS Fe(II)	0.43(1)	0.96(2)	0.33(2)	64(3)%
252↓	HS Fe(II)	0.90(2)	2.47(3)	0.28(3)	36(3)%
	LS Fe(II)	0.45(1)	0.98(2)	0.34(2)	64(3)%
242↓	HS Fe(II)	0.90(2)	2.43(4)	0.25(3)	32(3)%
	LS Fe(II)	0.43(2)	1.01(3)	0.33(2)	68(3)%
238↓	HS Fe(II)	0.90(2)	2.45(3)	0.23(3)	33(3)%
	LS Fe(II)	0.44(1)	0.98(2)	0.29(2)	67(3)%
232↓	HS Fe(II)	0.90(2)	2.43(3)	0.22(2)	33(3)%
	LS Fe(II)	0.43(1)	0.99(2)	0.28(2)	67(3)%
222↓	HS Fe(II)	0.90(1)	2.38(2)	0.18(2)	32(3)%
	LS Fe(II)	0.43(8)	1.01(2)	0.23(1)	68(3)%
212↓	HS Fe(II)	0.93(1)	2.34(2)	0.15(1)	32(2)%
	LS Fe(II)	0.41(1)	1.03(1)	0.18(1)	68(2)%
202↓	HS Fe(II)	0.95(1)	2.33(1)	0.13(1)	32(2)%
	LS Fe(II)	0.42(1)	1.04(1)	0.16(5)	68(2)%
192↓	HS Fe(II)	0.95(1)	2.33(1)	0.12(1)	31(2)%
	LS Fe(II)	0.42(1)	1.03(1)	0.15(1)	69(2)%
182↓	HS Fe(II)	0.96(1)	2.34(1)	0.13(1)	32(2)%
	LS Fe(II)	0.42(4)	1.03(1)	0.15(1)	68(2)%
78	HS Fe(II)	0.99(1)	2.39(1)	0.15(1)	30(1)%
	LS Fe(II)	0.45(1)	1.00(1)	0.18(4)	70(1)%
267↑	HS Fe(II)	0.92(1)	2.33(2)	0.13(1)	35(3)%
	LS Fe(II)	0.39(1)	1.03(1)	0.16(1)	65(3)%
272↑	HS Fe(II)	0.92(1)	2.31(2)	0.14(2)	36(3)%
	LS Fe(II)	0.38(1)	1.05(2)	0.16(1)	65(3)%
285↑	HS Fe(II)	0.91(1)	2.32(3)	0.14(2)	34(3)%
	LS Fe(II)	0.37(1)	1.05(2)	0.16(1)	66(3)%
298↑	HS Fe(II)	0.92(1)	2.33(3)	0.15(2)	36(3)%
	LS Fe(II)	0.37(3)	1.04(2)	0.18(1)	64(3)%
308↑	HS Fe(II)	0.92(2)	2.30(4)	0.16(2)	40(4)%
	LS Fe(II)	0.35(2)	0.98(4)	0.21(2)	60(4)%
318↑	HS Fe(II)	0.91(2)	2.30(4)	0.18(2)	45(4)%
	LS Fe(II)	0.33(2)	0.95(3)	0.19(2)	55(4)%
328↑	HS Fe(II)	0.94(2)	2.29(3)	0.12(2)	48(5)%
	LS Fe(II)	0.33(2)	0.95(4)	0.18(2)	52(5)%
338↑	HS Fe(II)	0.94(1)	2.28(2)	0.12(1)	53(4)%
	LS Fe(II)	0.31(2)	0.92(4)	0.19(2)	47(4)%
348↑	HS Fe(II)	0.93(1)	2.30(2)	0.13(1)	60(3)%
	LS Fe(II)	0.30(2)	0.85(4)	0.18(2)	40(4)%

Figure 4.11: Plots of the $\chi_M T$ product versus T for 1·0.5 MeOH, 1·0.5 EtOH and 1·2 H₂O.

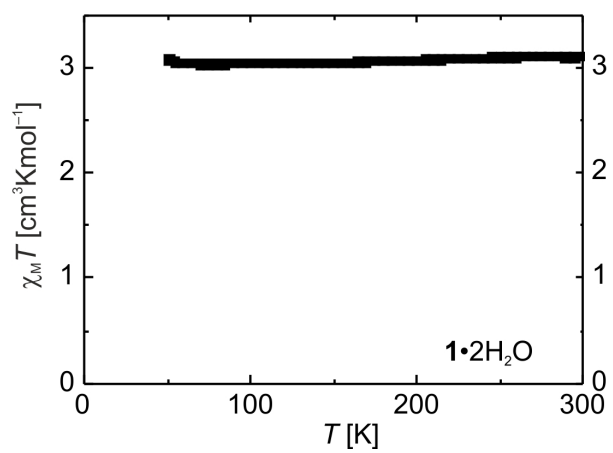
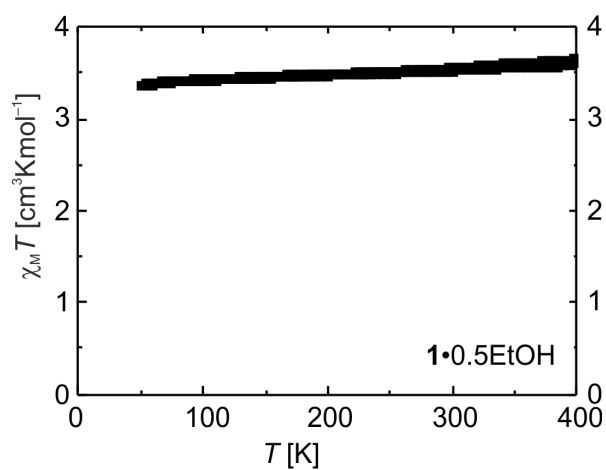
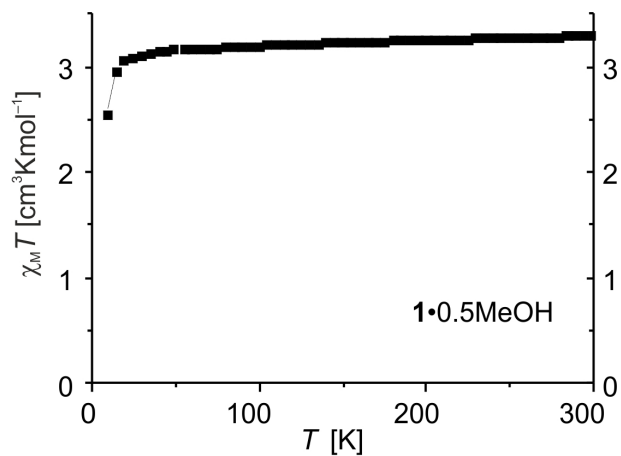
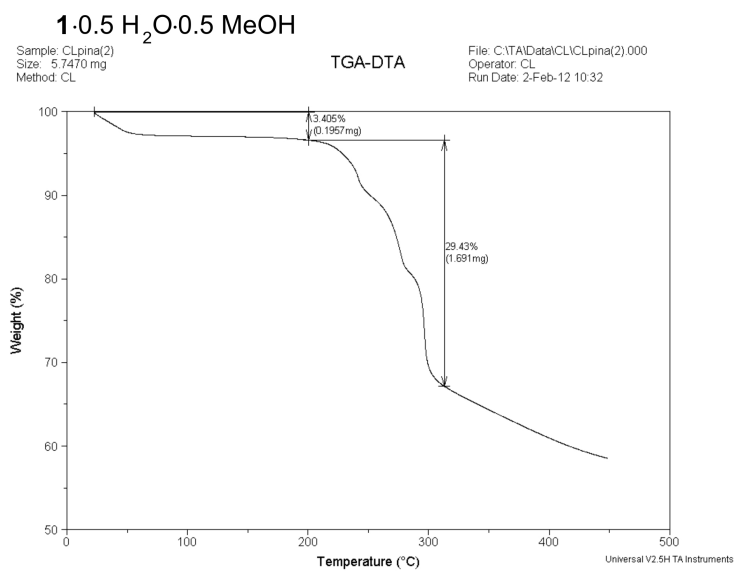
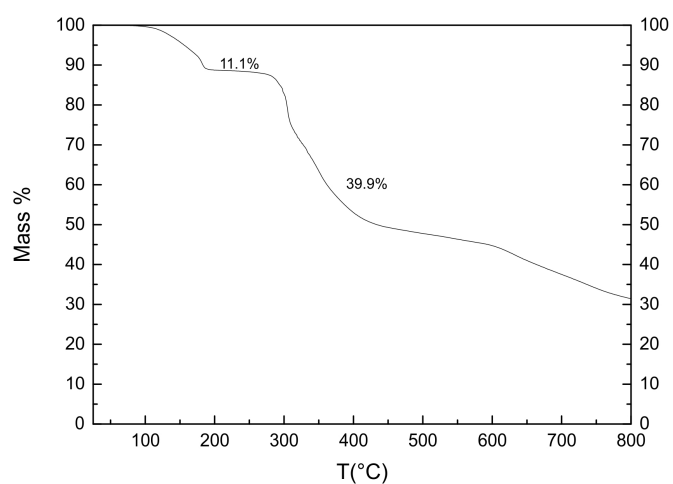


Figure 4.12: Results from TGA analysis for **1·DMF** (top) and **1·0.5 H₂O·0.5 MeOH**.



References

- [1] M. Halcrow, *Spin-Crossover Materials*, John Wiley & Sons Ltd., Chichester, UK, **2013**.
- [2] P. Gütllich, H. Goodwin, *Spin Crossover in Transition Metal Compounds I-III*, Springer, Berlin, DE, **2004**.
- [3] P. Gütllich, A. Hauser, H. Spiering, *Angew. Chem. Int. Ed.* **1994**, *33*, 2024–2054.
- [4] J.-F. Létard, *J. Mater. Chem.* **2006**, *16*, 2550–2559.
- [5] O. Sato, J. Tao, Y.-Z. Zhang, *Angew. Chem. Int. Ed.* **2007**, *46*, 2152–2187.
- [6] J. A. Kitchen, S. Crooker, *Coord. Chem. Rev.* **2008**, *252*, 2072–2092.
- [7] B. Weber, *Coord. Chem. Rev.* **2009**, *253*, 2432–2449.
- [8] M. A. Halcrow, *Coord. Chem. Rev.* **2009**, *253*, 2493–2514.
- [9] K. S. Murray, *Aust. J. Chem.* **2009**, *62*, 1081–1101.
- [10] A. Gaspar, M. Seredyuk, P. Gütllich, *J. Mol. Struct.* **2009**, *924–926*, 9–19.
- [11] S. Brooker, J. A. Kitchen, *Dalton Trans.* **2009**, 7331–7340.
- [12] A. B. Koudriavstsev, W. Linert, *J. Struct. Chem.* **2010**, *51*, 335–365.
- [13] G. A. B. M. M. C. Real, J. A., *Dalton Trans.* **2005**, 2062–2079.
- [14] J. Klingele, D. Kaase, M. Schmucker, Y. Lan, G. Chastanet, J.-F. Létard, *Inorg. Chem.* **2013**, *52*, 6000–6010.
- [15] H. Petzold, S. Heider, *Eur. J. Inorg. Chem.* **2011**, 1249–1254.
- [16] M. M. Khusniyarov, T. Weyhermüller, E. Bill, K. Wieghardt, *Angew. Chem. Int. Ed.* **2008**, *47*, 1228–1231.
- [17] P. Stock, T. Pedziński, N. Spintig, A. Grohmann, G. Hörner, *Chem. Eur. J.* **2013**, *19*, 839–842.
- [18] L. Cambi, L. Szegö, *Ber. dtsh. Chem. Ges. A/B* **1933**, *66*, 656–661.
- [19] L. Cambi, L. Szegö, *Ber. dtsh. Chem. Ges. A/B* **1931**, *64*, 2591–2598.
- [20] O. Kahn, *Science* **1998**, *279*, 44–48.
- [21] J.-F. Létard, P. Guionneau, L. Goux-Capes, *Spin Crossover in Transition Metal Compounds I-III*, Springer, Berlin, DE, **2004**.

-
- [22] A. B. Galet, A. and Gaspar, M. C. Muñoz, G. V. Bukin, G. Levchenko, J. A. Real, *Adv. Mater.* **2005**, *17*, 2949–2953.
- [23] J. Linares, E. Codjovi, Y. Garcia, *Sensors* **2012**, *12*, 4492–4479.
- [24] E. Coronado, J. R. Galán-Mascarós, M. Monrabal-Capilla, J. García-Martínez, P. Pardo-Ibáñez, *Adv. Mater.* **2007**, *19*, 1359–1361.
- [25] T. Forestier, S. Mornet, N. Daro, T. Nishihara, S.-i. Mouri, K. Tanaka, O. Fouche, E. Freysz, J.-F. Létard, *Chem. Commun.* **2008**, 4327–4329.
- [26] C. Göbel, T. Palamarciuc, C. Lochenie, B. Weber, *Chem. Asian. J.* **2014**, *9*, 2232–2238.
- [27] K. Kuroiwa, H. Kikuchi, N. Kimizuka, *Chem. Commun.* **2010**, *46*, 1229–1231.
- [28] M. Seredyuk, A. B. Gaspar, V. Ksenofontov, Y. Galyametdinov, M. Verdaguer, F. Villain, P. Gülich, *Inorg. Chem.* **2008**, *47*, 10232–10245.
- [29] M. Carmen Muñoz, J. A. Real, *Spin-Crossover Materials*, John Wiley & Sons Ltd., Chichester, UK, **2013**.
- [30] O. Roubeau, *Chem. Eur. J.* **2012**, *18*, 15230–15244.
- [31] S. Schlamp, P. Thoma, B. Weber, *Chem. Eur. J.* **2014**, *20*, 6462–6473.
- [32] B. Weber, W. Bauer, J. Obel, *Angew. Chem. Int. Ed.* **2008**, *47*, 10098–10101.
- [33] B. Weber, W. Bauer, T. Pfaffeneder, M. M. Dîrtu, A. D. Naik, A. Rotaru, Y. Garcia, *Eur. J. Inorg. Chem.* **2011**, 3193–3206.
- [34] S. Schlamp, B. Weber, A. D. Naik, Y. Garcia, *Chem. Commun.* **2011**, *47*, 7152–7154.
- [35] M. A. Halcrow, *Chem. Soc. Rev.* **2011**, *40*, 4119–4142.
- [36] B. Weber, J. Obel, D. Henner-Vasquez, W. Bauer, *Eur. J. Inorg. Chem.* **2009**, 5527–5534.
- [37] W. Bauer, C. Lochenie, B. Weber, *Dalton Trans.* **2014**, *43*, 1990–1999.
- [38] D. K. Kumar, D. A. Jose, P. Dastidar, A. Das, *Langmuir* **2004**, *20*, 10413–10418.
- [39] R. Nowak, W. Bauer, T. Ossiander, B. Weber, *Eur. J. Inorg. Chem.* **2013**, 975–983.
- [40] J. S. Costa, S. Rodríguez-Jiménez, G. A. Craig, B. Barth, C. M. Beavers, S. J. Teat, G. Aromí, *J. Am. Chem. Soc.* **2014**, *136*, 3869–3874.
- [41] V. Gómez, J. Benet-Buchholz, E. Martin, J. R. Galán-Mascarós, *Chem. Eur. J.* **2014**, *20*, 5369–5379.
-

-
- [42] H. G. O. Becker, *Organikum. Organisch-Chemisches Grundpraktikum 19th ed.*, Johann Ambrosius Barth, Berlin, DE, **1993**.
- [43] L. Wolf, E.-G. Jäger, *Z. Anorg. Allg. Chem.* **1966**, *346*, 76–91.
- [44] B. Weber, W. Betz, R. and Bauer, S. Schlamp, *Z. Anorg. Allg. Chem.* **2011**, *637*, 102–107.
- [45] E.-G. Jäger, E. Häussler, M. Rudolph, A. Schneider, *Z. Anorg. Allg. Chem.* **1985**, *525*, 67–85.
- [46] A. Altomare, M. C. Burla, M. Camalli, G. L. Cascarano, C. Giavazzo, A. Guagliardi, A. G. G. Moliterni, G. Polidori, R. Spagna, *J. Appl. Crystallogr.* **1999**, *35*, 115–119.
- [47] G. Sheldrick, *Acta Crystallogr., Sect. A* **2008**, *64*, 112–122.
- [48] L. Farrugia, *J. Appl. Crystallogr.* **1997**, *30*, 565.
- [49] E. Keller, *Schakal-99*, **1999**, University of Freiburg, Freiburg DE.
- [50] K. Lagarec, D. G. Rancourt, *Recoil, Mössbauer Spectral Analysis Software for Windows 1.0*, **1998**, Department of Physics, University of Ottawa, CA.
- [51] A. Rotaru, M. M. Dîrtu, C. Enachescu, R. Tanasa, J. Linares, A. Stancu, Y. Garcia, *Polyhedron* **2009**, *28*, 2531–2536.
- [52] W. Bauer, W. Scherer, S. Altmannshofer, B. Weber, *Eur. J. Inorg. Chem.* **2011**, 2803–2818.
- [53] T. M. Pfaffeneder, S. Thallmair, W. Bauer, B. Weber, *New J. Chem.* **2011**, *35*, 691–700.
- [54] Y. Garcia, P. J. van Koningsbruggen, E. Codjovi, R. Lapouyade, O. Kahn, L. Rabardel, *J. Mater. Chem.* **1997**, *7*, 857–858.
- [55] W. Bauer, T. Pfaffeneder, K. Achterhold, B. Weber, *Eur. J. Inorg. Chem.* **2011**, 3183–3192.
- [56] B. Weber, R. Tandon, D. Himsl, *Z. Anorg. Allg. Chem.* **2007**, *633*, 1159–1162.
- [57] E. Salje, *Annu. Rev. Mater. Res.* **2012**, *42*, 262–283.

5. Iron(II) spin crossover complexes with diamino-naphthalene-based Schiff base-like ligands: mononuclear complexes.

Charles Lochenie,^a Julia Heinz,^a Wolfgang Milius^b and Birgit Weber^{*,a}

^aInorganic Chemistry II, Universität Bayreuth, Universitätstrasse 30, NW I, 95440 Bayreuth, Germany.

^bInorganic Chemistry I, Universität Bayreuth, Universitätstrasse 30, NW I, 95440 Bayreuth, Germany.

Published in *Dalton Trans.* **2015**, *44*, 18065–18077.

Reproduced with the permission of the Royal Society of Chemistry.

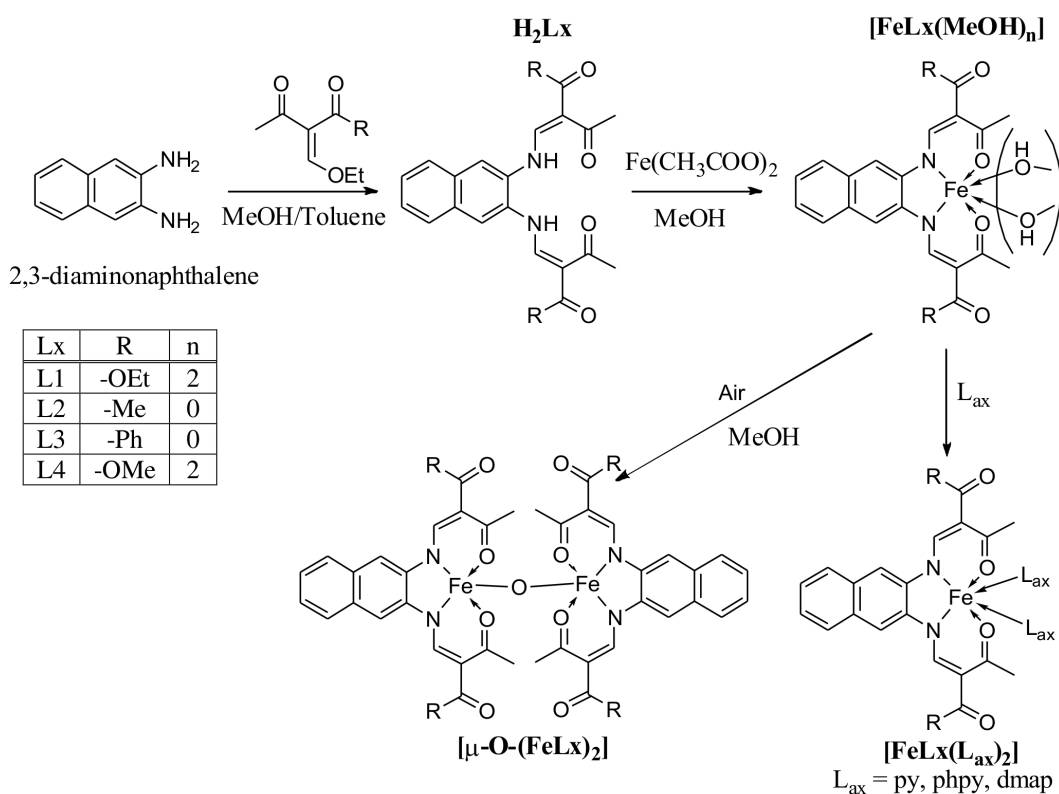
Abstract

The synthesis of new Schiff base-like ligands with extended π -system and their iron complexes is described. Some of the iron(II) complexes with N-heterocycles as axial ligands show spin crossover behaviour. The influence of the extended aromatic system on cooperative interactions is investigated by single crystal X-ray structure analysis, X-ray powder diffraction, and magnetic measurements. A combination of C–H $\cdots\pi$ and C–H \cdots O interactions is made responsible for up to 10 K wide thermal hysteresis loops.

5.1 Introduction

Molecular switches continue to attract the interest of synthetic chemists due to potential applications in the field of sensing or memory devices.^[1-3] Iron(II) spin crossover (SCO) complexes belong to this class of molecular switches as they can be switched between the diamagnetic low-spin (LS) and the paramagnetic high-spin (HS) state.^[4,5] This switching process can be triggered by many different means. Next to physical stimuli like temperature, pressure, or light irradiation, the interaction with guest molecules^[6,7] (especially for porous materials) or phase transitions^[8-11] (e.g. for SCO materials with liquid crystalline properties) can initiate the spin transition. Of the different types of spin transition (gradual, abrupt, step-wise, with hysteresis) a special focus is set on spin transition with hysteresis, as this gives rise to bistability (memory effect) over a certain temperature region. Cooperative spin transitions with hysteresis are usually only observed in the solid state (bulk material or nanostructured materials), however it was recently shown that such phenomenon is also observable in solution.^[12] For the display of hysteretic behaviour, intermolecular interactions are needed in order to transfer the structural changes associated with the spin transition from one molecule to another. Different strategies can be used to realise those intermolecular interactions that were also applied to the Schiff base-like ligands used in our group. Building short contacts between the complex molecules is one strategy to design SCO complexes with hysteresis.^[13] If wider hysteresis loops are desired, a combination of short range and long range interactions as it is often obtained for 1D coordination polymers or ladder-like compounds is promising.^[14,15] In the last years we investigated in detail the impact of hydrogen bonds on the hysteresis width of SCO complexes.^[16,17] One interaction we have not used in our iron(II) complexes so far is the π - π -interaction. However, there are examples in literature, where π -interactions between extended aromatic systems increase the width of the hysteresis loop. One series with the general composition $[\text{Fe}(\text{L})_2(\text{NCS})_2]$ (with L being a bidentate ligand 2,2'-bipyridine (bipy), phenantroline (phen), or dipyrido[3,2-a:2'3'-c]phenazine (dpp)) is discussed by Real and co-workers.^[18] The systematic increase of the aromatic part of the ligand leads to improved π -stacking and by this to wider hysteresis loops. Indeed, for the dpp ligand a 40 K wide thermal hysteresis loop is observed.^[19] Another example of a mononuclear

complex with a 37 K wide hysteresis loop due to π -stacking was reported by Létard and co-workers.^[20] Consequently we decided to modify our Schiff base-like ligands through the introduction of a naphthalene based ligand backbone. In Scheme 5.1, the general structure of the new ligands, their iron complexes, and the used abbreviations are given.



Scheme 5.1: Pathway of synthesis of the SCO complexes described in this work and used abbreviations.

5.2 Results

5.2.1 Syntheses

The spin crossover (SCO) complexes were produced in a three-step synthesis, whose synthetic pathway is given in Scheme 5.1. Firstly the new naphthalene-based Schiff base-like ligands H_2Lx (1-4) were synthesised, then the precursor methanol complexes $[FeLx(MeOH)_n]$ (5-8) were formed by reaction with iron(II) acetate, which were finally converted to the target SCO complexes $[FeLx(L_{ax})_2]$ (9-18). Oxidation of the intermedi-

ate complexes $[\text{FeL}x(\text{MeOH})_n]$ (**5-8**) in the air led to μ -oxido-bridged binuclear iron(III) complexes $[\mu\text{-O}-(\text{FeL}x)_2]$ (**19-20**).

Ligands The synthesis of the ligands $\text{H}_2\text{L}x$ (**1-4**) was achieved by condensing 2,3-diaminonaphthalene and the corresponding keto-enol ether following a modified method described by Wolf and Jäger.^[21] The four new ligands were obtained in good yield as yellowish powder and their purity was checked with $^1\text{H-NMR}$ and elemental analysis. All ligands present characteristic $^1\text{H-NMR}$ doublet signals around 13 and 8.2-8.5 ppm, accounting for the protons of the $-\text{NH}$ enamine and $=\text{C-H}$ of the chelate cycles. The rest of the proton signals can be found in their respective expected region. IR spectra show two strong characteristic signals for the $\text{C}=\text{O}$ vibrations, as well as a characteristic N-H band.

Methanol complexes $[\text{FeL}x(\text{MeOH})_n]$ The precursor complexes $[\text{FeL}x(\text{MeOH})_n]$ (**5-8**) were synthesised by converting the equatorial Schiff base-like ligands $\text{H}_2\text{L}x$ (**1-4**) with iron(II) acetate, with the acetate acting as a base for deprotonation of the equatorial ligand. IR spectra show that the $\text{C}=\text{O}$ bands shift compared to the free ligand, in agreement with the coordination of an iron metal centre. Also the colour of the compounds drastically changes towards dark brown/black in the solid state. This is due to strong charge transfer between the iron centre and the ligand, as observed for similar compounds in literature.^[22-25] It is usual for this type of complexes that two methanol molecules coordinate the iron(II) centre on axial positions, as shown for the phenyl-,^[26,27] dialkoxyphenyl-,^[28,29] and dihydroxyphenyl-^[30,31] derivatives of the same compound class. However, it was found by elemental analysis that for the naphthalene derivatives discussed in this manuscript the amount of coordinated methanol is depending on the substituents of the equatorial ligand. When the substituents are ester functions, like with L1 ($\text{R} = -\text{OEt}$) and L4 ($\text{R} = -\text{OMe}$), the complex will have two methanol coordinated to the iron centre. When the substituents are ketone functions, like L2 ($\text{R} = -\text{Me}$) and L3 ($\text{R} = -\text{Ph}$), no coordinating methanol was found. Those results were confirmed by the determination of the crystal structure of **[FeL2]**.

SCO complexes $[\text{FeL}x(\text{L}_{ax})_2]$ For the observation of SCO, the crystal field strength needs to be shifted into the right region. Thus the coordination sphere of the Fe(II) centre was changed from FeN_2O_4 to FeN_4O_2 by placing strong *N*-coordinating ligands such as pyridine (py), 4-(dimethylamino)pyridine (dmap), or 4-phenylpyridine (phpy) on the axial positions. By combining the different equatorial ligands, whose substituents allow a fine tuning of the crystal field strength, and the three different axial ligands, ten new potential iron(II) SCO complexes could be synthesised. The synthesis of complexes $[\text{FeL1}(\text{py})_2]$ and $[\text{FeL3}(\text{phpy})_2]$ was not possible so far. The first complex precipitates as the pentacoordinated specie $[\text{FeL1}(\text{py})]$, while the later would not precipitate from the solution. The exact formula of the complexes was determined with elemental analysis and mass spectrometry. A list of the different complexes, along with their solvent content, is shown in Table 5.1.

Oxidation products A crucial point during the synthesis is the identification of possible Fe(III) species produced during the synthesis of the SCO complexes. Therefore, mother liquors of the starting methanol complexes were left to slowly evaporate in the air. In the cases of compounds **5** and **8**, a few monocrystals of the corresponding μ -oxido-bridged binuclear iron(III) complexes **19** and **20** could be obtained. Those were sufficient for the analysis of the X-ray structures, however, the amount was too small for a further characterisation of the complexes.

Table 5.1: Overview of the SCO behaviour, characteristic $\chi_M T$ values [$\text{cm}^3 \cdot \text{K} \cdot \text{mol}^{-1}$], HS residue (γ_{HS}) at 50 K, and the $T_{\frac{1}{2}}$ values [K].

Compound	SCO behaviour	$\chi_M T$ (300 K)	$\chi_M T$ (50 K)	γ_{HS} (50 K)	$T_{\frac{1}{2}}$
9 $[\text{FeL2}(\text{py})_2] \cdot 2.5\text{H}_2\text{O}$	HS	3.87			
10 $[\text{FeL3}(\text{py})_2] \cdot \text{py}$	Abrupt	3.19	0.01	0	175
11 $[\text{FeL4}(\text{py})_2] \cdot \text{py}$	Two-step, gradual	2.90	0.84	0.29	150, 80
12 $[\text{FeL1}(\text{phpy})_2]$	Hysteresis, 10 K	3.65	0.08	0	↓238, ↑248
13 $[\text{FeL2}(\text{phpy})_2] \cdot 2\text{MeOH}$	HS	3.66			
14 $[\text{FeL4}(\text{phpy})_2]$	Hysteresis, 10 K	3.21	0.03	0	↓250, ↑260
15 $[\text{FeL1}(\text{dmap})_2]$	Two-step, gradual, abrupt	3.12	0.10	0.03	224, 149
16 $[\text{FeL2}(\text{dmap})_2]$	HS	3.39			
17 $[\text{FeL3}(\text{dmap})_2]$	HS	3.32			
18 $[\text{FeL4}(\text{dmap})_2]$	HS	3.31			

5.2.2 Magnetism

The magnetic properties of the ten synthesised potential SCO complexes were investigated with a SQUID magnetometer, and are summarised in Table 5.1. Out of those complexes, five (samples **9**, **13**, **16**, **17**, **18**) are HS compounds with a $\chi_M T$ value around $3.3 \text{ cm}^3 \cdot \text{K} \cdot \text{mol}^{-1}$ in the whole temperature range and no indication for SCO. The different values can be attributed to differences in the spin-orbit coupling. However, especially for the samples containing non-coordinating solvent molecules, small errors in the sample weight due to a solvent loss during the sample preparation are also possible. In the ESI, Fig. 5.10 the plot of $\chi_M T$ vs. T for those complexes is given. Compound **10** presents at 300 K a $\chi_M T$ value of $3.19 \text{ cm}^3 \cdot \text{K} \cdot \text{mol}^{-1}$, typical for iron(II) complexes in the HS state.^[22-34] Upon cooling, this value remains constant down to 175 K where compound **10** undergoes a complete abrupt spin transition (ST) towards the LS state (top left of Fig. 5.2). Below 160 K the $\chi_M T$ value stays constant with a value of $0.01 \text{ cm}^3 \cdot \text{K} \cdot \text{mol}^{-1}$ until 10 K. Upon warming, the compound goes back to the HS state with the same $T_{\frac{1}{2}}$ of 175 K. The ST properties of **10** are stable upon several measurement cycles.

Compound **11** exhibits at 300 K a $\chi_M T$ value of $2.90 \text{ cm}^3 \cdot \text{K} \cdot \text{mol}^{-1}$ which is in agreement with an iron(II) complex almost in the HS state (top left of Fig. 5.2). Upon cooling, the $\chi_M T$ product stays constant until 170 K where compound **11** starts a gradual two-step SCO until 60 K, with T_1 and T_2 , respectively, equal to 150 and 80 K. The SCO is incomplete with a residual HS fraction at 60 K of 0.29 ($\chi_M T = 0.84 \text{ cm}^3 \cdot \text{K} \cdot \text{mol}^{-1}$) which does not change down to 10 K. Upon warming, the compound **11** presents the same two-step transition towards the HS state at the same temperatures as upon cooling. When the compound is warmed above 380 K, the compound no longer exhibits SCO. Due to the conditions in the SQUID magnetometer (vacuum), uncoordinated as well as coordinated pyridine molecules could leave the sample, as already observed for other phenylene-based Fe(II) pyridine complexes.^[28,35] The loss of pyridine was confirmed with a TGA measurement, which is shown in the ESI: Fig. 5.11. As a result, the compound does not undergo SCO anymore upon cooling. This phenomenon could explain why a rather high HS fraction was observed for the original sample: a deficiency in pyridine in the powder, resulting from drying the compound under vacuum after the synthesis, could

be responsible for the HS fraction at low temperature.

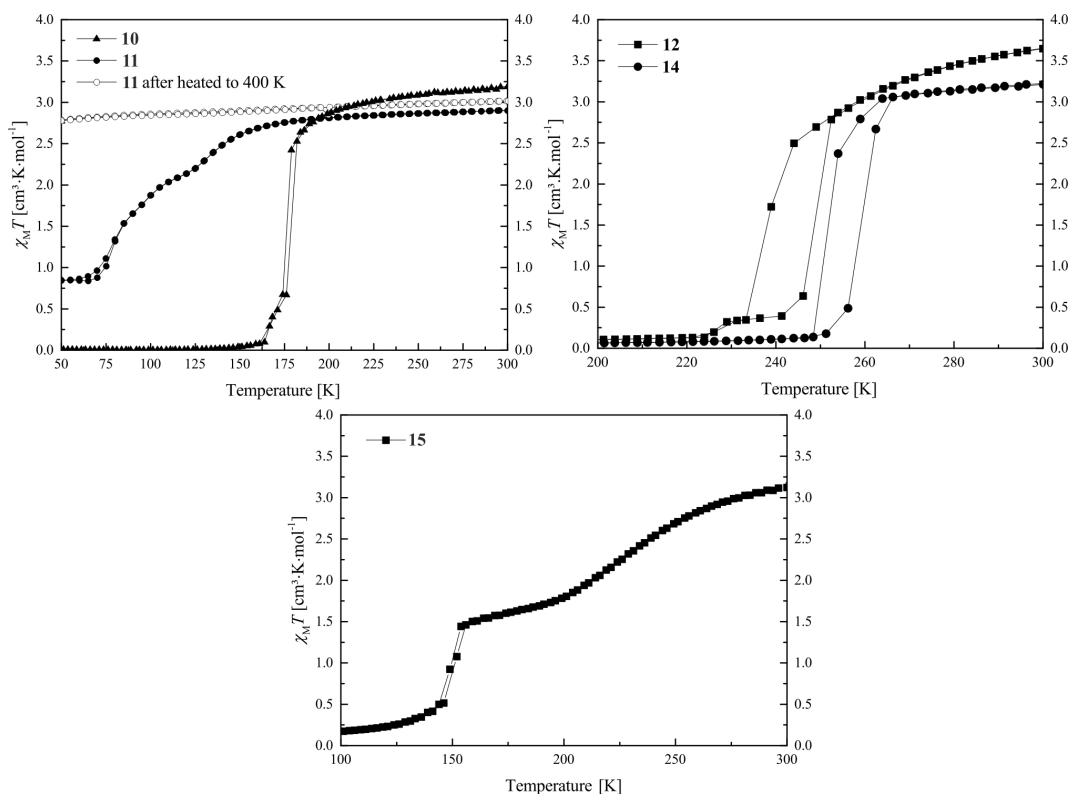


Figure 5.2: Magnetic susceptibility temperature product vs. temperature measurement for compounds **10** and **11** (top left), **12** and **14** (top right), and **15** (bottom).

Compounds **12** and **14** show very similar SCO properties: at 300 K both present, with 3.65 and 3.21 $\text{cm}^3 \cdot \text{K} \cdot \text{mol}^{-1}$, typical magnetic susceptibility with temperature product values for iron(II) HS complexes (top right of Fig. 5.2). Upon cooling, both show a rather abrupt ST with $T_{\frac{1}{2}\downarrow} = 238$ K and $T_{\frac{1}{2}\downarrow} = 250$ K, respectively, for compound **12** and **14**. Their $\chi_M T$ values at 50 K are with 0.08 and 0.03 $\text{cm}^3 \cdot \text{K} \cdot \text{mol}^{-1}$ in agreement with an iron(II) LS centre, and stay constant until 10 K. Upon heating, both samples show an abrupt ST back to the HS state at, respectively, $T_{\frac{1}{2}\uparrow} = 248$ K and $T_{\frac{1}{2}\uparrow} = 260$ K, revealing for both samples a 10 K hysteresis. As compounds **12** and **14** only differ by one substituent on the equatorial ligand ($-\text{OEt}$ for **12** and $-\text{OMe}$ for **14**), and show the same SCO behaviour displaced by 12 K, one could see the direct influence of the substituents of the equatorial ligand on the crystal field strength of the complexes, but only if **12** and **14** are isostructural. The magnetic properties of **12** and **14** are stable upon heating until

400 K and can be cycled several times. This is a surprisingly high thermal stability for mononuclear complexes of this ligand type and can be explained with the results from X-ray structure analysis.

Compound **15** exhibits at 300 K a $\chi_M T$ value of $3.12 \text{ cm}^3 \cdot \text{K} \cdot \text{mol}^{-1}$, corresponding to an iron(II) HS compound. Upon cooling, the sample undergoes a two-step SCO with a gradual part starting at 273 K and ending at 189 K with a T_1 of 224 K and an intermediate $\chi_M T$ value of $1.69 \text{ cm}^3 \cdot \text{K} \cdot \text{mol}^{-1}$ ($\gamma_{HS} = 0.54$, γ_{HS} was calculated as $\gamma_{HS} = (\chi_M T(50 \text{ K})) / (\chi_M T(300 \text{ K}))$) (bottom of Fig. 5.2). Then the sample undergoes a second abrupt SCO step with a T_2 of 149 K. The magnetic susceptibility product remains constant with a value of $0.10 \text{ cm}^3 \cdot \text{K} \cdot \text{mol}^{-1}$ until 10 K, which is in agreement with an iron(II) centre in the LS state. Upon several temperature cycles, the magnetic properties of **15** are stable.

5.2.3 X-ray structure analysis

H₂L2 (2) Suitable crystals for X-ray diffraction were obtained from water/dioxane vapour-vapour diffusion setup. The structure of yellow needles of the composition **2·0.5 H₂O·0.25 dioxane** was determined. Crystallographic data are summarised in Table 5.5. The compound crystallises in the triclinic space group $P\bar{1}$, and the asymmetric unit contains two H₂L2 molecules, a water molecule and half a dioxane solvent molecule. An ORTEP drawing of a H₂L2 molecule is displayed in Fig. 5.3. Refinement of the ligand molecules and dioxane solvent molecule went smoothly, however the hydrogen atoms of the water molecule could not be refined. The ligand molecule can exist in two different tautomers: a keto-enamine form or an imino-enol form.

The crystal structure shows the molecule in its keto-enamine form as the C1–C2 and C15–C16 bonds can be attributed to single bonds (respectively $1.459(6) \text{ \AA}$ and $1.452(6) \text{ \AA}$), and the C2–C3 and C14–C15 bonds can be attributed to double bonds (respectively $1.380(6) \text{ \AA}$ and $1.378(5) \text{ \AA}$). This observation is in agreement with similar phenylene Schiff base-like ligand published in literature.^[33,36] Two intramolecular hydrogen bonds are present, both between the nitrogen of the enamine and the oxygen of the ketone (Table 5.2). π - π interactions are present between the stacked ligand molecules, with a distance

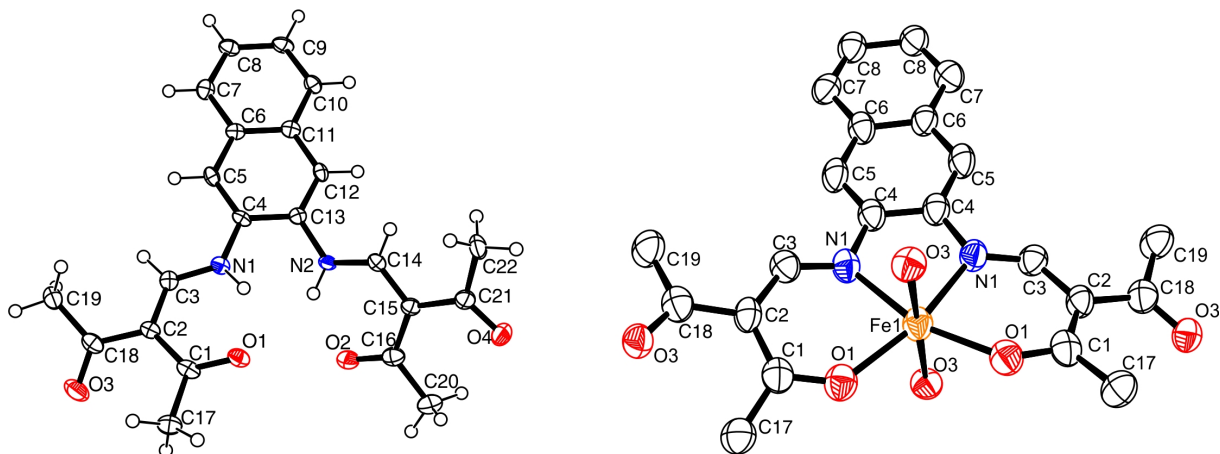


Figure 5.3: ORTEP drawing of **2** (left) and **6** (right). The thermal ellipsoids are shown at the 50% level. Hydrogen atoms and solvent molecules were omitted for clarity reasons.

of 3.55 Å between the centroids of the first ring of the naphthalene (C4–C5–C6–C11–C12–C13). This shows that the complexes produced with this ligand have potential to also form π - π interactions.

[FeL2] (6) Suitable crystals for X-ray diffraction were obtained from the synthesis. The determination of the structure was of high interest as the elemental analysis showed that no methanol was present in the compound, and therefore a square planar coordination sphere could be assumed. The crystallographic data are summarised in Table 5.2. The sample crystallises in the orthorhombic space group *Pbcn*. The asymmetric unit contains half a [FeL2] complex, and the ORTEP drawing of the molecule is shown in Fig. 5.3. The iron centre lies in an octahedral N₂O₄ coordination sphere, the ligand serves as equatorial ligand, and as axial ligand of the neighbouring molecules through its ketone substituents, forming a 2D coordination network. Selected bonds and angles are presented in Table 5.3. The angle O_{eq}-Fe-O_{eq} is critical in the determination of the spin state of the iron(II), as its value is about 90° in LS state and about 110° in the HS state.^[37,38] The iron(II) centre is here with 113.0(2) clearly in the HS state, in agreement with its weak field coordination sphere. The 2D coordination network is located in the [101] plane, where the iron centres are connected together to form a grid.

Table 5.2: Summary of the C-H...A short contacts.

Compound	D	H	A	D-H	H...A	D...A	D-H...A
2·0.5 H₂O ·0.25 dioxane	N1	H1	O1	0.88	1.87	2.563(5)	135
	N2	H2	O2	0.88	1.92	2.712(5)	129
	N31	H31	O31	0.88	1.93	2.566(5)	128
	N32	H32	O32	0.88	1.89	2.575(5)	133
10^{HS}	C12	H12	O3 ^a	0.95	2.50	3.443(6)	169
10^{LS}	C12	H12	O3 ^a	0.95	2.41	3.361(6)	174
11	C105	H105	O105 ^b	0.95	2.33	3.20(2)	152
	C212	H212	O206 ^c	0.95	2.36	3.22(2)	150
	C129	H129	O102 ^d	0.95	2.44	3.32(2)	154
	C229	H229	O201	0.95	2.67	3.56*	156
	C229	H229	O202	0.95	2.67	3.27*	122
	C224	H224	N302 ^b	0.95	2.58	3.52(2)	175
	C126	H126	N502	0.95	2.67	3.64*	166
	C304	H304	O203 ^e	0.95	2.56	3.33(3)	139
	C501	H501	O103 ^f	0.95	2.53	3.36(3)	145
	12	C45	H45	O5 ^g	0.95	2.70	3.24*
C46		H46	O5 ^g	0.95	2.46	3.135(7)	128
19	C20	H20A	O5 ^h	0.98	2.43	3.307(7)	148
	C23	H23A	O3 ⁱ	0.99	2.44	3.169(7)	130
20	C22	H22B	O33 ^j	0.98	2.55	3.359(9)	140

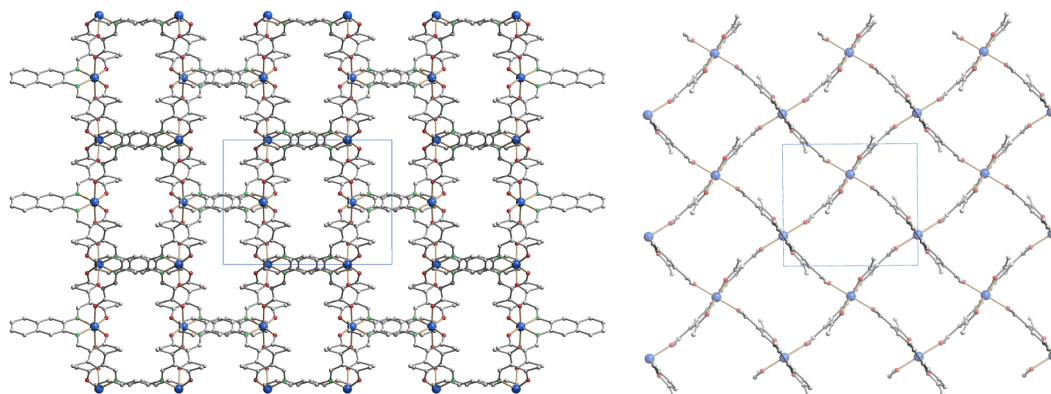
a = $-1+x, \frac{5}{2}-y, -\frac{1}{2}+z$; b = $x, \frac{3}{2}-y, -\frac{1}{2}+z$; c = $x, \frac{1}{2}-y, -\frac{1}{2}+z$; d = $1-x, \frac{1}{2}+y, \frac{1}{2}-z$; e = $-x, \frac{1}{2}+y, \frac{1}{2}-z$; f = $1-x, -\frac{1}{2}+y, \frac{1}{2}-z$; g = $1+x, y, z$; h = $2-x, 1-y, 1-z$; i = $x, -1+y, z$; j = $-1+x, 1+y, z$. *Short contacts measured with Mercury as the distances or angles exceed the threshold of PLATON.

Each 2D plane is succeeding each other along the axis [010] in a staggered fashion. Crystal packing pictures of the planes are shown in Fig. 5.4. Solvent accessible voids of 198.9 Å³ per unit cell (10%) were found by PLATON, however no solvent was found in the structure. Voids pictures are shown in Fig. 5.5. Although the structure shows voids, they seem to be inaccessible to solvent molecules, as the diameter of the "channels" is only 2 Å. Perhaps small gas molecules could be inserted in the network but this study falls out of the scope of this paper. Powder diffraction proved the bulk material to be isostructural to the crystals (ESI Fig. 5.12).

FeL3(py)₂·py (10), [FeL4(py)₂·py (11), and [FeL1(phpy)₂] (12) Suitable crystals for X-ray diffraction of compounds **10**, **11**, and **12** were obtained directly from the synthesis. The structures could be determined in the HS states for **10^{HS}** at 180 K and **11** at 175 K, and in the LS state for **10^{LS}** and **12** at 133 K. For the determination of **10^{HS}** and **10^{LS}**, the same crystal was used. In the case of **11**, although complete refinement of the crystal structure was proven difficult due to incomplete data set ($\theta_{max} = 17.31^\circ$)

Table 5.3: Selected bond lengths [\AA] and angles [$^\circ$].

	Fe-N _{eq}	Fe-O _{eq}	Fe-L _{ax}	O _{eq} -Fe-O _{eq}	L _{ax} -Fe-L _{ax}
6	2.095(6)	2.030(5)	2.246(5)	113.0(2)	176.06(19)
10^{HS}	2.063(4)	1.989(4)	2.138(5)	106.98(14)	174.22(17)
	2.040(4)	2.018(4)	2.226(5)		
10^{LS}	1.908(3)	1.949(3)	1.989(4)	90.49(12)	175.36(15)
	1.902(3)	1.953(3)	1.986(3)		
11	2.061(12)	2.014(10)	2.205(13)	111.5(4)	169.3(5)
	2.088(11)	2.019(10)	2.238(13)	112.6(4)	170.2(4)
	2.096(11)	2.004(10)	2.218(12)		
	2.089(11)	2.012(10)	2.276(12)		
12	1.903(4)	1.943(3)	1.996(4)	87.79(14)	173.85(16)
	1.906(4)	1.933(3)	2.004(4)		
19	2.066(4)	1.951(3)	1.771(3)	92.46(13)	148.18(19) ^a
	2.055(4)	1.965(3)	1.776(3)	92.50(13)	
	2.051(4)	1.958(3)			
	2.069(3)	1.961(3)			
20	2.037(5)	1.938(4)	1.950(4)	91.59(18)	140.9(2) ^a
	2.055(5)	1.964(4)	1.954(4)	90.18(17)	
	2.067(4)	1.954(4)			
	2.064(5)	1.950(4)			

^aFe-L_{ax}-Fe angle.Figure 5.4: Crystal packing pictures of **6** along [001] (left) and picture of a single plane along [010] (right). Hydrogen atoms were omitted for clarity.

because of the low stability of the crystals, a structural motif could be obtained. The crystallographic data are summarised in Table 5.5. Compounds **10** and **11** crystallise in the monoclinic space group $P21/c$ and the compound **12** in the triclinic space group $P\bar{1}$. The asymmetric unit of **10** contains one complex molecule and one non-coordinating pyridine solvent molecule, two different iron(II) complexes and two non-coordinating solvent pyridine molecules in the case of **11**, and one complex molecule for **12**. ORTEP drawings of the asymmetric units are displayed in Fig. 5.6. In all structures, the iron centres lie in

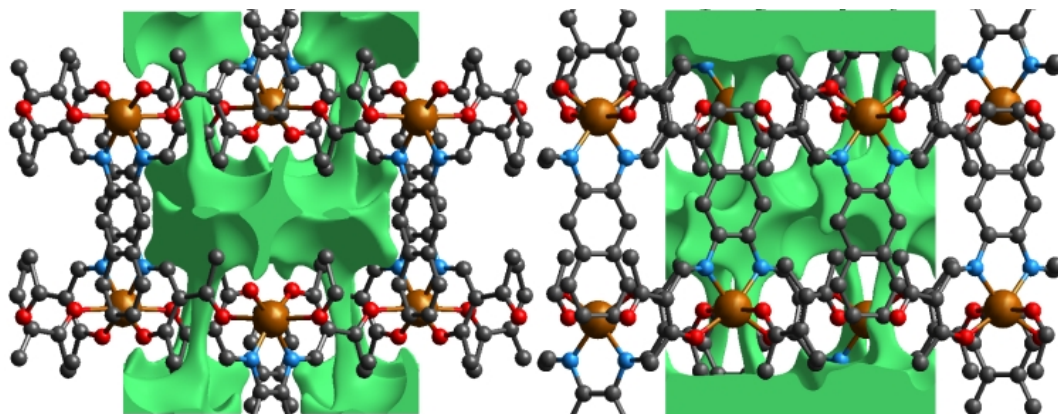


Figure 5.5: Solvent accessible voids pictures of **6** along [001] (left) and [100] (right). Hydrogen atoms were omitted for clarity.

a N_4O_2 coordination sphere, connected to the equatorial ligand and two (phenyl)pyridine molecules. The spin state of the iron centres can be determined by the value of the $O_{eq}-Fe-O_{eq}$ angle which goes from $\simeq 110^\circ$ in the HS state to $\simeq 90^\circ$ in the LS state.^[37,38] Measured $O_{eq}-Fe-O_{eq}$ angles for the HS structures ($106.98(14)^\circ$ for **10**^{HS}, $111.5(4)^\circ$, and $112.6(4)^\circ$ for **11**) and for the LS structures ($90.49(12)^\circ$ for **10**^{LS} and $87.79(14)^\circ$ for **12**) are in agreement with similar compounds in literature.^[16,39] Selected bond lengths and angles are listed in Table 5.3.

Upon SCO, the volume of the cell of **10** is reduced by 2.5%, in agreement with the volume reduction of the coordination sphere of the iron centre as it switches from HS to LS state.^[40] The complex shows a strong saddle shape with an angle of 11.54° in the HS and 10.53° in the LS state between the FeN_2O_2 plane ($Fe1-N1-N2-O1-O2$) and the plane containing the naphthalene cycles. The change in the saddle angle comes from changes in lengths of intermolecular contacts between the complexes. Indeed, $C-H \cdots \pi$ interactions are observed between the aromatic rings of the naphthalene and aromatic hydrogen atoms of the axial pyridine ligands, leading to the formation of 1D chains propagating along the vector [001]. Additionally, the 1D chains are linked through $C-H \cdots O$ bridges linking the naphthalene ring ($C12-H12$) to the ketone group ($O3$) of a neighbouring molecule, along the vector [100]. Such $C-H \cdots O$ bridges are known to be structure defining in many cases.^[41-46] Contribution from both types of interactions leads to the formation of a 2D network in the a,c plane of the packing. Crystal packing and a scheme of the

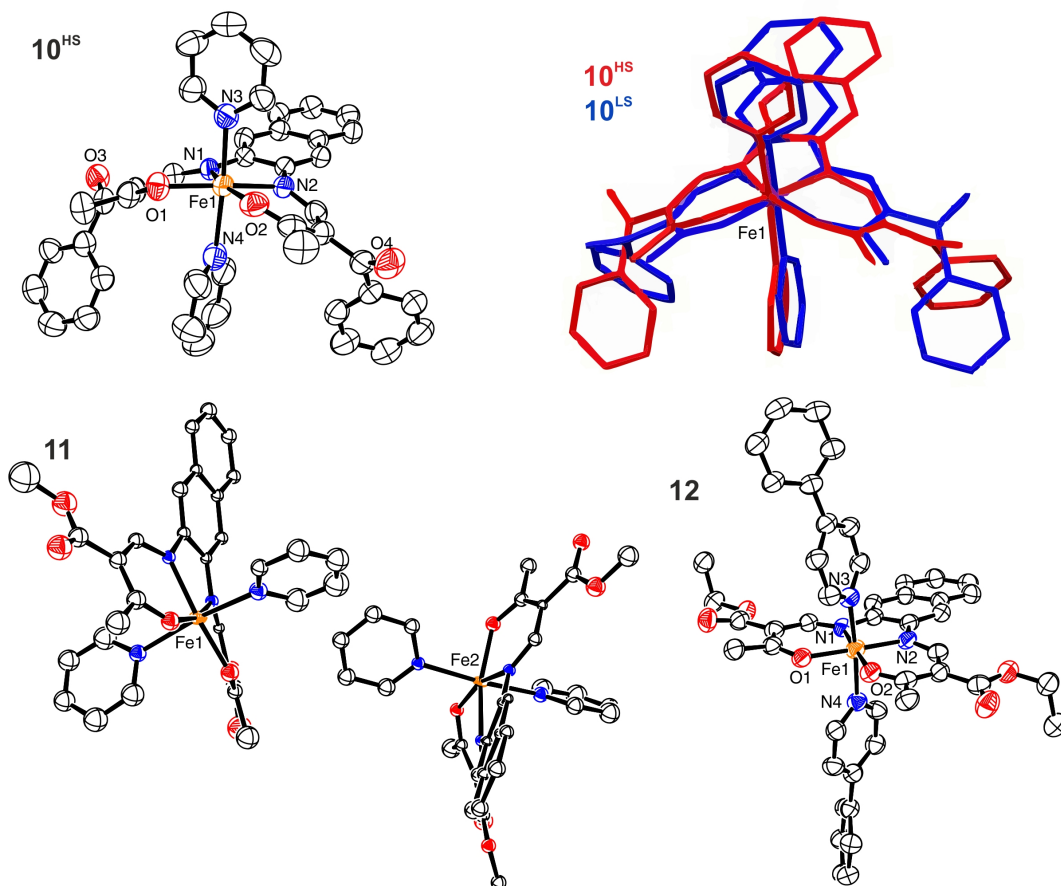


Figure 5.6: ORTEP drawing **10^{HS}** (top left), **11** (bottom left), and **12** (bottom right). The thermal ellipsoids are shown at the 50% level. Hydrogen atoms and non-coordinating solvent molecules were omitted for clarity reasons. The overlay of **10^{HS}** and **10^{LS}** is represented in the top right corner.

C–H $\cdots\pi$ interactions are shown in Fig. 5.7 and summarised in Tables 5.2 and 5.4. These intermolecular interactions have an influence on the slight change of the saddle angle of the molecule during SCO as the distance between the C–H and the aromatic rings partners in the interaction is increasing with the volume decrease of the coordination sphere.

The crystal packing of **11** presents a bi-layered structure: the different iron(II) complexes form planes perpendicular to vector [010], in a [Fe1Fe1–Fe2Fe2] fashion. The planes themselves are built by an intricate combination of C–H \cdots O bridges between naphthalene and methyl ester substituents of neighbouring molecules along [001]; and, along [010], of C–H \cdots O bridges and C–H $\cdots\pi$ interactions between axial pyridine and two neighbouring molecules. The latter C–H \cdots O bridges connect to the oxygen atoms of the coordination

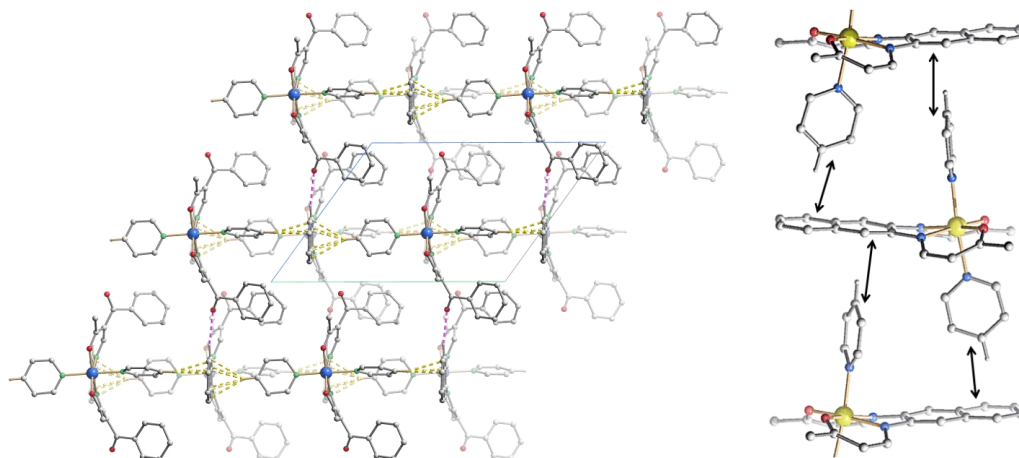


Figure 5.7: Left: crystal packing of 10^{HS} along $[0-10]$, hydrogen atoms not involved in short contacts were omitted for clarity reasons. $C-H \cdots \pi$ interactions are represented in dashed yellow lines, $C-H \cdots O$ in dashed pink lines. Right: excerpt of the crystal packing along $[100]$, hydrogen atoms, non-coordinating solvent molecules, and substituents were omitted for clarity. Black double arrows indicate the $C-H \cdots \pi$ interactions positions.

Table 5.4: Summary of the $X-Y \cdots \pi$ interactions in crystal structures 10^{HS} , 10^{LS} , 11 , and 12 .

Compound	X	Y	Cg	Y...Cg	X...Cg	X-Y...Cg
10^{HS}	C35	H35	C4-C6-C11-C13	2.41	3.358(7)	174
	C40	H40	C6-C11	2.58	3.497(8)	164
10^{LS}	C35	H35	C4-C6-C11-C13	2.42	3.364(6)	170
	C40	H40	C6-C11	2.63	3.554(5)	165
11	C131	H131	C104-C106-C111-C113	2.48	3.37(2)	156
	C231	H231	C204-C206-C211-C213	2.65	3.48(2)	147
12	C22	O5	C6-C11	3.807(4)	3.560(6)	69.3(3)

sphere, which has been shown to have dramatic influence on SCO properties.^[17] The two different planes (Fe1 and Fe2) actually build the same network, although similar short contacts do not have the exact same distance, especially regarding $C-H \cdots O$ bridges connecting to coordinating oxygen (O101, O102, O201, O202). The non-coordinating pyridine solvent molecules occupy interplanar position, binding to the planes through $C-H \cdots O$ and $C-H \cdots N$ bridges. Distances and angles of discussed short contacts are listed in Tables 5.2 and 5.4. The crystal packing of the 2D network is depicted in Fig. 5.8. The crystal packing of 12 is dominated by two strong interactions. Firstly, $C-H \cdots O$ bridges link one of the ethyl ester oxygens (O5) to a neighbouring phenylpyridine aromatic ring (C45-H45, C46-H46) and form a 1D chain of complexes along $[100]$. Secondly, an unusual overlap

of the methyl ester group with the nearby naphthalene ring ($-\text{O}6-\text{C}22=\text{O}5\cdots\pi$) forming pairs of complexes.^[43–46] Additional weaker stacking between adjacent phenylpyridine aromatic rings, and between naphthalene rings creates a complex network between the Fe(II) spin centres. Crystal packing pictures as well as an ORTEP representation of the $-\text{O}6-\text{C}22=\text{O}5\cdots\pi$ and $\text{C}-\text{H}\cdots\text{O}$ bridges are shown in Fig. 5.9, distances and angles of discussed short contacts are listed in Tables 5.2 and 5.4.

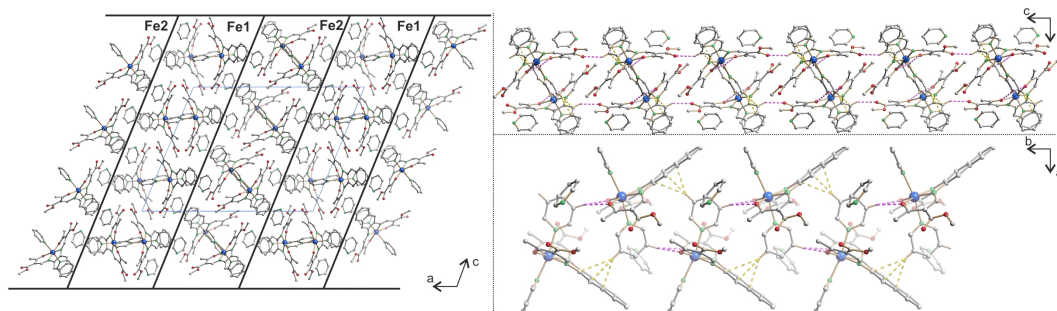


Figure 5.8: Crystal packing of **11** along [010] (left), illustrating the 2D network along [010] (top right) and [001] (bottom right); hydrogen atoms not involved in short contacts were omitted for clarity reasons. $\text{C}-\text{H}\cdots\pi$ interactions are represented in dashed yellow lines, $\text{C}-\text{H}\cdots\text{O}$ in dashed pink lines.

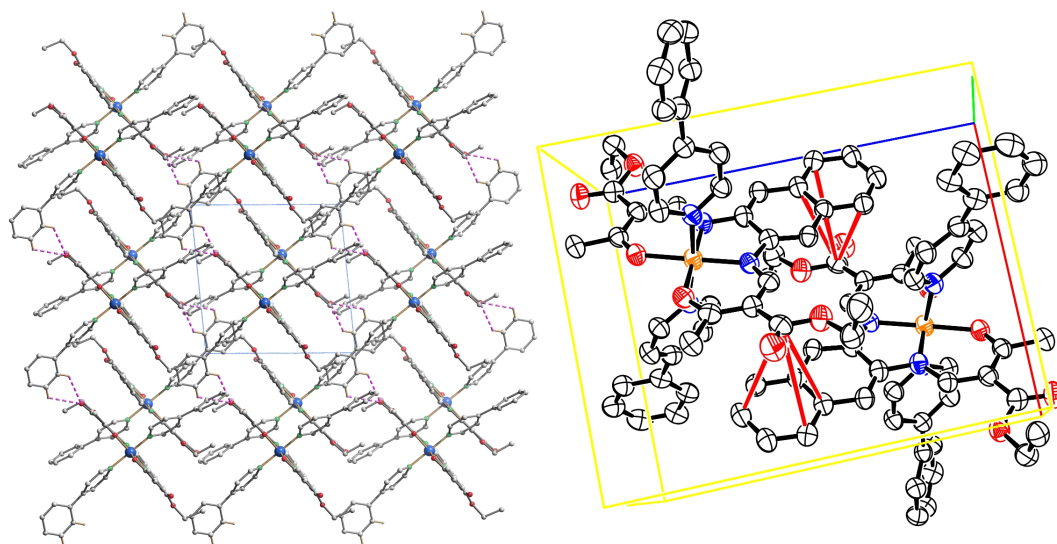


Figure 5.9: Crystal packing of **12** along [001] (left); $\text{C}-\text{H}\cdots\text{O}$ interactions represented in dashed pink lines; ORTEP representation of the $-\text{O}-\text{C}=\text{O}\cdots\pi$ interactions, the thermal ellipsoids are shown at the 50% level. Hydrogen atoms were omitted for clarity reasons.

$[\mu\text{-O-(FeL1)}_2]$ (**19**) and $[\mu\text{-O-(FeL4)}_2]$ (**20**) μ -Oxido complexes are the usual oxidation product of the iron(II) complexes when in contact with oxygen. Identifying such potential side-product is critical for the good proceedings of syntheses and analyses. Crystals suitable for X-ray diffraction were obtained from slow evaporation of a methanolic solution of $[\text{FeL}x(\text{MeOH})_2]$ in the air. The crystallographic data are summarised in Table 5.5. Both compounds crystallise in the triclinic space group $P\bar{1}$, with an asymmetric unit containing one μ -oxido complex with the two iron(III) centres lying in a N_2O_3 coordination sphere. All square based pyramid iron(III) are connected through a μ -oxido bridge. The ORTEP drawing of the asymmetric units are shown in ESI, Fig. 5.15. Bond lengths and angles within the coordination sphere are listed in Table 5.3, and are in agreement with similar published compounds.^[29,37] As for the SCO complexes, C–H \cdots O bridges between ester side substituents can be found in the crystal packings, and the complexes are stacking in column fashion. Although the conformation of the two bridged iron complexes **19** and **20** are different, the crystal packing is actually similar. Pictures of the crystal packing are shown in ESI, Fig. 5.16.

Table 5.5: Crystallographic data of the ligand and the complexes discussed in this work

Compound	2·0.5 H₂O ·0.25 dioxane	6	10^{HS}	10^{LS}	11	12	19	20
CCDC	1040379	1040378	1040374	1040375	1040380	104376	104375	104377
Sum formula	C ₄₆ H ₄₈ N ₄ O ₁₀	C ₂₂ H ₂₀ FeN ₂ O ₄	C ₄₇ H ₃₉ FeN ₅ O ₄	C ₄₇ H ₃₉ FeN ₅ O ₄	C ₃₇ H ₃₅ FeN ₅ O ₆	C ₄₆ H ₄₂ FeN ₄ O ₆	C ₄₈ H ₄₈ Fe ₂ N ₄ O ₁₃	C ₄₄ H ₄₀ Fe ₂ N ₄ O ₁₃
<i>M</i> [g·mol ⁻¹]	816.88	432.5	793.68	793.68	701.55	802.69	1000.60	944.50
Crystal system	Triclinic	Othorhombic	Monoclinic	Monoclinic	Monoclinic	Triclinic	Triclinic	Triclinic
Space group	<i>P</i> $\bar{1}$	<i>Pbcn</i>	<i>P</i> 2 ₁ / <i>c</i>	<i>P</i> 2 ₁ / <i>c</i>	<i>P</i> 2 ₁ / <i>c</i>	<i>P</i> $\bar{1}$	<i>P</i> $\bar{1}$	<i>P</i> $\bar{1}$
<i>a</i> [Å]	7.8382(10)	11.697(2)	12.179(2)	11.920(2)	28.083(5)	11.5899(7)	13.273(3)	9.027(1)
<i>b</i> [Å]	12.3303(11)	15.864(3)	24.655(4)	24.712(4)	12.058(6)	11.9233(7)	14.292(3)	12.475(1)
<i>c</i> [Å]	21.170(3)	10.566(2)	16.589(2)	16.280(2)	22.071(5)	14.3604(9)	14.510(3)	17.885(2)
α [°]	88.110(5)	90	90	90	90	77.012(5)	63.065(15)	89.132(10)
β [°]	87.730(5)	90	126.153(19)	125.183(19)	112.568(18)	88.090(5)	69.534(15)	85.598(10)
γ [°]	86.920(5)	90	90	90	90	84.122(5)	78.915(16)	85.422(10)
<i>V</i> [Å ³]	2040.4(16)	1960.6(14)	4022(2)	3919(2)	6902(3)	1923.4(2)	2297.1(9)	2001.6(4)
<i>Z</i>	2	4	4	4	8	2	2	2
ρ [g·cm ⁻³]	1.330	1.464	1.311	1.345	1.350	1.386	1.447	1.567
μ [mm ⁻¹]	0.094	0.801	0.426	0.437	0.490	0.449	0.702	0.801
Crystal size [mm]	0.02 × 0.09 × 0.14	0.103 × 0.114 × 0.124	0.100 × 0.163 × 0.262	0.100 × 0.163 × 0.262	0.03 × 0.100 × 0.12	0.07 × 0.100 × 0.19	0.23 × 0.24 × 0.24	0.292 × 0.309 × 0.380
<i>T</i> [K]	100(2)	133(2)	180(2)	133(2)	175(2)	133(2)	133(2)	133(2)
λ (MoK α) [Å]	0.71073	0.71073	0.71073	0.71073	0.71073	0.71073	0.71073	0.71073
θ -Range [°]	2.6–22.0	1.28–23.74	1.65–24.59	1.60–24.60	2.252–17.31	1.455–24.584	1.6–24.6	1.638–28.064
Reflns. Collected	12238	24192	47223	45921	26239	22912	27408	25770
Indep. reflns. (<i>R</i> _{int})	4998 (0.074)	1858 (0.4395)	6730 (0.156)	6540 (0.165)	4159 (0.154)	6444 (0.182)	7688 (0.134)	8940 (0.104)
Parameters	541	134	514	514	403	514	604	568
<i>R</i> 1(<i>F</i>) (all data)	0.0526 (0.1087)	0.0851 (0.1601)	0.0596 (0.1278)	0.0571 (0.1158)	0.0788 (0.1359)	0.0748 (0.1224)	0.0515 (0.1097)	0.0861 (0.1222)
<i>wR</i> 2	0.1299	0.1989	0.1205	0.1112	0.2073	0.1612	0.1049	0.2175
<i>Goof</i>	1.045	0.983	0.928	0.916	1.081	0.941	0.851	0.864

5.3 Discussion

Intermolecular interactions in the crystal packing result in cooperative interactions during the spin transition. These can result in abrupt spin transitions, thermal hysteresis loops, or step-wise spin transitions. Based on the structural data a deeper understanding of the different spin crossover properties is possible.

Compound **10** shows an abrupt SCO behaviour (Fig. 5.2), which can be due to either to a phase transition during SCO, or due to other cooperative effects between the complexes in the solid state. The determination of the crystal structure in both spin states proved that no phase transition is involved during SCO. Cooperative interactions can arise from intermolecular contacts, and the packing of the crystal structure of **10** revealed, in both spin states, the formation of 1D chains through C–H $\cdots\pi$ interactions and C–H \cdots O bridges between the complexes. Thus the Schiff base-like ligand was modified successfully and π -interactions are observed and lead to cooperative interactions between the complex molecules.

Compounds **12** and **14** show both an abrupt SCO with a hysteresis of 10 K. Powder diffraction of both samples in both spin states showed that no phase transition is involved through the ST, therefore attributing the hysteresis phenomena observed to cooperative effects. The powder diffraction patterns are shown in ESI (Fig. 5.13-5.14). In the crystal packing of **12**, strong interactions between complexes are present, especially C–H \cdots O bridges and $-\text{O}-\text{C}=\text{O}\cdots\pi$ interactions connect all spin centres in a 3D network. This is responsible for the high cooperativity observed for these mononuclear complexes. It would have been of course interesting to have the structure of the HS state in order to pinpoint which interaction plays a determining role in the SCO. Unfortunately the low quality and low stability of the crystal at high temperature did not allow the determination of the structure in the HS state. Powder diffractograms of **12** and **14** were compared in order to determine if the compounds are isostructural, as their SCO behaviour is very similar and just shifted in temperature. Because of the complexity of the diffractograms, arising from the low symmetry of the crystal structures, no clear conclusions can be drawn about

the isostructurality of samples **12** and **14**.

Compounds **11** and **15** show both a two-step SCO. Such spin crossover are often related to different iron sites within the structure of the samples.^[47] The crystal structure of **11** confirmed this hypothesis as it shows a bi-layered packing with two different iron(II) centres arranged in layers separated by layers of non-coordinating pyridine solvent molecules. As no crystals suitable for X-ray analysis could be obtained for compound **15**, a room temperature Mössbauer spectrum was measured. It shows an asymmetric doublet signal with the following hyperfine parameters: $\delta = 0.908(6)$, $\Delta E_Q = 2.066(12)$ and $\gamma/2 = 0.174(13)$, which are in the region for an HS Fe(II) complex.^[13,25,47] The asymmetry of the peaks is characteristic for two slightly different doublet, as the right peak is larger than the left peak. It was however not possible to correctly fit the doublet signal with two sites. The Mössbauer spectrum is presented in the ESI, Fig. 5.17.

For the crystal structures of the SCO complexes discussed in this work, C–H $\cdots\pi$ interactions and C–H \cdots O bridges strongly influence the crystal packing. For the related phenylene based complexes, only C–H \cdots O bridges were observed.^[24,25,38,47,48] The additional C–H $\cdots\pi$ interactions lead to a more frequent observation of interesting SCO properties. Out of the 10 naphthalene based complexes presented here, two showed a ST with a 10 K wide hysteresis and in two cases steps in the transition curve were observed. For comparison, for the **18** phenylene based mononuclear complexes reported so far, only one step-wise spin transition and two spin transitions with hysteresis (9 K and 70 K) were observed.^[38,49,50] The 70 K hysteresis does not fit into this comparison due to the use of imidazole as axial ligand that allowed the formation of an extended N–H \cdots O hydrogen bond network between the complexes.^[49] First attempts to combine the naphthalene based Schiff base-like complexes with axial ligands suitable for the formation of hydrogen bond networks (like imidazole) are underway. The results obtained so far for the new ligands indicate that the use of an extended π -system was successful for the design of complexes with interesting SCO properties.

5.4 Experimental section

Synthesis Methanol (MeOH) and ethanol (EtOH) were purified by distillation over magnesium under argon.^[51] Toluene and pyridine were of analytical grade and degassed under argon, pyridine was kept on a 4 Å molecular sieve. Ethoxymethyleneethylacetoacetate,^[52] ethoxymethyleneacetylacetone, ethoxymethylenebenzoylacetone,^[52] methoxymethylenemethylacetoacetate,^[33] and iron(II) acetate^[53] were synthesised as described in literature. Dioxane (Sigma, 99+%), 2,3-diaminonaphthalene (Alfa Aesar, 97%), 4-(dimethylamino)pyridine (dmap ; Merck, 99%), and 4-phenylpyridine (phpy ; Acros, 99%) were used without further purification. All syntheses with iron(II) were carried out under argon using Schlenk tube techniques. CHN analyses were measured with a Vario El III from Elementar Analysen-Systeme. Mass spectra were recorded with a Finnigan MAT 8500 with a data system MASPEC II.

H₂L1 (1) 2,3-Diaminonaphthalene (2 g) was dissolved in 40 mL toluene. Ethoxymethyleneethylacetoacetate (5.18 g) was dissolved in 40 mL EtOH and added to the 2,3-diaminonaphthalene solution. The brown solution was stirred and refluxed for 2 hours. The mixture was then allowed to cool down to room temperature, and the solvent was removed under reduced pressure to give crude H₂L1 as brown solid. The latter solid was dissolved in 50 mL EtOH, stirred and refluxed during 10 min, then allowed to cool down to room temperature. The beige crystals were filtered off, washed with EtOH (2 × 10 mL) and dried *in vacuo*. Yield: 3.99 g (72%). IR: $\tilde{\nu}$ = 3156(b) (NH), 1654(s) (CO), 1648(s) (CO) cm⁻¹ ; MS (DEI-(+), 70 eV) m/z (%): 438 (50) (H₂L1⁺) ; elemental analysis calculated (found) for C₂₄H₂₆N₂O₆·C₂H₆O (438.47 g·mol⁻¹) : C 64.45 (60.41), H 5.88 (5.95), N 6.17 (5.93). ¹H-NMR (CDCl₃, 300 MHz, ppm) δ = 13.03 (d, J = 12 Hz, -NH, 2H), 8.51 (d, J = 12 Hz, =CH, 2H), 7.81 (dd, J^3 = 6 Hz, J^4 = 3 Hz, Ar-H, 2H), 7.68 (s, Ar-H, 2H), 7.50 (dd, J^3 = 6 Hz, J^4 = 3 Hz, Ar-H, 2H), 4.29 (qua, J = 7 Hz, -CH₂-, 4H), 2.60 (s, -CH₃, 6H), 1.36 (t, J = 7 Hz, -CH₃, 6H).

H₂L2 (2) 2,3-Diaminonaphthalene (2 g) was dissolved in 40 mL toluene. Ethoxymethyleneacetylacetone (3.96 g) was dissolved in 40 mL MeOH and added to the 2,3-

diaminonaphthalene solution. The yellow solution was stirred and refluxed for 2 hours. The mixture was then allowed to cool down to room temperature, and the yellow crystals were filtered off, washed with MeOH (2×10 mL) and dried *in vacuo*. The crystals were recrystallized from dioxane to give pure H₂L2. Yield: 2 g (42%). IR: $\tilde{\nu} = 3223(\text{b})$ (NH), 1689(s) (CO), 1675(s) (CO) cm^{-1} ; MS (DEI-(+), 70 eV) m/z (%): 378 (11) (H₂L2⁺); elemental analysis calculated (found) for C₂₂H₂₂N₂O₄·0.5C₄H₈O₂ (422.47 $\text{g}\cdot\text{mol}^{-1}$): C 68.23 (67.91), H 6.20 (5.88), N 6.63 (6.89). ¹H-NMR (CDCl₃, 300 MHz, ppm) $\delta = 13.06$ (m, -NH, 2H), 8.24 (d, $J = 11$ Hz, =CH, 2H), 7.83 (m, Ar-H, 2H), 7.66 (s, Ar-H, 2H), 7.53 (m, Ar-H, 2H), 2.59 (s, -CH₃, 6H), 2.42 (s, -CH₃, 6H).

H₂L3 (3) 2,3-Diaminonaphthalene (2 g) was dissolved in 40 mL toluene. Ethoxymethylenebenzoylacetone (6.51 g) was dissolved in 40 mL MeOH and added to the 2,3-diaminonaphthalene solution. The brown solution was stirred and refluxed for 2 hours. The mixture was then allowed to cool down to room temperature, and the brown crystals were filtered off, washed with MeOH (2×10 mL) and dried *in vacuo*. The crystals were recrystallized from MeOH to give pure H₂L3. Yield: 5.04 g (72%). IR: $\tilde{\nu} = 3204(\text{b})$ (NH), 1663(s) (CO), 1598(s) (CO) cm^{-1} ; MS (DEI-(+), 70 eV) m/z (%): 502 (78) (H₂L3⁺); elemental analysis calculated (found) for C₃₂H₂₆N₂O₄·0.5CH₄O (518.59 $\text{g}\cdot\text{mol}^{-1}$): C 75.27 (74.90), H 5.442 (4.8), N 5.402 (5.377). ¹H-NMR (CDCl₃, 300 MHz, ppm) $\delta = 12.96$ (d, $J = 12$ Hz, -NH, 2H), 7.92 (d, $J = 12$ Hz, =CH, 2H), 7.76 (m, Ar-H, 4H), 7.68 (s, Ar-H, 2H), 7.48 (m, Ar-H, 10H), 2.56 (s, -CH₃, 6H).

H₂L4 (4) 2,3-Diaminonaphthalene (2 g) was dissolved in 40 mL toluene. Methoxymethylenemethylacetoacetate (4.39 g) was dissolved in 40 mL MeOH and added to the 2,3-diaminonaphthalene solution. The brown solution was stirred and refluxed for 2 hours. The mixture was then allowed to cool down to room temperature, and the dark yellow crystals were filtered off, washed with MeOH (2×10 mL) and dried *in vacuo*. The crystals were recrystallized from MeOH to give pure H₂L4. Yield: 5.15 g (99%). IR: $\tilde{\nu} = 3265(\text{b})$ (NH), 1652(s) (CO), 1622(s) (CO) cm^{-1} ; MS (DEI-(+), 70 eV) m/z (%): 410 (100) (H₂L4⁺); elemental analysis calculated (found) for C₂₂H₂₂N₂O₆·0.5CH₄O (426.4 $\text{g}\cdot\text{mol}^{-1}$): C 63.37 (62.97), H 5.672 (4.765), N 6.569 (6.592). ¹H-NMR (CDCl₃, 300 MHz, ppm) $\delta = 13.67$ (d, $J = 12$ Hz, -NH, 2H), 8.57 (d, $J = 12$ Hz, =CH, 2H), 7.81 (dd, $J^3 =$

6 Hz, $J^4 = 3$ Hz, Ar-H, 4H), 7.68 (s, Ar-H, 2H), 7.48 (dd, $J^3 = 6$ Hz, $J^4 = 3$ Hz, Ar-H, 10H), 3.82 (s, $-\text{CH}_3$, 6H), 2.60 (s, $-\text{CH}_3$, 6H).

[FeL1(MeOH)₂] (5) **1** (2 g) and iron(II) acetate (0.95 g) were dissolved in 130 mL MeOH. The red suspension was stirred and refluxed for 1 hour. The mixture was then allowed to cool down to room temperature, and the brown crystals were filtered off, washed with MeOH (2×5 mL) and dried *in vacuo*. Yield: 1.68 g (66%). IR: $\tilde{\nu} = 1614$ (s) (CO), 1597(s) (CO) cm^{-1} ; MS (DEI(+), 70 eV) m/z (%): 492 (100) ([FeL1]⁺); elemental analysis calculated (found) for $\text{C}_{26}\text{H}_{32}\text{FeN}_2\text{O}_8$ ($556.39 \text{ g}\cdot\text{mol}^{-1}$): C 56.13 (55.42), H 5.80 (4.20), N 5.03 (5.20).

[FeL2] (6) **2** (2 g) and iron(II) acetate (1.1 g) were dissolved in 100 mL MeOH. The red suspension was stirred and refluxed during 1 hour. The mixture was then allowed to cool down to room temperature, and the black crystals were filtered off, washed with MeOH (2×5 mL) and dried *in vacuo*. Yield: 1.35 g (60%). IR: $\tilde{\nu} = 1685$ (s) (CO), 1584(s) (CO) cm^{-1} ; MS (DEI(+), 70 eV) m/z (%): 432 (100) ([FeL2]⁺); elemental analysis calculated (found) for $\text{C}_{22}\text{H}_{20}\text{FeN}_2\text{O}_4$ ($432.08 \text{ g}\cdot\text{mol}^{-1}$): C 61.13 (60.43), H 4.66 (4.29), N 6.48 (6.36).

[FeL3] (7) **3** (1.5 g) and iron(II) acetate (0.59 g) were dissolved in 100 mL MeOH. The red suspension was stirred and refluxed for 15 min. The mixture was then allowed to cool down to room temperature, and the black crystals were filtered off, washed with MeOH (2×15 mL) and dried *in vacuo*. Yield: 1.22 g (78%). IR: $\tilde{\nu} = 1629$ (s) (CO), 1575(s) (CO) cm^{-1} ; MS (DEI(+), 70 eV) m/z (%): 556 (100) ([FeL3]⁺); elemental analysis calculated (found) for $\text{C}_{32}\text{H}_{24}\text{FeN}_2\text{O}_4$ ($556.39 \text{ g}\cdot\text{mol}^{-1}$): C 69.08 (68.37), H 4.35 (3.44), N 5.03 (4.997).

[FeL4(MeOH)₂] (8) **4** (1.5 g) and iron(II) acetate (0.76 g) were dissolved in 100 mL MeOH. The red suspension was stirred and refluxed for 1 hour. The mixture was then allowed to cool down to room temperature, and the brown crystals were filtered off, washed with MeOH (2×5 mL) and dried *in vacuo*. Yield: 1.57 g (81%). IR: $\tilde{\nu} = 1620$ (s) (CO), 1598(s) (CO) cm^{-1} ; MS (DEI(+), 70 eV) m/z (%): 528 (100) ([FeL4]⁺); elemental

analysis calculated (found) for $C_{24}H_{28}FeN_2O_8$ ($528.33 \text{ g}\cdot\text{mol}^{-1}$): C 54.56 (54.17), H 5.34 (5.12), N 5.30 (5.26).

[FeL2(py)₂] \cdot 2.5H₂O (9) 6 (0.2 g) were dissolved in 15 mL pyridine. The red solution was stirred and refluxed for 30 min. The mixture was then allowed to cool down and then 15 mL H₂O was added to the solution. Red crystals precipitated slowly, and the solution was left to stand at room temperature overnight. The red crystals were then filtered off, and dried *in vacuo*. Yield: 0.16 g (56%). IR: $\tilde{\nu} = 1612(\text{s})$ (CO), $1596(\text{s})$ (CO) cm^{-1} ; MS (DEI-(+), 70 eV) m/z (%): 432 (100) ([FeL2]⁺); elemental analysis calculated (found) for $C_{32}H_{35}FeN_4O_{6.5}$ ($635.49 \text{ g}\cdot\text{mol}^{-1}$): C 60.48 (60.46), H 5.55 (3.912), N 8.82 (7.865).

[FeL3(py)₂] \cdot py (10) 7 (0.2 g) were dissolved in 15 mL pyridine. The brown solution was stirred and refluxed for 30 min. The mixture was then allowed to cool down and then 15 mL H₂O was added to the solution, and the solution was left to stand at 277 K during 7 days. The black crystals were then filtered off, and dried *in vacuo*. Yield: 0.1 g (35%). IR: $\tilde{\nu} = 1623(\text{s})$ (CO), $1584(\text{s})$ (CO) cm^{-1} ; MS (DEI-(+), 70 eV) m/z (%): 556 (100) ([FeL3]⁺).

[FeL4(py)₂] \cdot py (11) 8 (0.2 g) were dissolved in 15 mL pyridine. The brown solution was stirred and refluxed for 30 min. The mixture was then allowed to cool down and then 15 mL H₂O was added to the solution. Red crystals precipitated slowly, and the solution was left to stand at room temperature overnight. The red crystals were then filtered off, and dried *in vacuo*. Yield: 0.14 g (59%). IR: $\tilde{\nu} = 1601(\text{s})$ (CO), $1582(\text{s})$ (CO) cm^{-1} ; MS (DEI-(+), 70 eV) m/z (%): 464 (100) ([FeL4]⁺); elemental analysis calculated (found) for $C_{35}H_{34}FeN_5O_6$ ($701.55 \text{ g}\cdot\text{mol}^{-1}$): C 63.34 (62.06), H 5.03 (4.59), N 9.98 (9.624).

[FeL1(phpy)₂] (12) 5 (0.2 g) and 4-phenylpyridine (1.67 g) were dissolved in 20 mL MeOH. The dark red suspension was stirred and refluxed for 1 hour. The mixture was then allowed to cool down and left to stand overnight at room temperature. The black crystals were then filtered off, and dried *in vacuo*. Yield: 0.06 g (21%). MS (DEI-(+), 70 eV) m/z (%): 492 (100) ([FeL1]⁺).

[FeL2(phpy)₂]·2MeOH (13) **6** (0.2 g) and 4-phenylpyridine (2.16 g) were dissolved in 20 mL MeOH. The dark red solution was stirred and refluxed for 1 hour. The mixture was then allowed to cool down and left to stand overnight at room temperature. The black crystalline precipitate was then filtered off, and dried *in vacuo*. Yield: 0.22 g. IR: $\tilde{\nu} = 1614(\text{s})$ (CO), $1587(\text{s})$ (CO) cm^{-1} ; MS (DEI-(+), 70 eV) m/z (%): 432 (100) ([FeL2]⁺); elemental analysis calculated (found) for C₃₆H₄₆FeN₄O₆ (742.64 g·mol⁻¹): C 66.97 (68.48), H 5.14 (5.74), N 7.103 (6.90).

[FeL4(phpy)₂] (14) **8** (0.2 g) and 4-phenylpyridine (1.76 g) were dissolved in 20 mL MeOH. The dark red solution was stirred and refluxed for 1 hour. The mixture was then allowed to cool down and left to stand overnight at room temperature. The black crystalline precipitate was then filtered off, and dried *in vacuo*. Yield: 0.18 g (61%). IR: $\tilde{\nu} = 1612(\text{s})$ (CO), $1596(\text{s})$ (CO) cm^{-1} ; MS (DEI-(+), 70 eV) m/z (%): 464 (100) ([FeL4]⁺); elemental analysis calculated (found) for C₄₄H₃₈FeN₄O₆ (774.64 g·mol⁻¹): C 68.22 (68.68), H 4.94 (5.20), N 7.23 (7.18).

[FeL1(dmap)₂] (15) **5** (0.2 g) and 4-(dimethylamino)pyridine (2.44 g) were dissolved in 20 mL MeOH. The dark red solution was stirred and refluxed for 1 hour. The mixture was then allowed to cool down and left to stand overnight at room temperature. The black crystalline precipitate was then filtered off, washed with MeOH (2 × 2 mL) and dried *in vacuo*. Yield: 0.18 g (68%). IR: $\tilde{\nu} = 1603(\text{s})$ (CO), $1574(\text{s})$ (CO) cm^{-1} ; MS (DEI-(+), 70 eV) m/z (%): 492 (75) ([FeL1]⁺), 121 (100) (dmap⁺); elemental analysis calculated (found) for C₃₈H₄₄FeN₆O₆ (736.64 g·mol⁻¹): C 61.96 (62.35), H 6.02 (5.65), N 11.41 (11.65).

[FeL2(dmap)₂] (16) **6** (0.2 g) and 4-(dimethylamino)pyridine (2.44 g) were dissolved in 20 mL MeOH. The dark red solution was stirred and refluxed for 1 hour. The mixture was then allowed to cool down and left to stand overnight at room temperature. The black crystalline precipitate was then filtered off, washed with MeOH (2 × 2 mL) and dried *in vacuo*. Yield: 0.1 g (32%). IR: $\tilde{\nu} = 1606(\text{s})$ (CO), $1569(\text{s})$ (CO) cm^{-1} ; MS (DEI-(+), 70 eV) m/z (%): 431 (23) ([FeL2]⁺), 121 (100) (dmap⁺); elemental analysis calculated (found) for C₃₆H₄₀FeN₆O₄ (676.59 g·mol⁻¹): C 63.91 (63.74), H 5.96 (5.69), N

12.42 (12.34).

[FeL3(dmap)₂] (**17**) **7** (0.2 g) and 4-(dimethylamino)pyridine (2.44 g) were dissolved in 20 mL MeOH. The brown solution was stirred and refluxed for 1 hour. The mixture was then allowed to cool down and left to stand overnight at room temperature. The black crystalline precipitate was then filtered off, washed with MeOH (2 × 2 mL) and dried *in vacuo*. Yield: 0.22 g (74%). IR: $\tilde{\nu} = 1617(\text{s})$ (CO), 1583(s) (CO) cm⁻¹; MS (DEI-(+), 70 eV) m/z (%): 556 (58) ([FeL3]⁺), 121 (100) (dmap⁺); elemental analysis calculated (found) for C₄₆H₄₄FeN₆O₄ (800.72 g·mol⁻¹): C 69.00 (69.73), H 5.54 (5.46), N 10.50 (10.11).

[FeL4(dmap)₂] (**18**) **8** (0.2 g) and 4-(dimethylamino)pyridine (2.44 g) were dissolved in 20 mL MeOH. The dark red solution was stirred and refluxed for 1 hour. The mixture was then allowed to cool down and left to stand overnight at room temperature. The black crystalline precipitate was then filtered off, washed with MeOH (2 × 2 mL) and dried *in vacuo*. Yield: 0.26 g (97%). IR: $\tilde{\nu} = 1614(\text{s})$ (CO), 1596(s) (CO) cm⁻¹; MS (DEI-(+), 70 eV) m/z (%): 464 (75) ([FeL4]⁺), 121 (100) (dmap⁺); elemental analysis calculated (found) for C₃₆H₄₀FeN₆O₆ (708.58 g·mol⁻¹): C 61.02 (59.20), H 5.69 (5.06), N 11.86 (11.48).

[μ -O-(FeL1)₂] (**19**) Suitable crystals for X-ray diffraction were obtained from slow evaporation of a solution of **5** in MeOH in the air.

[μ -O-(FeL4)₂] (**20**) Suitable crystals for X-ray diffraction were obtained from slow evaporation of a solution of **8** in MeOH in the air.

X-ray structure analysis The intensity data of 2·0.5 C₄H₈O·0.5 H₂O were collected with a Bruker D8 Venture diffractometer, the intensity data of **5**, **10^{HS}**, **10^{LS}**, **11**, **12**, **19**, and **20** were collected with a Stoe IPDS II diffractometer, both diffractometer using graphite-monochromated MoK α radiation. The data were corrected for Lorentz and polarization effects. The structures were dissolved by direct methods (SIR-97)^[54] and refined by full-matrix least-square techniques against F_o² - F_c² (SHELXL-97).^[55] All hy-

drogen atoms were calculated in idealised positions with fixed displacement parameters. ORTEP-III^[56,57] was used for the structure representation, SCHAKAL-99^[58] to illustrate molecule packing and CrystalExplorer^[59] for the representation of the voids. CCDC 1040373-1040380 contain the supplementary crystallographic data for this paper.

Magnetic measurements Magnetic susceptibility data were collected using a MPMSXL-5 SQUID magnetometer under an applied field of 0.5 T over the temperature range 2 to 400 K in the settle mode. The samples were placed in gelatin capsules held within a plastic straw. The data were corrected for the diamagnetic contributions of the ligands by using tabulated Pascal's constants and of the sample holder.^[34]

5.5 Conclusion

In this work we presented the synthesis of a new ligand system for iron(II) spin crossover complexes with an increased potential for the observation of π -interactions due to the extended aromatic naphthalene unit compared to the previously used benzene unit. Ten new complexes with a high potential for the observation of spin crossover were synthesised and 50% of those complexes showed the desired properties. Of those, three showed a cooperative spin transition with a maximum hysteresis width of 10 K. The X-ray structure analysis of **10** and **12** revealed C–H $\cdots\pi$ interactions, C–H \cdots O bridges, and –O–C=O $\cdots\pi$ interactions as reason for the abrupt spin transition, with hysteresis in the case of **12**. The next step will be to extend the aromatic system further, e.g. by going to phenazinederivatives^[60] in order to further increase the potential for π -stacking. Another possibility is to link the naphthalene-based Schiff base-like complexes to 1D chains and by this combine rigid linkers with π -stacking. This will be part of a following paper.

Acknowledgements

Financial supports from the German Science foundation (SFB840 ; project A10) and the University of Bayreuth are acknowledged. We thank S. Albrecht and P. Mayer (University of Munich) for the collection of single crystal XRD data of **2**.

5.6 Supporting Information

Figure 5.10: Magnetic susceptibility measurements of compounds **9**, **13**, **16**, **17** and **18**, displayed between 10 K and 300 K.

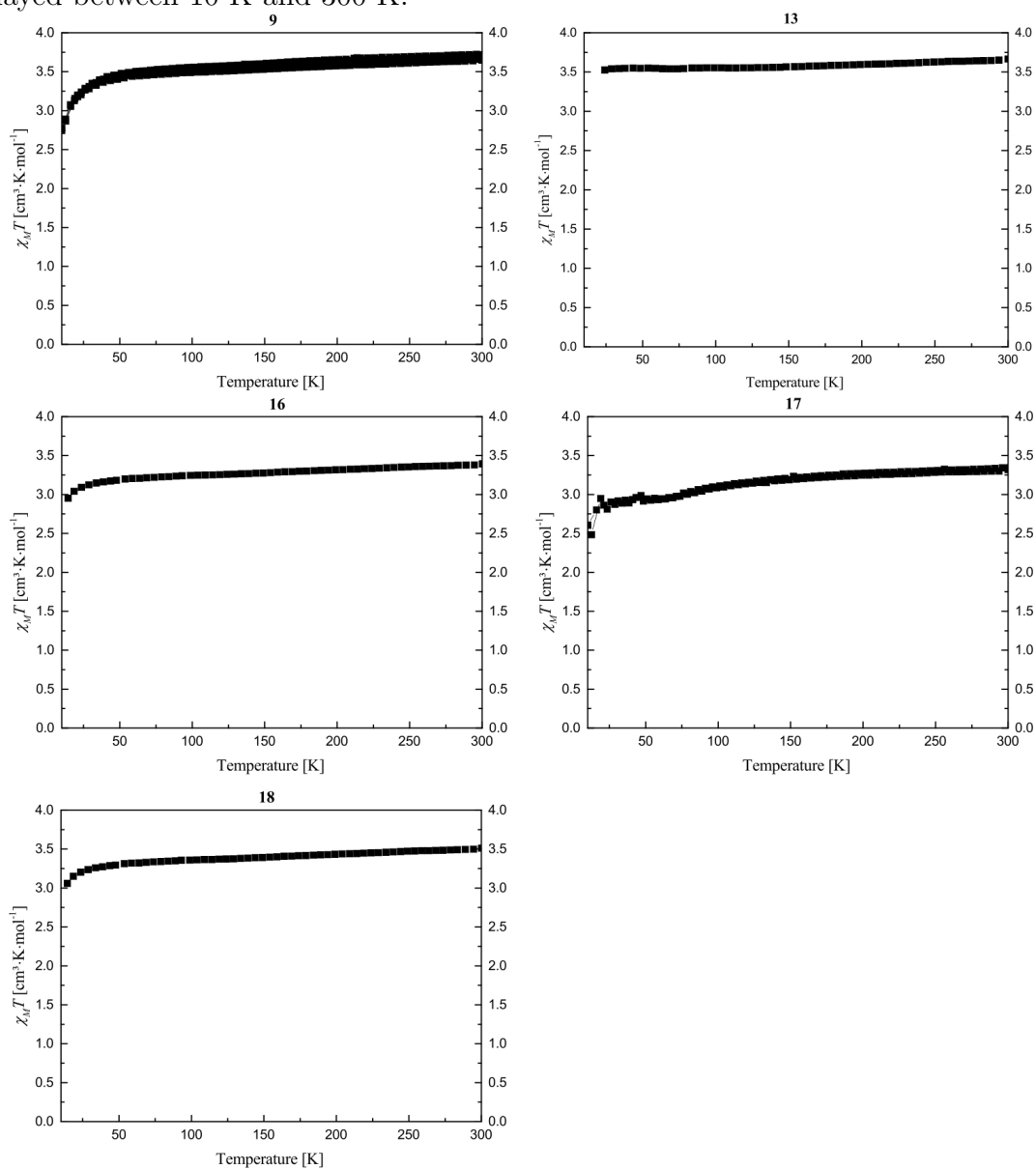


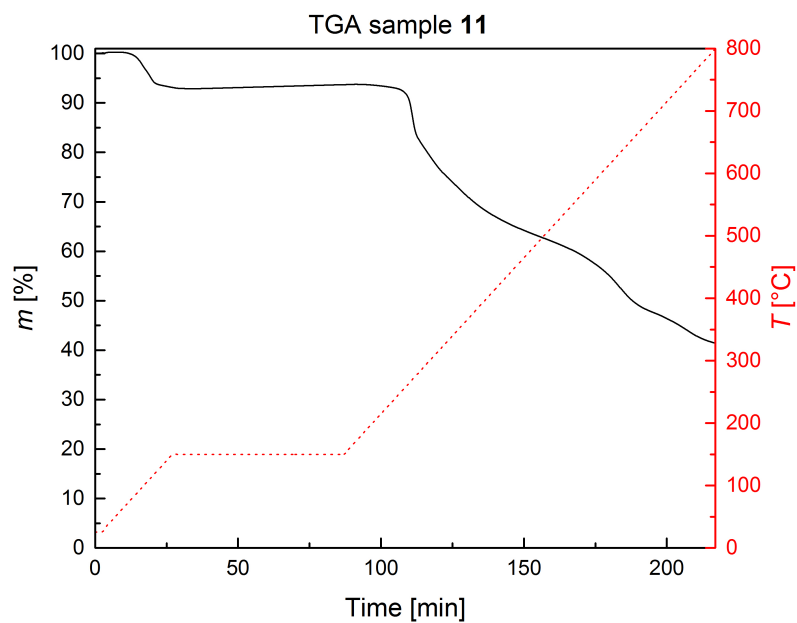
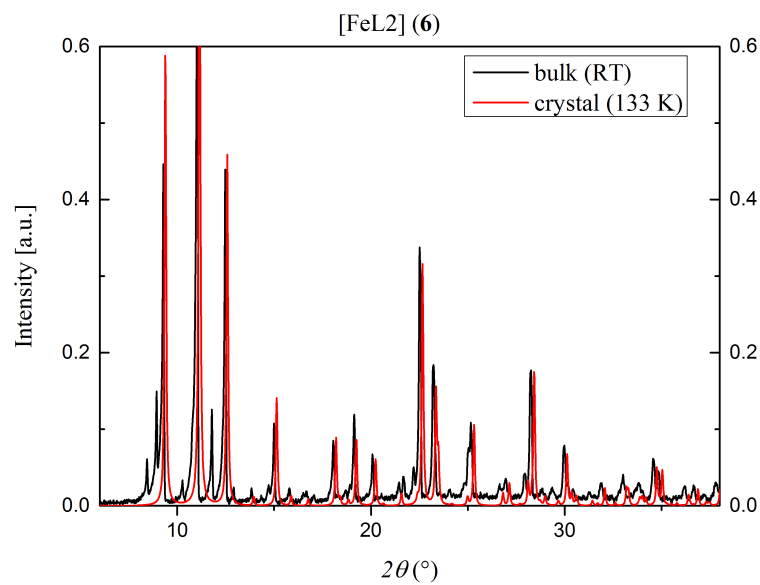
Figure 5.11: TGA measurement of sample **11**.Figure 5.12: Powder diffraction patterns of sample **6** as bulk material (black line, room temperature) and simulated powder diffraction pattern from the crystal structure of **6** (red line, 133 K).

Figure 5.13: Powder diffractograms of compound **14** in HS state (red line, RT) and in LS state (blue line, 133 K).

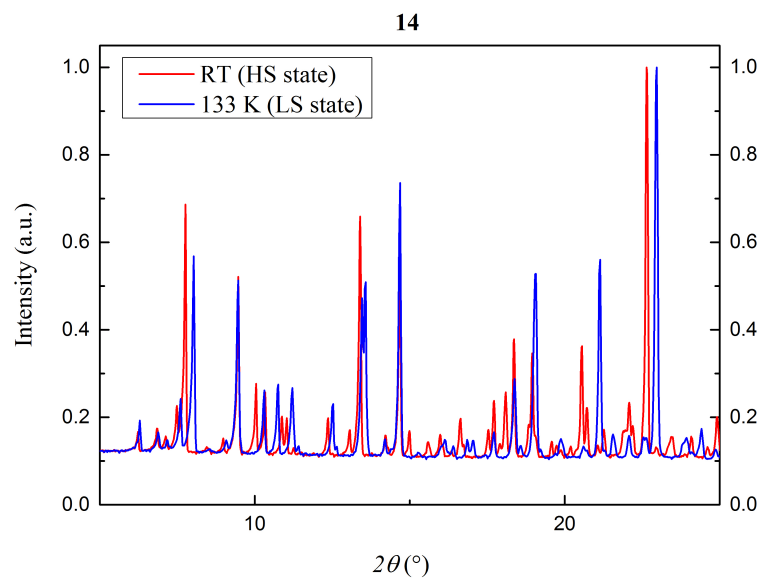


Figure 5.14: Comparison of powder diffractograms of compound **12** (black line, calculated at 133 K), and compound **14** (blue line, measured at 133 K).

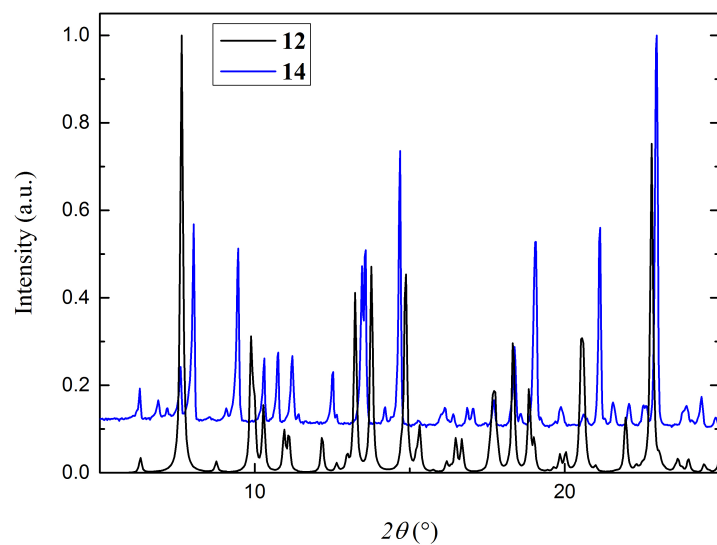


Figure 5.15: ORTEP drawing of **19** (left) and **20** (right). The thermal ellipsoids are shown at the 50% level. Hydrogen atoms and non-coordinating solvent molecules were omitted for clarity reasons.

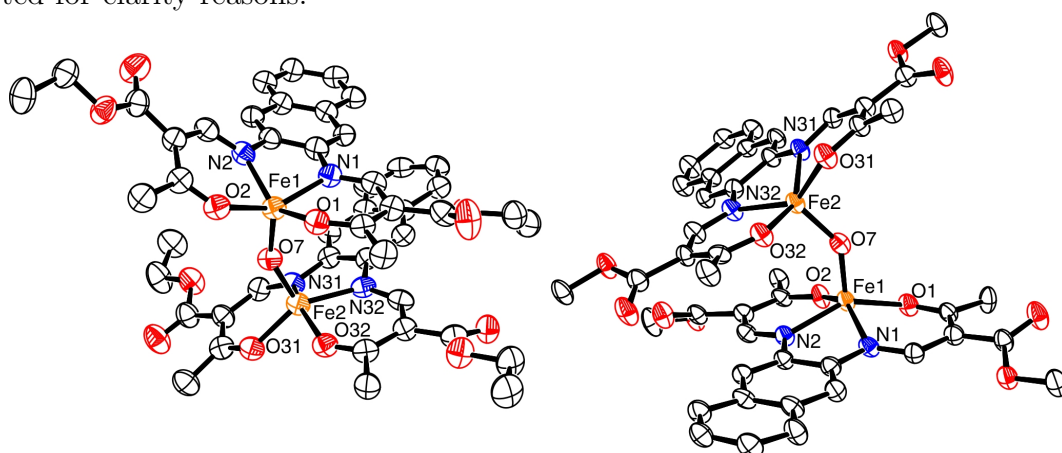


Figure 5.16: left: crystal packing of **19** along [100], hydrogen atoms for clarity reasons. Right: crystal packing of **20** along [010], hydrogen atoms for clarity reasons.

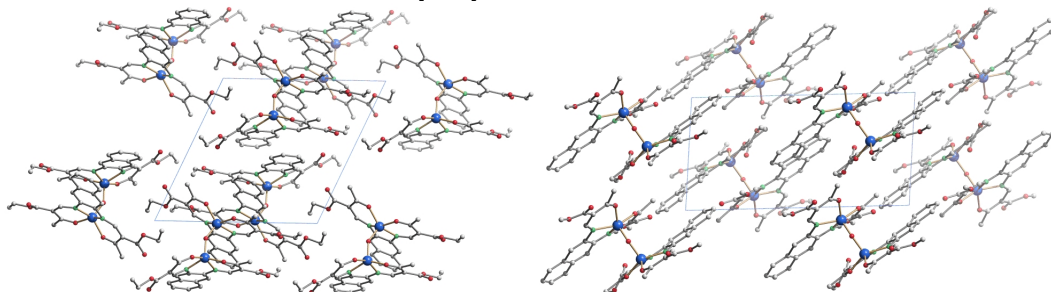
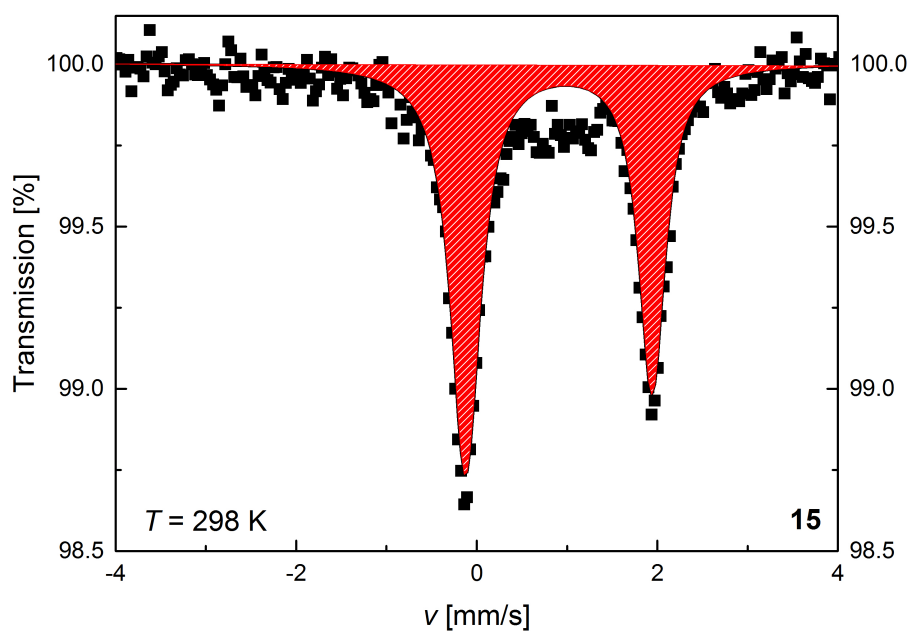


Figure 5.17: Mössbauer spectrum of **15**, hyperfine parameters: $\delta = 0.908(6)$ mm/s, $\Delta E_Q = 2.066(12)$ mm/s, and $\frac{\Gamma}{2} = 0.174(13)$ mm/s.



Mössbauer spectrometry: ^{57}Fe Mössbauer spectra were recorded in transmission geometry on a constant-acceleration using a conventional Mössbauer spectrometer with a 50 mCi $^{57}\text{Co}(\text{Rh})$ source. The samples were sealed in the sample holder under an argon atmosphere. The spectra were fitted using Recoil 1.05 Mössbauer Analysis Software. The isomer shift values are given with respect to a $\alpha\text{-Fe}$ reference at room temperature.

Recoil Software: K. Lagarec and D. G. Rancourt, Recoil, Mössbauer spectral analysis software for windows 1.0, Department of Physics, University of Ottawa, Canada, 1998.

References

- [1] O. Kahn, *Science* **1998**, *279*, 44–48.
- [2] J.-F. Létard, P. Guionneau, L. Goux-Capes, *Spin Crossover in Transition Metal Compounds I-III*, Springer, Berlin, DE, **2004**.
- [3] J. Linares, E. Codjovi, Y. Garcia, *Sensors* **2012**, *12*, 4492–4479.
- [4] M. Halcrow, *Spin-Crossover Materials*, John Wiley & Sons Ltd., Chichester, UK, **2013**.
- [5] P. Gütllich, H. Goodwin, *Spin Crossover in Transition Metal Compounds I-III*, Springer, Berlin, DE, **2004**.
- [6] P. D. Southon, L. Liu, E. A. Fellows, D. J. Price, G. J. Halder, K. W. Chapman, B. Moubaraki, K. Murray, J.-F. Létard, C. J. Kepert, *J. Am. Chem. Soc.* **2009**, *131*, 10998–11009.
- [7] E. Coronado, G. Mínguez Espallargas, *Chem. Soc. Rev.* **2013**, *42*, 1525.
- [8] S. Schlamp, B. Weber, A. D. Naik, Y. Garcia, *Chem. Commun.* **2011**, *47*, 7152–7154.
- [9] Y. H. Lee, A. Ohta, Y. Yamamoto, Y. Komatsu, K. Kato, T. Shimizu, H. Shinoda, S. Hayami, *Polyhedron* **2011**, *30*, 3001–3005.
- [10] J. A. Kitchen, N. G. White, C. Gandolfi, M. Albrecht, G. N. L. Jameson, J. L. Tallon, S. Brooker, *Chem. Commun.* **2010**, *46*, 6464.
- [11] K. Kuroiwa, H. Kikuchi, N. Kimizuka, *Chem. Commun.* **2010**, *46*, 1229–1231.
- [12] C. Gandolfi, G. G. Morgan, M. Albrecht, *Dalton Trans.* **2012**, *41*, 3726–3730.
- [13] B. Weber, E. S. Kaps, K. Achterhold, F. G. Parak, *Inorg. Chem.* **2008**, *47*, 10779–10787.
- [14] W. Bauer, S. Schlamp, B. Weber, *Chem. Commun.* **2012**, *48*, 10222.
- [15] J. Linares, H. Spiering, F. Varret, *Eur. Phys. J. B* **1999**, *10*, 271–275.
- [16] C. Lochenie, W. Bauer, A. P. Railliet, S. Schlamp, Y. Garcia, B. Weber, *Inorg. Chem.* **2014**, *53*, 11563–11572.
- [17] B. Weber, W. Bauer, T. Pfaffeneder, M. M. Dîrtu, A. D. Naik, A. Rotaru, Y. Garcia, *Eur. J. Inorg. Chem.* **2011**, 3193–3206.
- [18] J. A. Real, A. B. Gaspar, V. Niel, M. C. Muñoz, *Coord. Chem. Rev.* **2003**, *236*, 121–141.

-
- [19] Z. J. Zhong, J.-Q. Tao, Z. Yu, C.-Y. Dun, Y.-J. Liu, X.-Z. You, *J. Chem. Soc., Dalton Trans.* **1998**, 327–328.
- [20] J.-F. Létard, P. Guionneau, E. Coddjovi, O. Lavastre, G. Bravic, D. Chasseau, O. Kahn, *J. Am. Chem. Soc.* **1997**, *119*, 10861–10862.
- [21] L. Wolf, E.-G. Jäger, *Z. Anorg. Allg. Chem.* **1966**, *346*, 76–91.
- [22] B. Weber, E. S. Kaps, C. Desplanches, J.-F. Létard, *Eur. J. Inorg. Chem.* **2008**, 2963–2966.
- [23] C. Baldé, W. Bauer, E. Kaps, S. Neville, C. Desplanches, G. Chastanet, B. Weber, J.-F. Létard, *Eur. J. Inorg. Chem.* **2013**, 2744–2750.
- [24] B. Weber, E. S. Kaps, C. Desplanches, J.-F. Létard, *Eur. J. Inorg. Chem.* **2008**, 4891–4898.
- [25] B. Weber, E. S. Kaps, J. Weigand, C. Carbonera, J.-F. Létard, K. Achterhold, F. G. Parak, *Inorg. Chem.* **2008**, *47*, 487–496.
- [26] B. R. Müller, G. Leibeling, E.-G. Jäger, *Mol. Cryst. Liq. Cryst. Sci. Technol., Sect. A* **1999**, *334*, 389–394.
- [27] B. Weber, E.-G. Jäger, *Z. Anorg. Allg. Chem.* **2009**, *635*, 130–133.
- [28] S. Schlamp, P. Thoma, B. Weber, *Eur. J. Inorg. Chem.* **2012**, 2759–2768.
- [29] S. Schlamp, P. Thoma, B. Weber, *Chem. Eur. J.* **2014**, *20*, 6462–6473.
- [30] W. Bauer, C. Lochenie, B. Weber, *Dalton Trans.* **2014**, *43*, 1990–1999.
- [31] B. Weber, J. Obel, *Z. Anorg. Allg. Chem.* **2009**, *635*, 2474–2479.
- [32] S. Thallmair, W. Bauer, B. Weber, *Polyhedron* **2009**, *28*, 1796–1801.
- [33] W. Bauer, T. Ossiander, B. Weber, *Z. Naturforsch. B* **2010**, 323–328.
- [34] O. Kahn, *Molecular Magnetism*, VCH, New York, N. Y., USA, **1993**.
- [35] B. Weber, J. Obel, D. Henner-Vasquez, W. Bauer, *Eur. J. Inorg. Chem.* **2009**, 5527–5534.
- [36] C. Lochenie, S. Schlamp, A. P. Railliet, K. Robeyns, B. Weber, Y. Garcia, *CrystEngComm* **2014**, *16*, 6213.
- [37] B. Weber, Jäger, *Eur. J. Inorg. Chem.* **2009**, 465–477.
- [38] B. Weber, *Coord. Chem. Rev.* **2009**, *253*, 2432–2449.
- [39] S. Schlamp, K. Dankhoff, B. Weber, *New J. Chem.* **2014**, *38*, 1965–1972.
-

-
- [40] P. Guionneau, M. Marchivie, G. Bravic, J.-F. Létard, D. Chasseau, *Spin Crossover in Transition Metal Compounds I-III*, Springer, Berlin, DE, **2004**.
- [41] T. Steiner, G. R. Desiraju, *Chem. Commun.* **1998**, 891–892.
- [42] G. R. Desiraju, *Acc. Chem. Res.* **2002**, *35*, 565–573.
- [43] J. E. Gautrot, P. Hodge, D. Cupertino, M. Helliwell, *New J. Chem.* **2006**, *30*, 1801–1807.
- [44] R. J. Santos-Contreras, F. J. Martínez-Martínez, E. V. Garcí-Báez, I. I. Padilla-Martínez, A. L. Peraza, H. Höpfl, *Acta Crystallogr., Sect. C* **2007**, *63*, o239–o242.
- [45] F. H. Allen, C. A. Baalham, J. P. M. Lommerse, P. R. Raithby, *Acta Crystallogr., Sect. B* **1998**, *54*, 320–329.
- [46] T. J. Mooibroek, P. Gamez, J. Reedijk, *CrystEngComm* **2008**, *10*, 1501–1515.
- [47] B. Weber, C. Carbonera, C. Desplanches, J.-F. Létard, *Eur. J. Inorg. Chem.* **2008**, 1589–1598.
- [48] B. Weber, E. S. Kaps, J. Obel, W. Bauer, *Z. Anorg. Allg. Chem.* **2008**, *636*, 1421–1426.
- [49] B. Weber, W. Bauer, J. Obel, *Angew. Chem. Int. Ed.* **2008**, *47*, 10098–10101.
- [50] C. Lochenie, W. Bauer, S. Schlamp, P. Thoma, B. Weber, *Z. Anorg. Allg. Chem.* **2012**, *638*, 98–102.
- [51] H. G. O. Becker, *Organikum. Organisch-Chemisches Grundpraktikum 19th ed.*, Johann Ambrosius Barth, Berlin, DE, **1993**.
- [52] L. Claisen, *Justus Liebigs Ann. Chem.* **1897**, *297*, 1–98.
- [53] B. Weber, W. Betz, R. and Bauer, S. Schlamp, *Z. Anorg. Allg. Chem.* **2011**, *637*, 102–107.
- [54] A. Altomare, M. C. Burla, M. Camalli, G. L. Casciarano, C. Giavazzo, A. Guagliardi, A. G. G. Moliterni, G. Polidori, R. Spagna, *J. Appl. Crystallogr.* **1999**, *35*, 115–119.
- [55] G. Sheldrick, *Acta Crystallogr., Sect. A* **2008**, *64*, 112–122.
- [56] C. K. Johnson, M. N. Burnett, *ORTEP-III*, **1996**, Oak-Ridge National Laboratory, Oak-Ridge, TN.
- [57] L. Farrugia, *J. Appl. Crystallogr.* **1997**, *30*, 565.
- [58] E. Keller, *Schakal-99*, **1999**, University of Freiburg, Freiburg DE.
- [59] S. K. Wolff, D. J. Grimwood, J. J. McKinnon, M. J. Turner, *Crystal Explorer*, **2012**, University of Western Australia.
- [60] C. Lochenie, K. G. Wagner, M. Karg, B. Weber, *J. Mater. Chem. C* **2015**, *3*, 7925–7935.
-

6. Iron(II) spin crossover complexes with diamino-naphthalene-based Schiff base-like ligands: 1D coordination polymers.

Charles Lochenie,^a Andreas Gebauer,^a Ottokar Klimm,^a Florian Puchtler^b and Birgit Weber^{*,a}

^aInorganic Chemistry II, Universität Bayreuth, Universitätsstrasse 30, NW I, 95440 Bayreuth, Germany.

^bInorganic Chemistry I, Universität Bayreuth, Universitätsstrasse 30, NW I, 95440 Bayreuth, Germany.

Published in *New J. Chem.* **2016**, *40*, 4687–4695.

Reproduced with the permission of the Royal Society of Chemistry.

Abstract

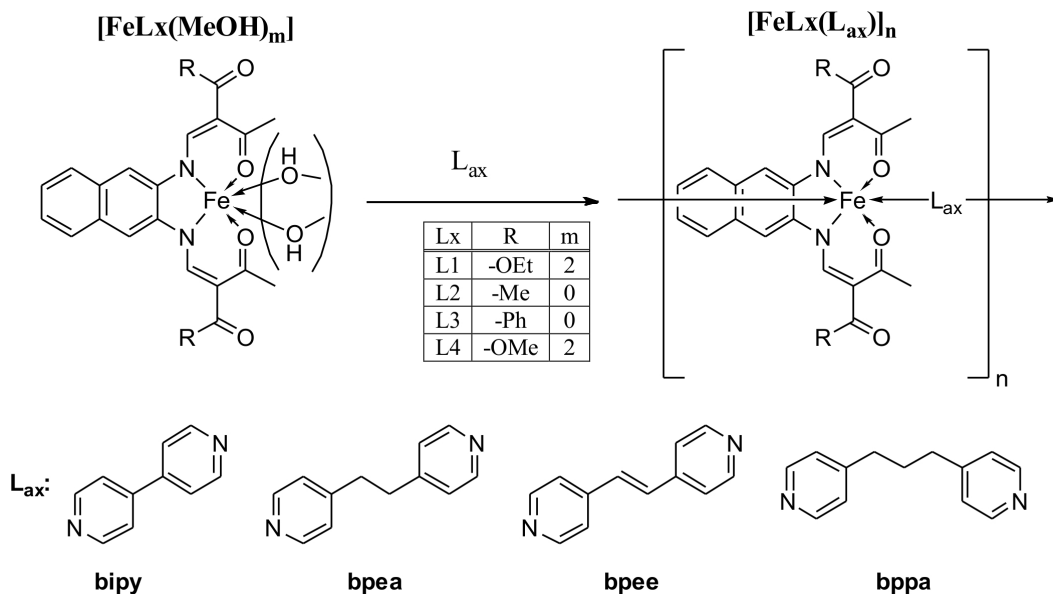
The synthesis of iron(II) coordination polymers of new Schiff base-like ligands with extended π -system is described. In total sixteen new compounds were synthesised. The complexes were characterised by X-ray powder diffraction and magnetic measurements. Four of those complexes remain in the low-spin state and six remain in the high-spin state in the entire temperature range investigated. The remaining six complexes show spin crossover behaviour with a cooperative spin transition (28 and 40 K wide hystere-

sis loops) in two cases. The influence of the extended aromatic system on cooperative interactions is discussed.

6.1 Introduction

Iron(II) spin crossover (SCO) complexes that show a cooperative spin transition (ST) with hysteresis belong to a class of bistable molecular materials that continue to attract the interest of many groups all over the world.^[1–19] This is due to possible applications in the field of sensors or memory devices.^[19–23] A very attractive aspect special to SCO materials is that the switching process, which can be triggered by different physical or chemical stimuli and can be combined with additional properties (e.g. magnetic exchange interaction, liquid crystalline behaviour, luminescence) leading to multifunctional materials with synergetic effects between the different properties.^[24–29]

In order to achieve cooperative STs with hysteresis, intermolecular interactions, such as hydrogen bonds,^[30,31] van der Waals interactions,^[32] or C-H $\cdots\pi$ contacts,^[33] are needed to transfer the structural changes associated with the spin transition from one molecule to another. A very promising approach is a combination of such short range interactions with long range interactions as it is often observed for 1D coordination polymers or ladder-like compounds.^[32,34,35] Although, there are examples in literature, that π -interactions between extended aromatic systems can increase the width of the hysteresis loop,^[33,36,37] this concept of π -stacking was so far not combined with the long range interactions expected for coordination polymers. Consequently we decided to use our modified naphthalene based Schiff base-like ligands^[38] for the synthesis of iron(II) 1D coordination polymers and to investigate their spin crossover properties, especially with regard to the observation of thermal hysteresis loops. In Scheme 6.1, the general structure of the new ligands and their iron complexes and the used abbreviations are given.



Scheme 6.1: Pathway of synthesis of the SCO complexes described in this work and used abbreviations.

6.2 Results

6.2.1 Syntheses

The spin crossover (SCO) coordination polymers $[\text{FeLx}(\text{L}_{ax})]_n$ (**1–16**) were synthesised from a precursor complex $[\text{FeLx}(\text{MeOH})_m]$,^[38] whose axial methanol ligands were exchanged with a bridging *N*-donating ligand such as 4,4'-bipyridine (bipy), 1,2-bis(4-pyridyl)ethane (bpea), 1,2-bis(4-pyridyl)ethylene (bpee), and 1,3-bis(4-pyridyl)propane (bppa). The molecular structures and the synthetic pathway are given in Scheme 6.1. The different -R substituents allow a fine tuning of the crystal field strength.

All coordination polymers precipitated in the boiling heat as black fine crystalline material. The dark colour of those complexes, in both, the HS and the LS state, arises from a strong charge transfer bands usually observed for this type of complexes.^[39–42] This prevents the identification of the spin state of the sample or the occurrence of a SCO phenomenon upon heating or cooling with the naked eye. In some cases, methanol was included in the samples, a list of the different complexes, along with their solvent content, is shown in Table 6.1. All complexes were characterised with IR spectroscopy,

CHN analysis and mass spectrometry. The solvent contents of the SCO complexes were calculated from the CHN and TGA data. TGA data of the SCO complexes are presented in Supporting Information: Figure 6.6. The IR spectra show two strong characteristic CO bands (1550–1650 cm^{-1}), as well as a large OH band for the compounds with incorporated methanol (3200–3300 cm^{-1}).

Table 6.1: Overview of the synthesised complexes, their SCO behaviour, characteristic $\chi_M T$ values [$\text{cm}^3 \cdot \text{K} \cdot \text{mol}^{-1}$], HS residue (γ_{HS} as $\chi_M T(T)/(\chi_M T(\text{HS}) - \chi_M T(\text{LS}))$) at 50 K and the $T_{\frac{1}{2}}$ values [K] ($T_{\frac{1}{2}}$ defined as the temperature where half of the SCO active sites transited).

Compound	SCO behaviour	$\chi_M T$ (300 K)	$\chi_M T$ (50 K)	γ_{HS} (50 K)	$T_{\frac{1}{2}}$
1 ([FeL1(bipy)]·2 MeOH) _n	Gradual	3.40 ^a	0.13	0.04	330
2 [FeL1(bpea)] _n	HS	3.38			
3 [FeL1(bpee)] _n	LS	0.12			
4 ([FeL1(bppa)]·MeOH) _n	LS	0.25			
5 ([FeL2(bipy)]·2 MeOH) _n	Gradual	3.50 ^a	0.12	0.03	251
6 ([FeL2(bpea)]·2 MeOH) _n	HS	3.56			
7 ([FeL2(bpee)]·2 MeOH) _n	HS	3.28			
8 ([FeL2(bppa)]·2 MeOH) _n	HS	3.79			
9 [FeL3(bipy)] _n	HS	3.30			
10 ([FeL3(bpea)]·MeOH) _n	abrupt, hysteresis	3.36 ^b 3.37 ^c	0.35 ^b 0.37 ^c	0.10 ^b 0.11 ^c	↓195, ↑223 ^b ↓205, ↑228 ^c
11 ([FeL3(bpee)]·MeOH) _n	abrupt, hysteresis	3.74 ^b 3.76 ^c	0.28 ^b 0.30 ^c	0.07 ^b 0.08 ^c	↓210, ↑250 ^b ↓210, ↑247 ^c
12 [FeL3(bppa)] _n	HS	3.53			
13 [FeL4(bipy)] _n	LS	0.17			
14 [FeL4(bpea)] _n	abrupt	3.36	0.06	0.02	149
15 ([FeL4(bpee)]·1.5 MeOH) _n	LS	0.42			
16 ([FeL4(bppa)]·MeOH) _n	gradual	2.07 ^b 2.94 ^c	0.64 ^b 0.52 ^c	0.18 ^b 0.15 ^c	276 ^b 206 ^c

a = 400 K; b = first loop; c = after annealing at 400 K.

Scanning electron microscopy images of all probes were measured and are displayed in the SI, Figures 6.11–6.14. All samples are homogeneous, fine crystalline powders. Samples **1**, **2**, **4**, **5**, **9**, **10**, **11**, **12**, **14**, and **15** have an elongated block-like shape, whereas samples **3**, **6**, **7**, **8**, **13**, and **16** have a platelet-like morphology. All crystallites have a size between 0.5 and 10 μm .

6.2.2 Magnetism

The magnetic properties of all synthesised coordination polymers were investigated with a SQUID magnetometer in the temperature range between 10 and 400 K in the settle mode. Measurements with higher velocities in the sweep mode did not reveal significant indications for kinetic effects as observed for other systems.^[43] Selected parameters are summarised in Table 6.1. Out of sixteen synthesised complexes, six (samples **2**, **6**, **7**, **8**, **9**, **12**) are HS compounds which do not show any SCO properties (SI Figure 6.7: plot of $\chi_M T$ vs T), in contrast to compounds **3**, **4**, **13**, and **15** which are LS over the investigated temperature range (SI Figure 6.8: plot of $\chi_M T$ vs T). This shows that the use of different substituents R is needed in order to bring the SCO complexes in the right range of crystal field strength, depending on the different axial ligands used. The two 4,4'-bipyridine-bridged samples **1** and **5** exhibit a gradual spin crossover, above room temperature (RT) ($T_{\frac{1}{2}} = 330$ K), and below RT ($T_{\frac{1}{2}} = 251$ K), respectively. The $\chi_M T$ vs T plot is shown in Figure 6.2. Their magnetic susceptibility with temperature product is with $3.40 \text{ cm}^3 \cdot \text{K} \cdot \text{mol}^{-1}$ and $3.50 \text{ cm}^3 \cdot \text{K} \cdot \text{mol}^{-1}$ at 400 K in the typical range for iron(II) HS complexes. At 50 K, both samples show a small HS residue (0.04 and 0.03) in agreement with complexes being almost completely in a LS state.

Although both SCO are gradual, the SCO of sample **1** is more abrupt, indicating of a higher cooperativity through a network of inter-chain contracts (the bridging ligand is in both cases 4,4'-bipyridine). Interestingly, for the phenylene-based complexes always an abrupt spin transitions with hysteresis or no spin transition at all was observed if 4,4'-bipyridine was used as bridging ligand. Additionally those samples showed a strong dependence on the solvent contents in the crystal packing.^[39,44,45] In the case of the slightly larger 3,4-dihydroxyphenylene-based ligands either small hysteresis or only gradual spin transitions are observed, also depending on the solvent contents.^[46] The SCO properties of **1** and **5** illustrate clearly that the use of a rigid bridging ligand alone is not sufficient for obtaining abrupt cooperative ST.^[34,45] This is in agreement with results obtained for other SCO coordination polymers as the triazole-based systems, where depending on the substituents very different SCO properties are observed.^[47,48] Both samples contain MeOH as crystal solvent, however annealing at 400 K under vacuum does not change the SCO

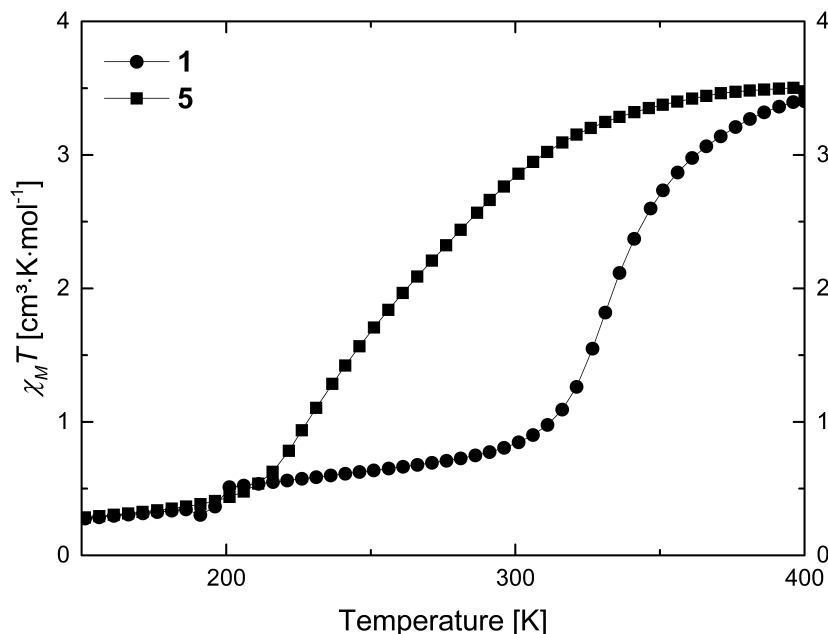


Figure 6.2: Magnetic susceptibility temperature product *vs* temperature measurement for compounds **1** and **5** displayed between 175 and 400 K.

properties. The curve progression is stable and can be repeated several times. Apparently, the increasing size of the equatorial ligands reduces the intermolecular interactions between the single chains and leads to the gradual spin transitions.

The magnetic measurements of the samples **10** and **11** reveal interesting examples of spin transition with hysteresis. The corresponding $\chi_M T$ *vs* T plot is shown in Figure 6.3. Both samples are at room temperature with, respectively, $3.36 \text{ cm}^3 \cdot \text{K} \cdot \text{mol}^{-1}$ and $3.74 \text{ cm}^3 \cdot \text{K} \cdot \text{mol}^{-1}$ clearly in the region for iron(II) HS centres. Upon cooling, the compounds undergo an abrupt ST towards the LS state with $T_{\frac{1}{2}\downarrow} = 195 \text{ K}$ and $T_{\frac{1}{2}\downarrow} = 210 \text{ K}$, respectively. At 50 K, the compounds are with $\chi_M T$ values of $0.35 \text{ cm}^3 \cdot \text{K} \cdot \text{mol}^{-1}$ and $0.28 \text{ cm}^3 \cdot \text{K} \cdot \text{mol}^{-1}$ clearly in the LS state. Upon warming, both compounds return abruptly to their original HS state at $T_{\frac{1}{2}\uparrow} = 223 \text{ K}$ and $T_{\frac{1}{2}\uparrow} = 250 \text{ K}$ revealing 28 K and 40 K-wide hystereses. As both samples contain MeOH solvent molecules in the crystal packing, the magnetic behaviour of the samples was investigated after heating the samples at 400 K under vacuum. Sample **10** still shows an hysteretic behaviour, but the

transition temperatures are slightly shifted to higher temperature ($T_{\frac{1}{2}\downarrow} = 205$ K and $T_{\frac{1}{2}\uparrow} = 228$ K) with a reduction of the hysteresis width to 23 K. Compound **11** is less sensitive to the loss of included solvent molecules, as it only affects the LS to HS transition ($T_{\frac{1}{2}\downarrow} = 210$ K and $T_{\frac{1}{2}\uparrow} = 247$ K) and reduces the hysteresis span from 40 K to 37 K. After annealing, the magnetic properties are stable and can be measured several times. A comparison of the bpee- and bpea-bridged coordination polymers with phenylene-based, 3,4-dihydroxyphenylene-based and naphthylene-based Schiff base-like ligands reveals an opposite trend compared to the bipy-bridged complexes. The widest hysteresis observed for those coordination polymers increases from 27 K (phenylene-based with bpea)^[45] 19 to 28 K (3,4-dihydroxyphenylene-based and bpee)^[46] and the here described 37 K for **11**. The results suggest that the ratio between the size of the equatorial ligand and the size of the axial ligand is important for optimising intermolecular interactions. A similar observation was already made for the mononuclear SCO complexes of this ligand type^[40] and for the formation and self-assembly behaviour of amphiphilic complexes of this ligand type.^[49,50]

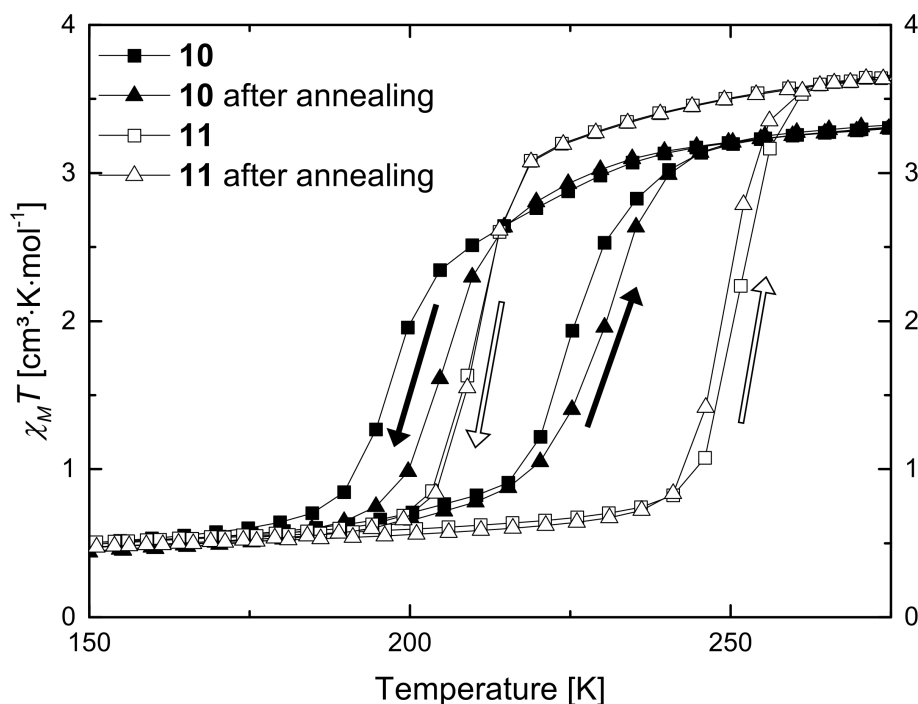


Figure 6.3: Magnetic susceptibility temperature product *vs* temperature measurement for compounds **10** and **11**, displayed between 150 and 275 K.

The results from the magnetic measurements of **14** and **16** are shown in Figure 6.4. Compound **14** is at RT in the HS state ($\chi_M T = 3.36 \text{ cm}^3 \cdot \text{K} \cdot \text{mol}^{-1}$), and undergoes an abrupt SCO at 149 K towards LS state (at 50 K, $\chi_M T = 0.06 \text{ cm}^3 \cdot \text{K} \cdot \text{mol}^{-1}$). Upon warming up, the compound goes back to the HS state at the same temperature. Compound **16** is at RT, with a $\chi_M T$ value of $2.07 \text{ cm}^3 \cdot \text{K} \cdot \text{mol}^{-1}$, in an intermediate state between LS and HS. Upon cooling, the sample goes very gradually to LS, with a rather high residual γ_{HS} of 0.18. Upon warming, the compound undergoes the same gradual transition towards HS state, revealing a $T_{\frac{1}{2}}$ of 276 K. As included MeOH solvent molecules were revealed by the CHN analysis, sample **16** was heated at 400 K under vacuum and its magnetic properties measured again. Upon cooling from 400 K, the compound stays in the HS state ($\chi_M T = 2.94 \text{ cm}^3 \cdot \text{K} \cdot \text{mol}^{-1}$) until 275 K, where it starts a gradual two-step transition towards LS state ($T_{\frac{1}{2}} = 206 \text{ K}$), displacing the SCO of 70 K towards lower temperatures. The behaviour of those two bpea and bppa bridged complexes, especially the occurrence of steps in the transition curve in the case of **16**, is similar to those of previously published SCO complexes with such flexible bridging ligands.^[39,44,45,51]

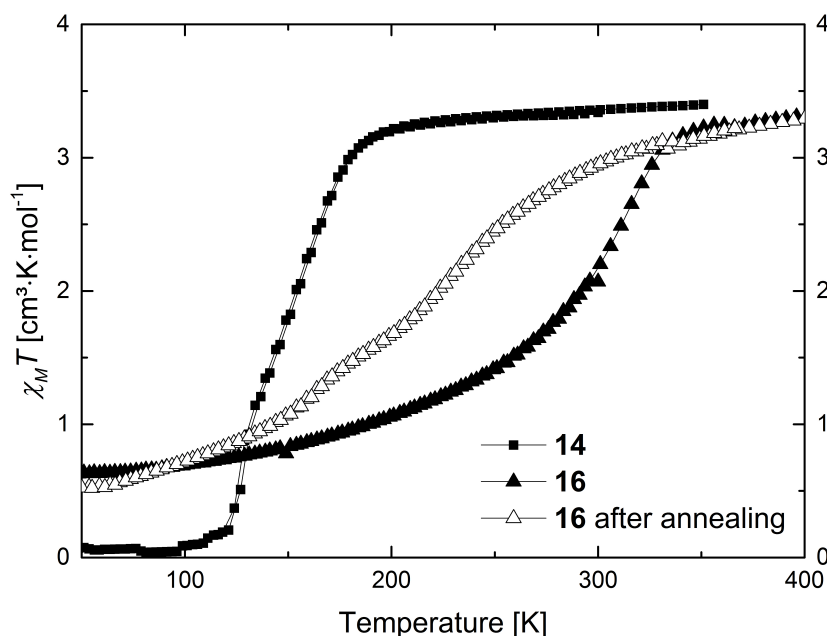


Figure 6.4: Magnetic susceptibility temperature product *vs* temperature measurement for compounds **14** and **16**, displayed between 50 and 400 K.

6.2.3 Structural analysis

Growing single crystals suitable for X-ray structure analysis appeared to be difficult, as all coordination polymers are precipitating very fast. Vapour-vapour as well as liquid-liquid diffusion setups unfortunately only yielded microcrystals, whose size were far too small for single crystal X-ray analysis. Therefore, an X-ray analysis has been made of the powders. Powder diffractograms of the SCO complexes were measured at RT and 133 K in order to have the structural data of the HS and the LS state of samples **5**, **10**, **11**, **14**, and **16**. Sample **1** was only measured at RT in the LS state. The powder patterns are presented in Figure 6.5. The diffractograms can be analysed in order to, firstly, attest the polymeric nature of the samples by comparison with other similar Fe(II) coordination polymers published,^[30,45,46] and secondly, gain information about the nature of the SCO, i.e. if phase transitions are involved in the process. At lower diffraction angles (typically $2\theta = 8^\circ\text{--}12^\circ$), typical strong peaks for the Fe–Fe distance within a chain can be found. One can see that for the compounds, those peaks are located at higher angle for the compounds with the shorter axial ligand (i.e. sample **5** with bipy), and at lower angle for the compounds with longer axial ligand (i.e. sample **16** with bppa), indicating that the Fe–Fe distance is increasing with the length of the axial ligand. The Fe–Fe distance is here between $\approx 9 \text{ \AA}$ for the sample with bipy (**5**), and $\approx 12.5 \text{ \AA}$ for the sample with bppa (**16**). Sample **1** displays more peaks at low diffraction angle, presumably because of a more complicated crystal structure.

Crystallographic phase transitions associated with the SCO can be at the origin of a wide hysteresis,^[2] and therefore it is interesting to compare the diffractograms of the compounds in HS and LS state. The powder patterns of samples **5**, **14**, and **16** show great similarities between the HS and LS states, as only the peak positions are shifted to higher diffraction angles. It was then assumed that no crystallographic phase transition is happening during SCO. The shift corresponds to a reduction of the Fe–Fe distance of $\approx 0.3 \text{ \AA}$ for sample **5**, $\approx 0.2 \text{ \AA}$ for sample **14** and $\approx 0.05 \text{ \AA}$ for sample **16**. The smaller shift Fe–Fe distance of the latter sample **16** can be on one hand explained by the fact that the ligand bppa is a “flexible” ligand, therefore absorbing partially the volume change of the Fe(II) centre upon SCO, and on the other hand because the compound at RT is not

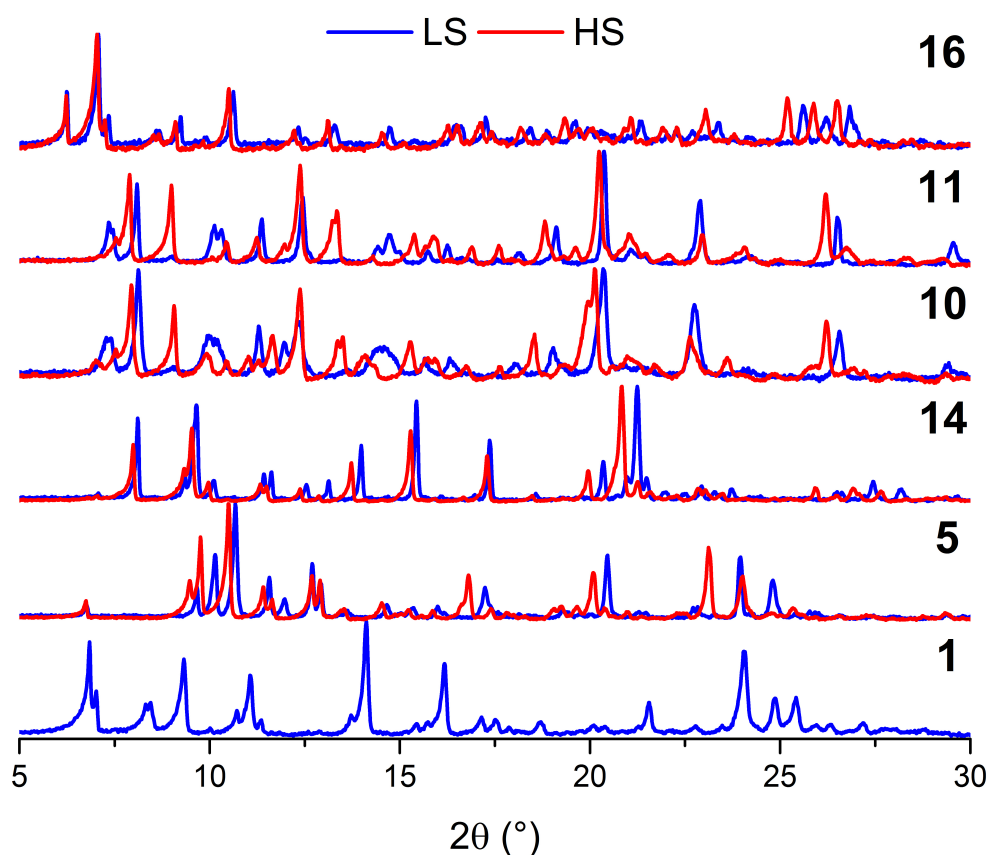


Figure 6.5: Powder diffractograms for samples **1**, **5**, **10**, **11**, **14**, and **16**, in the HS state (red) and LS state (blue)

in a full HS state according to the magnetic measurement.

In the case of samples **10** and **11**, one can see the high similarity between the powder patterns in HS state of the two samples. In the LS state, the patterns also look very similar; however between the HS and LS state, more differences appear, presumably indicating phase transition happening during the SCO. A decrease of the Fe–Fe distance of $\approx 0.25 \text{ \AA}$ upon SCO was observed.

Powder diffraction patterns of samples **2**, **3**, **4**, **6**, **7**, **8**, **9**, **12**, **13**, and **15** were also measured in order to confirm their polymeric structure. All compounds present the same features as the SCO samples, with strong diffraction peak around $2\theta = 8^\circ\text{--}12^\circ$ accounting for the typical Fe–Fe distance within a chain. The patterns are shown in the SI, Figure 6.9.

6.2.4 Differential scanning calorimetry

Samples **1**, **5**, **10**, **11**, and **16** were investigated with the help of DSC in order to measure the enthalpy and entropy changes associated to the SCO phenomenon itself, but also analyse the presence of supplementary phase transition related or not with the spin transition. Sample **14** could not be investigated as the spin transition falls out of the temperature range of the calorimeter. All DSC measurements are shown in the SI, Figure 6.10. Table 6.2 sums up peak temperatures as well as enthalpy and entropy values integrated from the heat curve. All samples present an exothermic peak for the HS to LS transition, and an endothermic peak for the LS to HS transition. For samples **1**, **5**, **10**, and **11** a heat response could be measured for both HS to LS and LS to HS transitions at temperatures in good agreement with the temperatures from the magnetic measurements taking into account the different measurement rates. Sample **1** presents rather broad peaks in agreement with the rather gradual transition, the same observation is made for sample **5**, where the peaks are very broad and flat over almost 100 K span, as seen for the spin transition in the SQUID measurement. Both samples have similar enthalpy and entropy values for both HS to LS and LS to HS transitions, and those values are similar to those obtained for other spin crossover complexes from the same class.^[30,52]

Table 6.2: Sum up of the peak temperatures, enthalpy, and entropy values for the DSC measurements of samples **1**, **5**, **10**, **11**, and **16**.

Compound	SCO behaviour	$T_{\frac{1}{2}}$ [K]	ΔH [kJ·mol ⁻¹]	ΔS [J·mol ⁻¹ ·K ⁻¹]
1 ([FeL1(bipy)]·2 MeOH) _n	Gradual	↑325	3.2(5)	10.7(10)
		↓325	3.6(5)	14.3(10)
5 ([FeL2(bipy)]·2 MeOH) _n	Gradual	↑245	9.1(9)	24.8(16)
		↓238	9.1(9)	47(2)
10 ([FeL3(bpea)]·MeOH) _n	abrupt, hysteresis	↑220	3.9(5)	17.4(13)
		↓185	3.5(5)	18.6(12)
11 ([FeL3(bpee)]·MeOH) _n	abrupt, hysteresis	↑244	10.2(12)	42(3)
		↓199	2.7(9)	12.6(16)
16 ([FeL4(bppa)]·MeOH) _n	gradual	↑331	13.0(5)	41(2)

Samples **10** and **11** presents in the SQUID similar spin transitions with hysteresis, however in the case of sample **11**, the hysteresis is almost 20 K broader. In the DSC measurement, the same observation was made. Interestingly, for sample **11** the HS to LS and the LS to HS peaks present a huge discrepancy in their enthalpy and entropy

values. The HS to LS transition upon cooling shows almost no DSC response, with rather small $\Delta H = 2.7(9)$ kJ·mol⁻¹ and $\Delta S = 12.6(16)$ J·mol⁻¹·K⁻¹ values, although the LS to HS transition shows rather big $\Delta H = 10.2(12)$ kJ·mol⁻¹ and $\Delta S = 42(3)$ J·mol⁻¹·K⁻¹ values. Presumably, a supplementary phase transition, i.e. an order-disorder transition, with an endothermic response taking place at the same time as the exothermic HS to LS transition could be responsible for the disappearance of the peak, however it could only be confirmed by X-ray structure determination at different temperatures.

Sample **16** present an asymmetric peak, which reflects the discontinuous behaviour of the spin transition upon heating. Upon cooling, no peaks were observed, because of the very gradual character of the stepwise HS to LS transition after annealing. The enthalpy and entropy values are in agreement with previously reported compounds.^[30,52]

6.2.5 ⁵⁷Fe Mössbauer spectrometry

Room temperature Mössbauer spectra of all samples were taken in order to confirm the spin state obtained from the magnetic measurements and the purity of the materials (e.g. absence of penta-coordinated species). In the SI, Figures 6.15–6.17, Mössbauer spectra from all samples are displayed, and the corresponding hyperfine parameters are listed in Table 6.3. The samples **1**, **4**, **13**, and **15** present a single Fe(II) LS doublet site with typical $\delta \approx 0.34$ mm/s and $\Delta E_Q = 0.90$ – 1.10 mm/s for such octahedral complexes in LS state. Sample **3** is also in the LS state at room temperature, however the signal was fitted with two Fe(II) LS sites as the peaks are asymmetric in intensity and width. The difference between the two sites lies in the quadrupole splitting, with $\Delta E_Q = 0.76(7)$ mm/s for one site, and $\Delta E_Q = 1.04(13)$ mm/s for the other site. Such small changes were already observed and often originate in different conformations of the pyridine rings of the axial ligand (perpendicular or coplanar).^[53,54] Samples **2**, **6**, **7**, **8**, **9**, **10**, **11**, **12**, and **14** show a large doublet site with $\delta \approx 0.90$ mm/s and $\Delta E_Q = 2.10$ – 2.30 mm/s. Those parameters are typical for octahedral HS iron(II) complexes of this ligand type with *N*-heterocycles as axial ligand.^[53,54] Sample **5** presents an Fe(II) HS site and an Fe(II) LS site, as at room temperature the compound is in the middle of a gradual spin transition (see Figure 6.2). The ratio of the HS area is with 65(8)% in good agreement with a γ_{HS}

value of 0.75 at 300 K. In all cases, no indication for pentacoordinated species or N_3O_3 coordinated species is found.

Table 6.3: ^{57}Fe Mössbauer hyperfine parameters of all samples at room temperature.

Compound	Site	δ [mm/s]	ΔE_Q [mm/s]	$\Gamma/2$ [mm/s]	Area [%]
1 $([\text{FeL1}(\text{bipy})]\cdot 2 \text{ MeOH})_n$	Fe(II) LS	0.346(9)	0.875(17)	0.165(12)	100
2 $[\text{FeL1}(\text{bpea})]_n$	Fe(II) HS	0.889(9)	2.239(9)	0.136(7)	100
3 $[\text{FeL1}(\text{bpee})]_n$	Fe(II) LS(1)	0.335(9)	1.04(13)	0.20(2)	59(10)
	Fe(II) LS(2)	0.346(8)	0.76(7)	0.14(4)	41(10)
4 $([\text{FeL1}(\text{bppa})]\cdot \text{MeOH})_n$	Fe(II) LS	0.335(6)	0.785(12)	0.153(8)	100
5 $([\text{FeL2}(\text{bipy})]\cdot 2 \text{ MeOH})_n$	Fe(II) LS	0.38(5)	1.10(10)	0.31(9)	35(8)
	Fe(II) HS	0.94(8)	2.19(10)	0.23(2)	65(8)
6 $([\text{FeL2}(\text{bpea})]\cdot 2 \text{ MeOH})_n$	Fe(II) HS	0.87(2)	2.11(4)	0.17(3)	100
7 $([\text{FeL2}(\text{bpee})]\cdot 2 \text{ MeOH})_n$	Fe(II) HS	0.87(2)	2.06(12)	0.25(9)	100
8 $([\text{FeL2}(\text{bppa})]\cdot 2 \text{ MeOH})_n$	Fe(II) HS	0.86(2)	2.16(13)	0.15(2)	100
9 $[\text{FeL3}(\text{bipy})]_n$	Fe(II) HS	0.95(3)	2.26(5)	0.17(4)	100
10 $([\text{FeL3}(\text{bpea})]\cdot \text{MeOH})_n$	Fe(II) HS	0.95(2)	2.26(2)	0.18(2)	100
11 $([\text{FeL3}(\text{bpee})]\cdot \text{MeOH})_n$	Fe(II) HS	0.94(2)	2.21(2)	0.21(2)	100
12 $[\text{FeL3}(\text{bppa})]_n$	Fe(II) HS	0.95(3)	2.19(2)	0.15(2)	100
13 $[\text{FeL4}(\text{bipy})]_n$	Fe(II) LS	0.33(5)	1.02(7)	0.15(2)	100
14 $[\text{FeL4}(\text{bpea})]_n$	Fe(II) HS	0.93(2)	2.23(2)	0.15(4)	100
15 $([\text{FeL4}(\text{bpee})]\cdot 1.5 \text{ MeOH})_n$	Fe(II) LS	0.33(2)	1.15(8)	0.16(2)	100

6.3 Discussion

Of the sixteen newly synthesised coordination polymers, compounds **1** and **5** shows both a gradual SCO, indication that although a rigid bridging ligand is used, the coordination polymer does not show cooperativity, most likely due to a lack of intermolecular interactions. Compound **14** shows an abrupt spin transition, thus a cooperative phenomenon, but as no crystal structure could be obtained yet, the nature of the intermolecular interactions responsible for this can only be presumed. As no solvent molecules are included in the compound, strong $\text{C-H}\cdots\pi$ and $\text{C-H}\cdots\text{O}$ interactions between the complexes could give rise to cooperativity, as it has been shown for similar mononuclear complexes that such interactions can be the source of abrupt ST.^[38] The coordination polymer **16** showed a very gradual transition around RT that is then shifted 70 K to lower temperatures after annealing. Then the sample exhibits a two-step transition. Such behaviour (two-step SCO or SCO that stops at an intermediate plateau) is very frequently observed for coordination polymers of those Schiff base-like ligands with flexible bridging axial lig-

ands.^[42,45,52,55] Restraining interactions between the polymer chains are made responsible for this observation.^[45]

It was shown for compounds **10** and **11** that the simple substitution of a single bond (bpea) for a double bond (bpee) in the axial ligand leads to an increase of 15 K of the hysteresis width. Indeed, the DSC curves for both samples are quite different, with compound **11** presumably presenting an accompanying phase transition upon the HS to LS transition. This transition could be of order-disorder type, or a crystallographic phase transition as the powder patterns of the HS and LS states change drastically upon SCO. It was already suggested for other systems with wide hysteresis that a crystallographic phase transitions are responsible for such properties.^[2] Moreover, the sample **11** with bpee was less sensitive to a loss of the SCO properties upon annealing, leaving the insight that the included MeOH is not crucial for the exhibition of the wide hysteresis. Interestingly, the cooperative spin transition is observed for the complexes of the ligand L3 with phenyl rings as substituent R. The related mononuclear complex with two pyridines as axial ligands showed an abrupt spin transition due to C–H $\cdots\pi$ and C–H \cdots O interactions. The step from the mononuclear complex to coordination polymers did help to significantly increase the hysteresis width. The hysteresis width is wider than those observed for related 1D chain compounds with phenylene-based Schiff base-like ligands^[45] and in the same order of magnitude as those observed for modified ligands with hydroxyl groups at the phenylene ring.^[46] The extent of the interchain interactions (C–H $\cdots\pi$ and C–H \cdots O) appears to depend on the ratio between the size of the equatorial ligand and the size of the bridging axial ligand. A similar observation was already made for mononuclear complexes of this ligand type.^[40] The results of this work highlight one more time that the synthesis of coordination polymers^[56–58] or networks^[59,60] is highly suitable for obtaining highly cooperative spin crossover complexes.

6.4 Experimental Section

Synthesis Methanol (MeOH) was purified by distillation over Mg under argon atmosphere.^[61] Starting MeOH complexes [**FeL1**(MeOH)₂], [**FeL2**], [**FeL3**], and [**FeL4**

(**MeOH**)₂] were synthesised as described in literature.^[38] 4,4'-Bipyridine (**bipy**) (Alfa Aesar, 99,9%), 1,2-Bis(4-pyridiyl)ethane (**bpea**) (Aldrich, 99%), 1,2-Bis(4-pyridiyl)ethylene (**bpee**) (Aldrich, 98%), and 1,3-Bis(4-pyridiyl)propane (**bppa**) (Alfa Aesar, 97%) were used without further purification. All syntheses with iron(II) were carried out under argon using Schlenk tube techniques. CHN analyses were measured with a Vario El III from Elementar Analysen-Systeme. Mass spectra were recorded with a Finnigan MAT 8500 with a data system MASPEC II. Samples were dissolved in an acetonitrile-methanol mixture. IR spectra were recorded with a Perkin Elmer Spectrum 100 FT-IR spectrometer.

[FeL1(bipy)]·2 MeOH_n (**1**) **[FeL1(MeOH)₂]** (0.2 g) and **bipy** (0.6 g) were dissolved in 20 mL MeOH. After stirring the red solution for a few minutes, a dark purple crystalline precipitate appeared. The suspension was heated to reflux during 1 hour, then allowed to cool down. The purple crystalline precipitate was filtered off, and dried *in vacuo*. Yield: 0.14 g (63 %). IR: $\tilde{\nu} = 3250(\text{b})$ (OH), 1623(s) (CO), 1584(s) (CO) cm⁻¹; MS (DEI-(+), 70 eV) m/z (%): 492 (100) ([FeL1]⁺), 156 (43) (bipy⁺); elemental analysis calculated (found) for C₃₆H₄₀FeN₄O₈ (712.57 g/mol): C 60.48 (60.67), H 5.65 (4.88), N 7.86 (7.62).

[FeL1(bpea)]_n (**2**) **[FeL1(MeOH)₂]** (0.2 g) and **bpea** (0.7 g) were dissolved in 20 mL MeOH. The red solution was heated to reflux during 1 hour then allowed to cool down. Upon cooling, a red powder precipitated. The red powder was filtered off, and dried *in vacuo*. Yield: 0.08 g (33 %). IR: $\tilde{\nu} = 1617(\text{s})$ (CO), 1576(s) (CO) cm⁻¹; MS (DEI-(+), 70 eV) m/z (%): 492 (18) ([FeL1]⁺), 184 (100) (bpea⁺); elemental analysis calculated (found) for C₃₆H₃₆FeN₄O₆ (676.54 g/mol): C 63.91 (63.75), H 5.36 (4.96), N 8.28 (8.01).

[FeL1(bpee)]_n (**3**) **[FeL1(MeOH)₂]** (0.2 g) and **bpee** (0.66 g) were dissolved in 20 mL MeOH. After stirring the red solution for a few minutes, a dark purple crystalline precipitate appeared. The suspension was heated to reflux during 1 hour then allowed to cool down. The purple powder was filtered off, and dried *in vacuo*. Yield: 0.09 g (34 %). IR: $\tilde{\nu} = 1625(\text{s})$ (CO), 1598(s) (CO) cm⁻¹; MS (DEI-(+), 70 eV) m/z (%): 492 (18) ([FeL1]⁺), 182 (100) (bpee⁺); elemental analysis calculated (found) for C₃₆H₃₄FeN₄O₆ (674.52 g/mol): C 64.10 (63.79), H 5.08 (4.86), N 8.31 (8.25).

([FeL1(bppa)]·MeOH)_n (4) [FeL1(MeOH)₂] (0.2 g) and **bppa** (0.7 g) were dissolved in 20 mL MeOH. The red solution was heated to reflux during 1 hour, and then allowed to cool down. Upon cooling, a dark red crystalline precipitate appeared. The dark red crystalline precipitate was filtered off, and dried **in vacuo**. Yield: 0.04 g (16 %). IR: $\tilde{\nu} = 3264(\text{b})$ (OH), 1631(s) (CO), 1579(s) (CO) cm⁻¹; MS (DEI-(+), 70 eV) m/z (%): 492 (48) ([FeL1]⁺), 198 (100) (bppa⁺); elemental analysis calculated (found) for C₃₈H₄₂FeN₄O₇ (722.61 g/mol): C 63.16 (62.57), H 5.858 (5.281), N 7.753 (7.652).

([FeL2(bipy)]·MeOH)_n (5) [FeL2] (0.2 g) and **bipy** (0.7 g) were dissolved in 20 mL MeOH. The red solution was heated to reflux during 1 hour, and then allowed to cool down. Upon cooling, a dark pink crystalline precipitate appeared. The dark pink crystalline precipitate was filtered off, and dried *in vacuo*. Yield: 0.25 g (88 %). IR: $\tilde{\nu} = 3241(\text{b})$ (OH), 1636(s) (CO), 1589(s) (CO) cm⁻¹; MS (DEI-(+), 70 eV) m/z (%): 432 (37) ([FeL2]⁺), 156 (100) (bipy⁺); elemental analysis calculated (found) for C₃₃H₃₂FeN₄O₅ (620.48 g/mol): C 63.88 (63.12), H 5.20 (4.62), N 9.02 (9.245).

([FeL2(bpea)]·2 MeOH)_n (6) : [FeL2] (0.2 g) and **bpea** (0.85) were dissolved in 20 mL MeOH. The red solution was heated to reflux during 1 hour, and then allowed to cool down. Upon cooling, a brown powder precipitated. The brown powder was filtered off, and dried *in vacuo*. Yield: 0.19 g (60 %). IR: $\tilde{\nu} = 3256(\text{b})$ (OH), 1617(s) (CO), 1596(s) (CO) cm⁻¹; MS (DEI-(+), 70 eV) m/z (%): 432 (17) ([FeL2]⁺), 184 (100) (bpea⁺); elemental analysis calculated (found) for C₃₆H₄₀FeN₄O₆ (680.57 g/mol): C 63.53 (63.45), H 5.92 (4.66), N 8.23 (8.09).

([FeL2(bpee)]·2 MeOH)_n (7) [FeL2] (0.2 g) and **bpee** (0.84 g) were dissolved in 20 mL MeOH. The brown solution was heated to reflux during 1 hour, and then allowed to cool down. Upon cooling, a purple powder precipitated. The purple powder was filtered off, and dried *in vacuo*. Yield: 0.27 g (95 %). IR: $\tilde{\nu} = 3265(\text{b})$ (OH), 1604(s) (CO), 1586(s) (CO) cm⁻¹; MS (DEI-(+), 70 eV) m/z (%): 432 (65) ([FeL2]⁺), 182 (100) (bpee⁺); elemental analysis calculated (found) for C₃₆H₃₈FeN₄O₆ (678.55 g/mol): C 63.72 (63.41), H 5.64 (4.57), N 8.26 (7.93).

(**[FeL2(bppa)]·2 MeOH**)_n (**8**) **[FeL2]** (0.15 g) and **bppa** (0.7 g) were dissolved in 20 mL MeOH. The brown solution was heated to reflux during 1 hour, and then allowed to cool down. Upon cooling, a brown powder precipitated. The brown powder was filtered off, and dried *in vacuo*. Yield: 0.11 g (45 %). IR: $\tilde{\nu} = 3267(\text{b})$ (OH), 1611(s) (CO), 1587(s) (CO) cm^{-1} ; MS (DEI-(+), 70 eV) m/z (%): 432 (32) (**[FeL2]⁺**), 198 (100) (**bpee⁺**); elemental analysis calculated (found) for $\text{C}_{37}\text{H}_{42}\text{FeN}_4\text{O}_6$ (694.60 g/mol): C 63.98 (63.36), H 6.09 (5.25), N 8.07 (7.99).

[FeL3(bipy)]_n (**9**) **[FeL3]** (0.2 g) and **bipy** (0.6 g) were dissolved in 20 mL MeOH. The red solution was heated to reflux during 1 hour, then allowed to cool down. Upon cooling, a dark purple crystalline precipitate appeared. The dark purple crystalline precipitate was filtered off, and dried *in vacuo*. Yield: 0.09 g (35 %). IR: $\tilde{\nu} = 1640(\text{s})$ (CO), 1598(s) (CO) cm^{-1} ; MS (DEI-(+), 70 eV) m/z (%): 556 (4) (**[FeL3]⁺**), 156 (100) (**bipy⁺**); elemental analysis calculated (found) for $\text{C}_{42}\text{H}_{32}\text{FeN}_4\text{O}_4$ (712.57 g/mol): C 70.79 (70.08), H 4.52 (3.7), N 7.86 (8.16).

(**[FeL3(bpea)]·MeOH**)_n (**10**) **[FeL3]** (0.2 g) and **bpea** (0.85 g) were dissolved in 20 mL MeOH. The red solution was heated to reflux during 1 hour, then allowed to cool down. Upon cooling, a brown crystalline precipitate appeared. The brown crystals was filtered off, and dried *in vacuo*. Yield: 0.18 g (65 %). IR: $\tilde{\nu} = 3254(\text{b})$ (OH), 1601(s) (CO), 1587(s) (CO) cm^{-1} ; MS (DEI-(+), 70 eV) m/z (%): 556 (68) (**[FeL3]⁺**), 184 (100) (**bpea⁺**); elemental analysis calculated (found) for $\text{C}_{45}\text{H}_{40}\text{FeN}_4\text{O}_5$ (772.67 g/mol): C 69.95 (69.88), H 5.22 (4.43), N 7.25 (7.49).

(**[FeL3(bpee)]·MeOH**)_n (**11**) **[FeL3]** (0.2 g) and **bpee** (0.66 g) were dissolved in 20 mL MeOH. The red solution was heated to reflux during 1 hour, and then allowed to cool down. Upon cooling, a purple crystalline precipitate appeared. The dark purple crystals was filtered off, and dried *in vacuo*. Yield: 0.20 g (75 %). IR: $\tilde{\nu} = 3221(\text{b})$ (OH), 1603(s) (CO), 1592(s) (CO) cm^{-1} ; MS (DEI-(+), 70 eV) m/z (%): 556 (68) (**[FeL3]⁺**), 182 (100) (**bpee⁺**); elemental analysis calculated (found) for $\text{C}_{45}\text{H}_{38}\text{FeN}_4\text{O}_5$ (770.57 g/mol): C 70.13 (69.46), H 4.97 (5.125), N 7.27 (7.12).

[FeL3(bppa)]_n (12) **[FeL3]** (0.2 g) and **bppa** (0.66 g) were dissolved in 20 mL MeOH. The red solution was heated to reflux during 1 hour, and then allowed to cool down. Upon cooling, a purple crystalline precipitate appeared. The dark purple crystals were filtered off, and dried *in vacuo*. Yield: 0.03 g (8 %). IR: $\tilde{\nu} = 1604(\text{s})$ (CO), $1585(\text{s})$ (CO) cm^{-1} ; MS (DEI-(+), 70 eV) *m/z* (%): 556 (24) (**[FeL3]⁺**), 198 (100) (**bppa⁺**); elemental analysis calculated (found) for $\text{C}_{45}\text{H}_{38}\text{FeN}_4\text{O}_4$ (754.65 g/mol): C 71.62 (71.87), H 5.08 (4.76), N 7.42 (7.39).

[FeL4(bipy)]_n (13) **[FeL4(MeOH)₂]** (0.2 g) and **bipy** (0.6 g) were dissolved in 20 mL MeOH. After stirring the red solution for a few minutes, a dark purple crystalline precipitate appeared. The suspension was heated to reflux during 1 hour, and then allowed to cool down. The purple crystalline precipitate was filtered off, and dried *in vacuo*. Yield: 0.2 g (56 %). IR: $\tilde{\nu} = 3214(\text{b})$ (OH), $1609(\text{s})$ (CO), $1576(\text{s})$ (CO) cm^{-1} ; MS (DEI-(+), 70 eV) *m/z* (%): 464 (100) (**[FeL4]⁺**), 156 (5) (**bipy⁺**); elemental analysis calculated (found) for $\text{C}_{32}\text{H}_{28}\text{FeN}_4\text{O}_6$ (620.43 g/mol): C 61.95 (61.76), H 4.55 (4.08), N 9.03 (8.86).

[FeL4(bpea)]_n (14) **[FeL4(MeOH)₂]** (0.2 g) and **bpea** (0.6 g) were dissolved in 20 mL MeOH. After stirring the red solution for a few minutes, a dark purple crystalline precipitate appeared. The suspension was heated to reflux during 1 hour, and then allowed to cool down. The purple crystalline precipitate was filtered off, and dried *in vacuo*. Yield: 0.16 g (61 %). IR: $\tilde{\nu} = 3278(\text{b})$ (OH), $1612(\text{s})$ (CO), $1589(\text{s})$ (CO) cm^{-1} ; MS (DEI-(+), 70 eV) *m/z* (%): 464 (47) (**[FeL4]⁺**), 184 (100) (**bpea⁺**); elemental analysis calculated (found) for $\text{C}_{34}\text{H}_{32}\text{FeN}_4\text{O}_6$ (648.49 g/mol): C 62.97 (62.64), H 4.97 (4.58), N 8.64 (8.60).

([FeL4(bpee)]·1.5 MeOH)_n (15) **[FeL4(MeOH)₂]** (0.2 g) and **bpee** (0.7 g) were dissolved in 20 mL MeOH. After stirring the red solution for a few minutes, a dark blue crystalline precipitate appeared. The suspension was heated to reflux during 1 hour, and then allowed to cool down. The blue crystalline precipitate was filtered off, and dried *in vacuo*. Yield: 0.19 g (70 %). IR: $\tilde{\nu} = 3221(\text{b})$ (OH), $1630(\text{s})$ (CO), $1589(\text{s})$ (CO) cm^{-1} ; MS (DEI-(+), 70 eV) *m/z* (%): 464 (69) (**[FeL4]⁺**), 182 (100) (**bpee⁺**); elemental analysis calculated (found) for $\text{C}_{35.5}\text{H}_{36}\text{FeN}_4\text{O}_{7.5}$ (694.53 g/mol): C 61.39 (60.88), H 5.22 (4.71), N 8.07 (8.02).

([FeL4(bppa)]·MeOH)_n (**16**) [FeL4(MeOH)₂] (0.2 g) and **bppa** (0.7 g) were dissolved in 20 mL MeOH. The red solution was heated to reflux during 1 hour, and then allowed to cool down. Upon cooling, a dark purple crystalline precipitate appeared. The dark purple crystalline precipitate was filtered off, and dried *in vacuo*. Yield: 0.1 g (35 %). IR: $\tilde{\nu} = 3236(\text{b})$ (OH), 1624(s) (CO), 1589(s) (CO) cm⁻¹ ; MS (DEI-(+), 70 eV) m/z (%): 464 (78) ([FeL4]⁺), 198 (100) (bppa⁺); elemental analysis calculated (found) for C₃₆H₃₈FeN₄O₇ (694.55 g/mol): C 63.45 (63.12), H 5.17 (4.89), N 8.46 (8.35).

Thermo-gravimetric analysis Thermo-gravimetric analyses were recorded with a TGA250 instrument from TA instruments at a heating rate of 10 K·min⁻¹ under nitrogen flow. The temperature was first increased to 65°C (boiling point methanol, drop of the sample mass for all samples) and then kept at this temperature for one hour to check if with time a further mass loss is detected. For the samples **11** and **16**, no change is observed and in the case of **5** a slight drop is observed. The increase of the sample mass in the case of **1** and **10** with time is most likely due to a slight oxidation of the sample in the instrument. A complete removal of the included Methanol is only observed after heating the sample above 65°C.

X-ray Powder Diffraction Powder diffractograms were measured with a STOE StadiP Powder Diffractometer (STOE, Darmstadt) using Cu[K α 1] radiation with a Ge Monochromator, and a Mythen 1K Strip detector in transmission geometry.

Differential Scanning Calorimetry Calorimetric measurements were carried out with a differential scanning calorimeter DSC821e from Mettler Toledo, with a scan rate of 5 K·min⁻¹.

Mössbauer spectrometry ⁵⁷Fe Mössbauer spectra were recorded in transmission geometry on a constant-acceleration using a conventional Mössbauer spectrometer with a 50 mCi ⁵⁷Co(Rh) source. The samples were sealed in the sample holder under an argon atmosphere. The spectra were fitted using Recoil 1.05 Mössbauer Analysis Software.^[62] The isomer shift values are given with respect to α -Fe as reference at room temperature.

Scanning Electron Microscopy Scanning electron microscopy pictures were gathered at a Zeiss LEO 1530. Samples were prepared on carbon tape.

Magnetic Measurements Magnetic susceptibility data were collected using a MPMS XL-5 SQUID magnetometer under an applied field of 0.5 T over the temperature range 2 to 400 K in the settle mode. The samples were placed in gelatine capsules held within a plastic straw. The data were corrected for the diamagnetic contributions of the ligands by using tabulated Pascal's constants and of the sample holder.^[63]

6.5 Conclusions

For two of the 1D chain compounds discussed here 28 and 40 K wide hysteresis loops were observed that are stable for several cycles. An increase of the hysteresis width compared to related 1D chain compounds with phenylene-based Schiff base-like ligands is observed. The cooperative interactions are in the same order of magnitude as those observed for modified ligands with hydroxyl groups at the phenylene ring. Thus the introduction of the extended π -system in combination with the synthesis of coordination polymers was successfully used for the rational design of SCO complexes with cooperative spin transition.

Acknowledgements

Financial supports from the German Science foundation (SFB840; project A10) and the University of Bayreuth are acknowledged.

6.6 Supporting Information

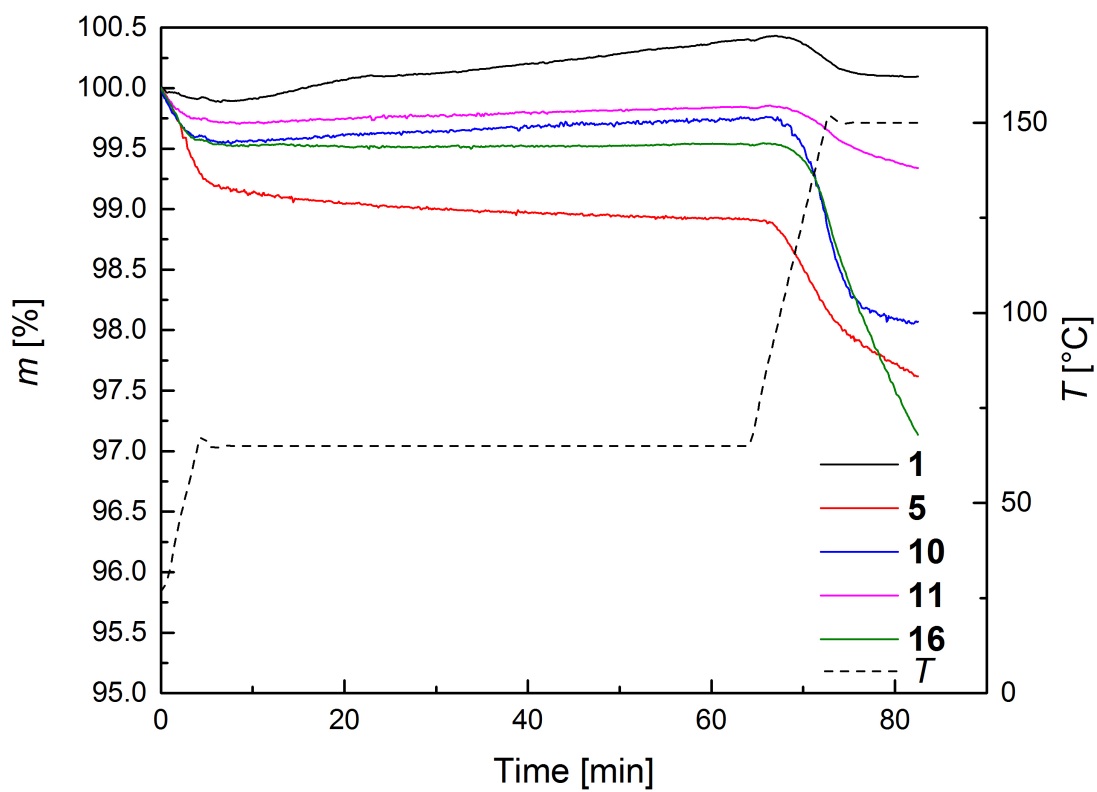
Figure 6.6: TGA measurements of samples **1**, **5**, **10**, **11**, and **16**.

Figure 6.7: Magnetic susceptibility measurements of compounds **2**, **6**, **7**, **8**, **9**, and **12**, displayed between 10 K and 300 K.

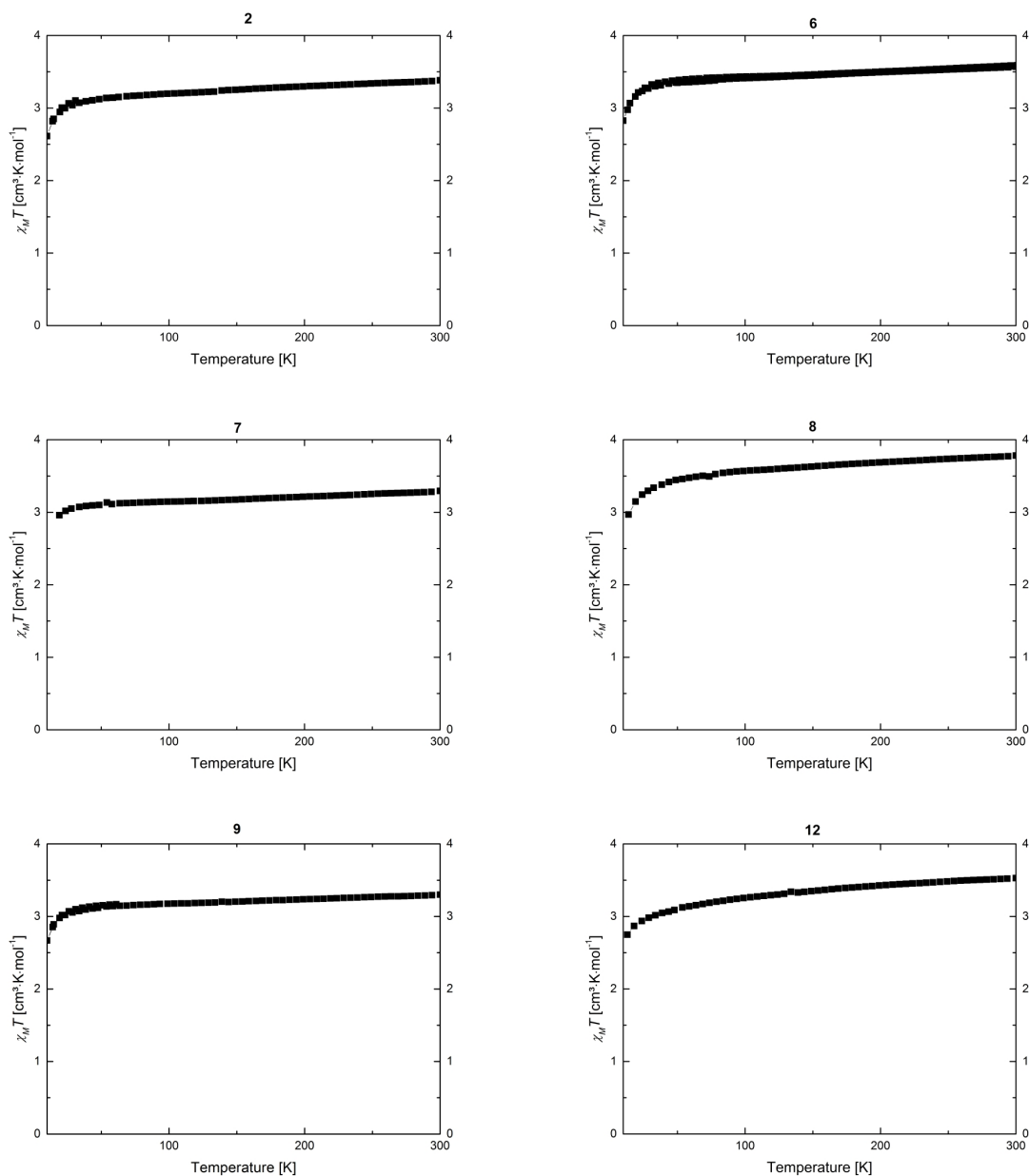


Figure 6.8: Magnetic susceptibility measurements of compounds **3**, **4**, **13**, and **15**, displayed between 10 K and 300 K.

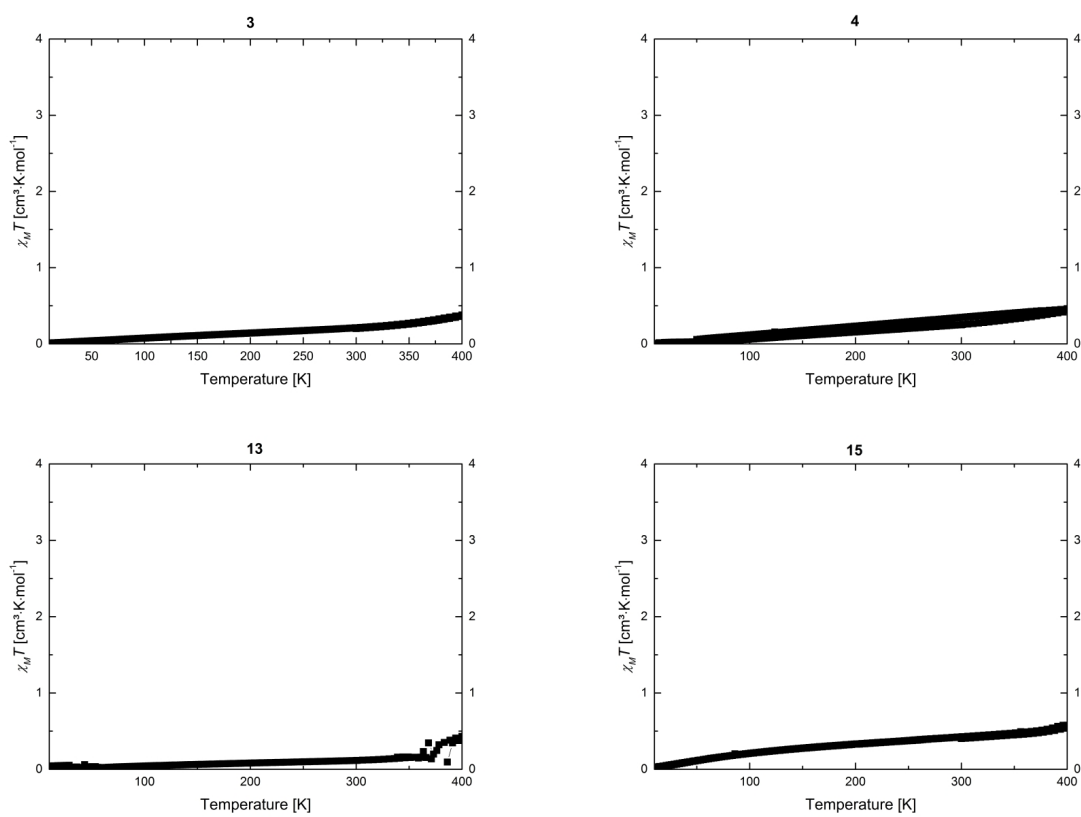


Figure 6.9: Powder diffraction patterns of samples 2, 3, 4, 6, 7, 8, 9, 12, 13, and 15 at room temperature.

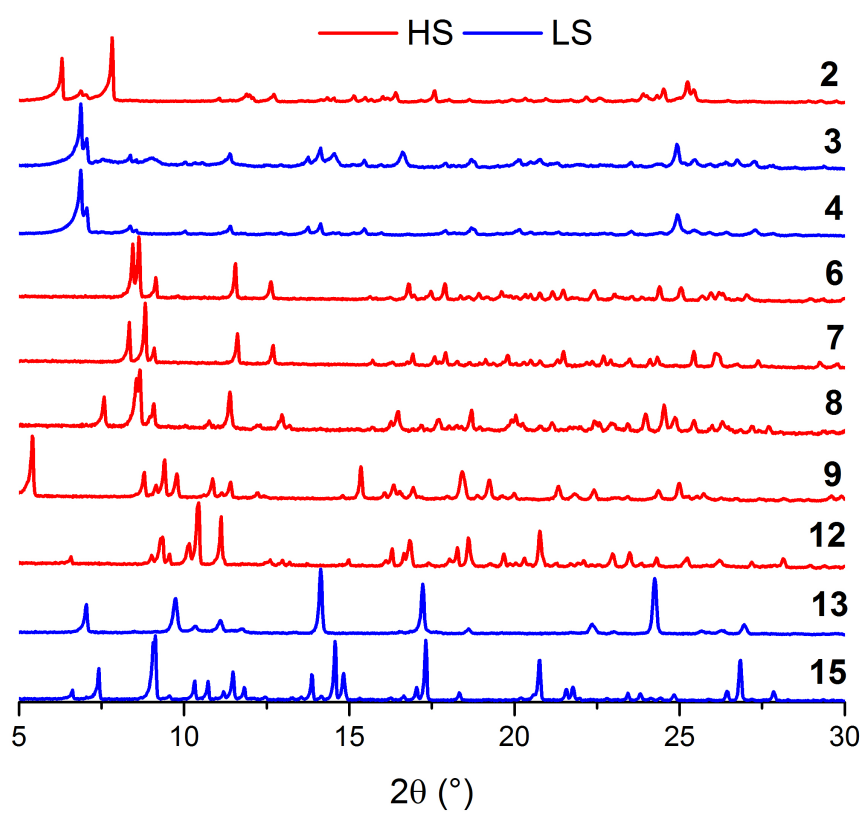


Figure 6.10: DSC plots of samples **1**, **5**, **10**, **11**, and **16**. Peak temperatures are indicated on the graphs, as well as the scanning direction.

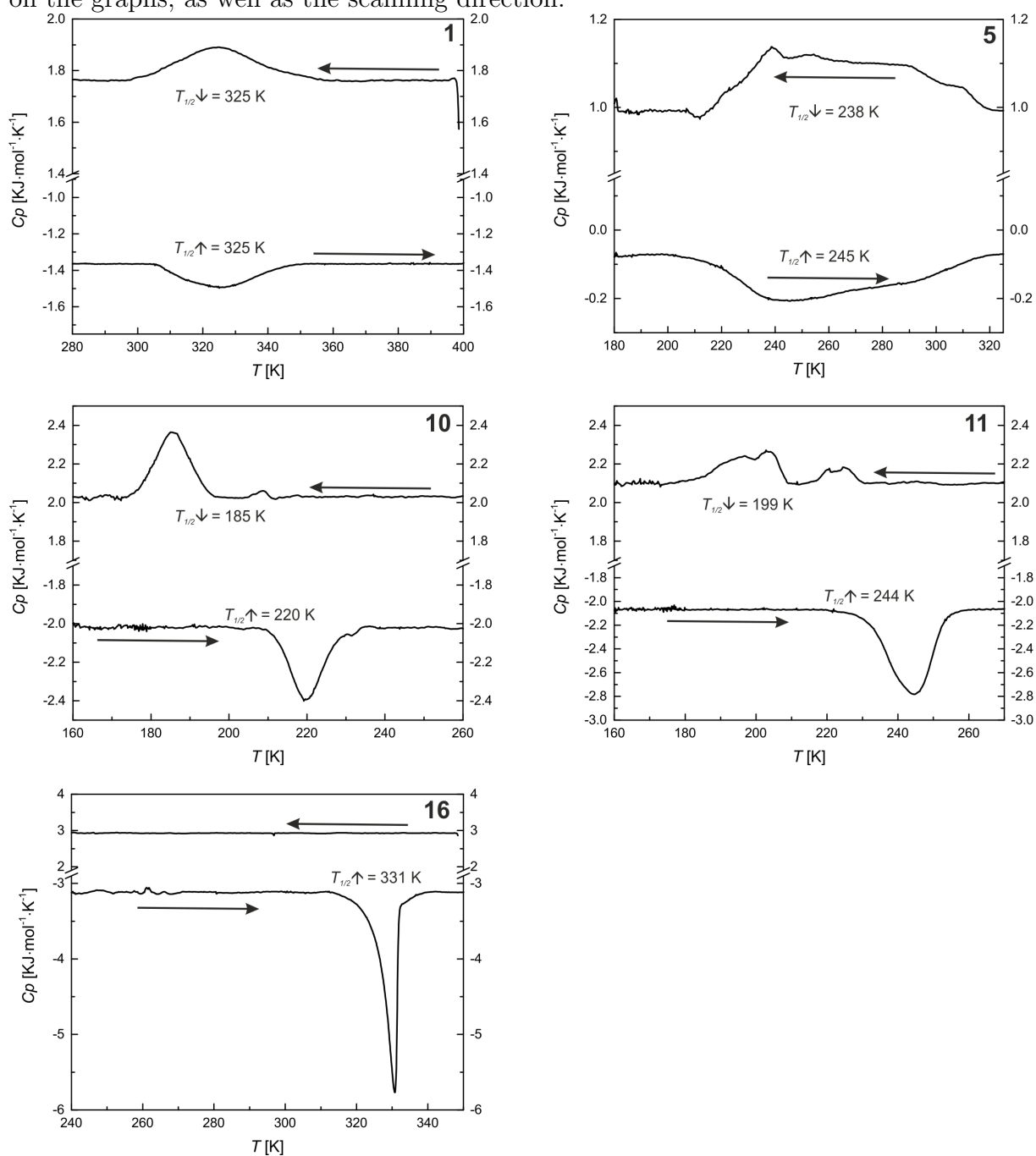


Figure 6.11: Scanning electron microscopy images of samples 1–4.

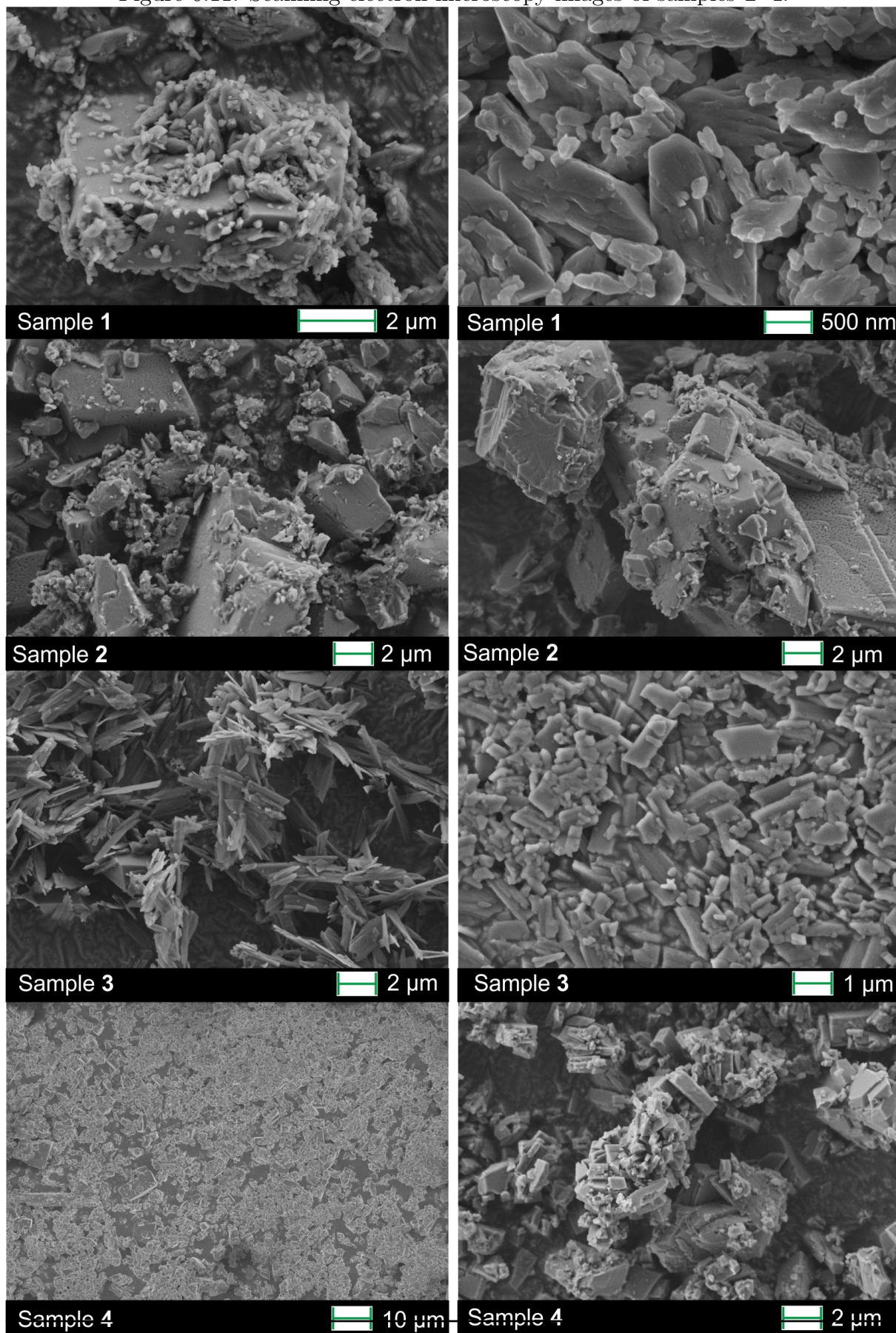


Figure 6.12: Scanning electron microscopy images of samples 5–8.

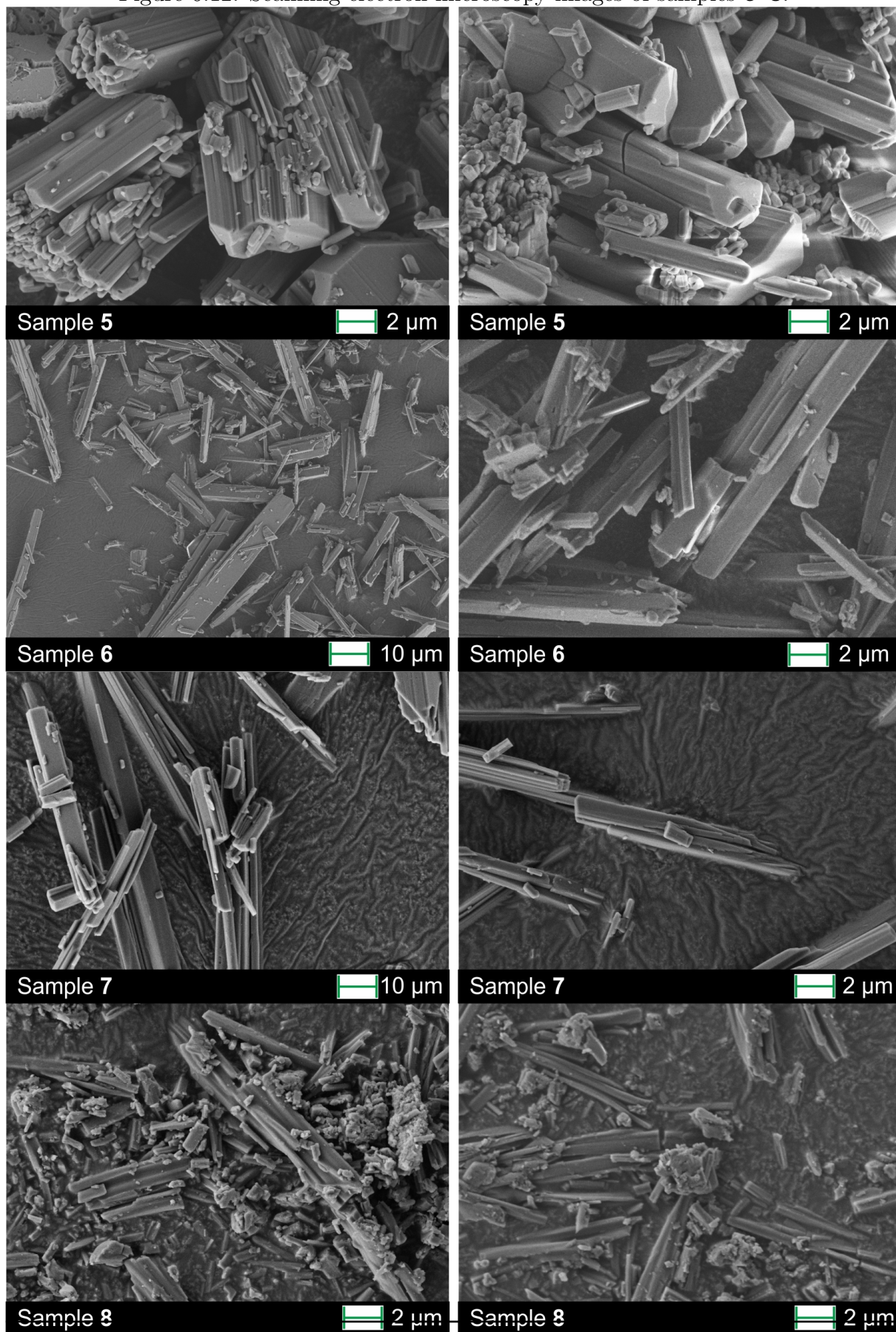


Figure 6.13: Scanning electron microscopy images of samples 9–12.

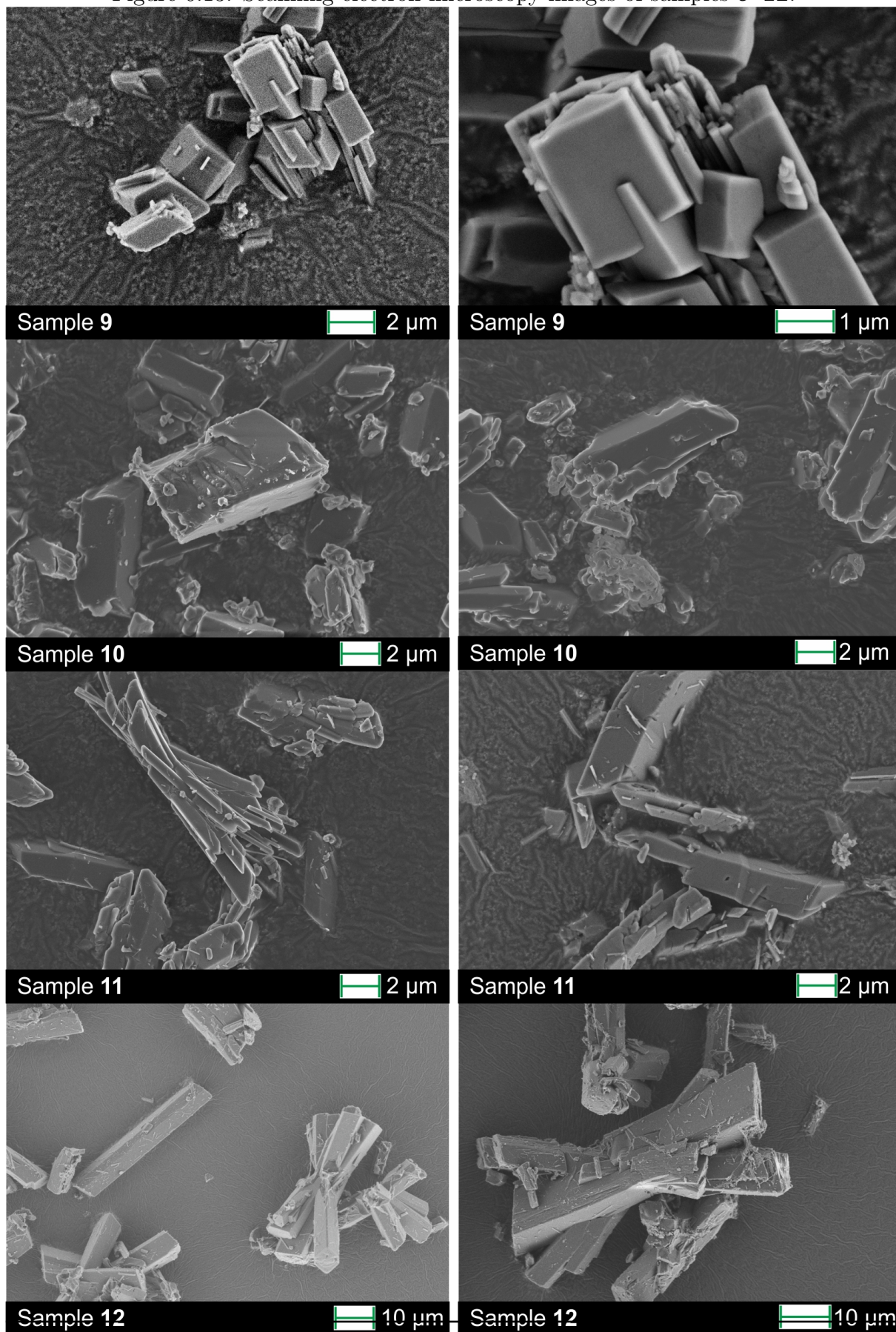


Figure 6.14: Scanning electron microscopy images of samples 13–16.

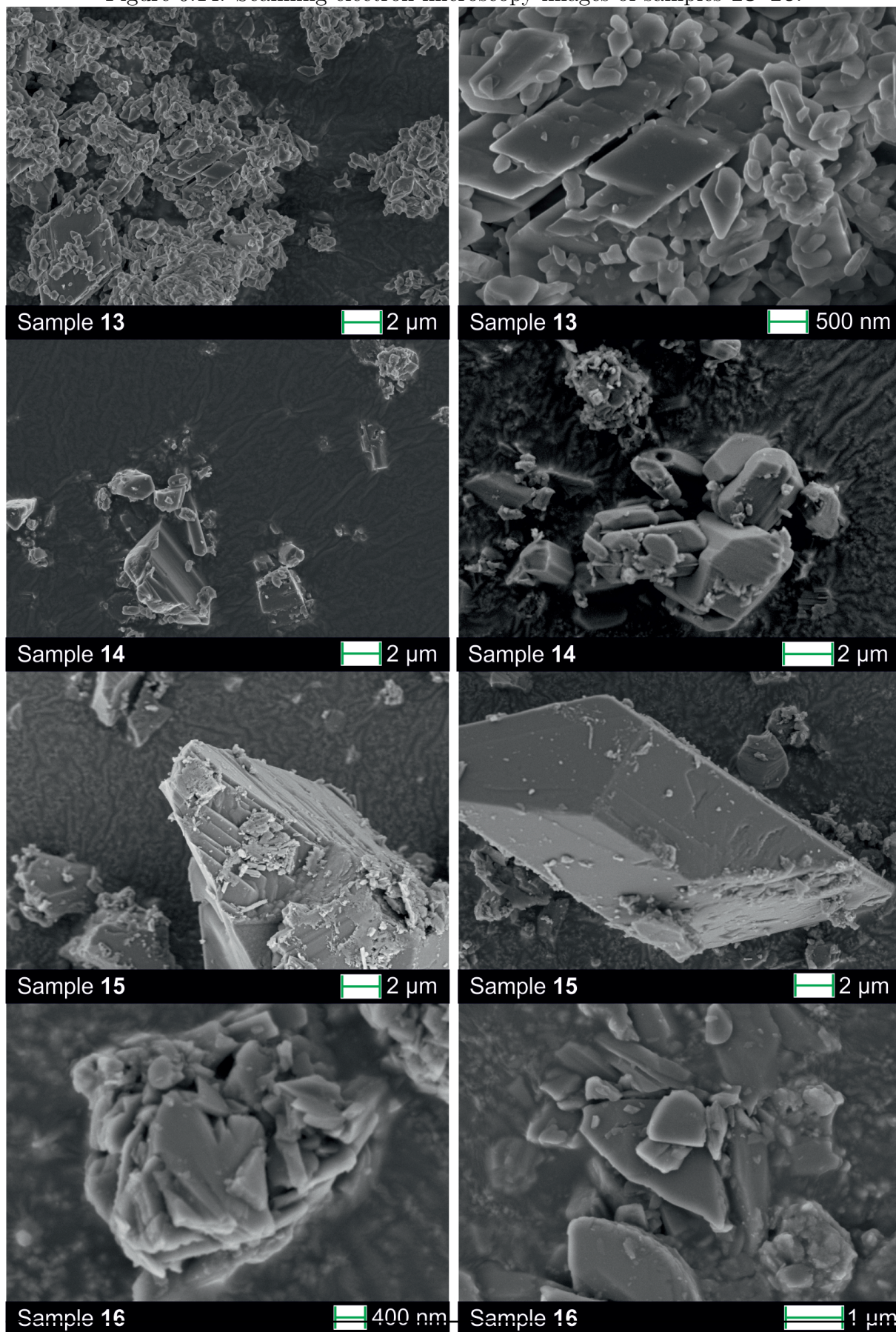


Figure 6.15: Mössbauer spectra of samples 1–6 at room temperature.

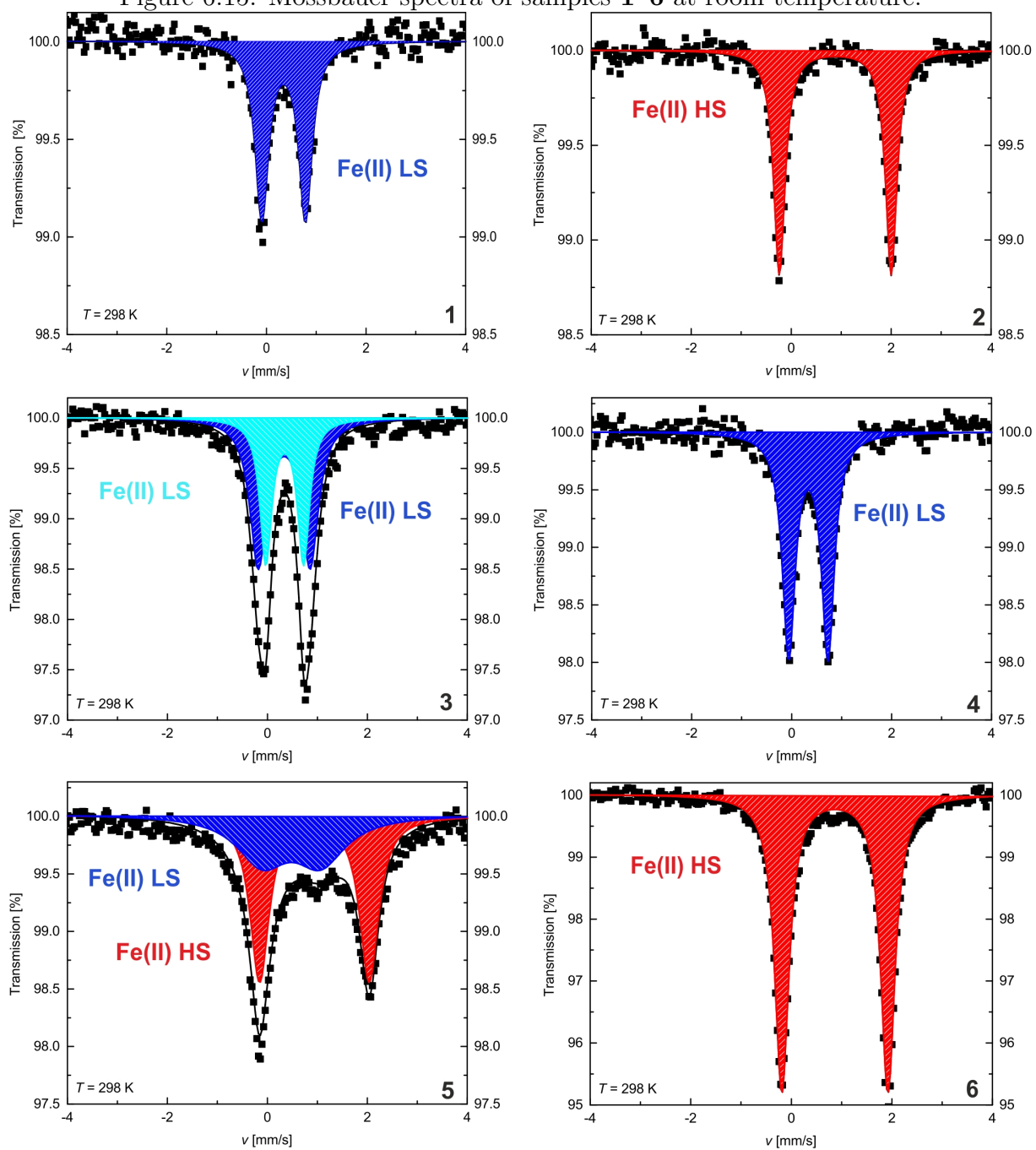


Figure 6.16: Mössbauer spectra of samples 7–12 at room temperature.

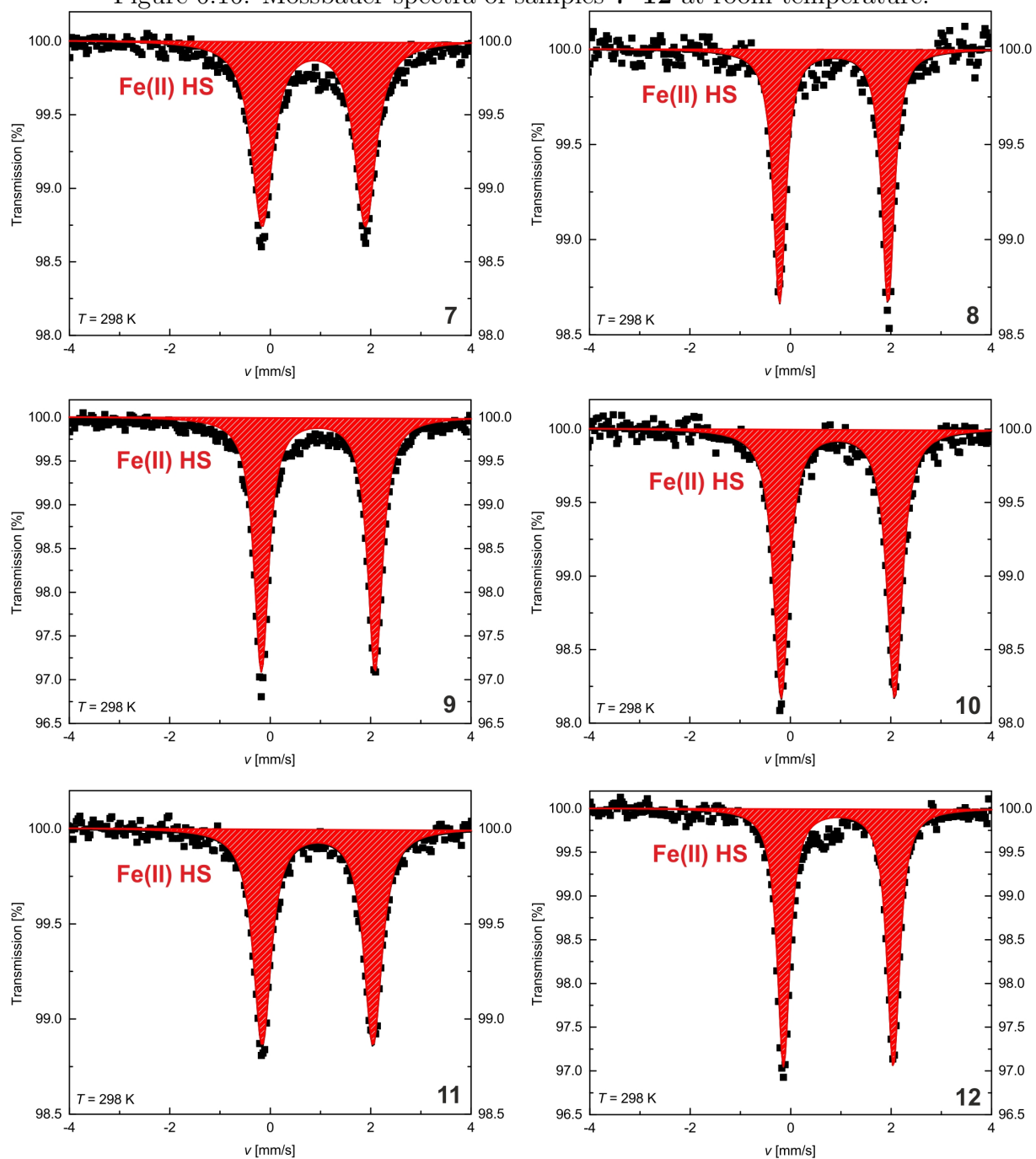
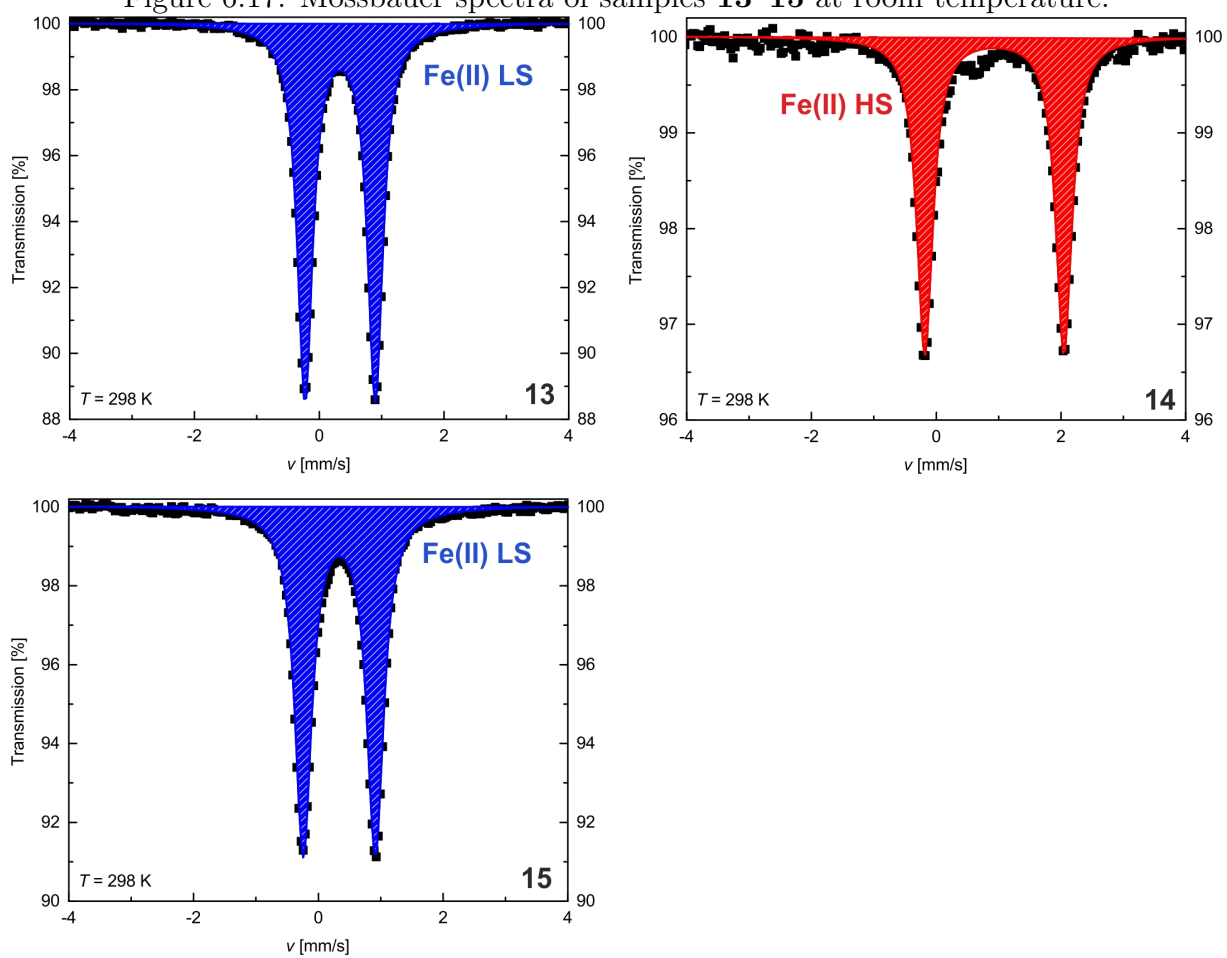


Figure 6.17: Mössbauer spectra of samples **13–15** at room temperature.

References

- [1] M. Halcrow, *Spin-Crossover Materials*, John Wiley & Sons Ltd., Chichester, UK, **2013**.
- [2] M. A. Halcrow, *Chem. Soc. Rev.* **2011**, *40*, 4119–4142.
- [3] P. Gülich, H. Goodwin, *Spin Crossover in Transition Metal Compounds I-III*, Springer, Berlin, DE, **2004**.
- [4] A. Bousseksou, G. Molnar, L. Salmon, W. Nicolazzi, *Chem. soc. Rev.* **2011**, *40*, 3313–3335.
- [5] M. C. Muñoz, J. A. Real, *Coord. Chem. Rev.* **2011**, *255*, 2068–2093.
- [6] J. Olguín, S. Brooker, *Coord. Chem. Rev.* **2011**, *255*, 203–240.
- [7] A. B. Koudriavstsev, W. Linert, *J. Struct. Chem.* **2010**, *51*, 335–365.
- [8] S. Brooker, J. A. Kitchen, *Dalton Trans.* **2009**, 7331–7340.
- [9] J. Klingele, D. Kaase, M. Schmucker, Y. Lan, G. Chastanet, J.-F. Létard, *Inorg. Chem.* **2013**, *52*, 6000–6010.
- [10] S. Heider, H. Petzold, G. Chastanet, S. Schlamp, T. Rüffer, B. Weber, *Dalton Trans.* **2013**, *47*, 8575–8584.
- [11] S. K. Hain, F. W. Heinemann, K. Gieb, P. Müller, G. Hörner, A. Grohmann, *Eur. J. Inorg. Chem.* **2010**, 221–232.
- [12] M. Milek, F. Heinemann, M. M. Khusniyarov, *Inorg. Chem.* **2013**, *52*, 11585–11592.
- [13] K. S. Murray, *Aust. J. Chem.* **2009**, *62*, 1081–1101.
- [14] A. Gaspar, M. Seredyuk, P. Gülich, *J. Mol. Struct.* **2009**, *924–926*, 9–19.
- [15] J.-F. Létard, *J. Mater. Chem.* **2006**, *16*, 2550–2559.
- [16] O. Sato, J. Tao, Y.-Z. Zhang, *Angew. Chem. Int. Ed.* **2007**, *46*, 2152–2187.
- [17] B. Weber, *Spin-Crossover Materials*, John Wiley & Sons Ltd., Chichester, UK, **2013**.
- [18] P. Stock, N. Spintig, J. Scholz, J. D. Epping, C. Oelsner, D. Wiedemann, A. Grohmann, G. Hörner, *J. Coord. Chem.* **2015**, *68*, 3099–3115.
- [19] J. Linares, E. Codjovi, Y. Garcia, *Sensors* **2012**, *12*, 4492–4479.
- [20] O. Kahn, C. Jay, J. Krober, R. Claude, F. Groliere, *EP0666561*, **1995**.

-
- [21] O. Kahn, *Science* **1998**, *279*, 44–48.
- [22] J.-F. Létard, P. Guionneau, L. Goux-Capes, *Spin Crossover in Transition Metal Compounds I-III*, Springer, Berlin, DE, **2004**.
- [23] A. B. Galet, A. and Gaspar, M. C. Muñoz, G. V. Bukin, G. Levchenko, J. A. Real, *Adv. Mater.* **2005**, *17*, 2949–2953.
- [24] M. Seredyuk, M. C. Muñoz, M. Castro, T. Romero-Morcillo, A. B. Gaspar, J. A. Real, *Chem. Eur. J.* **2013**, *19*, 6591–6596.
- [25] A. B. Gaspar, M. Seredyuk, *Coord. Chem. Rev.* **2014**, *268*, 41–58.
- [26] P. Brown, A. Bushmelev, C. P. Butts, J. Cheng, J. Eastoe, I. Grillo, R. K. Heenan, A. M. Schmidt, *Angew. Chem. Int. Ed.* **2012**, *51*, 2414–2416.
- [27] C. Gandolfi, G. G. Morgan, M. Albrecht, *Dalton Trans.* **2012**, *41*, 3726–3730.
- [28] C. M. Quintero, I. A. Gural'skiy, L. Salmon, G. Molnar, C. Bergaud, A. Bousseksou, *J. Mater. Chem.* **2012**, *22*, 3745–3751.
- [29] Y. Raza, F. Volatron, S. Moldovan, O. Ersen, V. Huc, C. Martini, F. Brisset, A. Gloter, O. Stephan, A. Bousseksou, L. Catala, T. Mallah, *Chem. Commun.* **2011**, *47*.
- [30] C. Lochenie, W. Bauer, A. P. Railliet, S. Schlamp, Y. Garcia, B. Weber, *Inorg. Chem.* **2014**, *53*, 11563–11572.
- [31] B. Weber, W. Bauer, T. Pfaffeneder, M. M. Dîrtu, A. D. Naik, A. Rotaru, Y. Garcia, *Eur. J. Inorg. Chem.* **2011**, 3193–3206.
- [32] W. Bauer, S. Schlamp, B. Weber, *Chem. Commun.* **2012**, *48*, 10222.
- [33] J. A. Real, A. B. Gaspar, V. Niel, M. C. Muñoz, *Coord. Chem. Rev.* **2003**, *236*, 121–141.
- [34] J. Linares, H. Spiering, F. Varret, *Eur. Phys. J. B* **1999**, *10*, 271–275.
- [35] D. Chiruta, C.-M. Jureschi, J. Linares, Y. Garcia, A. Rotaru, *J. Appl. Phys.* **2014**, *115*, 053523.
- [36] Z. J. Zhong, J.-Q. Tao, Z. Yu, C.-Y. Dun, Y.-J. Liu, X.-Z. You, *J. Chem. Soc., Dalton Trans.* **1998**, 327–328.
- [37] J.-F. Létard, P. Guionneau, E. Coddjovi, O. Lavastre, G. Bravic, D. Chasseau, O. Kahn, *J. Am. Chem. Soc.* **1997**, *119*, 10861–10862.
- [38] C. Lochenie, J. Heinz, W. Milius, B. Weber, *Dalton Trans.* **2015**, *44*, 18065–18077.
-

-
- [39] B. Weber, E. S. Kaps, C. Desplanches, J.-F. Létard, *Eur. J. Inorg. Chem.* **2008**, 2963–2966.
- [40] B. Weber, E. S. Kaps, C. Desplanches, J.-F. Létard, *Eur. J. Inorg. Chem.* **2008**, 4891–4898.
- [41] B. Weber, E. S. Kaps, J. Weigand, C. Carbonera, J.-F. Létard, K. Achterhold, F. G. Parak, *Inorg. Chem.* **2008**, *47*, 487–496.
- [42] C. Baldé, W. Bauer, E. Kaps, S. Neville, C. Desplanches, G. Chastanet, B. Weber, J.-F. Létard, *Eur. J. Inorg. Chem.* **2013**, 2744–2750.
- [43] R. Kulmaczewski, J. Olguin, J. A. Kitchen, H. L. C. Feltham, G. N. L. Jameson, J. L. Tallon, S. Brooker, *J. Am. Chem. Soc.* **2014**, *136*, 878–881.
- [44] B. Weber, R. Tandon, D. Himsl, *Z. Anorg. Allg. Chem.* **2007**, *633*, 1159–1162.
- [45] W. Bauer, W. Scherer, S. Altmannshofer, B. Weber, *Eur. J. Inorg. Chem.* **2011**, 2803–2818.
- [46] W. Bauer, C. Lochenie, B. Weber, *Dalton Trans.* **2014**, *43*, 1990–1999.
- [47] O. Roubeau, *Chem. Eur. J.* **2012**, *18*, 15230–15244.
- [48] M. Carmen Muñoz, J. A. Real, *Spin-Crossover Materials*, John Wiley & Sons Ltd., Chichester, UK, **2013**.
- [49] S. Schlamp, P. Thoma, B. Weber, *Chem. Eur. J.* **2014**, *20*, 6462–6473.
- [50] S. Schlamp, B. Weber, A. D. Naik, Y. Garcia, *Chem. Commun.* **2011**, *47*, 7152–7154.
- [51] S. M. Neville, B. A. Leita, G. J. Halder, C. Kepert, B. Moubaraki, J.-F. Létard, K. S. Murray, *Chem. Eur. J.* **2008**, *14*, 10123–10133.
- [52] W. Bauer, M. M. Dîrtu, Y. Garcia, B. Weber, *CrystEngComm* **2012**, *14*, 1223.
- [53] B. Weber, *Möss. Eff. Ref. Data J.* **2012**, *35*, 238–254.
- [54] B. Weber, C. Carbonera, C. Desplanches, J.-F. Létard, *Eur. J. Inorg. Chem.* **2008**, 1589–1598.
- [55] T. M. Pfaffeneder, S. Thallmair, W. Bauer, B. Weber, *New J. Chem.* **2011**, *35*, 691–700.
- [56] C. L. Zilverentant, G. A. van Albada, A. Bousseksou, J. G. Haasnoot, J. Reedijk, *Inorg. Chim. Acta* **2000**, *303*, 287–290.
- [57] V. Gómez, J. Benet-Buchholz, E. Martin, J. R. Galán-Mascarós, *Chem. Eur. J.* **2014**, *20*, 5369–5379.
- [58] O. Roubeau, M. Castro, R. Buörriel, J. G. Haasnoot, J. Reedijk, *J. Phys. Chem. B* **2011**, *115*, 3003.
-

- [59] G. Agusti, R. Ohtani, K. Yoneda, A. B. Gaspar, M. Ohba, J. F. Sánchez-Royo, M. C. Muñoz, S. Kitagawa, J. A. Real, *Angew. Chem. Int. Ed.* **2009**, *48*, 8944–8947.
- [60] S. M. Neville, G. J. Halder, K. W. Chapman, M. B. Duriska, P. D. Southon, D. Cashion, J.-F. Létard, B. Moubaraki, K. S. Murray, *J. Am. Chem. Soc.* **2008**, *130*, 2869–2876.
- [61] H. G. O. Becker, *Organikum. Organisch-Chemisches Grundpraktikum 19th ed.*, Johann Ambrosius Barth, Berlin, DE, **1993**.
- [62] K. Lagarec, D. G. Rancourt, *Recoil, Mössbauer Spectral Analysis Software for Windows 1.0*, **1998**, Department of Physics, University of Ottawa, CA.
- [63] O. Kahn, *Molecular Magnetism*, VCH, New York, N. Y., USA, **1993**.

7. Modulation of the ligand-based fluorescence of 3d metal complexes upon spin state change.

Charles Lochenie,^a Kristina G. Wagner,^b Matthias Karg^{*,b} and Birgit Weber^{*,a}

^aInorganic Chemistry II, Universität Bayreuth, Universitätstrasse 30, NW I, 95440 Bayreuth, Germany.

^bPhysical Chemistry I, Universität Bayreuth, Universitätstrasse 30, NW I, 95440 Bayreuth, Germany.

Dedicated to Prof. Manfred Scheer on the occasion of his 60th birthday.

Published in *J. Mater. Chem. C* **2015**, *3*, 7925–7935.

Reproduced with the permission of the Royal Society of Chemistry.

Abstract

Two new Schiff base-like ligands bearing a heteroaromatic fluorophore were synthesised and converted into the corresponding Ni(II), Cu(II), and Zn(II) square planar complexes. The Ni(II) complexes were studied with regard to a coordination change-induced spin state change upon addition of pyridine in solution. An inverse correlation between the fluorescence properties and the spin state of the metal centre was observed, and investigated with steady state fluorescence and time-resolved spectroscopy.

7.1 Introduction

Spin crossover (SCO) complexes are switchable molecules where the change of the spin state can be triggered by a wide range of physical or chemical stimuli such as temperature, pressure, light irradiation, or absorption/desorption of guest molecules. This switching process is accompanied by magnetic, optical, and structural changes that can be coupled to additional properties (e.g. liquid crystal phase transition).^[1-6] Due to their high variability with regard to the factors triggering the spin transition and the accompanying changes that can be "read out", SCO complexes are one of the most important molecule-based switchable materials and excellent candidates for technological application.^[7-10] Iron(II) is the most widely used metal centre for the synthesis of SCO complexes. For those complexes wide hysteresis loops around room temperature^[11] — even at nanoscale^[10,12,13] or photoinduced spin state changes^[14,15] at high temperatures could already be realised. However, the phenomenon itself is not limited to iron(II) or other $3d^{4-7}$ metal centres with an octahedral coordination sphere.^[16] The coordination induced spin state change of nickel(II) complexes from diamagnetic ($S = 0$) square planar to paramagnetic ($S = 1$) square pyramidal or octahedral coordination sphere shifted recently back into focus. With respect to potential applications for example in the field of smart contrast agents for magnetic resonance imaging, it is of interest to realise ligand systems which allow for light induced switching between these states. Ideally the transitions can be induced at room temperature in solution and on a single molecule level.^[17-21]

The combination of the spin transition with luminescence, if possible in a molecular system, would provide another "readout" feature with a high application potential in the field of drug delivery, biomarkers, or thermometry. Several attempts were already reported for the realisation of such bifunctional materials, mostly with iron(II). One possibility to achieve such systems is the synthesis of composite materials such as thin films doped with SCO complexes for electroluminescence,^[22-24] functionalised SCO-core-luminescence-shell nanoparticles,^[25,26] or SCO complexes with fluorescent counter anions.^[25,27] Another possibility is to covalently link the fluorophore to the SCO centre through ligand design.^[26,28] However, this approach is not always successful with respect to a coupling between spin

transition and fluorescence.^[29–31] So far only one example for a nickel(II) based fluorescent molecular thermometer is known, where the emission colour and intensity can be switched through a spin state change.^[32]

Here we present a new ligand system that shows a modulation of the fluorescence intensity upon a spin state change. The fluorescence properties of the free ligands, the diamagnetic zinc(II) complexes, the paramagnetic copper(II) complexes and the $S = 0 \leftrightarrow S = 1$ switchable nickel(II) complexes were investigated with steady-state extinction and fluorescence spectroscopy as well as time-resolved fluorescence spectroscopy.

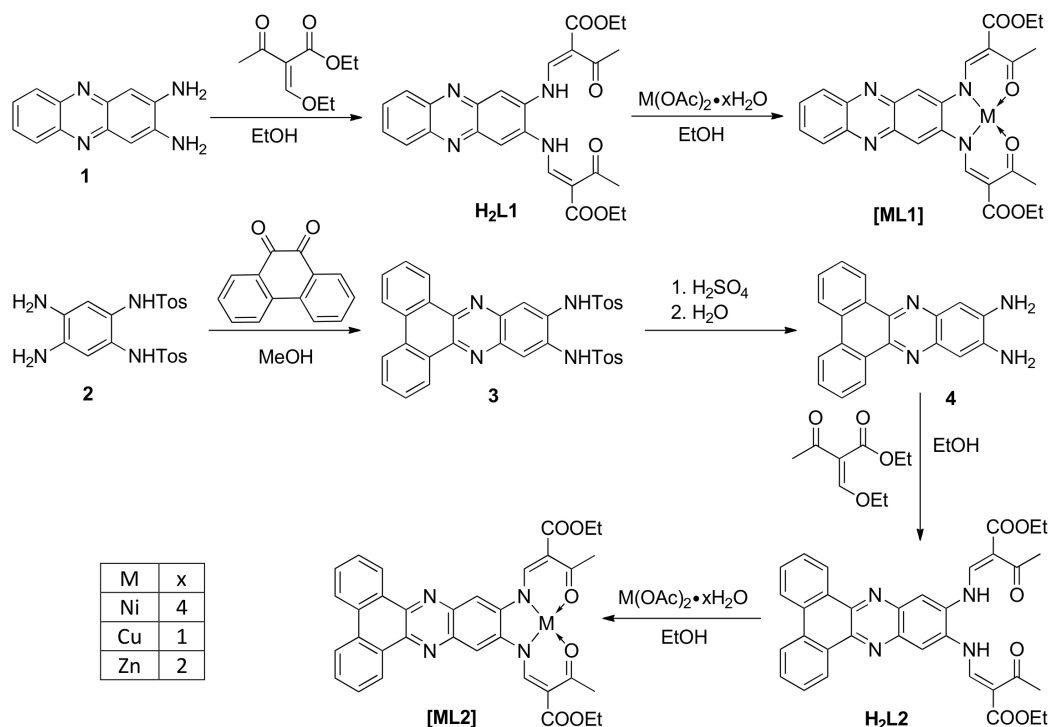
7.2 Results

7.2.1 Syntheses

All metal complexes were synthesised in two steps. Starting with the diamines **1** and **4**, firstly a condensation with a keto-enol ether forms the chelate cycles, which then react with metal acetate to give the respective complexes [**ML1**] and [**ML2**] ($M = \text{Ni}^{II}, \text{Cu}^{II}, \text{Zn}^{II}$), the counter anionic acetates acting as bases for deprotonation of the ligand. The molecular structures and the synthetic pathway are given in Scheme 7.1. All complexes were obtained as pure powder with the general formula [**ML1**] or [**ML2**]. All ligands and intermediates were characterised with IR, CHN, and $^1\text{H-NMR}$. All complexes were characterised with IR, CHN analysis, and mass spectrometry.

7.2.2 Crystal structure analysis

Single crystals suitable for X-ray diffraction analysis of [**NiL1**] and [**CuL1**] were obtained from a vapour-vapour slow diffusion setup between a trichloromethane solution of the complex and ethanol. All crystallographic data are given in the ESI: Table 7.5. While the complex [**NiL1**] crystallises with the same composition as the bulk material, the structure of compound [**CuL1**] was determined as [**CuL1(EtOH)**] $\cdot 2 \text{CHCl}_3$. Both compounds crystallise in the triclinic space group $P\bar{1}$, and the asymmetric units contain one complex molecule. ORTEP drawings of the asymmetric units are displayed in Fig.



Scheme 7.1: Pathway of synthesis of the metal complexes described in this work and used abbreviations.

7.2. The nickel(II) centre in **[NiL1]** lies in a N_2O_2 square planar coordination sphere. Ni–N (1.83 Å) and Ni– O_{eq} (1.85 Å) bond lengths are in agreement with other complexes with similar coordination sphere.^[33,34] The sum of the angles is with $\Sigma = 717^\circ$, not far from a perfect square planar coordination sphere ($\Sigma = 720^\circ$). In the case of **[CuL1(EtOH)]·2CHCl₃**, the copper(II) lies in a N_2O_3 square pyramidal geometry. Cu–N (1.92 Å), Cu– O_{eq} (1.92 Å), and Cu– O_{ax} (2.378(5) Å) bond lengths are generally longer than for the nickel complex, due to the different geometry of the coordination sphere and the increase of the covalent radius from 124 pm (Ni) to 132 pm (Cu). Selected bond lengths and angles are presented in Table 7.1.

The crystal packing of **[NiL1]** shows the complexes stacked over each other, forming columns along the vector [100]. π - π interactions between the aromatic rings of the ligand, as well as metal-aromatic interactions between the nickel centre and the chelate rings of neighbouring complexes lead to the formation of the columns in the packing. Illustrations of the packing are shown in Fig. 7.3, and selected distances of the π - π interactions

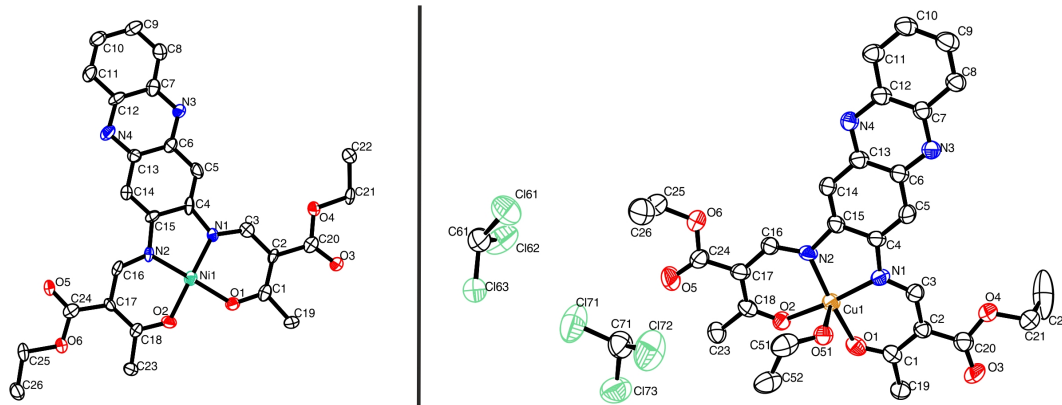


Figure 7.2: ORTEP drawing of $[\text{NiL1}]$ (left) and $[\text{CuL1}(\text{EtOH})] \cdot 2 \text{CHCl}_3$ (right). Thermal ellipsoids are shown at 50% level. Hydrogen atoms are omitted for clarity.

Table 7.1: Selected bond lengths [\AA] and angles [$^\circ$].

Compound	M–N	M–O _{eq}	M–O _{ax}	O _{eq} –M–O _{eq}	N–M–N	N–M–O _{eq}	N/O _{eq} –M–O _{ax}
$[\text{NiL1}]$	1.837(5)	1.856(4)		85.32(17)	87.1(2)	94.17(19)	
	1.825(4)	1.848(4)				93.4(2)	
						178.3(2)	
						178.73(19)	
$[\text{CuL1}(\text{EtOH})] \cdot 2 \text{CHCl}_3$	1.930(7)	1.905(5)	2.378(5)	90.8(2)	84.8(3)	92.5(5)	91.8(2)
	1.921(6)	1.943(5)				90.9(3)	92.0(2)
						171.8(3)	95.3(2)
						171.9(2)	96.1(2)

are presented in Table 7.2. The crystal packing of $[\text{CuL1}(\text{EtOH})] \cdot 2 \text{CHCl}_3$ shows a similar stacking than the one observed for $[\text{NiL1}]$, with the formation of pairs through π - π interactions. However, since an ethanol molecule is coordinated axially at the copper centre, no metal-aromatic interactions are observed. Only the aromatic rings of the ligands are interacting, with the copper centres looking in opposing directions in a "head-to-toes" fashion. Furthermore, hydrogen bonds are present between the trichloromethane solvent molecules and the complexes, as well as between the coordinating ethanol and neighbouring complex molecules. Illustrations of the packing are shown in Fig. 7.4, selected distances and angles of the π -interactions and of the hydrogen bonds are presented in Tables 7.2 and 7.3, respectively.

Powder diffraction patterns of all investigated complexes were measured; the results are displayed in the ESI, Fig. 7.9. The diffraction pattern of the powder sample $[\text{CuL1}]$ differs

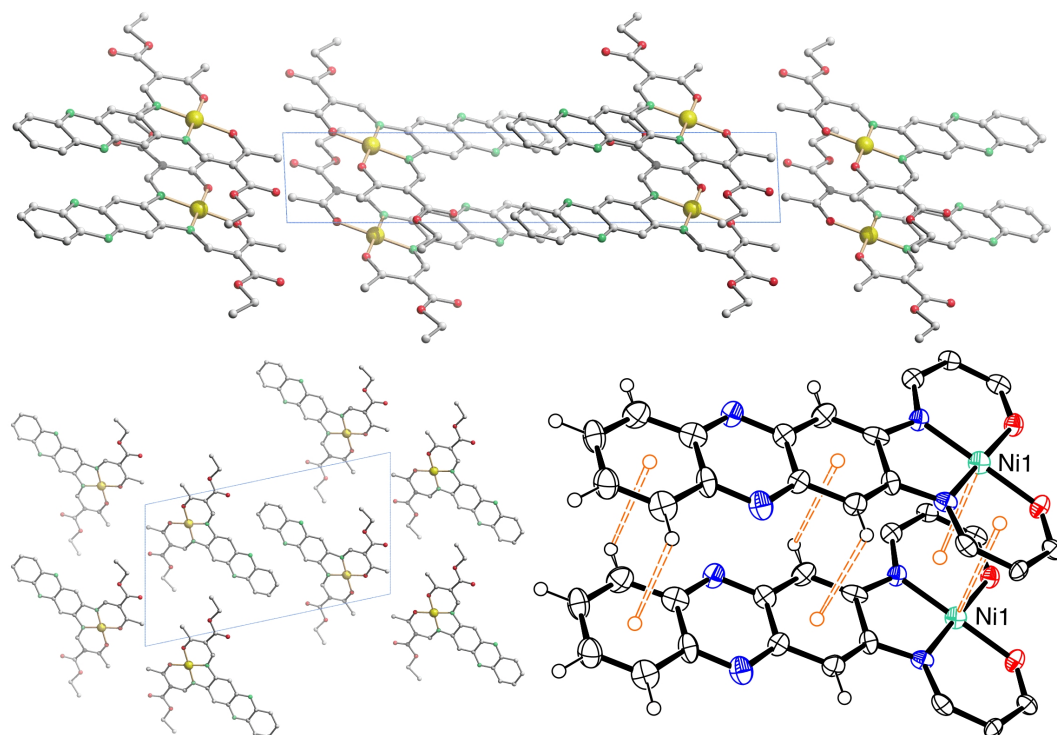


Figure 7.3: Illustrations of the crystal packing of $[\text{NiL1}]$ along $[010]$ (top) and $[100]$ (bottom left); scheme of the π - π and M- π interactions involved in the packing (bottom right).

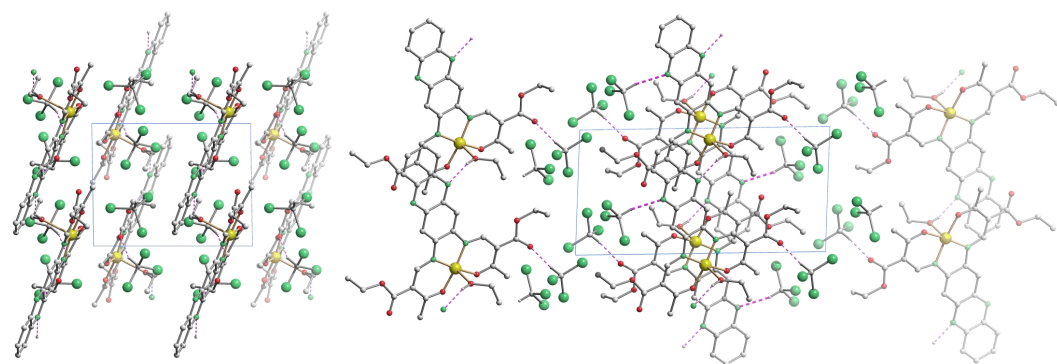


Figure 7.4: Illustrations of the crystal packing of $[\text{CuL1}(\text{EtOH})] \cdot 2 \text{CHCl}_3$ along $[001]$ (left) and along $[010]$ (right).

significantly from the calculated one for the single crystals of $[\text{CuL1}(\text{EtOH})] \cdot 2 \text{CHCl}_3$. This is not unexpected since the additional solvent molecules will strongly influence the packing pattern. The diffraction patterns of the three solvent-free complexes of **L1** show only little similarities. The packing of the molecules in the crystals is influenced by the metal centre. In contrast to this the diffraction patterns of $[\text{CuL2}]$ and $[\text{NiL2}]$ are very

Table 7.2: Selected distances [\AA] and angles [$^\circ$] of the π - π and M- π interactions. Cg(I) is the centroid of the ring number I, α is the dihedral angle between the rings, β is the angle between the vector Cg(I) \rightarrow Cg(J) and the normal to ring I, γ is the angle between the vector Cg(I) \rightarrow Cg(J) and the normal to ring J.

Cg(I)	Cg(J)	Cg-Cg	α	β	γ
[NiL1]					
C4-C5-C6-C13-C14-C15	C4-C5-C6-C13-C14-C15 ^a	4.084(3)	0	33.42	33.42
C4-C5-C6-C13-C14-C15	C4-C5-C6-C13-C14-C15 ^b	4.084(3)	0	33.42	33.42
C6-N3-C7-C12-N4-C13	C6-N3-C7-C12-N4-C13 ^a	4.084(3)	0	32.92	32.92
C6-N3-C7-C12-N4-C13	C6-N3-C7-C12-N4-C13 ^b	4.084(3)	0	32.92	32.92
C7-C8-C9-C10-C11-C12	C7-C8-C9-C10-C11-C12 ^a	4.084(4)	0	32.65	32.65
C7-C8-C9-C10-C11-C12	C7-C8-C9-C10-C11-C12 ^b	4.084(4)	0	32.65	32.65
Ni1-O1-C1-C2-C3-N1	Ni1 ^b	3.301		12.75	
Ni1-O1-C1-C2-C3-N1	Ni1 ^a	3.258		11.40	
[CuL1(EtOH)]·2 CHCl₃					
C4-C5-C6-C13-C14-C15	C7-C8-C9-C10-C11-C12 ^c	3.837(5)	1.1(4)	25.66	29.54
C6-N3-C7-C12-N4-C13	C6-N3-C7-C12-N4-C13 ^c	3.807(5)	0	28.68	28.68
C7-C8-C9-C10-C11-C12	C4-C5-C6-C13-C14-C15 ^c	3.838(5)	1.1(4)	29.54	28.66

Symmetry code. a = $-1+x, y, z$; b = $1-x, y, z$; c = $3-x, 1-y, 1-z$.

Table 7.3: Selected distances [\AA] and angles [$^\circ$] of the hydrogen bonds present in the packing of **[CuL1(EtOH)]·2 CHCl₃**.

D	H	A	D-H	H...A	D...A	D-H...A
O51	H51	N4 ^a	0.84	2.11	2.820(8)	142
C61	H61	N3 ^b	1.00	2.35	3.297(14)	158
C71	H71	O5	1.00	2.07	3.007(14)	155

Symmetry code. a = $-1+x, y, z$; b = $x, y, 1+z$.

similar, for **[ZnL2]** the differences are more pronounced. For the ligand **L2** with the extended aromatic system the packing of the molecules in the crystal is mostly influenced by the ligand and less by the metal centre.

7.2.3 Steady state spectroscopy

The optical properties of the ligands and the complexes were studied by extinction and fluorescence spectroscopy. First of all the pure ligand systems were investigated in trichloromethane. Fig. 7.5A compares the absorbance and emission spectra of **H₂L1** and **H₂L2**. The spectral features of both ligands are very similar. Both ligands show a pronounced absorption peak at approx. 440 nm and emission with a maximum at approx. 470 nm. Furthermore the absorption peaks show a weak shoulder at lower wavelength,

as well as a weak shoulder in the emission spectra at higher wavelength as compared to the peak maximum. These shoulders can be attributed to the equilibrium between imino-enol/keto-enamine tautomers of the ligands in solution.^[34,35]

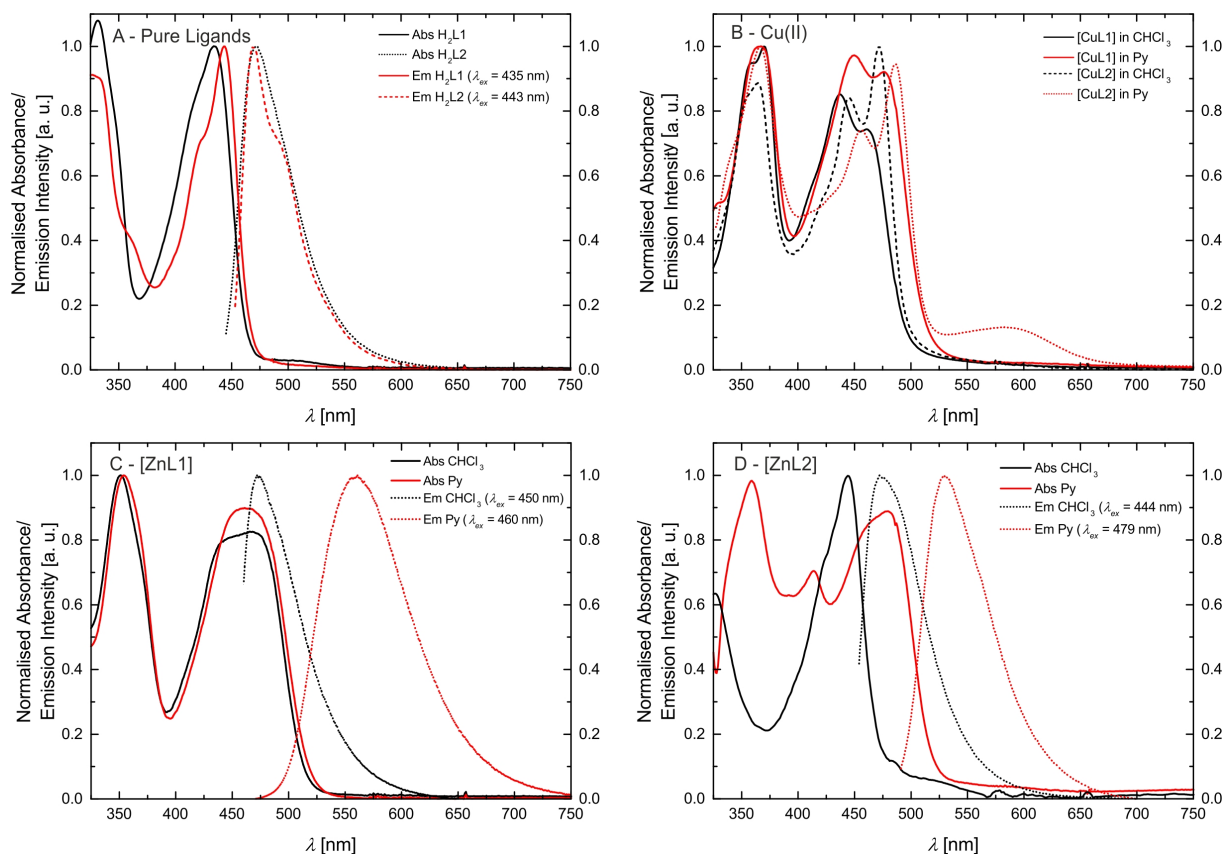


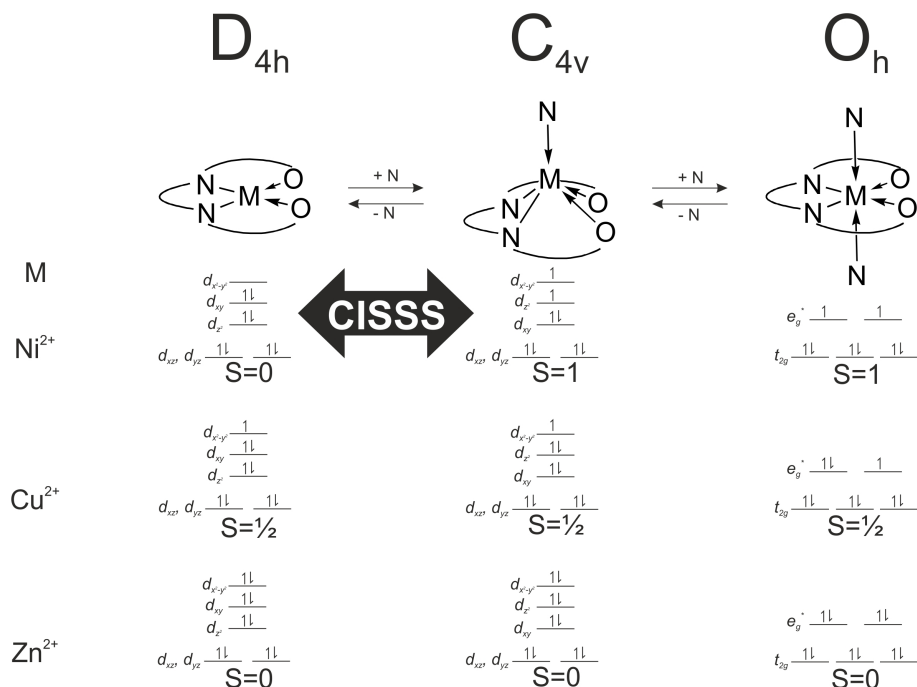
Figure 7.5: Absorption and emission spectra. (A) Pure ligands. (B) Cu(II) complexes. (C and D) Zn(II) complexes.

The spectral analyses of the metal complexes (Cu and Zn) are shown in Fig. 7.5B–D. In order to investigate the influence of the spin state on the absorption and fluorescence, spectra of the complexes were measured in trichloromethane and pyridine. Fig. 7.5B compares the absorbance spectra for the Cu(II) complexes **[CuL1]** and **[CuL2]**. Comparing the spectra measured in trichloromethane similar absorption spectra are observed with the same number of bands. In contrast to this the absorption peaks are red-shifted when pyridine is used as solvent (solvatochromism). In case of **[CuL2]**, a weak band appears at 585 nm in the pyridine solution, that can be attributed to *d-d* transitions by comparison with similar complexes.^[34] In agreement with many examples for fluorophores

in literature, fluorescence was not observed for the copper complexes indicating strong quenching due to the presence of the metal centre.^[36–38]

The absorption spectra of the zinc(II) complexes [**ZnL1**] in trichloromethane and pyridine shown in Fig. 7.5C resemble the spectra of the pure ligand systems. In addition almost no difference in band position and the number of bands is observed comparing the spectra in the two solvents. In contrast to this the complex emission is significantly influenced by changing the solvent from trichloromethane to pyridine. In trichloromethane the emission maximum is at 473 nm, whereas the emission shifts to 560 nm in pyridine. The absorption spectrum of [**ZnL2**] in trichloromethane resembles also the spectrum of the corresponding ligand, however changes in the number of bands and their position appear in pyridine solution. The emission spectrum also displays a red-shift as observed for sample [**ZnL1**], but with a smaller difference between trichloromethane solution ($\lambda_{em} = 475$ nm) and pyridine solution ($\lambda_{em} = 529$ nm). The optical properties of the nickel(II) complexes [**NiL1**] and [**NiL2**] were investigated by adding a pyridine solution of the complex into an equimolar trichloromethane solution of the same complex, as the nickel centre undergoes a spin state change upon coordination change (see Scheme 7.6).^[16,32] Respective absorbance and emission spectra are shown in Fig. 7.7. The trichloromethane solutions of the nickel complexes show three absorption bands at 365, 414, and 448 nm for [**NiL1**], and at 412, 440, and 465 nm for [**NiL2**]. Upon progressive coordination of pyridine molecules onto the nickel centre, the absorption spectra dramatically change. In the case of [**NiL1**], the bands at 414 and 448 nm tend to disappear whereas the band at 365 nm increases and a new band at 493 nm appears. For the sample [**NiL2**] the intensity of the bands at 412 and 440 nm decreases and two new bands at 375 and 500 nm appear. The drastic changes in the absorbance spectra of the nickel complexes confirm the change of geometry and by this the spin state upon coordination with pyridine. The spin state change also affects the fluorescence properties of the complexes (Fig. 7.7B and D). As pyridine is added to the complex [**NiL1**], its emission band at 478 nm progressively red-shifts and its intensity dramatically decreases. The red-shift seems in good agreement with the emergence of a new band at higher wavelength (493 nm) in the absorption spectrum upon addition of pyridine. For the complex [**NiL2**], a completely different effect

is observed. Upon addition of the first equivalents of pyridine, the emission band at 491 nm is shifted to 538 nm, and its intensity increases until $\simeq 400$ equivalents of pyridine are added. Further addition of pyridine leads to a decrease of the emission intensity.



Scheme 7.6: Electronic configuration, spin number, and geometry of the different complexes in equilibrium in solution upon addition of pyridine.

The reversibility of the coordination of the pyridine molecules was investigated with absorption spectroscopy. First, a pyridine solution of the [NiL1] complex was progressively added to an equimolar trichloromethane solution of the complex. In the next step, the pyridine concentration of this solution was reduced by addition of the original trichloromethane solution. The intensity of the characteristic absorption bands of the complex in pyridine ($\lambda = 365$ nm) and in trichloromethane ($\lambda = 414$ nm) varies in agreement with a reversible coordination of the pyridine molecules to the metal centre. Fig. 7.10 in the ESI illustrates those results. The absorption spectra of the fluorescent Ni(II) and Zn(II) complexes were also measured in trichloromethane solutions containing triethylamine (Et₃N) as non-coordinating base, or formic acid (HCOOH), in order to rule out possible effects due to (de)protonation of the complexes. The corresponding UV-vis spectra are presented in the ESI: Fig. 7.11. The spectra show that in all cases, no

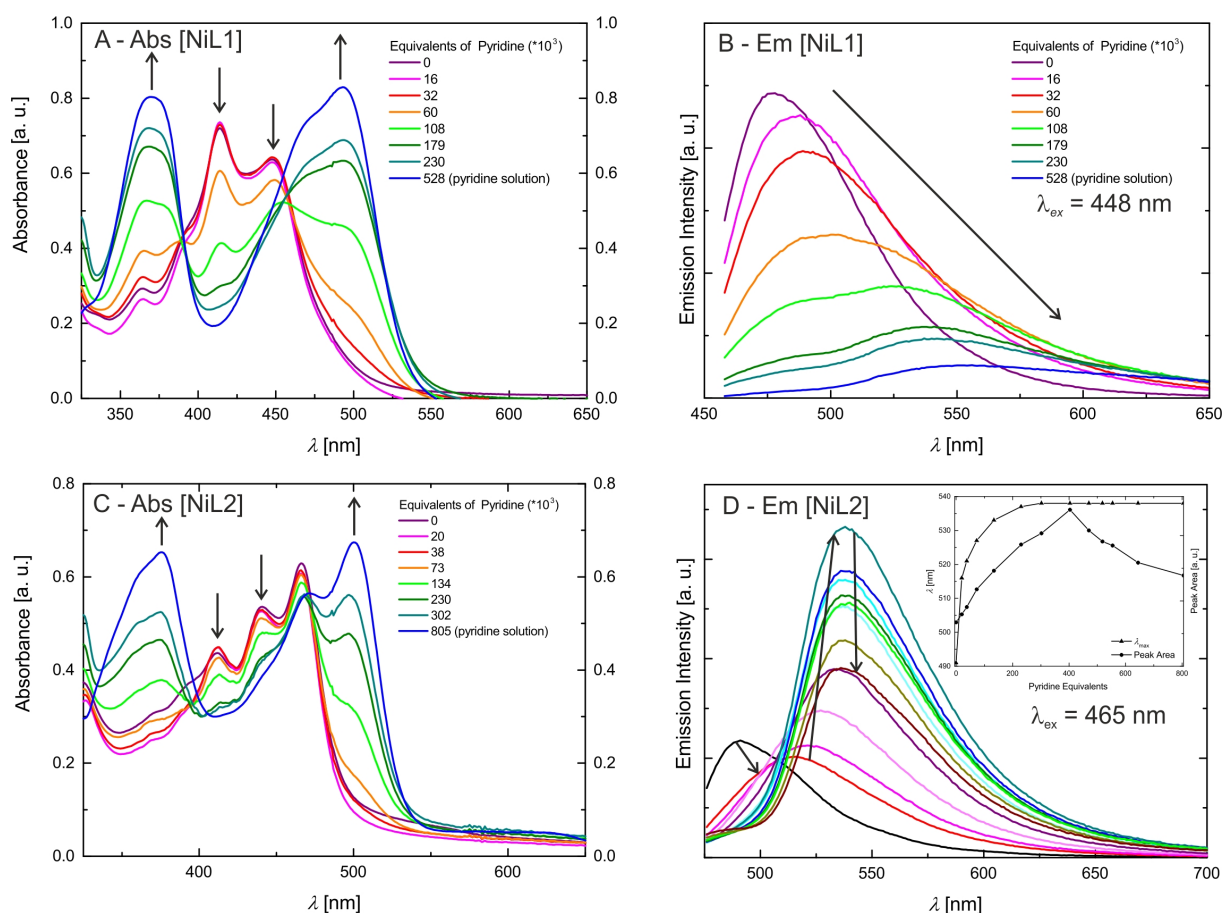


Figure 7.7: Absorption and steady state fluorescence measurements of the Ni(II) complexes. The inset in D gives the integrated peak area and λ_{max} as guide for the reading of the graph.

significant changes are observed for the $\text{CHCl}_3\text{-Et}_3\text{N}$ solutions, proving that the changes observed for the pyridine addition are due to coordination of pyridine at the axial positions of the nickel centre. Spectra of the complexes in $\text{CHCl}_3/\text{HCOOH}$ solutions show a pronounced red-shift upon protonation of the heteroaromatic *N*-atoms of the complex. This is not surprising as phenazine-derivatives are used as pH-indicators (e.g. neutral red). As the effects of the spin state change on the intensity of the emission properties of [NiL1] and [NiL2] are extremely different and intriguing, lifetime measurements of the fluorescence were performed and are discussed further.

7.2.4 Fluorescence lifetime analysis

In addition to the steady-state fluorescence spectra shown in Fig. 7.7B and D for the complexes **[NiL1]** and **[NiL2]**, lifetime measurements were performed on the same samples at 298 K. The fluorescence decays were analysed using deconvolution fitting with double exponential decay functions. Fig. 7.8 compares selected fluorescence decays for complex solutions in trichloromethane and pyridine. It is clearly visible that the lifetime depends strongly on the type of solvent. In pyridine a significantly faster decay is observed as compared to trichloromethane. Table 7.4 summarises the results of the lifetime analysis for all measured solutions. The fluorescence decays for the complexes show monoexponential behaviour for trichloromethane as solvent with relatively short lifetimes of $\tau = 0.7$ ns for **[NiL1]** and $\tau = 1.3$ ns for **[NiL2]**. For small equivalents of added pyridine the lifetime decreases in case of **[NiL1]** and the decays remain monoexponential. For higher amounts of pyridine, monoexponential decays could not be used to satisfyingly describe the decay profiles as a second longer lifetime component emerges. However this second contribution has very small amplitudes except for the highest amount of pyridine used. In the latter case the data analysis will be less reliable since the fast component provides lifetimes which are significantly smaller than the half width of the instrument response function. Therefore no conclusions will be drawn from the latter analysis result. As a general trend, it can be observed that the first lifetime component for **[NiL1]** systematically shortens with increasing amount of added pyridine.

For compound **[NiL2]**, a different trend is observed upon addition of pyridine: the compound starts with a relatively longer lifetime of $\tau = 1.3$ ns, which slightly increases upon addition of pyridine, reaching 1.8 ns in pure pyridine solution. For this complex all fluorescence decays were fitted with a monoexponential model and satisfying χ^2 values were obtained.

7.3 Discussion

The complexes **[ML1]** and **[ML2]** were designed with the aim to favour possible non-radiative energy transfer between the heteroaromatic fluorophore, the donor, and the

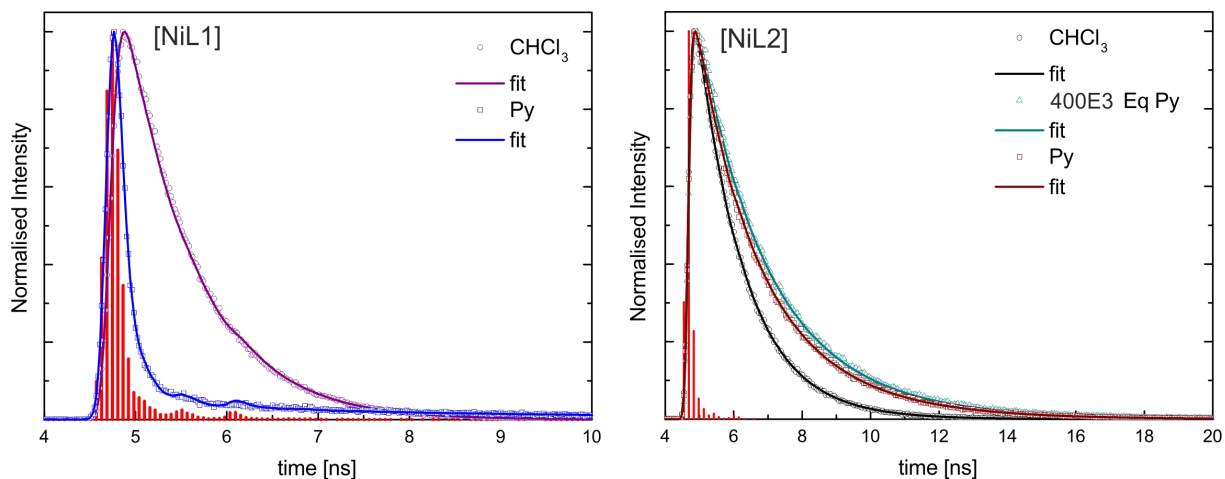


Figure 7.8: Measured fluorescence decays for the nickel complexes. The instrument response function (IRF) is represented by the red vertical bars. The solid lines are deconvolution fits of the lifetime traces.

Table 7.4: Lifetime measurements data with the decay constant τ in ns. The error for the measured τ values are given in [%].

Py Equivalents	τ
[NiL1]	
0 (CHCl ₃ solution)	0.7 [1%]
16	0.6 [2%]
32	0.5 [2%]
60	0.4 [2%]
108	0.3 [4%]
179	<0.2
230	<0.2
528 (Py solution)	<0.2
[NiL2]	
0 (CHCl ₃ solution)	1.3 [<1%]
20	1.3 [<1%]
38	1.6 [<1%]
73	1.8 [<1%]
134	2.0 [<1%]
230	2.0 [<1%]
302	1.9 [<1%]
403	1.9 [<1%]
470	1.8 [<1%]
518	1.7 [<1%]
554	1.7 [<1%]
644	1.8 [<1%]
805 (Py solution)	1.7 [<1%]

metal centre, the acceptor. Such design could give a control on the fluorescence properties of the fluorophore through changes of the spin state of the metal centre. As the

distance between the donor and the acceptor plays a crucial role in the effectiveness of a non-radiative energy transfer,^[38] two different fluorophores with extended π -systems were used. The crystal structure of **[NiL1]** and **[CuL1(EtOH)]·2 CHCl₃** were successfully analysed by X-ray diffraction. The obtained crystal structures present π - π interactions in the packing between the complexes, as well as a hydrogen bond network in case of **[CuL1(EtOH)]·2 CHCl₃**. In the latter crystal structure, it is observed that the copper complex crystallises in a square pyramidal geometry, although it is obtained as square planar complex in the bulk material. It was already observed in corresponding phenylene-derivatives copper(II) complexes that the metal centre is always trying to break its square planar symmetry, either by coordinating solvent molecules, or by sitting in a distorted coordination sphere.^[34] Unfortunately no crystals suitable for X-ray diffraction were obtained for the **[ML2]** samples, even when using vapour-vapour or liquid-liquid slow diffusion setups.

The spin state of the different complexes is usually due to their electronic configuration, with $S = \frac{1}{2}$ for the 3d⁹ Cu(II) complexes, and $S = 0$ for the 3d¹⁰ Zn(II) complexes. In the case of the Ni(II) complexes, their spin state depends also on the geometry of the coordination sphere of the Ni(II) centre. In a square planar geometry, the nickel centre has a spin number of $S = 0$, with all its electrons paired, however, upon coordination of pyridine on the axial position(s), the changes on the splitting of the d orbitals will induce a spin state change ($S = 1$), as described in the literature.^[17-21,33] The magnetic moment of the complex **[NiL1]** was determined with the Evans method: an effective magnetic moment $\mu_{eff} = 0$ was measured in CDCl₃ solution, in contrast to a $\mu_{eff} = 2.78$ in pyridine-d₅ solution, in good agreement with a theoretical value of $\mu_{SO} = 2.83$ for $S = 1$.

The investigation of the steady-state fluorescence of **[ML1]** compounds shows that the emission properties depend on the spin state of the metal centre. Indeed, diamagnetic metal centres, Zn(II) or Ni(II) in square planar geometry are fluorescent whereas for paramagnetic metal centres, Cu(II) or Ni(II) in square pyramidal/octahedral geometry, the fluorescence is quenched. The presence of unpaired electrons, and therefore partially filled orbitals, can give rise to an energy transfer between the fluorophore and the metal

centre. A shortening of the lifetime of a given fluorophore is often observed when an energy transfer occurs, and this effect is observed for the complex **[NiL1]**, as the emission lifetime gets shorter upon addition of pyridine, or in other words, upon coordination change induced spin state change (see Scheme 7.6). It has to be pointed out here that the sample **[NiL1]** exhibits a second contribution with a longer lifetime once a certain amount of pyridine equivalents is reached. The origin of this second component is not yet well understood and requires further investigations. The type of non-radiative energy transfer, whether it is a Förster or Dexter type cannot be pinpointed on the basis of the current investigation and requires further experiments or calculations.

The corresponding Zn(II) complex **[ZnL1]** displays a strong red-shift (87 nm) of the fluorescence upon coordination with pyridine. The same effect is observed for sample **[ZnL2]** but the red-shift is only in the order of 54 nm, indicating that the metal centre has a reduced influence on the fluorescence properties of the bigger fluorophore.

The complex **[NiL2]** presents a very different behaviour than **[NiL1]** upon addition of pyridine. Instead of being quenched, its emission properties are actually intensifying upon the addition of the first equivalents of pyridine. After reaching a maximum, the emission band intensity is decreasing ; however the sample in pure pyridine solution shows stronger fluorescence than the sample in pure trichloromethane solution. The opposite trend was observed for the complex **[NiL1]**. The lifetime measurements also present different results for **[NiL2]** than for **[NiL1]**. The lifetime of the emission is slightly increasing from 1.3 ns to 2.0 ns upon pyridine coordination. Then as the intensity of the emission peak is decreasing, the lifetime stays approximately constant ($t = 1.7$ ns in pyridine solution).

Two hypotheses can be drawn about the big difference in the luminescence properties of the two nickel complexes. A difference in the nature of the transitions involved in the fluorophore could be the reason. It is described in literature that phenanthrene, and phenanthrene-derivatives like the ligand **H₂L2**, undergo forbidden transitions, leading generally to longer lifetimes.^[39] Another reason could be a too long distance between the metal centre and the fluorophore, preventing any energy transfer. In this case, the effect observed on addition of pyridine would be of the same nature as solvatochromism. Finally,

it is also possible that the first excited state of the fluorophore is at a lower energy than the first excited state of the metal centre, making the energy transfer impossible. Further investigations about the compound [NiL2], with varying temperature, or changing the coordinating solvent molecule i.e. for acetonitrile, are needed in order to understand the luminescence properties. Calculations of the different ground and excited states of the donor-acceptor pair would also give useful insights.

As complex [NiL1] showed an interesting coupling of the fluorescence properties with the spin state change, corresponding iron(II) complexes will be investigated in order to determine if such coupling is also obtained with a thermally-induced spin crossover.

7.4 Experimental Section

Synthesis 2,3-Diaminophenazine (**1**), 4,5-diamino-*NN'*-ditoluene-*p*-sulphonyl-*o*-phenylenediamine (**2**), and ethoxymethylene-ethylacetoacetate were synthesised as described in literature.^[40–43] Methanol, ethanol, trichloromethane, and pyridine were of analytical grade and used without further purification. Nickel(II) acetate tetrahydrate (99%, Fluka), copper(II) acetate monohydrate (99%, Fluka), zinc(II) acetate dihydrate (97%, Alfa Aesar), 9,10-phenanthrenequinone (95%, Alfa Aesar), and sulphuric acid (97%, Sigma Aldrich) were used without further purification. CHN analyses were measured with a Vario El III from Elementar Analysen-Systeme. Mass spectra were recorded with a Finnigan MAT 8500 with a data system MASPEC II. NMR spectra were measured with a Varian INOVA 300. Toluene was used as reference for the Evans method.

6',7'-Bis-(toluenesulfonamido)-quinoxaline-[2',3'-d]-1,10-phenanthrene (3) 4,5-diamino-*NN'*-ditoluene-*p*-sulphonyl-*o*-phenylenediamine (**2**) (2.23 g) and 9,10-phenanthrenequinone (1.05 g) were dissolved in methanol (50 mL). The orange solution was refluxed during 1 h, the colour of the solution changes progressively to yellow during the reflux. The solution is let to cool down to room temperature and a yellow powder precipitates. The yellow powder is filtered and washed with ice-cold methanol (3 × 20 mL), and dried *in vacuo* to give the pure product **3**. Yield: 1.96 g (63%). MS (DEI-+), 70 eV *m/z* (%): 618 (100) (M+); elemental analysis calculated (found) for C₃₄H₃₆N₄O₄S₂ (618.72

$\text{g}\cdot\text{mol}^{-1}$): C 66.00 (65.97), H 4.24 (4.05), N 9.06 (9.18). $^1\text{H-NMR}$ (DMSO, 300 MHz, ppm): $\delta = 10.14$ (bs, $-\text{NH}$, 2H), 9.04 (d, $J = 9$ Hz, Ar-H, 4H), 8.64 (d, $J = 9$ Hz, Ar-H, 4H), 7.79 (s, Ar-H, 2H), 7.76 (m, Ar-H, 8H), 2.34 (s, $-\text{CH}_3$, 6H).

6',7'-Diaminoquinoxaline-[2',3'-d]-1,10-phenanthrene (4) 6',7'-Bis-(toluenesulfonamido)-quinoxaline-[2',3'-d]-1,10-phenanthrene (**3**) (1.29 g) was dissolved in concentrated sulphuric acid (10 mL) and heated to 100°C during 4 h. A change of colour of the solution from yellow to purple was observed. The solution was cooled down to 0°C and 50 mL H_2O was added dropwise to the solution, and a brown powder precipitates from the solution. The brown powder was filtered and washed with 10 mL H_2O , then suspended in 20 mL H_2O . Ammonium hydroxide solution (25%) was added to the suspension under vigorous stirring until its pH reaches 8. The solid turned redbrown during the addition, was then filtered, washed with H_2O (2×5 mL), and dried *in vacuo* to give the pure product **4**. Yield: 0.47 g (72%). MS (DEI(+), 70 eV) m/z (%): 310 (100) (M+); elemental analysis calculated (found) for $\text{C}_{20}\text{H}_{14}\text{N}_4$ ($310.35 \text{ g}\cdot\text{mol}^{-1}$): C 77.40 (77.24), H 4.55 (4.15), N 18.05 (18.25). $^1\text{H-NMR}$ (DMSO, 300 MHz, ppm): $\delta = 9.17$ (m, Ar-H, 2H), 8.74 (m, Ar-H, 2H), 7.73 (m, Ar-H, 4H), 7.12 (s, Ar-H, 2H), 6.11 (bs, $-\text{NH}_2$, 4H).

H₂L1 2,3-Diaminophenazine (**1**) (0.5 g) and ethoxymethyleneethylacetoacetate (0.93 g) were dissolved in 20 mL ethanol. The solution was refluxed during 1 hour, and a brownish yellow powder precipitated upon reflux. The brownish yellow powder was filtered, washed with 5 mL cold ethanol. Recrystallisation from ethanol gives the pure product **H₂L1** as brownish yellow crystals. Yield: 0.48 g (42%). MS (DEI(+), 70 eV) m/z (%): 490 (100) (M+); elemental analysis calculated (found) for $\text{C}_{34}\text{H}_{30}\text{N}_4\text{O}_6$ ($490.51 \text{ g}\cdot\text{mol}^{-1}$): C 63.66 (66.30), H 5.34 (5.15), N 11.42 (11.65). $^1\text{H-NMR}$ (DMSO, 300 MHz, ppm): $\delta = 12.67$ (d, $J = 12$ Hz, $-\text{NH}$, 2H), 8.52 (d, $J = 12$ Hz, $=\text{C-H}$, 2H), 8.25 (s, Ar-H, 2H), 8.18 (dd, $J^3 = 6$ Hz, $J^4 = 3$ Hz, Ar-H, 2H), 7.94 (dd, $J^3 = 6$ Hz, $J^4 = 3$ Hz, Ar-H, 2H), 4.18 (qua, $J = 7.5$ Hz, $-\text{CH}_2$, 4H), 2.49 (s, $-\text{CH}_3$, 6H), 1.32 (t, $J = 7.5$ Hz, $-\text{CH}_3$, 6H).

H₂L2 6',7'-Diaminoquinoxaline-[2',3'-d]-1,10-phenanthrene (**4**) (0.17 g) and ethoxymethyleneethylacetoacetate (0.26 g) were dissolved in 10 mL ethanol. The solution was refluxed during 1 hour, and a yellow powder precipitated upon reflux. The yellow powder was fil-

tered, washed with 5 mL cold ethanol. Recrystallisation from ethanol gives the pure product **H₂L2** as yellow crystals. Yield: 0.24 g (74%). MS (DEI-+), 70 eV) *m/z* (%): 590 (100) (M⁺); elemental analysis calculated (found) for C₃₄H₃₀N₄O₆ (590.63 g·mol⁻¹): C 69.14 (69.30), H 5.12 (5.15), N 9.49 (9.65). ¹H-NMR (DMSO, 300MHz, ppm): δ = 12.59 (d, *J* = 12Hz, -NH, 2H), 9.13 (m, Ar-H, 2H), 8.69 (m, Ar-H, 2H), 8.65 (d, *J* = 12Hz, =C-H, 2H), 7.68 (m, Ar-H, 4H), 7.10 (s, Ar-H, 2H), 4.17 (qua, *J* = 7.5 Hz, -CH₂, 4H), 2.47 (s, -CH₃, 6H), 1.33 (t, *J* = 7.5Hz, -CH₃, 6H).

[**NiL1**] **H₂L1** (0.2 g) and nickel(II) acetate tetrahydrate (0.12 g) were dissolved in 20 mL ethanol. The solution was refluxed during 1 hour, and an orange powder precipitated upon reflux. The orange powder was filtered, washed with 5 mL cold ethanol. Recrystallisation from ethanol gives the pure complex as orange powder. Yield: 0.20 g (88%). MS (DEI-+), 70 eV) *m/z* (%): 546 (100) (M⁺); elemental analysis calculated (found) for C₂₆H₂₄N₄NiO₆ (547.19 g·mol⁻¹): C 57.07 (56.98), H 4.42 (4.15), N 10.24 (10.42).

[**CuL1**] **H₂L1** (0.2 g) and copper(II) acetate monohydrate (0.10 g) were dissolved in 20 mL ethanol. The solution was refluxed during 1 hour, and a brown powder precipitated upon reflux. The brown powder was filtered, washed with 5 mL cold ethanol. Recrystallisation from ethanol gives the pure complex as brown powder. Yield: 0.21 g (91%). MS (DEI-+), 70 eV) *m/z* (%): 551 (100) (M⁺); elemental analysis calculated (found) for C₂₆H₂₄N₄CuO₆ (552.04 g·mol⁻¹): C 56.57 (56.48), H 4.38 (4.23), N 10.15 (10.05).

[**ZnL1**] **H₂L1** (0.2 g) and zinc(II) acetate dihydrate (0.11 g) were dissolved in 20 mL ethanol. The solution was refluxed during 1 hour, and a red powder precipitated upon reflux. The red powder was filtered, washed with 5 mL cold ethanol. Recrystallisation from ethanol gives the pure complex as red powder. Yield: 0.18 g (79%). MS (DEI-+), 70 eV) *m/z* (%): 552 (100) (M⁺); elemental analysis calculated (found) for C₂₆H₂₄N₄O₆Zn (553.87 g·mol⁻¹): C 56.38 (56.29), H 4.37 (4.43), N 10.12 (10.13).

[**NiL2**] **H₂L2** (0.2 g) and nickel(II) acetate tetrahydrate (0.10 g) were dissolved in 20 mL ethanol. The solution was refluxed during 1 hour, and a yellow powder precipitated upon reflux. The yellow powder was filtered, washed with 5 mL cold ethanol. Recrys-

tallisation from ethanol gives the pure complex as yellow powder. Yield : 0.17 g (76%). MS (DEI-+), 70 eV) m/z (%): 646 (100) (M+) ; elemental analysis calculated (found) for $C_{34}H_{28}N_4NiO_6$ ($647.30 \text{ g}\cdot\text{mol}^{-1}$): C 63.09 (63.16), H 4.36 (4.45), N 9.07 (9.05).

[CuL2] **H₂L2** (0.2 g) and copper(II) acetate monohydrate (0.08 g) were dissolved in 20 mL ethanol. The solution was refluxed during 1 hour, and a brown powder precipitated upon reflux. The brown powder was filtered, washed with 5 mL cold ethanol. Recrystallisation from ethanol gives the pure complex as brown powder. Yield: 0.19 g (86%). MS (DEI-+), 70 eV) m/z (%): 651 (100) (M+) ; elemental analysis calculated (found) for $C_{34}H_{28}N_4CuO_6$ ($652.16 \text{ g}\cdot\text{mol}^{-1}$): C 62.62 (62.58), H 4.33 (4.18), N 8.59 (8.65).

[ZnL2] **H₂L2** (0.2 g) and zinc(II) acetate dihydrate (0.06 g) were dissolved in 20 mL ethanol. The solution was refluxed during 1 hour, and an orange powder precipitated upon reflux. The orange powder was filtered, washed with 5 mL cold ethanol. Recrystallisation from ethanol gives the pure complex as orange powder. Yield: 0.12 g (82%). MS (DEI-+), 70 eV) m/z (%): 652 (100) (M+) ; elemental analysis calculated (found) for $C_{26}H_{24}N_4O_6Zn$ ($653.99 \text{ g}\cdot\text{mol}^{-1}$): C 62.44 (62.32), H 4.32 (4.27), N 8.57 (8.51).

X-ray structure analysis The X-ray analysis of the **[NiL1]** and **[CuL1(EtOH)]·2CHCl₃** complexes was performed with a Stoe StadiVari diffractometer using graphite-monochromated MoK α radiation. The data were corrected for Lorentz and polarization effects. The structures were solved by direct methods (SIR-97)^[44] and refined by full-matrix least-square techniques against $F_o^2-F_c^2$ (SHELXL-97).^[45] All hydrogen atoms were calculated in idealised positions with fixed displacement parameters. ORTEP-III^[46] was used for the structure representation, SCHAKAL-99^[47] to illustrate molecule packing. CCDC 1055605 and 1055606. Powder diffractograms were measured with a STOE StadiP Powder Diffractometer (STOE, Darmstadt) using Cu K α 1 radiation with a Ge Monochromator, and a Mythen 1K Stripdetector in transmission geometry.

Optical measurements Absorbance spectra were obtained using a Agilent UV-vis spectrophotometer 8453 (Agilent Technologies, USA) operating in a spectral range of 190–1100 nm. The spectra were measured at 298 K in quartz cells with 1 cm lightpath

(Hellma, Germany). Fluorescence measurements were performed with a FLS980 (Edinburgh Instruments, UK) fluorescence spectrometer equipped with double monochromators (1800 grooves per mm) in excitation and emission. A Xe lamp (360 W) was used as excitation source for steady-state fluorescence measurements. Time-resolved measurements were performed with a pulsed supercontinuum fiber laser (WhiteLase SC-400, Fianium, UK) with a pulse width <10 ps and a repetition rate of 5 MHz. Emission from the sample was collected at an angle of 90° with respect to the excitation path. The emitted beam was focused onto a single photon counting photomultiplier (R928P, Hamamatsu, Japan) or a microchannel plate photomultiplier (MCP-PMT) for steady-state and lifetime measurements respectively. All spectra were measured at 298 K in quartz cells (Hellma, Germany) with 1 cm lightpath. The excitation wavelength and time range for lifetime measurements were selected according to the sample requirements. The time-resolved fluorescence decays were analysed by deconvolution fits accounting for the instrument response function (IRF) obtained from a Rayleigh scatterer.

7.5 Conclusion

Two new Schiff base-like ligands bearing a fluorophore were synthesised and successfully used for complexation of Ni(II), Cu(II), and Zn(II). While for the Cu(II) complexes the fluorescence is quenched, the Zn(II) and Ni(II) complexes retain the photoluminescent properties. We have shown that the addition of pyridine induces a change in the geometry of the complex, and consequently a change of the spin state. While the Zn(II) complexes only display a red-shift of the emission upon coordination, the nickel(II) complexes exhibit a more complex behaviour. The sample [NiL1] showed a quenching of its fluorescence correlated to a coordination change-induced spin state change, with a dramatic decrease of the intensity and lifetime of the emission band. This is in agreement with the appearance of non-radiative energy transfer between the fluorophore and the Ni(II) centre in its $S = 1$ paramagnetic state. The sample [NiL2], bearing a more extended phenanthrene-based fluorophore, displays a more complex behaviour upon coordination of pyridine which requires further investigation. This will be addressed in a future work. Corresponding iron(II) complexes will also be investigated with regard to possible correlation effects

between fluorescence and thermally-induced spin crossover.

Acknowledgements

Financial supports from the German Science foundation (SFB840) and the University of Bayreuth are acknowledged. Mathias Karg and Kristina G. Wagner acknowledge financial support from the German Research Foundation (DFG) via the Emmy-Noether Programme. We thank F. Puchtler (University of Bayreuth) for the collection of powder diffraction data.

7.6 Supporting Information

Table 7.5: Crystallographic data.

Compound	[NiL1]	[CuL1(EtOH)]·2 CHCl ₃
formula	C ₂₆ H ₂₄ N ₄ NiO ₆	C ₃₀ H ₃₂ N ₄ Cl ₆ CuO ₇
CCDC number	1055605	1055606
<i>M</i> [g·mol ⁻¹]	547.20	836.83
crystal system	Triclinic	Triclinic
space group	<i>P</i> $\bar{1}$	<i>P</i> $\bar{1}$
<i>a</i> [Å]	4.084(1)	8.651(1)
<i>b</i> [Å]	12.918(3)	11.798(2)
<i>c</i> [Å]	22.854(6)	18.199(3)
α [°]	101.906(19)	71.833(11)
β [°]	91.82(2)	86.734(12)
γ [°]	94.00(2)	88.122(12)
<i>V</i> [Å ³]	1175.6(5)	1761.8(4)
<i>Z</i>	2	2
ρ [g·cm ⁻³]	1.546	1.577
μ [mm ⁻¹]	0.877	1.126
crystal size [mm]	0.06 × 0.14 × 0.29	0.084 × 0.103 × 0.115
<i>T</i> [K]	133(2)	133(2)
λ (MoK α) [Å]	0.71073	0.71073
θ -range [°]	1.7–27.8	1.179–28.0
reflns. collected	8045	7594
indep. reflns. (<i>R</i> _{int})	4136 (0.084)	3682 (0.173)
parameters	334	434
<i>R</i> (<i>F</i>) (all data)	0.0497 (0.1498)	0.1176 (0.1779)
<i>wR</i> ²	0.0720	0.2963
<i>Goof</i>	0.680	0.988

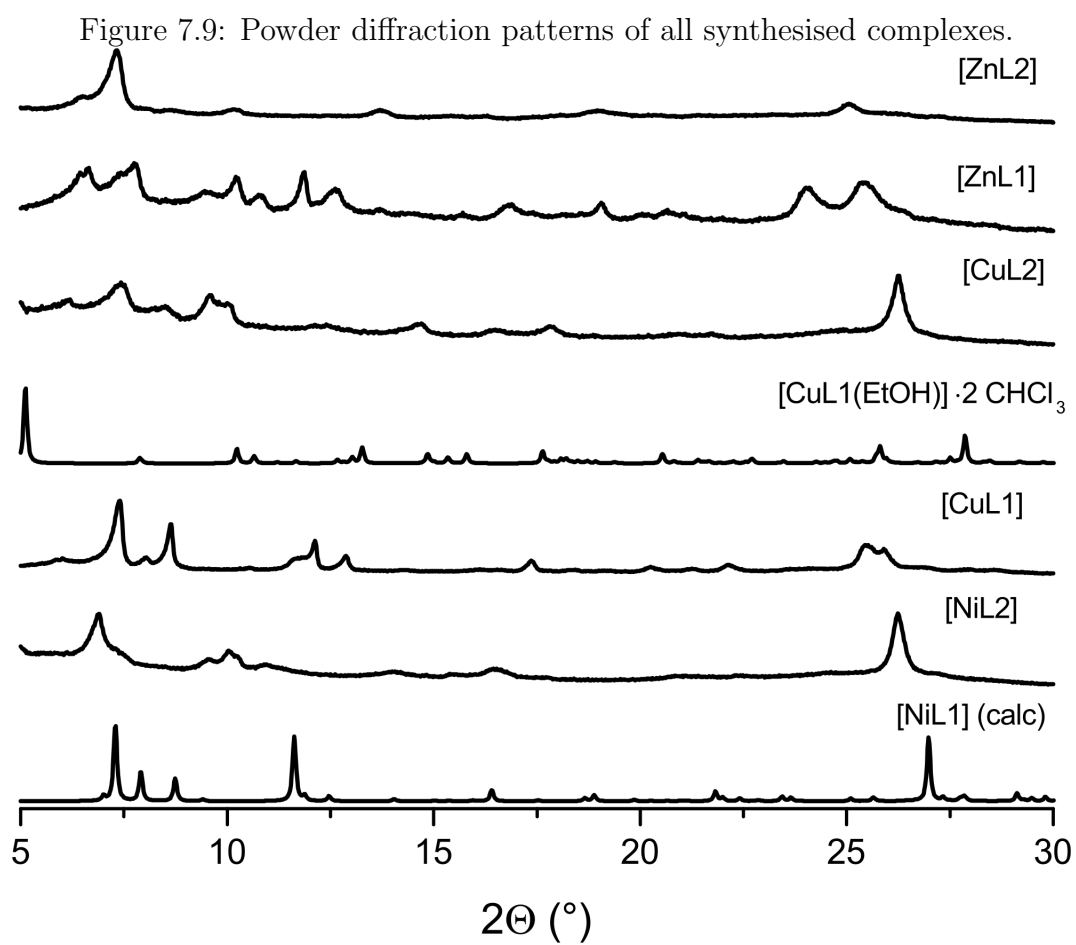


Figure 7.10: Intensity of characteristic absorption bands for the complex [NiL1] in trichloromethane and pyridine solutions, upon complexation and de-complexation of the pyridine molecules.

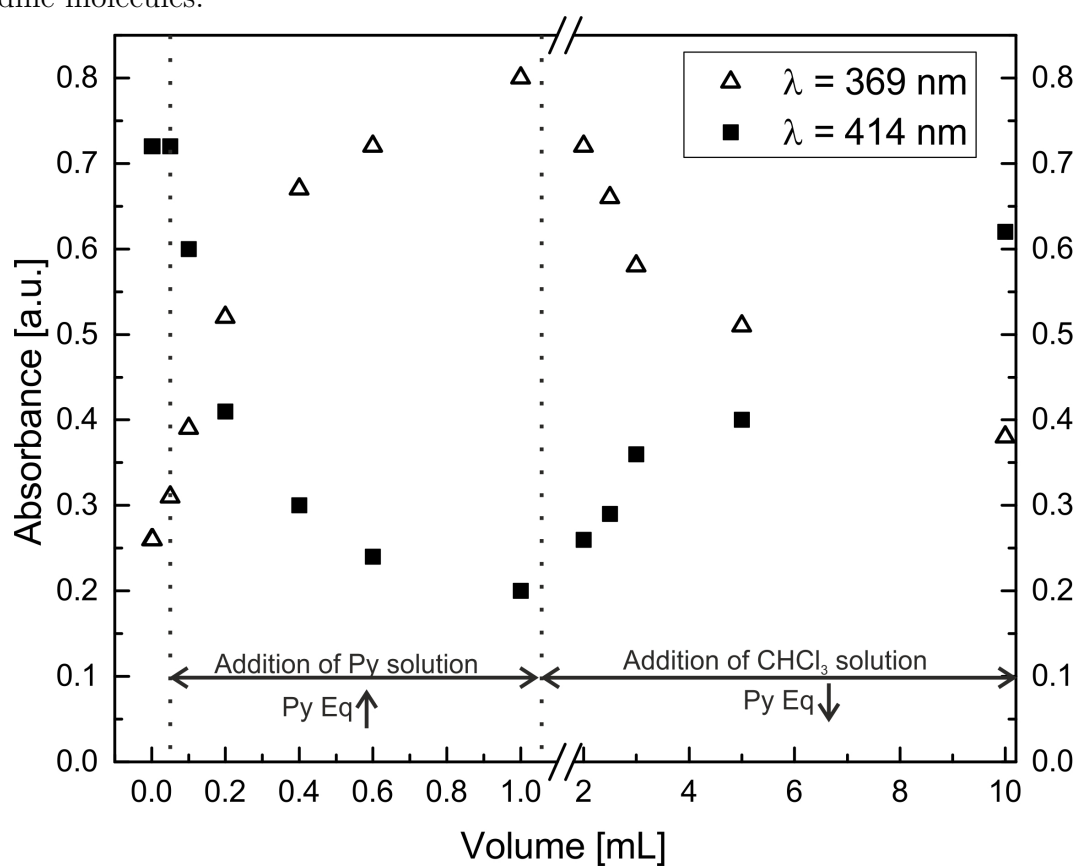
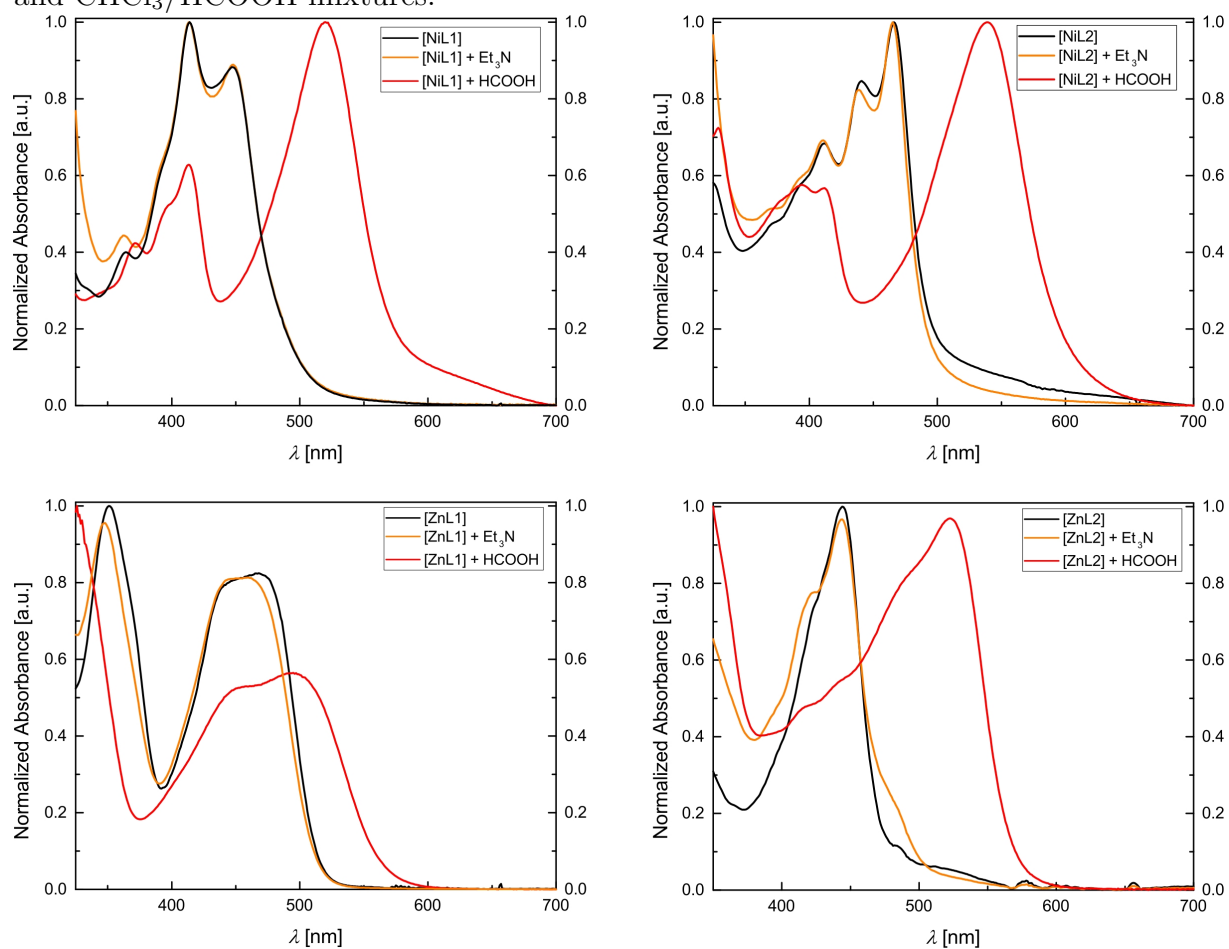


Figure 7.11: UV-Vis spectra of [NiL1], [NiL2], [ZnL1], and [ZnL2] in $\text{CHCl}_3/\text{Et}_3\text{N}$ and $\text{CHCl}_3/\text{HCOOH}$ mixtures.



References

- [1] M. Halcrow, *Spin-Crossover Materials*, John Wiley & Sons Ltd., Chichester, UK, **2013**.
- [2] P. Gülich, H. Goodwin, *Spin Crossover in Transition Metal Compounds I-III*, Springer, Berlin, DE, **2004**.
- [3] P. Gülich, A. B. Gaspar, Y. Garcia, *Beilstein J. Org. Chem.* **2013**, *9*, 342–391.
- [4] A. B. Gaspar, M. Seredyuk, *Coord.Chem. Rev.* **2014**, *268*, 41–58.
- [5] E. Coronado, G. Mínguez Espallargas, *Chem. Soc. Rev.* **2013**, *42*, 1525.
- [6] P. D. Southon, L. Liu, E. A. Fellows, D. J. Price, G. J. Halder, K. W. Chapman, B. Moubaraki, K. Murray, J.-F. Létard, C. J. Kepert, *J. Am. Chem. Soc.* **2009**, *131*, 10998–11009.
- [7] J. Linares, E. Codjovi, Y. Garcia, *Sensors* **2012**, *12*, 4492–4479.
- [8] A. Dei, *Angew. Chem. Int. Ed.* **2005**, *44*, 1160–1163.
- [9] C. Edder, C. Piguet, J.-C. G. Bünzli, G. Hopfgartner, *Chem. Eur. J.* **2001**, *7*, 3014–3024.
- [10] P. N. Martinho, C. Rajnak, M. Ruben, *Spin-Crossover Materials*, John Wiley & Sons Ltd., Chichester, UK, **2013**.
- [11] B. Weber, W. Bauer, J. Obel, *Angew. Chem. Int. Ed.* **2008**, *47*, 10098–10101.
- [12] J. Larionova, L. Salmon, Y. Guari, A. Tokarev, K. Molvinger, G. Molnár, A. Bousseksou, *Angew. Chem. Int. Ed.* **2008**, *47*, 8236–8240.
- [13] E. Coronado, J. R. Galán-Mascarós, M. Monrabal-Capilla, J. García-Martínez, P. Pardo-Ibáñez, *Adv. Mater.* **2007**, *19*, 1359–1361.
- [14] J.-F. Létard, *J. Mater. Chem.* **2006**, *16*, 2550–2559.
- [15] S. Bonhommeau, G. Molnár, A. Galet, A. Zwick, J.-A. Real, J. J. McGarvey, A. Bousseksou, *Angew. Chem. Int. Ed.* **2005**, *44*, 4069–4073.
- [16] B. Weber, *Spin-Crossover Materials*, John Wiley & Sons Ltd., Chichester, UK, **2013**.
- [17] S. Venkataramani, U. Jana, M. Dommaschk, F. D. Sonnichsen, F. Tuzcek, R. Herges, *Science* **2011**, *331*, 445–448.
- [18] S. Thies, H. Sell, C. Schütt, C. Bornholdt, C. Näther, F. Tuzcek, R. Herges, *J. Am. Chem. Soc.* **2011**, *133*, 16243–16250.

-
- [19] S. Thies, C. Bornholdt, F. Köhler, F. D. Sönnichsen, C. Näther, F. Tuzcek, R. Herges, *Chem. Eur. J.* **2010**, *16*, 10074–10083.
- [20] D. Achey, G. J. Meyer, *Inorg. Chem.* **2013**, *52*, 9574–9582.
- [21] C. J. Ballhausen, A. D. Liehr, *J. Am. Chem. Soc.* **1959**, *81*, 538–542.
- [22] M. Matsuda, H. Isozaki, H. Tajima, *Chem. Lett.* **2008**, *37*, 374–375.
- [23] M. Matsuda, K. Kiyoshima, R. Uchida, N. Kinoshita, H. Tajima, *Thin Solid Films* **2013**, *531*, 451–453.
- [24] M. Matsuda, H. Isozaki, H. Tajima, *Thin Solid Films* **2008**, *517*, 1465–1467.
- [25] L. Salmon, G. Molnár, D. Zitouni, C. Quintero, C. Bergaud, J.-C. Micheau, A. Bousseksou, *J. Mater. Chem.* **2010**, *20*, 5499.
- [26] C.-F. Wang, R.-F. Li, X.-Y. Chen, R.-J. Wei, L.-S. Zheng, J. Tao, *Angew. Chem. Int. Ed.* **2015**, *54*, 1574–1577.
- [27] H. Matsukizono, K. Kuroiwa, N. Kimizuka, *Chem. Lett.* **2008**, *37*, 446–447.
- [28] Y. Garcia, F. Robert, A. D. Naik, G. Zhou, B. Tinant, K. Robeyns, S. Michotte, L. Piraux, *J. Am. Chem. Soc.* **2011**, *133*, 15850–15853.
- [29] A. Santoro, L. J. Kershaw Cook, R. Kulmaczewski, S. A. Barrett, O. Cespedes, M. A. Halcrow, *Inorg. Chem.* **2015**, *54*, 682–693.
- [30] M. Hasegawa, F. Renz, T. Hara, Y. Kikuchi, Y. Fukuda, J. Okubo, T. Hoshi, W. Linert, *Chem. Phys.* **2002**, *277*, 21–30.
- [31] L. J. Kershaw Cook, M. A. Halcrow, *Polyhedron* **2015**, *87*, 91–97.
- [32] M. Engeser, L. Fabbrizzi, M. Licchelli, D. Sacchi, *Chem. Commun.* **1999**, 1191–1192.
- [33] L. Wolf, E.-G. Jäger, *Z. Anorg. Allg. Chem.* **1966**, *346*, 76–91.
- [34] C. Lochenie, S. Schlamp, A. P. Railliet, K. Robeyns, B. Weber, Y. Garcia, *CrystEngComm* **2014**, *16*, 6213.
- [35] W. Bauer, T. Ossiander, B. Weber, *Z. Naturforsch. B* **2010**, 323–328.
- [36] N. Chopin, M. Médebielle, O. Maury, G. Novitchi, G. Pilet, *Eur. J. Inorg. Chem.* **2014**, 6185–6195.
- [37] H. S. Jung, P. S. Kwon, J. W. Lee, J. I. Kim, C. S. Hong, J. W. Kim, S. Yan, J. Y. Lee, J. H. Lee, T. Joo, J. S. Kim, *J. Am. Chem. Soc.* **2009**, *131*, 2008–2012.
-

- [38] Z. Liu, W. He, Z. Guo, *Chem. Soc. Rev.* **2013**, *42*, 1568–1600.
- [39] B. Valeur, M. N. Berberan-Santos, *Molecular Fluorescence. Principles and applications*, Wiley-VCH, Weinheim, DE, **2013**.
- [40] N. P. Loveless, K. C. Brown, R. H. Horrocks, *J. Org. Chem.* **1981**, *46*, 1182–1185.
- [41] G. W. H. Cheeseman, *J. Chem. Soc.* **1962**, 1170.
- [42] X. Shang, X. Li, N. Xi, Y. Zhai, J. Zhang, X. Xu, *Sens. Actuators B* **2011**, *160*, 1112–1119.
- [43] L. Claisen, *Justus Liebigs Ann. Chem.* **1897**, *297*, 1–98.
- [44] A. Altomare, M. C. Burla, M. Camalli, G. L. Cascarano, C. Giavazzo, A. Guagliardi, A. G. G. Moliterni, G. Polidori, R. Spagna, *J. Appl. Crystallogr.* **1999**, *35*, 115–119.
- [45] G. Sheldrick, *Acta Crystallogr., Sect. A* **2008**, *64*, 112–122.
- [46] C. K. Johnson, M. N. Burnett, *ORTEP-III*, **1996**, Oak-Ridge National Laboratory, Oak-Ridge, TN.
- [47] E. Keller, *Schakal-99*, **1999**, University of Freiburg, Freiburg DE.

8. Synthesis and analysis of the optical properties of a phenanthroline-derived Schiff base-like Ru(II)-Ni(II) complex

Hannah Kurz,^{a,†} Charles Lochenie,^{a,†} Kristina G. Wagner,^b Matthias Karg^b and Birgit Weber^{*,a}

[†]Those authors equally contributed to the publication

^aInorganic Chemistry II, Universität Bayreuth, Universitätstrasse 30, NW I, 95440 Bayreuth, Germany.

^bPhysical Chemistry I, Heinrich-Heine-Universität Düsseldorf, Universitätstrasse 1, Geb. 26.43.02, 40204 Düsseldorf, Germany.

to be submitted

Abstract

A phenanthroline-derived Schiff base-like ligand with a covalently linked Ru(II) phosphorescent unit was synthesised and converted into a bimetallic Ru(II)-Ni(II) complex. The optical properties were studied to examine a possible phosphorescence quenching through a non-radiative energy transfer upon coordination induced spin state switch. Therefore the ligand and the Ni(II) complex were studied by UV-Vis and fluorescence spectroscopy in water and pyridine solutions.

8.1 Introduction

Complexes with a $3d^4$ to $3d^7$ transition metal centre and an octahedral coordination sphere can exist in different spin states, which enable the design of switchable, bistable molecules called spin crossover (SCO) complexes. Mostly, spin transition (ST) is triggered by external stimuli such as temperature, light irradiation, or pressure and occurs without a change of the coordination number.^[1,2] In contrast, a ST can be observed as well with a change of the coordination number; this phenomenon is called *Coordination Induced Spin State Switch* (CISSS). A well-known example is the switching of Ni(II) complexes from the diamagnetic ($S = 0$) square planar to the paramagnetic ($S = 1$) square pyramidal or octahedral coordination sphere. This phenomenon can be triggered in solution by the coordination of (solvent) molecule(s), the CISSS being chemically-stimulated. CISSS can also be photoinduced when a coordinating partner is covalently linked to the ligand of the complex (LD-CISSS).^[3-6]

A CISSS, which includes a change of the electronic state, is accompanied by a change of the magnetic, optical, and structural properties. The coupling of these changes with additional properties such as photoluminescence can lead to multifunctional molecular devices with possible applications in temperature or chemical sensing.^[7,8] Based on this concept a fluorescent molecular thermometer with a Ni(II) CISSS system was reported, with a temperature-dependent coordination of acetonitrile.^[9] We recently reported a phenazine-derived Schiff base-like ligand and the corresponding Ni(II), Cu(II), and Zn(II) complexes. It was demonstrated that complexes with a diamagnetic metal centre like Zn(II) or Ni(II) (in a square planar coordination sphere) show fluorescence, whereas paramagnetic metal centres like Cu(II) or Ni(II) (in a square pyramidal or octahedral coordination sphere) quench the emission properties through a non-radiative energy transfer. The nature of the energy transfer (Förster or Dexter type) could at this time not be assessed, and required further experiment. In order to get more information about the type of energy transfer, we decided to exchange the phenazine fluorophore for another fluorophore and perform the same experiments.^[10]

Here we present a new ligand system in which the heteroaromatic fluorophore was replaced by a phosphorescent Ru(II) unit that is linked covalently to the mentioned Schiff base-like ligand system. The Ni(II) complex was synthesised to examine the influence of the spin state of the Nickel metal centre for the emission properties. Therefore, the optical properties of the new metallaligand and the Ni(II) complex were studied by UV-Vis and fluorescence spectroscopy in water and pyridine solutions.

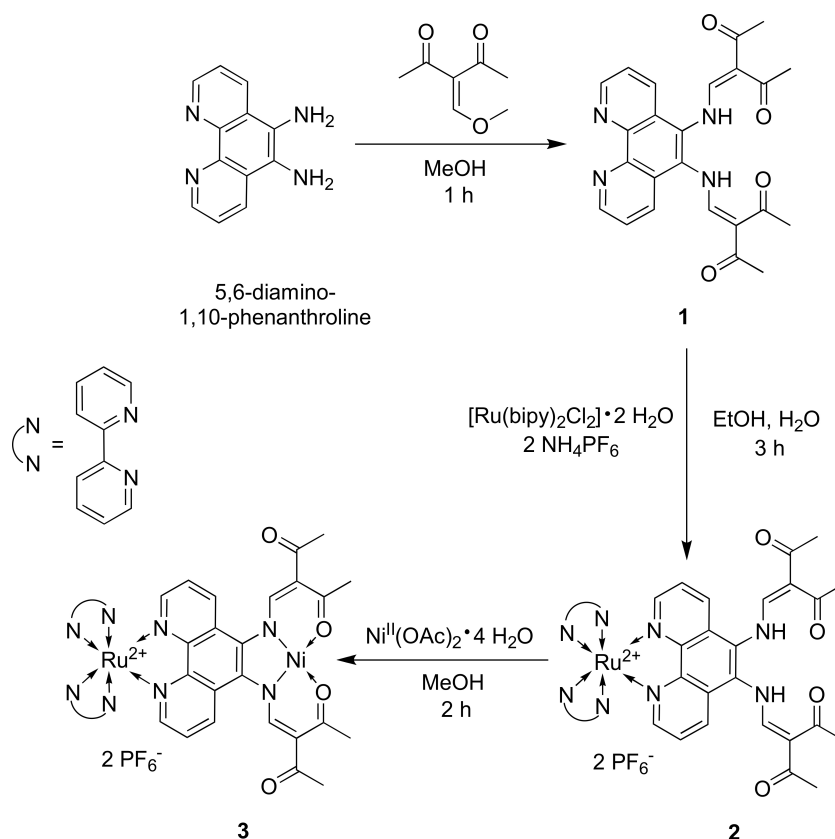
8.2 Results and Discussion

8.2.1 Synthesis

The bimetallic Ru(II)-Ni(II) complex is obtained in three steps from 5,6-diamino-1,10-phenanthroline.^[11] The synthesis pathway is depicted in Scheme 8.1. In the first step, the ligand **1** was obtained from a condensation reaction between the 5,6-diamino-1,10-phenanthroline and a keto-enol ether, using a method already developed for similar Schiff base-like ligands.^[12–14] The compound was characterised with ¹H- and ¹³C-NMR spectroscopy, as well as CHN analysis, mass spectrometry, and IR spectroscopy. In the ¹H-NMR, characteristic peaks for the N–H proton at 12.18 ppm, and as well as the corresponding IR band were found. Also important is the C=O band at 1611 cm⁻¹. The crystal structure of **1** could be determined and is described further.

In the next step, the phosphorescent Ru(II) centre was formed by ligation of **1** with [Ru(bipy)₂Cl₂] (bipy = 2,2'-bispyridine). The resulting orange Ru(II) complex **2** was precipitated with hexafluorophosphate as counter-anion, and characterised with CHN analysis, ESI mass spectrometry, and IR spectroscopy. In the IR spectrum, a strong band at 830 cm⁻¹ for the P–F bond appears, and only a small shift of the C=O bands to 1616 cm⁻¹ was observed. In the mass spectra the [M]²⁺ and [M+PF₆]⁺ could be identified.

In the last step, the Ni(II) is inserted into the chelate cycles of the ligand. The Ni(II) is inserted at last, as we could not get a clean product while reacting Nickel(II) acetate with the ligand **1**, there is probably a competition between the phenanthroline and the chelate cycles of the ligand for the complexation of the Nickel(II). For the complexation,



Scheme 8.1: Pathway of synthesis of the Ni(II) complex **3** described in this work.

the Nickel(II) acetate is used as the acetate deprotonates the chelate cycles of **1**. The compound **3** was obtained as red material, and was characterised with CHN analysis, ESI mass spectrometry, and IR spectroscopy. In the IR spectrum, the P–F band of the counter-anion is still present, and the C=O band is shifted to 1659 cm^{-1} , in agreement with the coordination of a metal centre. As for **2**, the mass peak for $[M]^{2+}$ and $[M+PF_6]^+$ could be identified. Single crystals could be obtained from this compound, and the determination of the structure is discussed further.

8.2.2 Crystal structure analysis

Suitable crystals of **1** for X-ray structure analysis were obtained by slow evaporation of a methanol solution at room temperature. The structure of the yellowish block crystals with the composition $1 \cdot \text{MeOH} \cdot \text{H}_2\text{O}$ was determined. The crystallographic data are summarised in Table 8.1. The compound crystallises in the triclinic space group $P\bar{1}$. The asymmetric unit consists of one ligand molecule, one water molecule, and one methanol

molecule as shown in the ORTEP drawing in Figure 8.2. The chelate cycles have two different tautomeric forms: keto-enamine and imino-enol. Selected bond lengths within the chelate cycles are presented in Table 8.2. Analysis of the C–C bond lengths clearly shows that the ligand crystallises as its keto-enamine tautomer as already reported for other Schiff base-like ligands with similar chelate cycles.^[12–14] The molecule twists the chelate cycles in opposite directions, out of the phenanthroline plane. An explanation for the non-planarity of the ligand is the steric hindrance between the protons H4(C4) and H17(C17) of the chelate cycles and the aromatic protons H7(C7) and H14(C14) of the phenanthroline group.

Table 8.1: Crystallographic data of **1**·MeOH·H₂O and **(3)**₂· acetone.

Compound (unit cell)	1 ·MeOH·H ₂ O	(3) ₂ · acetone
description	yellowish block	red platelet
sum formula	C ₂₅ H ₂₈ N ₄ O ₆	C ₈₈ H ₇₂ F ₂₄ N ₁₆ Ni ₂ O ₈ P ₄ Ru ₂
<i>M</i> [g·mol ⁻¹]	480.52	2381.01
crystal system	triclinic	triclinic
space group	<i>P</i> $\bar{1}$	<i>P</i> $\bar{1}$
<i>a</i> [Å]	8.5658(8)	14.763(3)
<i>b</i> [Å]	11.4830(11)	18.459(2)
<i>c</i> [Å]	12.4529(12)	20.580(2)
α [°]	72.910(8)	111.282(8)
β [°]	82.776(8)	95.483(12)
γ [°]	88.143(7)	97.412(12)
<i>V</i> [Å ³]	1178.6(2)	5120.2(12)
<i>Z</i>	2	2
ρ [g·cm ⁻³]	1.354	1.544
μ [mm ⁻¹]	0.098	0.817
crystal size [mm]	0.165 × 0.160 × 0.128	0.198 × 0.170 × 0.074
<i>T</i> [K]	133(2)	140(2)
λ (MoK α) [Å]	0.71069	0.71069
θ -range [°]	1.70–27.47	1.40–24.98
reflns. collected	12190	22768
indep. reflns (<i>R</i> _{int})	5252 (0.037)	4202 (0.239)
parameters	335	798
<i>R</i> (<i>F</i>) (all data)	0.0432 (0.0952)	0.1842 (0.4175)
<i>wR</i> ²	0.851	0.4137
<i>Goof</i>	0.820	0.965

The crystal packing of **1**·MeOH·H₂O is characterised by a hydrogen bond network. The crystal packing is depicted in Figure 8.3 and selected distances and angles are listed in Table 8.3. The crystal packing is defined by solvent molecules that form a hydrogen bond

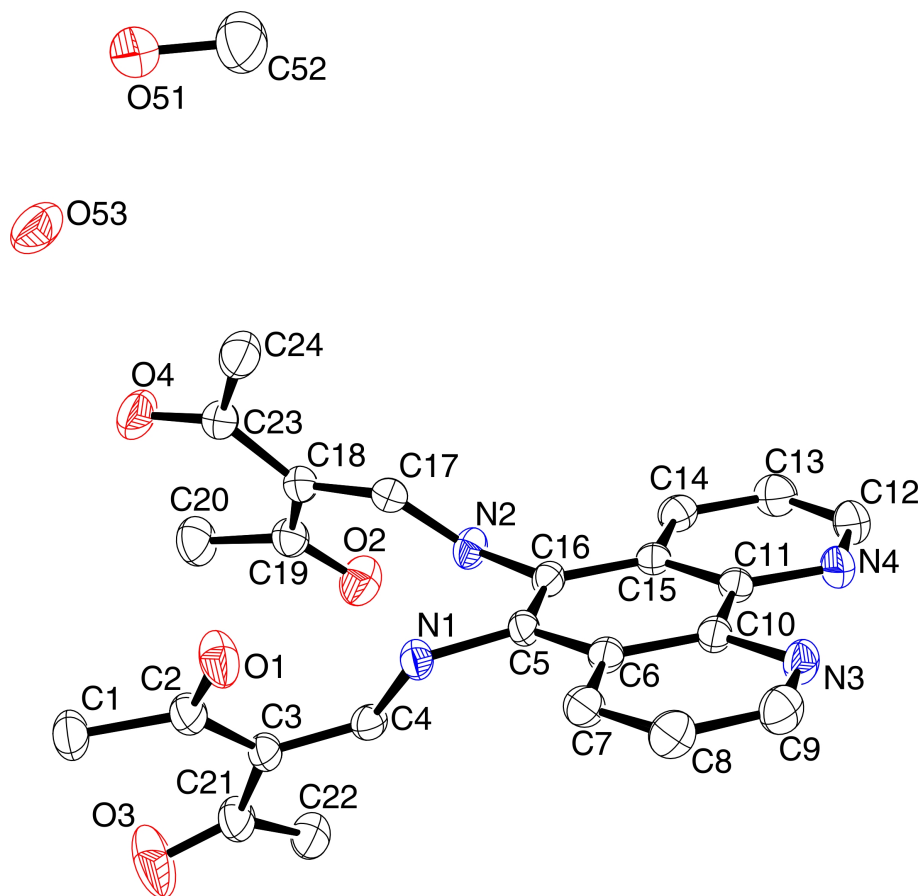


Figure 8.2: ORTEP drawing of the asymmetric unit of $1 \cdot \text{MeOH} \cdot \text{H}_2\text{O}$. Thermal ellipsoids are shown at 50% probability level. Hydrogen atoms are omitted for clarity.

chain with the sequence $[\text{MeOH}-\text{H}_2\text{O}-\text{H}_2\text{O}-\text{MeOH}]_n$ propagating towards $[100]$. The water solvent molecule binds with its own image molecule over an inversion centre of the cell, and with the methanol solvent molecule, which also binds to its image molecule over an inversion centre. Formally, the propagation of the hydrogen bond chain is incompatible with the symmetry of the space group, and was refined using disorder commands. In addition to this chain, the water molecule acts as a donor for the ketonic oxygen O4 of the ligand molecule, which means that each solvent chain is "decorated" with ligand molecules. Furthermore, one of the chelate cycles of the ligand molecule makes also an hydrogen bond with its image over an inversion centre, forming molecule pairs. Here the nitrogen N1 of the chelate cycle acts as the donor and the oxygen O1 of the chelate cycle from another ligand molecule acts as the acceptor. As one "arm" of the ligand molecule interacts with the solvent chain through its ketonic oxygen, and the other "arm" with its

Table 8.2: Selected bond lengths for the chelate cycle of **1·MeOH·H₂O**.

Bond	Length [Å]	Bond	Length [Å]
O1–C2	1.234(2)	O2–C19	1.241(3)
C2–C3	1.462(3)	C19–C18	1.449(3)
C3–C4	1.387(3)	C18–C17	1.387(3)
C4–N1	1.330(2)	C17–N2	1.339(2)

image, a 2D hydrogen bond network with base vectors [100] and [0-11] is formed. Although the phenanthroline group presents an extended π -system, no π -interactions were observed.

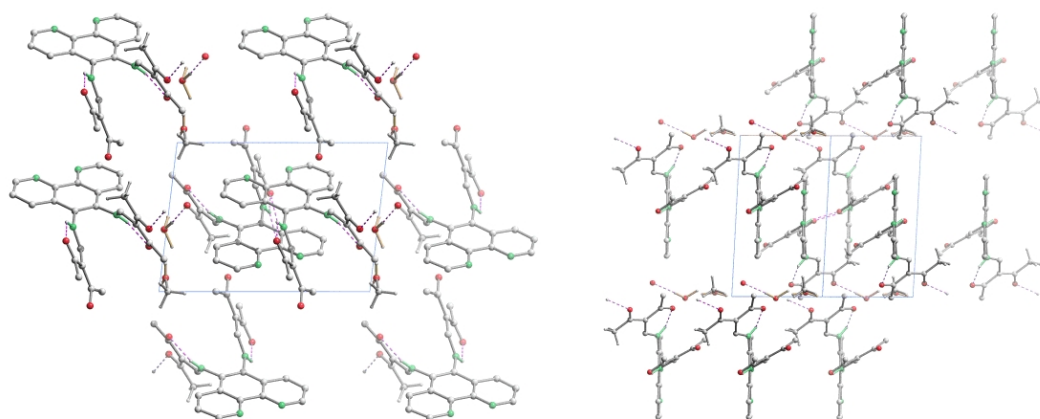


Figure 8.3: Illustration of the crystal packing of **1·MeOH·H₂O** along [010] (left) and [110] (right). Hydrogen atoms not involved in hydrogen bonds are omitted for clarity. Hydrogen bonds are illustrated as dashed lines.

Table 8.3: Selected distances and angles of the hydrogen bonds of **1·MeOH·H₂O**.

D–H···A	D–H [Å]	H···A [Å]	D···A [Å]	D–H···A [°]
N1–H1···O1	0.88	2.04	2.650(2)	125
N1–H1···O1 ^a	0.88	2.15	2.923(2)	147
N2–H2···O2	0.88	2.00	2.590(2)	123
O53–H53C···O4	0.87(3)	1.92(3)	2.791(3)	176(2)
O53–H53A···O51	1.10(14)	1.85(15)	2.765(3)	138(9)
O51–H51A···O53	0.94(7)	1.99(7)	2.765(3)	139(5)

a = 3-x, 1-y, 1-z

Crystals of **3** for X-ray structure analysis were obtained by slow evaporation of an acetone solution at room temperature. Although solving the structure went smoothly, the red platelet with the composition (**3**)₂·**acetone** were unfortunately too small and of

too poor quality for a complete refinement of the structure. Only the metal centres and the oxygen atoms could be set anisotropic, and the PF_6^- anions present strong disorder. The structure is here presented as structural motif, and no conclusions will be made from the bond lengths or angles. The crystallographic data are summarised in Table 8.1. The compound crystallises in the triclinic space group $P\bar{1}$. The asymmetric unit consists of two complex molecules, four PF_6^- anions, and one acetone molecule. An ORTEP drawing of one complex molecule is shown in Figure 8.4. The ORTEP drawing illustrates that the target molecule was obtained, with a Ru(II) metal centre bound to two bipy ligands and connected to the Ni(II) centre through the phenanthroline-derived Schiff base-like ligand. Despite the poor quality, the structure shows that the chelate cycles coordinating the Ni(II) centre are not coplanar with the phenanthroline group binding the Ru(II) centre, which means that the two metal centres are not part of the same π -system, in contrast to the phenazine-derived compounds already reported. In the Supporting Information: Figure 8.7, the asymmetric unit of $\mathbf{1}\cdot\text{MeOH}\cdot\text{H}_2\text{O}$ is illustrated.

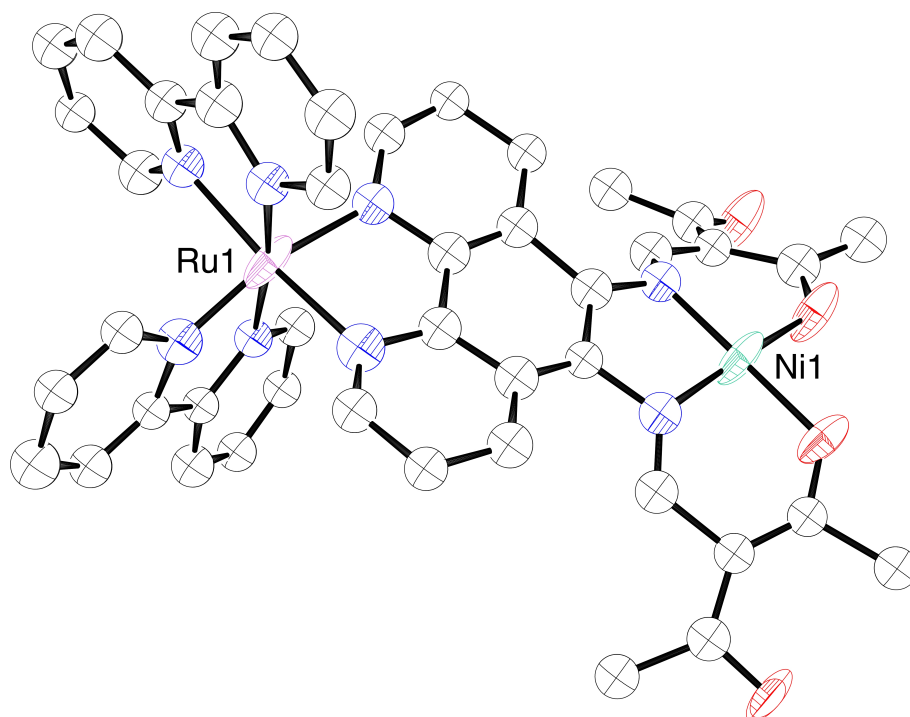


Figure 8.4: ORTEP drawing of **3**. Thermal ellipsoids are shown at 50% probability level. Hydrogen atoms are omitted for clarity. Only the Ru(II), Ni(II), and the oxygen atoms are set anisotropic.

8.2.3 UV-Vis spectroscopy

The optical properties of the metallaligand **2** and the complex **3** were studied by UV-Vis spectroscopy using water or pyridine as solvent. As pyridine exhibits a high affinity for coordination on the metal centre and water shows a lower affinity to the metal centre, the influence of coordinating solvent molecules on the absorption properties can be determined. In the case of compound **3**, it means that the Ni(II) centre lies in a square planar coordination sphere in water solution, and in a square pyramidal/octahedral coordination sphere in pyridine. The absorption spectra of **2** show great similarity between the water and the pyridine solution, with two main peaks at $\lambda = 430$ and $\lambda = 457$ nm (Figure 8.5A). The absorbance peaks at approximately 457 nm features the highest absorbance intensity and belongs to the MLCT transition towards the bipy as the MLCT transition of $[\text{Ru}(\text{bipy})_3]^{2+}$ was measured at 455 nm.^[15] Similar luminescent phenanthroline-derivative Ru(II) complexes have shown a MLCT transition around 430 nm, therefore we can attribute the peak at 430 nm to the MLCT transition towards the phenanthroline-derived Schiff base-like ligand.^[16–18]

Sample **3**, in contrast to its precursor **2**, shows a drastic change of the absorption properties when solved in pyridine (Figure 8.5C). The main absorption peak at 425 nm in water is shifted to 454 nm in pyridine, and a new absorption band at 366 nm appears, in agreement with the coordination of pyridine molecules on the Ni(II) centre. The maximum absorption wavelength and emission wavelength are given in Table 8.4.

Table 8.4: Maximum absorption and emission wavelength of **2** and **3** in water and pyridine.

sample	$\lambda_{abs,1}$ [nm]	$\lambda_{abs,2}$ [nm]	$\lambda_{abs,3}$ [nm]	λ_{em} [nm]
2 (water)	-	428	456	624
2 (pyridine)	375	431	458	624
3 (water)	-	425	-	624
3 (pyridine)	366	454	-	630

8.2.4 Steady-state emission spectroscopy

The fluorescence spectra were measured with irradiation at $\lambda_{ex} = 455$ nm. The emission data of **2** and **3** are shown in Figure 8.6B and Figure 8.6D. In water, both samples present

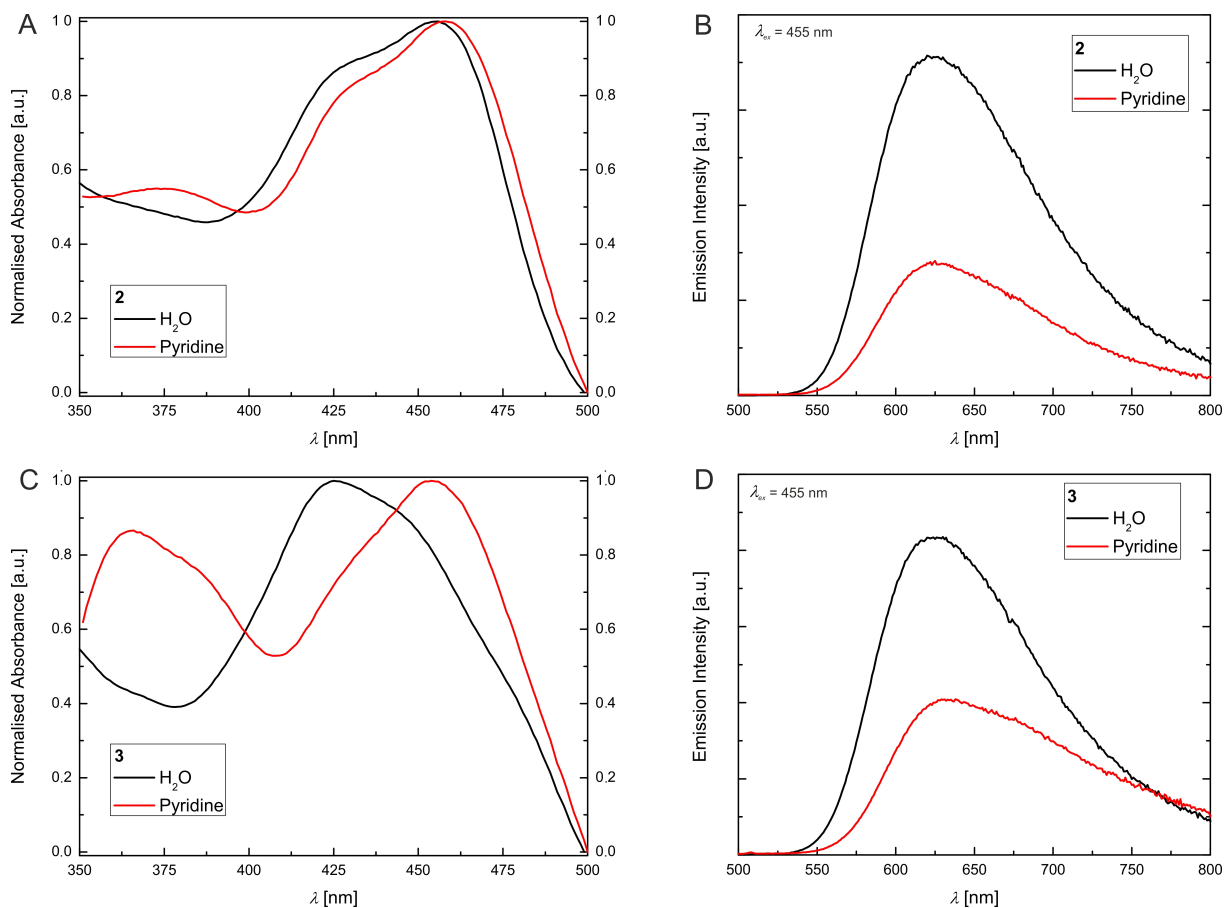


Figure 8.5: Absorption and emission data of **2** and **3** in water (black line) and pyridine (red line) solutions.

an emission band at 624 nm, belonging to a radiative MLCT deactivation. In pyridine, the emission properties of **2** and **3** differ a bit, with a slight shift of the emission maximum from 624 nm for **2** to 630 nm for **3**. When equimolar solutions of **2** and **3** are measured with the same instrument parameters, one can see that the emission intensity in pyridine is lower than in water. However, this change appears to be only solvatochromism, as this effect was observed for both samples **2** and **3**, and only **3** contains the Ni(II) centre, which is coordinated by the pyridine.

8.2.5 Time-resolved emission spectroscopy

In order to investigate a possible photoluminescence quenching through an energy transfer between the Ru(II) and the Ni(II) centres upon coordination the latter one, time-resolved emission spectroscopy measurements were performed under aerobic and argon

atmosphere. The lifetime measurements for sample **2** and **3** are presented in Figure 8.6. In all measurements two lifetimes were observed, a rather long-lived state with $\tau_1 = 350$ –750 ns, and a short-lived state with $\tau_2 = 5$ –200 ns, which indicates the existence of two deactivation processes. The long-lived state is the triplet state, commonly observed for Ru(II) polypyridine complexes, the short-lived state could come from fluorescence, or from another quenching effect taking place. Two observations come out of the measurements: firstly, the lifetimes in both solvents are shorter for the Ni(II) complex **3** than for the metallaligand **2**, leading to the conclusion that metallation of the chelate cycles partially deactivates the emission. Secondly, the lifetimes in pyridine solutions are shorter than for the water solutions, but as this effect is seen for both the metallaligand **2** and the complex **3**, this can probably be attributed to solvatochromism. All lifetimes of the solutions measured under aerobic conditions are shorter than for the solutions measured under argon atmosphere, confirming that the excited state measured is a triplet state, quenched in presence of molecular oxygen. All lifetime constants τ_1 and τ_2 are presented in Table 8.5.

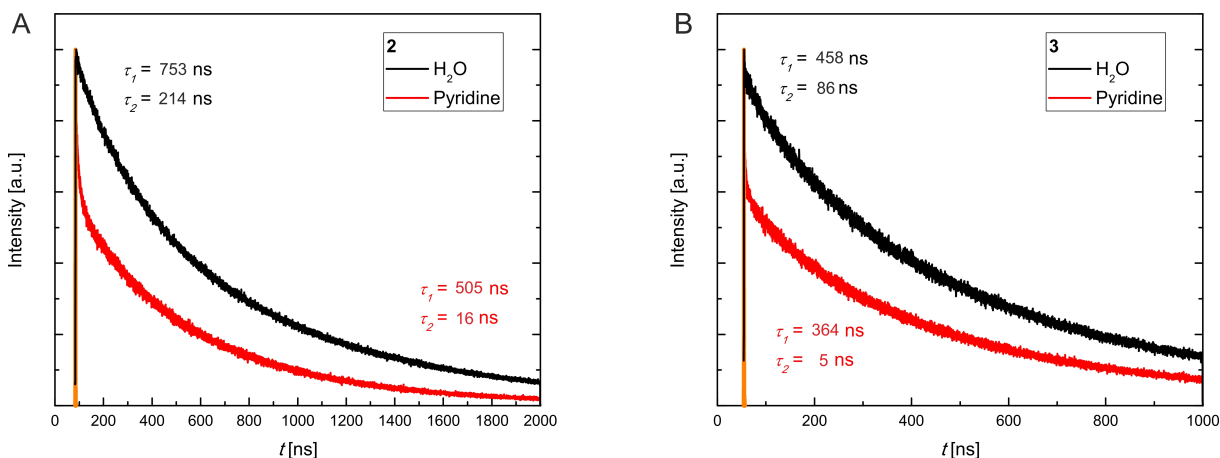


Figure 8.6: Time-resolved emission measurements of **2** and **3** in water (red line) and pyridine (black line) solutions.

8.2.6 Discussion

In previous work, we demonstrated that the emission of a phenazine-derived Schiff base-like Ni(II) complex could be effectively quenched through the coordination of pyridine

Table 8.5: Excited lifetimes τ_1 and τ_2 of **2** and **3** in water and pyridine under aerobic and argon atmosphere.

sample	τ_1 (water) [ns]	τ_2 (water) [ns]	τ_1 (pyridine) [ns]	τ_2 (pyridine) [ns]
2 (aerobic)	401(3)	156(8)	276.6(8)	74(5)
2 (argon)	753(6)	214(4)	504.7(6)	15.6(2)
3 (aerobic)	334(10)	38(5)	227.5(15)	6.2(3)
3 (argon)	458(4)	86(4)	363.6(7)	4.57(10)

molecule on the metal centre, inducing a *Coordination Induced Spin State Switch*. Time-resolved fluorescence spectroscopy revealed that a non-radiative energy transfer between the fluorophore and the paramagnetic Ni(II) centre was the quenching mechanism. The type of energy transfer (Förster or Dexter) could at this moment not be pinpointed. A very important point was the inclusion of the Ni(II) complex in the emitting π -system of the complex. We presented in this work the case of a similar system (sample **3**), where the phenazine fluorophore was exchanged for a phosphorescent polypyridine Ru(II) unit. However, no evidences of a quenching effect arising from the coordination of the Ni(II) centre and the subsequent CISSS were found. When analysing structural differences between the two systems, one can see that in case of sample **3**, the Ni(II) centre is not part of the π -system of the fluorophore, as the chelate cycles bend out of the phenanthroline plane. In the case of a Dexter electron transfer as quenching mechanism, the inclusion of the acceptor and the donor in the same π -system is needed to effectively transfer electrons. As in this case the Ni(II) centre is not included in the π -system of the Ru(II) unit, it cannot exchange electrons and effectively quench the emission.

8.3 Experimental Section

Synthesis The synthesis of **2** and **3** were carried out under argon using Schlenk tube techniques. The starting materials 5,6-diamino-1,10-phenanthroline,^[11] ethoxymethyleneethylacetate,^[19] and Ru(bipy)₂Cl₂·2H₂O^[20] were synthesised according to literature. Ammonium hexafluorophosphate (99.5%, Alfa Aesar) and Nickel(II) acetate tetrahydrate (99%, Fluka) were used without further purification. Methanol and ethanol were of analytical grade. NMR spectra were measured with a *Varian INOVA 300*. Elemental analyses were measured with a *Vario El III* from *Elementar Analysen-Systeme*. Mass spectra were

recorded with a *Finnigan MAT 8500* with a data system *MASPEC II*. IR spectra were recorded with a *Perkin Elmer Spectrum 100* FT-IR spectrometer.

1. 5,6-diamino-1,10-phenanthroline (0.2 g, 0.95 mmol) and ethoxymethylene-ethylacetate (0.40 g, 2.89 mmol, 3 eq) were dissolved in methanol (10 mL) and heated to reflux during 1 h. The solvent of the red solution was reduced and the suspension was stored at -25°C overnight. The yellow precipitate was filtrated off, recrystallised from methanol and dried *in vacuo*. Yield: 0.14 g (35 %). $\text{C}_{24}\text{H}_{22}\text{N}_4\text{O}_4\cdot\text{MeOH}$ (462.51 g/mol) found (calculated): C 61.80 (calc. 64.92); H 5.750 (5.670); N 12.14 (12.11). MS (DEI(+), 70 eV): $m/z = 430$ (M^+ , 33%), 43 (COMe, 100%). $^1\text{H-NMR}$ (300 MHz, DMSO, 23°C): $\delta = 12.18$ (d, $J = 12.9$ Hz, 2 H, N-H), 9.18 (d, $J = 3.3$ Hz, 2 H, HArom.), 8.41 (d, $J = 8.1$ Hz, 2 H, HArom.), 8.27 (d, $J = 12.9$ Hz, 2 H, CH=), 7.90 (dd, $J^1 = 8.1$ Hz, $J^2 = 8.4$ Hz, 2 H, HArom.), 2.41 (s, 6 H, $-\text{CH}_3$), 2.14 (s, 6 H, $-\text{CH}_3$). $^{13}\text{C-NMR}$ (300 MHz, DMSO, 23°C) $\delta = 200$ ($\text{C}_2\text{C}=\text{O}$); 195 ($\text{C}_2\text{C}=\text{O}$); 160 (NCH=C); 155 ($\text{C}_2\text{C}=\text{C}$); 151 (NCH=C); 144 (NCC $_2$); 132 (C_2CH); 130 ($\text{C}_2\text{C}=\text{C}$); 125 (C_2CH); 124 (NCC=C); 52 (CCH $_3$); 47 (CCH $_3$). IR: $\tilde{\nu} = 3410$ (O-H), 3164 (N-H), 1611 (C=O), 1559 (C=O) cm^{-1} .

2. $\text{Ru}(\text{bipy})_2\text{Cl}_2\cdot 2\text{H}_2\text{O}$ (0.49 g, 1.01 mmol) and **1** (0.52 g, 1.21 mmol, 1.2 eq) were dissolved in a mixture of degassed ethanol (10 mL) and degassed water (10 mL). The solution was heated to reflux during 3 h. NH_4PF_6 (2.00 g, 12.1 mmol, 10 eq) was solved in water (10 mL) and the aqueous solution was added to the red, fluorescent solution. The mixture was stirred for 25 min at room temperature. The orange suspension was stored at room temperature overnight. The orange precipitate was filtrated off, washed with cold water and cold diethylether and dried *in vacuo*. Yield: 0.94 g (82 %). $\text{C}_{44}\text{H}_{38}\text{F}_{12}\text{N}_8\text{O}_4\text{P}_2\text{Ru}$ (1133.84 g/mol) found (calculated): C 41.56 (calc. 46.61); H 3.136 (3.380); N 10.16 (9.88). MS (ESI(+), 70 eV): $m/z = 989.1$ ($[\text{M}+\text{PF}_6]^+$, 8%), 422.2 ($[\text{M}]^{2+}$, 21%), 157.2 (bipy, 59%). IR: $\tilde{\nu} = 1616$ (C=O), 1568 (C=O), 828 (P-F) cm^{-1} .

3. **2** (0.40 g, 0.35 mmol) and $\text{Ni}(\text{OAc})_2\cdot 4\text{H}_2\text{O}$ (0.10 g, 0.42 mmol, 1.2 eq) were dissolved in degassed methanol (15 mL). The solution was heated to reflux during 2 h. After cooling to room temperature the dark red precipitate was filtrated off, washed with cold water and cold diethylether and dried *in vacuo*. Yield: 0.15 g (36 %). $\text{C}_{44}\text{H}_{36}\text{F}_{12}\text{N}_8\text{NiO}_4\text{P}_2\text{Ru}\cdot\text{H}_2\text{O}$

(1208.53 g/mol) found (calculated): C 41.87 (43.73); H 3.117 (3.170); N 9.16 (9.27). MS (ESI-(+), 70 eV): m/z = 1045.1 ($[M+PF_6]^+$, 12%), 450.0 ($[M]^{2+}$, 23%), 273.3 ($[M^{2+}-COMe-(bipy)_2]$, 100%), 157.2 (bipy, 11%). IR: $\tilde{\nu}$ = 1659 (C=O), 1563 (C=O), 832 (P-F) cm^{-1} .

X-ray structure analysis The X-ray analysis of **1** and **3** was performed with a Stoe StadiVari diffractometer using graphite-monochromated MoK α radiation. The data were corrected for Lorentz and polarization effects. The structures were solved by direct methods (SIR-97)^[21] and refined by full-matrix least-square techniques against $F_o^2-F_c^2$ (SHELXL-97).^[22] All hydrogen atoms were calculated in idealised positions with fixed displacement parameters. ORTEP-III^[23,24] was used for the structure representation, SCHAKAL-99^[25] to illustrate molecule packing.

Optical measurements Absorbance spectra were obtained using an Agilent UV-Vis spectrophotometer 8453 (Agilent Technologies, USA) operating in a spectral range of 190–1100 nm. The spectra were measured at 298 K in quartz cells with 1 cm lightpath (Hellma, Germany). Fluorescence measurements were performed with a FLS980 (Edinburgh Instruments, UK) fluorescence spectrometer equipped with double monochromators (1800 grooves per mm) in excitation and emission. A Xe lamp (360 W) was used as excitation source for steady-state fluorescence measurements. Time-resolved measurements were performed with a pulsed supercontinuum fiber laser (WhiteLase SC-400, Fianium, UK) with a pulse width <10 ps. Emission from the sample was collected at an angle of 90° with respect to the excitation path. The emitted beam was focused onto a single photon counting photomultiplier (R928P, Hamamatsu, Japan) or a microchannel plate photomultiplier (MCP-PMT) for steady-state and lifetime measurements respectively. The excitation wavelength and time range for lifetime measurements were selected according to the sample requirements. The time-resolved fluorescence decays were analysed by exponential tail fitting.

8.4 Conclusion

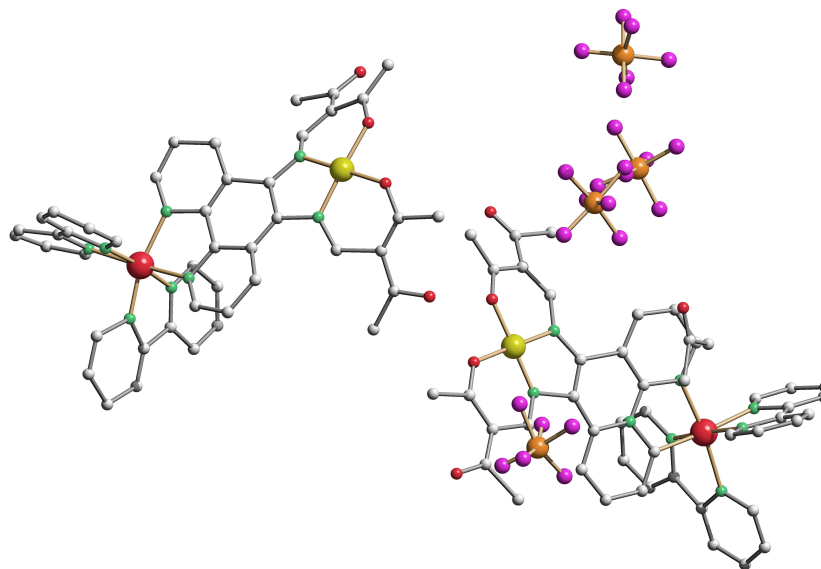
We have shown the synthesis of a new phenanthroline-derived Schiff base-like ligand **1**, the corresponding Ru(II) metallaligand **2**, as well as the bimetallic Ru(II)-Ni(II) complex **3**. The optical properties of **2** and **3** were investigated with absorption, steady-state emission, and time-resolved emission spectroscopy, and show that the coordination of a pyridine solvent molecule on the Ni(II) centre, inducing a CISSS, had no quenching effect on the emission properties. The crystal motif revealed that the Ni(II) centre is not included in the conjugated π -system of the emitting unit of the molecule because of steric hindrance between protons. In the future, a new Schiff base-like ligand will be designed to tackle this problem and allow the Ni(II) centre to be in the same conjugated π -system as the fluorophore. Other metal centres such as Cu(II) and Zn(II) will be included in the place of the Ni(II), as the molecule shows strong structural similarity with published photocatalytic systems.^[26]

Acknowledgement

Financial supports from the German Science foundation (SFB840; project A10), the BayNAT program, and the University of Bayreuth are acknowledged.

8.5 Supporting Information

Figure 8.7: Illustration of the unit cell of $(\mathbf{3})_2 \cdot \text{acetone}$. Hydrogen atoms are omitted for clarity. Colour code: Ru large red, Ni large yellow, C gray, N green, O red, P orange, F purple.



SCHAKAL

References

- [1] M. Halcrow, *Spin-Crossover Materials*, John Wiley & Sons Ltd., Chichester, UK, **2013**.
- [2] P. Gütllich, A. B. Gaspar, Y. Garcia, *Beilstein J. Org. Chem.* **2013**, *9*, 342–391.
- [3] M. Dommaschk, G. Gutzeit, S. Boretius, R. Haag, R. Herges, *Chem. Commun.* **2015**, *50*, 12476–12478.
- [4] S. Thies, C. Bornholdt, F. Köhler, F. D. Sönnichsen, C. Näther, F. Tuczek, R. Herges, *Chem. Eur. J.* **2010**, *16*, 10074–10083.
- [5] S. Thies, H. Sell, C. Schütt, C. Bornholdt, C. Näther, F. Tuczek, R. Herges, *J. Am. Chem. Soc.* **2011**, *133*, 16243–16250.
- [6] S. Venkataramani, U. Jana, M. Dommaschk, F. D. Sönnichsen, F. Tuczek, R. Herges, *Science* **2011**, *331*, 445–448.
- [7] B. Valeur, M. N. Berberan-Santos, *Molecular Fluorescence. Principles and applications*, Wiley-VCH, Weinheim, DE, **2013**.
- [8] B. Daly, J. Ling, A. de Silva, *Chem. Soc. Rev.* **2015**, *44*, 4203–4211.
- [9] M. Engeser, L. Fabbrizzi, M. Licchelli, D. Sacchi, *Chem. Commun.* **1999**, 1191–1192.
- [10] C. Lochenie, K. G. Wagner, M. Karg, B. Weber, *J. Mater. Chem. C* **2015**, *3*, 7925–7935.
- [11] S. Bodige, F. Macdonnell, *Tetrahedron Lett.* **1997**, *38*, 8159–8160.
- [12] C. Lochenie, J. Heinz, M. Milius, B. Weber, *Dalton Trans.* **2015**, *44*, 18065–18077.
- [13] B. Weber, Jäger, *Eur. J. Inorg. Chem.* **2009**, 465–477.
- [14] L. Wolf, E.-G. Jäger, *Z. Anorg. Allg. Chem.* **1966**, *346*, 76–91.
- [15] V. Balzani, S. Campagna, *Photochemistry and Photophysics of Coordination Compounds I*, Springer, Berlin, DE, **2007**.
- [16] C.-T. Lin, W. Böttcher, M. Chou, C. Creutz, N. Sutin, *J. Am. Chem. Soc.* **1976**, *98*, 6536–6544.
- [17] M. R. Reddy, P. V. Reddy, Y. P. Kumar, A. Srishailam, N. Nambigari, S. Satyanarayana, *J. Fluoresc.* **2014**, *24*, 803–817.
- [18] C. Hiort, P. Lincoln, B. Nordén, *J. Am. Chem. Soc.* **1993**, *115*, 3448–3454.
- [19] L. Claisen, *Justus Liebigs Ann. Chem.* **1897**, *297*, 1–98.

- [20] P. Giordano, C. Bock, M. Wrighton, *J. Am. Chem. Soc.* **1978**, *100*, 6960–6965.
- [21] A. Altomare, M. C. Burla, M. Camalli, G. L. Cascarano, C. Giavazzo, A. Guagliardi, A. G. G. Moliterni, G. Polidori, R. Spagna, *J. Appl. Crystallogr.* **1999**, *35*, 115–119.
- [22] G. Sheldrick, *Acta Crystallogr., Sect. A* **2008**, *64*, 112–122.
- [23] C. K. Johnson, M. N. Burnett, *ORTEP-III*, **1996**, Oak-Ridge National Laboratory, Oak-Ridge, TN.
- [24] L. Farrugia, *J. Appl. Crystallogr.* **1997**, *30*, 565.
- [25] E. Keller, *Schakal-99*, **1999**, University of Freiburg, Freiburg DE.
- [26] C. Matlachowski, M. Schwalbe, *Dalton Trans.* **2013**, *42*, 3490–3503.

9. Spin crossover iron(II) coordination polymer with fluorescent properties: correlation between emission properties and spin state.

Charles Lochenie,^a Bernadette Maier,^a Konstantin Schötz,^b Fabian Panzer,^b Florian Puchtler,^c Anna Köhler^b and Birgit Weber^{*,a}

^aInorganic Chemistry II, Universität Bayreuth, Universitätstrasse 30, NW I, 95440 Bayreuth, Germany.

^bExperimental Physics II, Universität Bayreuth, Universitätstrasse 30, NW I, 95440 Bayreuth, Germany.

^cInorganic Chemistry I, Universität Bayreuth, Universitätstrasse 30, NW I, 95440 Bayreuth, Germany.

to be submitted

Abstract

A spin crossover coordination polymer $[\text{Fe}(\text{L1})(\text{bipy})]_n$ (where L is a $\text{N}_2\text{O}_2^{2-}$ coordinating Schiff base-like ligand bearing a phenazine fluorophore and $\text{bipy} = 4,4'$ -bipyridine) was synthesized and exhibits a 48 K wide thermal hysteresis above room temperature ($T_{\frac{1}{2}\uparrow} = 371$ K and $T_{\frac{1}{2}\downarrow} = 323$ K) that is stable for several cycles. The spin transition was characterized using SQUID magnetometry, Mössbauer spectroscopy, and DSC measurements. T -dependent X-ray powder diffraction reveals a structural phase transition coupled with

the spin transition phenomenon. The dimeric excerpt $((\mu\text{-bipy})[\text{FeL1}(\text{MeOH})]_2) \cdot 2 \text{ MeOH}$ of the coordination polymer chain crystallizes in the triclinic space group $P\bar{1}$ and reveals that the packing of the molecules in the crystal is dominated by hydrogen bonds. Investigation of the emission properties of the complexes regards to temperature shows that the spin crossover behavior can be followed through measurement of the fluorescence properties.

9.1 Introduction

Iron(II) spin crossover (SCO) complexes are a class of molecules where the spin state can be reversibly switched between a paramagnetic high spin (HS) and a diamagnetic low spin (LS) state upon physical stimuli such as temperature or pressure change, or light irradiation.^[1,2] Upon spin transition (ST), the structural, vibrational, electronic, and magnetic properties of the molecule are changing. This makes the field attractive to researchers all over the world due to possible applications in the domain of sensors or memory devices.^[3-6] Particularly suitable for the latter application are cooperative STs presenting thermal hysteresis, if possible around room temperature. In order to achieve cooperativity between the spin centers, intermolecular interactions such as hydrogen bonds,^[7-9] van der Waals interactions,^[10-14] or π -interactions^[15-17] are needed to propagate the structural change associated with the SCO phenomenon through the crystal packing of a SCO material. We recently reported a series of mononuclear Fe(II) spin crossover complexes and coordination polymers functionalized with a naphthalene ring, which increased C-H $\cdots\pi$ and C-H \cdots O interactions within the crystal packing, leading to wider thermal hysteresis loops in comparison to similar phenyl derivatives.^[17,18] In a next step, the naphthalene π -system was extended further to the phenazine system, which added ligand-based fluorescence to our Schiff base-like system. We have shown that the ligand-based fluorescence of the corresponding Ni(II) complex could be switched on or off upon Coordination Induced Spin State Switch (CISSS) between a diamagnetic square planar geometry and a paramagnetic octahedral/square pyramidal geometry.^[19]

SCO materials that also exhibit fluorescence would have a supplementary spin state "read out" possibility and therefore a supplementary interest for applications, as one could see a change of emitted wavelength and/or emission intensity upon SCO. Until now, two major strategies are adopted to build such systems: the first is to build a composite material made of a luminescent material and a SCO compound such as electroluminescent thin films doped with SCO complexes,^[20–22] functionalized SCO-core-luminescent-shell nanoparticles,^[23–25] or SCO complexes with fluorescent counter anion.^[23,26] The second is to covalently bind the spin center to the fluorophore in a single (macro)molecule, however this approach does not guarantee a coupling between the spin transition and the emission properties.^[24,27–30]

Here we present a 1D SCO coordination polymer built from our phenazine-derived Schiff base-like ligand, which exhibits a wide thermal hysteresis above room temperature, characterized using magnetic measurements, DSC, and temperature-dependent X-ray powder diffraction. The emission properties of the SCO coordination polymer as well as of the corresponding high spin dimer were studied with varying temperature. To the best of our knowledge, this is the first SCO-luminescent molecular device with thermal hysteresis reported yet.

9.2 Results

9.2.1 Synthesis

The synthesis pathway of all compounds presented in this work is pictured in Scheme 9.1. The spin crossover coordination polymer $[\text{FeL1}(\text{bipy})]_n$ (**4**) was obtained in two steps from the phenazine-based ligand $\text{H}_2\text{L1}$.^[19] In a first step, iron(II) acetate is used as metal source to include the iron center in the chelate cycle, using the acetate anions as base, to give the methanol complex $[\text{FeL1}(\text{MeOH})_2]$ (**2**). The complexation of the iron(II) is accompanied with a typical color change of the solution from yellow to dark red, in agreement with similar complexes reported in literature.^[18,31–35] In the solid state, compound **2** is a greenish black crystalline material. The purity of compound **2** was assessed with elemental analysis (CHN) as well as mass spectrometry. Additionally, the

IR spectrum shows a typical shift of the C=O bands in comparison to the free ligand, consistent with the coordination of an iron(II) metal center.

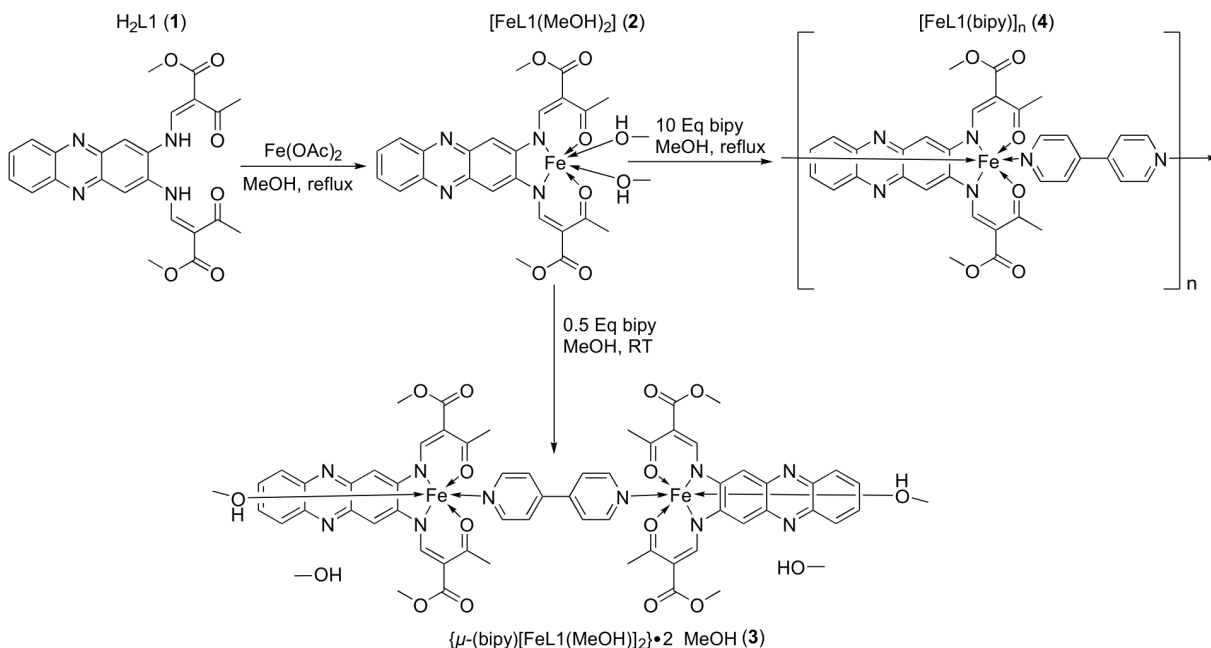


Figure 9.1: Pathway of synthesis of the compounds **3** and **4** described in this work.

From the starting compound **2**, the dimeric specie ($\mu\text{-bipy}$) $[FeL1(MeOH)_2]_2 \cdot 2 \text{ MeOH}$ (**3**) and the coordination polymer $[FeL1(bipy)]_n$ (**4**) can be obtained by substitution of the axial MeOH ligands with 4,4'-bipyridine (**bipy**). The dimer **3** was firstly obtained as single crystals in an attempt to grow single crystals of polymer **4** using a liquid-liquid slow diffusion setup. **3** could also be obtained in a controlled fashion as a red fine crystalline material when the starting complex **2** is converted with 0.5 equivalents of **bipy** at room temperature. The exact formula of the dimer was determined on the basis of the elemental analysis, mass spectrometry, and the determined crystal structure. The formation of dimeric iron(II) complexes instead of the expected coordination polymers was recently reported to depend strongly on the size ratio of the used equatorial and axial ligands.^[35,36] Upon reflux of starting material **2** with an excess of **bipy** bridging ligand (10 equivalents), precipitates the black fine crystalline material $[FeL1(bipy)]_n$ (**4**). The exact formula of **4** was confirmed with elemental analysis and mass spectrometry. The polymeric nature of the material was assessed with powder X-ray diffraction and is discussed further.

All attempts to obtain single crystals of **4** using slow diffusion techniques (liquid-liquid) were so far unsuccessful regardless of the equivalent of **bipy**. Only single crystals of the dimer **3** could be obtained. Presumably, the dimer **3** is too insoluble and precipitates right away, hindering the formation of any polymeric structures.

SEM pictures of **3** and **4** confirmed the purity and assess the morphology of the samples, (see Supporting Information: Figure 9.11). The dimer **3** forms block-shaped crystallites with an average size of 1 μm , similar to the monocrystals grown using slow diffusion setup. The SCO coordination polymer **4** precipitates as platelet-like crystallites, with the smaller dimension measuring 100–150 nm. The other two dimensions of the platelet measures 500 nm to several mm, the platelets presenting then a large surface.

9.2.2 Magnetism

The magnetic properties of both compounds **3** and **4** were investigated with a SQUID magnetometer in the range from 50 K to 400 K in the settle mode. The dimer **3** is with a magnetic susceptibility temperature product ($\chi_M T$) value of $7.40 \text{ cm}^3 \cdot \text{K} \cdot \text{mol}^{-1}$ at room temperature in typical range for a complex with two iron(II) HS centers, and stays HS over the whole temperature range investigated (Supporting Information: Figure 9.10). This result is not surprising as the FeN_3O_3 coordination sphere for this ligand system is too weak and leads to pure HS complexes.^[35,36] The $\chi_M T$ versus T plot of **4** is displayed in Figure 9.2. The coordination polymer **4** is with a $\chi_M T$ value of $0.095 \text{ cm}^3 \cdot \text{K} \cdot \text{mol}^{-1}$ at room temperature in typical range for an iron(II) center in its LS state. Upon warming, the compound undergoes a first spin transition at $T_{\frac{1}{2}\uparrow} = 380 \text{ K}$ ending in its HS state with a $\chi_M T$ value of $3.11 \text{ cm}^3 \cdot \text{K} \cdot \text{mol}^{-1}$ at 400 K. Upon cooling, the $\chi_M T$ product stays constant until 330 K, where the compound transits towards its LS state ($T_{\frac{1}{2}\downarrow} = 323 \text{ K}$), revealing a first hysteresis of 57 K. If the compound is heated again, the LS to HS transition occurs again, however at a lower temperature $T_{\frac{1}{2}\uparrow} = 371 \text{ K}$, then upon cooling, the compound undergoes its HS to LS at the same temperature as in the first cycle, reducing the hysteresis width to 48 K. This hysteresis is then stable and can be measured several times. Leaving the sample at 400 K under vacuum in order to remove possible solvent molecules showed no further influence on the SCO behavior.

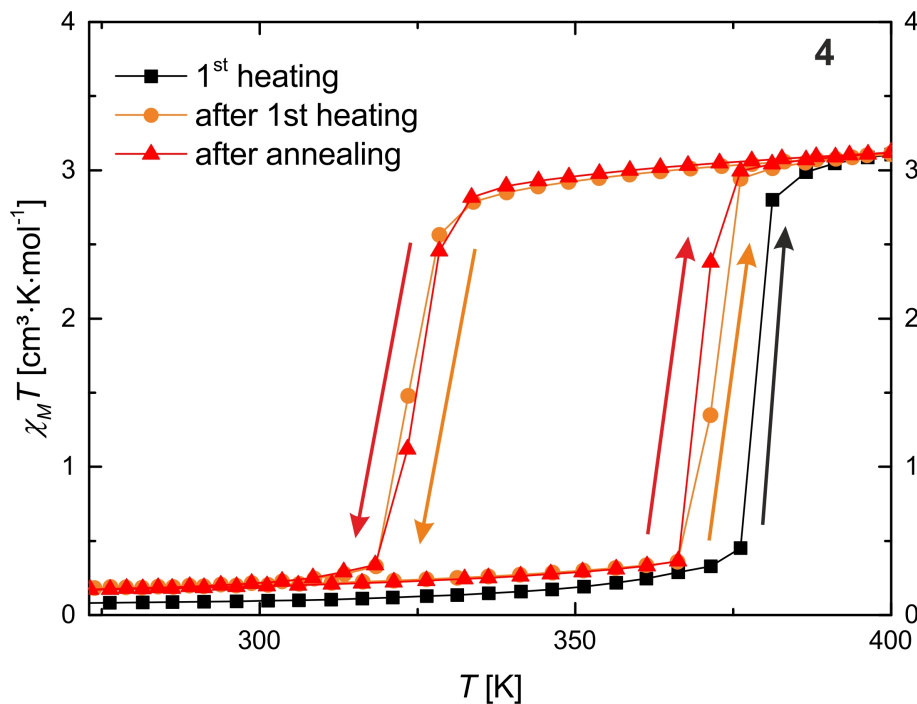


Figure 9.2: Magnetic susceptibility temperature product ($\chi_M T$) vs. temperature measurement for compound **4** displayed between 275 and 400 K.

9.2.3 X-ray Structure Analysis

Monocrystals of **3** suitable for X-ray structure determination were obtained from a liquid-liquid slow diffusion setup between methanolic solutions of **2** and **bipy** under argon atmosphere. The structure was determined at 133 K and the crystallographic data are presented in Supporting Information: Table 9.3. The dimer **3** crystallizes in the triclinic space group $P\bar{1}$ and the asymmetric unit contains half a dimer molecule and one non-coordinating methanol solvent molecule. An ORTEP drawing of the dimer molecule is shown in Figure 9.3. The iron center has an octahedral FeN_3O_3 coordination sphere, with a methanol molecule and the bridging **bipy** as axial ligands. The iron center, whose spin state can be determined by measuring the O1–Fe–O2 angle, which has in the HS state a value of $\approx 110^\circ$,^[17,37,38] is here with $107.34(7)^\circ$ in the HS state, in agreement with the magnetic data. Selected bond lengths and angles are listed in Table 9.1.

The crystal packing of **3** presents a hydrogen bond network, where the axial methanol (O3–H3) of the iron center binds to the phenazine nitrogen atom (N5) of a neighboring

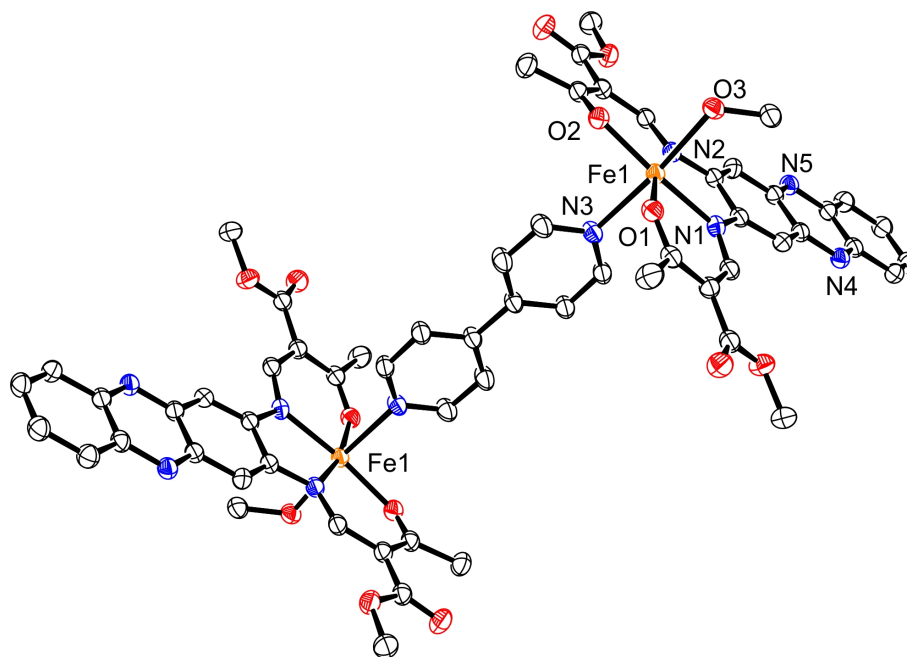


Figure 9.3: ORTEP drawing of the dimer **3**. The thermal ellipsoids are shown at 50% level. Hydrogen atoms and non-coordinating solvent molecules were omitted for clarity reasons.

Table 9.1: Selected bond lengths [\AA] and angles [$^\circ$] of **3**.

Bond	[\AA]	Angle	[$^\circ$]
Fe1–O1	2.0249(19)	O1–Fe1–O2	107.34(7)
Fe1–O2	1.9953(18)	N1–Fe1–N2	79.78(8)
Fe1–O3	2.2839(19)	O3–Fe1–N3	174.40(7)
Fe1–N1	2.070(2)		
Fe1–N2	2.083(2)		
Fe1–N3	2.279(2)		

molecule, which binds back to the first molecule in the same way. A consequence of this interaction is the formation of 1D chain of the dimers, which propagate along the vector $[1\ 1\ -1]$. The chains are further connected through a non-classical hydrogen bond between the methyl group of the axial methanol (C30–H30C) and one of the oxygen atoms (O6) of the ester substituents of a neighboring chain. This leads to the formation of a 2D network with base vectors $[1\ 1\ -1]$ and $[0\ 0\ 1]$. One more hydrogen bond is observed between the non-coordinating methanol solvent molecule (O51–H51) and the second phenazine nitrogen atom (N4). The crystal packing is depicted in Figure 9.4 and the D–H \cdots A distances and angles are given in Table 9.2.

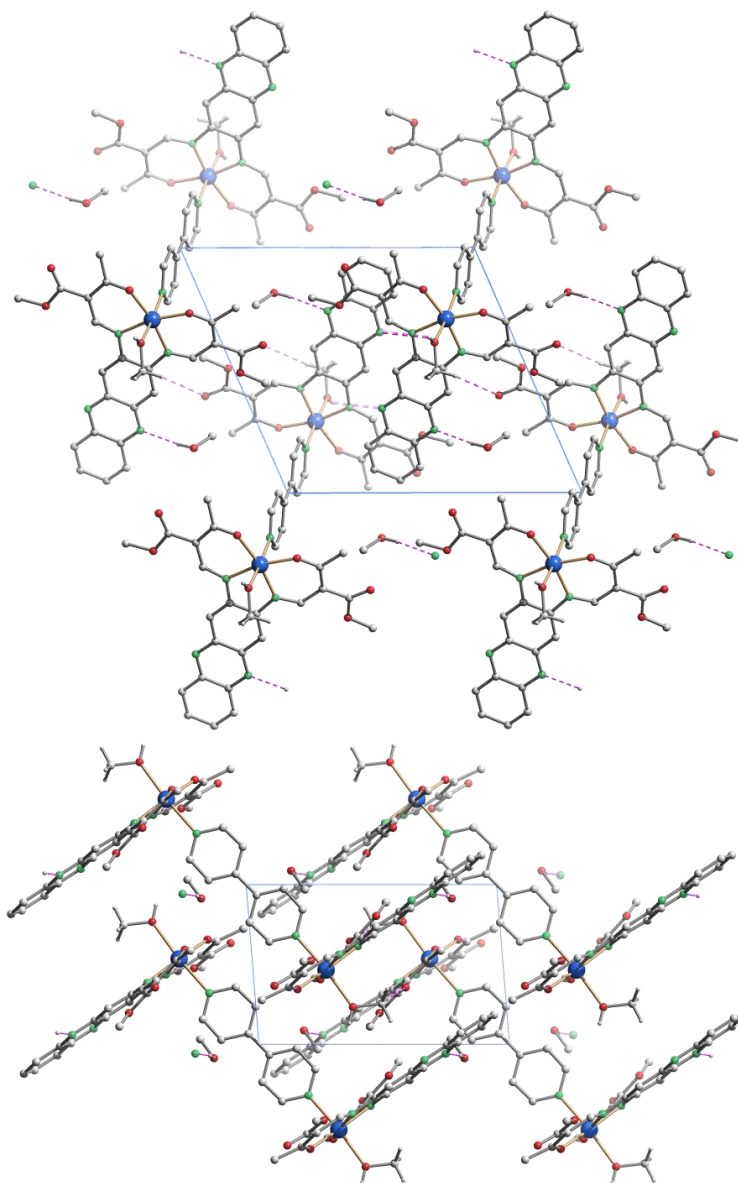


Figure 9.4: Crystal packing of **3** along vectors $[1\ 0\ 0]$ (top) and $[0\ 0\ 1]$ (bottom). Hydrogen atoms non-participating in hydrogen bond were omitted for clarity. Hydrogen bonds are depicted as pink dashed lines.

Table 9.2: Summary of the D–H \cdots A interactions in the crystal packing of **3**. Distances are given in [\AA] and angles in [$^\circ$].

D–H \cdots A	D–H [\AA]	H \cdots A [\AA]	D \cdots A [\AA]	D–H \cdots A [$^\circ$]
O3–H3 \cdots N5 ^a	0.84	2.50	2.874(3)	108
N51–H51 \cdots N4	0.84	2.09	2.923(4)	172
C30–H30C \cdots O6 ^b	0.98	2.44	3.411(4)	172

a = 1-x, 1-y, 1-z; b = 1-x, 1-y, 1-z

9.2.4 Differential Scanning Calorimetry

DSC measurements of **4** were done to determine the enthalpy and entropy changes associated with the SCO phenomenon itself, but also to investigate the possible presence of supplementary phase transitions, linked or not, with the spin transition. The DSC measurement is shown in Figure 9.5. Upon heating, the sample presents a sharp endothermic transition at 375 K, corresponding to the LS to HS spin transition observed in the SQUID measurement. Upon cooling a relatively broader peak at 327 K corresponding to the HS to LS spin transition was observed. The transition temperatures are in good agreement with the magnetic measurement taken into account the different measurement modes and scanning velocities. The different broadness of the peaks reflects how abrupt the ST is, in accordance with the results of the SQUID measurement where the HS to LS transition is less abrupt than the LS to HS transition. Another feature of the SQUID measurement is the different transition temperatures between the very first LS to HS transition and the subsequent LS to HS transitions. This feature was also observed in the DSC measurement. The integrated enthalpy and entropy values are with $\Delta H = 16.1(3) \text{ kJ}\cdot\text{mol}^{-1}$ and $\Delta S = 44.7(12) \text{ J}\cdot\text{mol}^{-1}\cdot\text{K}^{-1}$ for the LS to HS transition, and with $\Delta H = 15.7(2) \text{ kJ}\cdot\text{mol}^{-1}$ and $\Delta S = 47.4(13) \text{ J}\cdot\text{mol}^{-1}\cdot\text{K}^{-1}$ for the HS to LS transition, similar to the values obtained for other spin crossover complexes of the same family.^[7,8,18,39] The enthalpy and entropy values of the very first LS to HS transition ($\Delta H = 16.1(3) \text{ kJ}\cdot\text{mol}^{-1}$ and $\Delta S = 44.7(12) \text{ J}\cdot\text{mol}^{-1}\cdot\text{K}^{-1}$) and the subsequent LS to HS transition ($\Delta H = 16.3(3) \text{ kJ}\cdot\text{mol}^{-1}$ and $\Delta S = 43.8(12) \text{ J}\cdot\text{mol}^{-1}\cdot\text{K}^{-1}$) are in the same order of magnitude. No supplementary phase transitions were observed in the investigated temperature range (300 K – 400 K).

9.2.5 Temperature-dependent Powder X-ray Diffraction

The X-ray diffraction powder pattern of polymer **4** was measured at 5 different temperatures in the following sequence: 300 K, 350 K, 390 K, 350 K, and 300 K. The powder patterns of both HS and LS states could then be obtained, as well as in the middle of the thermal hysteresis at the same temperature (350 K) depending on the history of the compound. The powder patterns are presented in Figure 9.6. At 300 K, the powder pattern exhibit five strong reflections at $2\theta = 6^\circ$, 10° , 12.5° , 17.5° , and 24° . Typically, strong

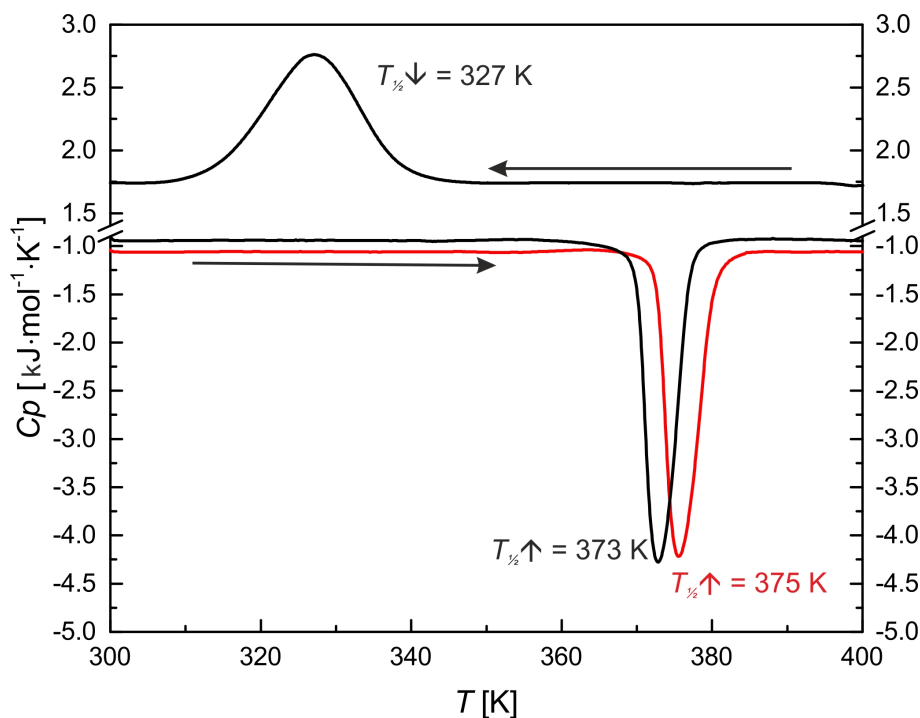


Figure 9.5: DSC measurement of polymer **4** displayed between 300 and 400 K. The red line corresponds to the first heating.

reflections in the 2θ range of 8° – 12° corresponds to the Fe–Fe distance within a chain, as previously reported for similar coordination polymers.^[7,18,35] In this case, the peak at 10° would correspond to a Fe–Fe distance of $\approx 9 \text{ \AA}$, which is in agreement with the length of a Fe–bipy–Fe distance.^[40] Upon heating, the pattern at 350 K is very similar to the pattern at 300 K, with minor shifts due to the temperature change. At 390 K, the spin transition took place and the diffractogram is different. Starting with five reflections in the LS state, the sample shows now six main reflections in the HS state as the peak at 24° splits into two peaks at 23.2° and 23.5° . Moreover the reflections at 10° and 17.5° are shifted to a lower diffraction angle, respectively at 9.6° and 16.7° . A shift of the reflection at 10° in the LS state to 9.6° in the HS state corresponds a elongation of the Fe–Fe distance of $\approx 1 \text{ \AA}$, which is in agreement with the coordination sphere volume increase upon LS to HS transition. Upon cooling, the pattern at 350 K is still characteristic for the HS state. This is a further proof of the bistability of the material, as it was measured at 350 K in both spin states. When the compound is back to 300 K, a diffractogram similar to the starting diffractogram was recorded, and the sample is back to its LS state.

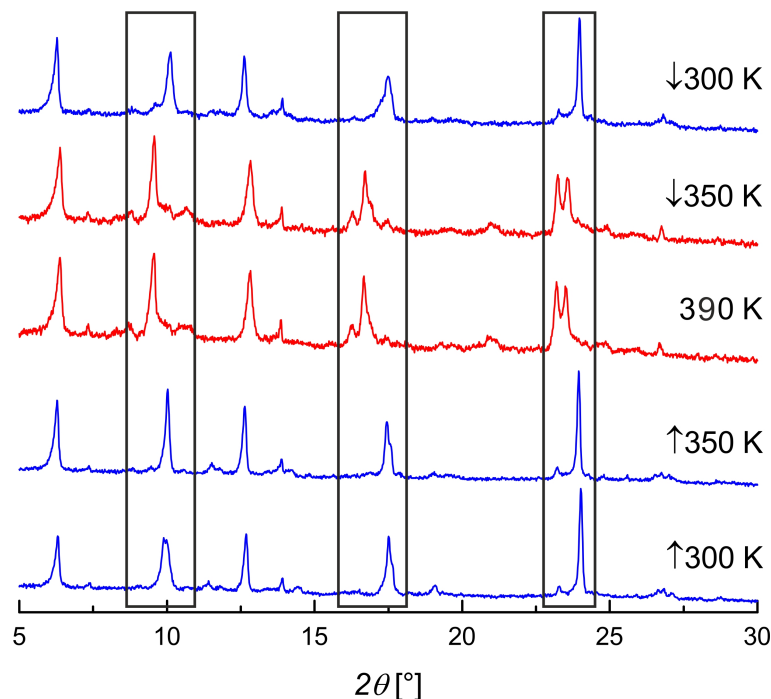


Figure 9.6: Temperature-dependent X-ray powder patterns of **4**. The HS state is represented with a red line, the LS state with a blue line. Diffractograms with \uparrow were measured upon heating and with \downarrow upon cooling.

9.2.6 Fluorescence Spectroscopy

Emission spectra of the dimer **3** and the polymer **4** in the solid state were measured with varying temperature between 300 K and 400 K, using a 337 nm nitrogen laser as excitation. Normalized spectra measured at 300 K, 350 K, and 400 K are presented in Figure 9.7. The dimer **3** shows a dominant peak at $\lambda_2 = 686$ nm. In addition, a broad shoulder with lower intensity, centered around $\lambda_1 = 550$ nm is observed. The spectra do not change with temperature, though the overall intensity reduces upon heating. This is shown in Figure 9.8A.

Similar to the emission spectrum of the dimer **3**, the photoluminescence (PL) spectra of the polymer **4** exhibits two prominent emission features at $\lambda_1 = 550$ nm and at $\lambda_2 = 673$ nm. For ease of reference, the spectra of the dimer **3** and the polymer **4** at 300 K and 400 K are compared in the supporting information (Figure 9.12), so that the coincidence of their spectral features, albeit with different intensities, is particularly evident.

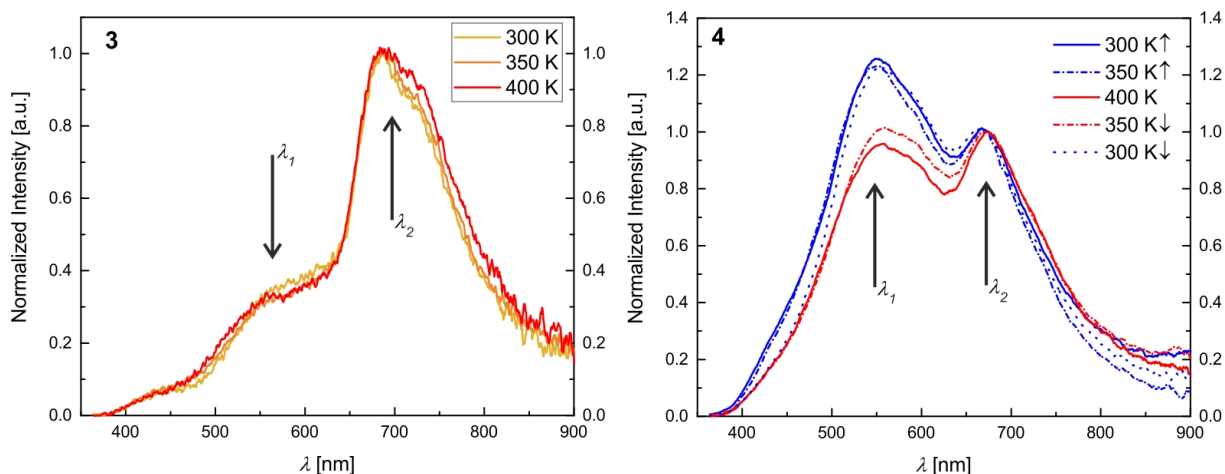


Figure 9.7: Temperature-dependent emission spectra taken from powders of the dimer **3** (left) and the polymer **4** (right) with $\lambda_{ex} = 337$ nm upon heating(\uparrow) and cooling(\downarrow).

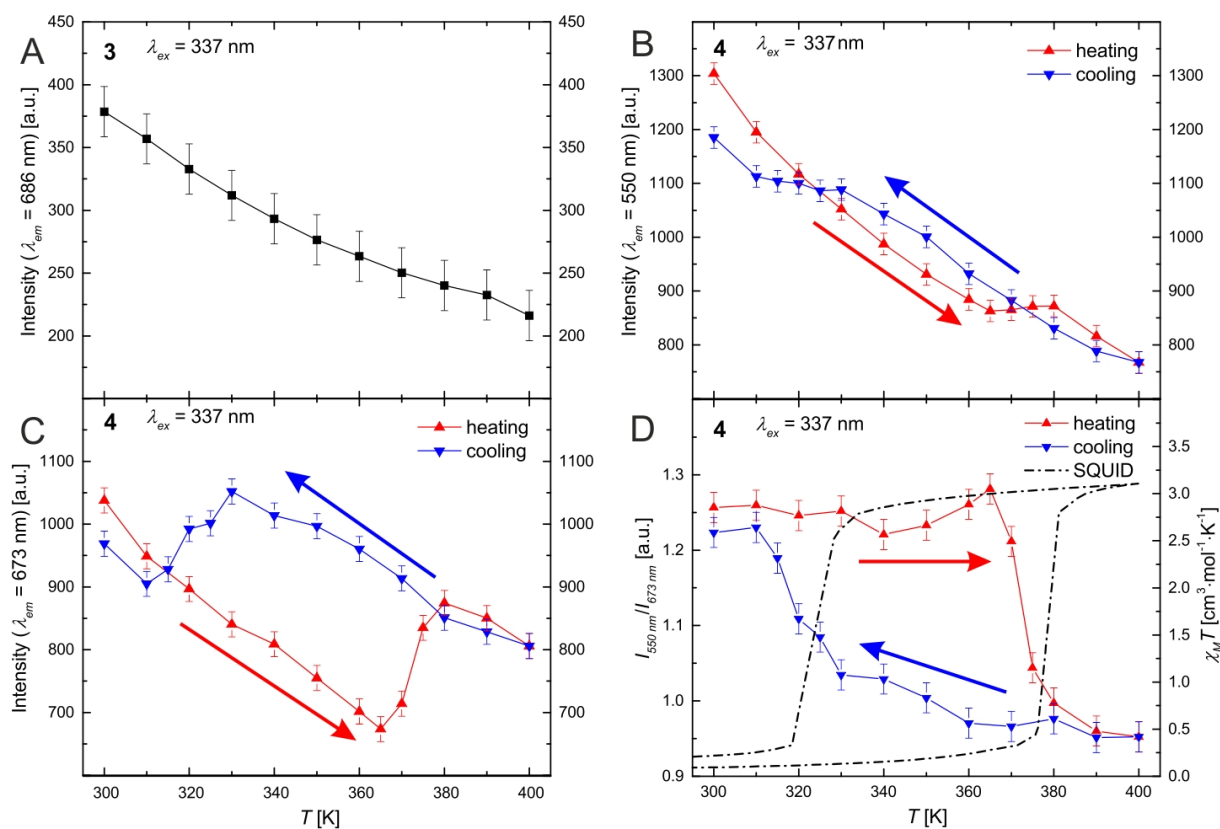


Figure 9.8: Plot of the emission intensity of **3** and **4** against temperature. A: compound **3** for detection at $\lambda_2 = 686$ nm, B: compound **4** for detection at $\lambda_1 = 550$ nm, C: compound **4** for detection at $\lambda_2 = 673$ nm, D: the ratio of λ_1/λ_2 for compound **4**.

When comparing the temperature dependent magnetic susceptibility shown in Figure 9.2 with the temperature dependent photoluminescence spectra of the polymer in Figure

9.7, it becomes evident that the relative intensities of the peaks λ_1 and λ_2 correlate with the spin state of the polymer. At 300 K i.e. in its LS state, the peak at λ_1 is more intense than at λ_2 . Upon heating, at 350 K, the sample **4** is still in the LS state and the emission spectrum stays unchanged. At 400 K, after the sample underwent spin transition, the ratio between λ_1 and λ_2 changes and λ_1 becomes as intense as λ_2 . Upon cooling, at 350 K, the sample is still in the HS state and the spectrum is similar to the spectrum at 400 K. Finally, when back in the LS state at 300 K, the spectrum is similar to the starting spectrum. This temperature dependent behavior demonstrates that the spin state of the sample impacts on the shape of the emission bands, where in the LS state of the sample the corresponding emission spectrum shows an increased intensity at λ_1 , while in the HS state, the emission intensities at λ_1 and λ_2 are similar.

This behavior is further analyzed in Figures 9.8B–D which display the evolution of the PL intensity at λ_1 , λ_2 , and the ratio of both features in regard to the temperature. Both features at λ_1 and λ_2 show the same general trend: their intensity decreases with rising temperature. However, the trend is not followed in the region from 365 to 380 K upon heating, and from 330 to 310 K upon cooling. Those regions corresponds to the spin transition temperatures of **4** ($T_{\frac{1}{2}\uparrow} = 371$ K and $T_{\frac{1}{2}\downarrow} = 323$ K). In other words, the SCO phenomenon can be followed using the fluorescence spectroscopy. One can see on the plot of the intensities (Figures 9.8B–D) that after a full measurement cycle, the overall PL intensity at 300 K has slightly diminished. We attributed this effect to photobleaching, as rather harsh measurement conditions are used (337 nm laser, heating up to 400 K, several hours of measurements for a full cycle). Non-normalized emission spectra of **3** and **4**, as well as a superposition of the spectra, can be found in the Supporting Information: Figure 9.12.

9.3 Discussion

The SCO coordination polymer **4** presents remarkable magnetic properties, exhibiting a 48 K wide hysteresis above room temperature. Wide thermal hystereses are usually associated with a coupling between the electronic transition and structural changes. This

is also true for our complex, as the DSC measurement showed that the STs have rather high enthalpy and entropy values, and the powder X-ray diffraction analysis showed that the HS and the LS states present different diffractograms. All this indicates that a major structural change happens upon SCO, however a single crystal X-ray structure analysis would be needed to confirm this hypothesis. The very first LS to HS ST happens at a higher temperature as all sub-sequent STs, and this phenomenon was confirmed with SQUID and DSC measurements. A reason could be that minor structural changes upon the first ST, i.e. order-disorder phase transition, movement of a substituent upon ST, happen in an irreversible way, and upon the subsequent HS to LS, the exact original structure is not recovered. As SCO is an extremely sensitive phenomenon regards to environmental changes, such minor structural change will have an influence on the SCO properties.

The emission properties of both dimer **3** and polymer **4** were measured at different temperatures. From the fact that the peaks at λ_1 and λ_2 change their intensity depending on the spin state of the polymer we infer that these two peaks have a different electronic origin. Since the same two peaks also occur at λ_1 and λ_2 for the dimer **3**, albeit with different intensity, we suggest that for the high spin dimer, the two peaks can also be attributed to two electronic origins. In other words, upon photoexcitation, two different radiative relaxation processes take place. In the case of the corresponding Ni(II) complex, two relaxation processes were also observed, however only the diamagnetic specie was luminescent.^[19]

The loss of the emission properties for the paramagnetic specie is presumably due to an electron transfer between the ligand-based π and π^* orbitals and the metal-centered d orbitals. For the compounds presented in this paper, the hypothesis that similar processes occur can be made. We observe that the emission λ_1 has similar energy than the emission of the ligand **1** in solution and its corresponding octahedral Zn(II) complex.^[19] The energy of the λ_2 emission feature, is in the range of the crystal field strength (energy splitting between the t_{2g} and e_g^* orbitals) for an iron(II) in the HS state. From those observations, two hypothetical relaxation processes are proposed: the first one is a ligand-centered relaxation process in which an electron of a π_L ligand-based orbital is excited into a π_L^*

ligand-based orbital, and then relaxes directly back in the original π_L ligand-based orbital and the emission λ_1 is observed. The second is a metal-centered relaxation process for which, after the excitation of an electron into the π_L^* orbital, an electron exchange takes place between the metal-based orbitals and the ligand-based orbital. The excited electron goes from the π_L^* orbital to the e_g^* orbital, while an electron of the t_{2g} orbital goes to the π_L orbital. After this electron exchange, the excited electron in the e_g^* orbital can relax towards the t_{2g} orbital by light emission at a wavelength λ_2 . Both processes in both spin states are depicted in Figure 9.9.

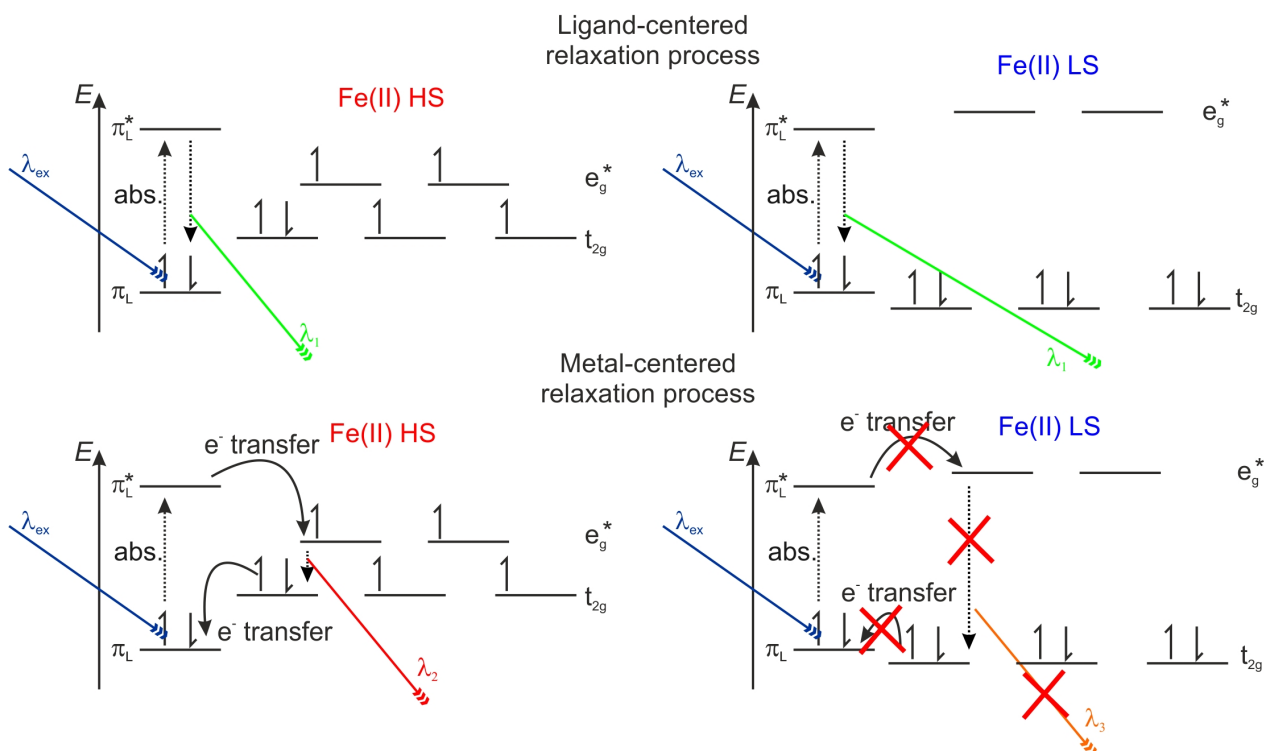


Figure 9.9: Simplified schema representing the two hypothetical relaxation processes, in the HS state (left) and LS state (right).

The observation of dual emission is unusual. It would imply that the rates for the two processes are in competition, with the key parameter being how fast the electron exchange takes place. The main influence on the electron transfer arises from the spin state of the iron(II) center, as the crystal field strength is smaller in the HS state than in the LS state. In the HS state, when the crystal field strength is smaller than the energy gap between π_L and π_L^* , energy transfer (for example by dual electron transfer) from the photoexcited

ligand to the metal would be favorable. However in the LS state, we estimate that the crystal field strength is larger than the energy gap between π_L and π_L^* , thus preventing energy transfer from photoexcited ligand to the metal. Rather, transfer could occur from the photoexcited metal to the ligand. Overall, the ligand-centered relaxation process at λ_1 would be favored.

Sample **3** does not show any change in the shape of the spectra upon temperature change, in agreement with the fact that it is a pure HS specie. The hypothesis we formulated complies with the observed emission properties, where a stronger λ_2 emission peak is observed, resulting from the electron exchange and concomitant energy transfer. Sample **4** shows both emission peaks in both spin states. In principle, the emission from the HS state should give a dominant contribution at λ_2 analogous to dimer **3**, yet we observe about equal intensities of the peaks at λ_1 and λ_2 . This arises probably from the fact that the two compounds **3** and **4**, when in the HS state, do not have exactly the same crystal field energy, and therefore the electron transfer rate is more or less favored.

In the LS state, the λ_1 peak is enhanced compared to the peak at λ_2 , confirming that the ligand-centered relaxation process is favored. The fact that we still observe a significant contribution from λ_2 may be attributed to effects from the HS chain ends. Sample **4** is a coordination polymer, and usually the properties of such coordination polymers are analyzed and interpreted taking into account that the polymer chain is of infinite dimension, and that the contribution of the ends of the polymer chain is negligible. However, in case of nanosized material, the contribution of the end of the chains (localized on the surface) is no longer negligible.^[41] As the SEM pictures of **4** showed that the SCO polymer consists of thin platelet-shaped crystals, with a rather high surface, and as during the PL measurements, the surface of the material is irradiated, and PL typically takes place from the surface of the investigated materials, it can be speculated that the resulting spectrum obtained is a superposition of the emission of the surface which is HS and the emission of the SCO-core. As the dimer **3** can also be considered as a "polymer chain" consisting only of two end groups, it is expected that the emission properties of **3** will be similar to those of the surface of **4**.

To sum up, for the polymer **4**, when in the HS state, we observe similar spectra as for the dimer **3**, with the two proposed relaxation processes competing with each other. However in the LS state, the metal-centered process is not happening in the core of the material, so that the emission is ligand-centered at λ_1 and the λ_2 emission observed originates from the surface of the material. In order to verify the proposed hypothesis, further measurements are needed. Temperature-dependent measurements of the absorption properties, as well as the determination of the lifetime of the different relaxation processes would be helpful. Calculations of the energy of the different orbitals could also give useful formation. Finally, the growth and measurement of much larger crystallites (μm to cm) could also help understanding the observed phenomena; however this last possibility is experimentally difficult to realize.

9.4 Experimental Section

Synthesis Methanol (MeOH) was purified by distillation over Mg under argon atmosphere.^[42] Starting ligand H₂L1 (**1**) and iron(II) acetate were synthesized as described in literature.^[19,43] 4,4'-bipyridine (**bipy**) (Alfa Aesar, 99.9%) was used without further purification. All syntheses were carried out under argon using Schlenk techniques. CHN analyses were measured with a Vario El III from Elementar Analysen-Systeme. Mass spectra were recorded with a Finnigan MAT 8500 with a data system MASPEC II. IR spectra were recorded with a Perkin Elmer Spectrum 100 FT-IR spectrometer.

[FeL1(MeOH)₂] (2) H₂L1 (0.2 g) and iron(II) acetate (0.11 g) were dissolved in 40 mL MeOH. The black solution was refluxed during 2 hours and then allowed to cool down. Upon cooling a dark green crystalline precipitate appeared. The dark green precipitate was filtered off, washed with MeOH (2×5 mL), and dried *in vacuo*. Yield: 0.22 g (88 %). IR: $\tilde{\nu} = 3246(\text{b})$ (OH), 1625(s) (CO), 1589(s) (CO) cm^{-1} ; MS (DEI-+), 70 eV m/z (%): 516 (100) ([FeL1]⁺); elemental analysis calculated (found) for C₂₆H₂₈FeN₄O₈ (580.37 $\text{g}\cdot\text{mol}^{-1}$): C 53.81 (53.21), H 4.86 (4.23), N 9.65 (9.62).

((μ -bipy)[FeL1(MeOH)₂]₂)·2 MeOH (3) **2** (0.2 g) and bipy (0.03 g) were dissolved in 10 mL MeOH. The dark red solution was left to stir at room temperature during 2

hours. After a few minutes, a red crystalline precipitate appeared in the flask. The red crystalline precipitate was filtered off, washed with MeOH (2×1 mL), and dried *in vacuo*. Yield: 0.16 g (70 %). IR: $\tilde{\nu} = 3240(\text{b})$ (OH), 1615(s) (CO), 1596(s) (CO) cm^{-1} ; MS (DEI-(+), 70 eV) m/z (%): 516 (65) ($[\text{FeL1}]^+$), 156 (100) ($[\text{bipy}]^+$); elemental analysis calculated (found) for $\text{C}_{62}\text{H}_{64}\text{Fe}_2\text{N}_{10}\text{O}_{16}$ ($1316.94 \text{ g}\cdot\text{mol}^{-1}$): C 56.55 (55.98), H 4.90 (4.32), N 10.64 (10.62).

$[\text{FeL1}(\text{bipy})]_n$ (**4**) **2** (0.2 g) and bipy (0.54 g) were dissolved in 20 mL MeOH. The black solution was refluxed during 1 hour and then allowed to cool down to room temperature. A black crystalline material precipitated upon cooling. The black crystalline material was filtered off, washed with MeOH (2×2 mL), and dried *in vacuo*. Yield: 0.19 g (82 %). IR: $\tilde{\nu} = 1630(\text{s})$ (CO), 1587(s) (CO) cm^{-1} ; MS (DEI-(+), 70 eV) m/z (%): 516 (13) ($[\text{FeL1}]^+$), 156 (84) ($[\text{bipy}]^+$); elemental analysis calculated (found) for $\text{C}_{34}\text{H}_{28}\text{FeN}_6\text{O}_6$ ($672.47 \text{ g}\cdot\text{mol}^{-1}$): C 60.73 (60.53), H 4.20 (4.376), N 12.50 (12.96).

X-ray Structure Analysis The intensity data of **3** were collected with a STOE Stadi-Vari diffractometer using graphite-monochromated $\text{MoK}\alpha$ radiation. The data were corrected for Lorentz and polarization effects. The structure was solved by direct methods (SIR-97)^[44] and refined by full-matrix least-square techniques against $F_o^2 - F_c^2$ (SHELXL-97).^[45] All hydrogen atoms were calculated in idealized positions with fixed displacement parameters. ORTEP-III^[46,47] was used for the structure representation, SCHAKAL-99^[48] to illustrate the crystal packing. cif file deposited at the CCDC database (CCDC 1473427).

X-ray Powder Diffraction Powder diffractograms were measured with a STOE StadiP diffractometer using $\text{CuK}\alpha 1$ radiation with a Ge monochromator, and a Mythen 1K Stripdetector in transmission geometry.

Scanning Electron Microscopy Scanning electron microscopy pictures were gathered at a Zeiss LEO 1530. Samples were prepared on carbon tape.

Magnetic Measurements Magnetic susceptibility data were collected using a MPMS XL-5 SQUID magnetometer under an applied field of 0.5 T over the temperature range 50 to 400 K in the settle mode. The samples were placed in gelatin capsule held within a plastic straw. The data were corrected for the diamagnetic contributions of the ligands by using tabulated Pascal's constants and of the sample holder.^[49]

Fluorescence Spectroscopy The emission spectra were measured in a home build setup. The samples were placed between a fused silica substrate and a coverslip, sealed with glue under argon atmosphere. A supplementary Indium wire was placed between the sample and the glue to avoid contact. The metal ring separates powder and glue thus preventing a reaction of glue and complex. The sample was then placed in an electrically heatable continuous flow cryostat (Oxford Instruments). It was excited using a nitrogen laser with 337 nm emission. The light emitted by the complex was focused into a spectrograph (Andor Technology Shamrock SR303i) and detected with a CCD-camera (Andor iDus). Each temperature was stabilized during 15 min before measurement in order to ensure homogeneous temperature of the sample. The emission spectra were corrected for the transmission through the setup.

9.5 Conclusion

We presented the synthesis of a new dimer **3** and a new SCO coordination polymer **4** based on a phenazine-derived Schiff base-like ligand. The compound **4** presents a 48 K wide thermal hysteresis which was characterized with SQUID, DSC, and X-ray powder diffraction. The large hysteresis probably originates from a structural phase transition coupled with the electronic transition, as HS and LS states present different diffraction patterns. The emission properties in the solid state were measured and showed that not only the band structure is depending on the spin state, but the SCO can also be followed through measurement of the emission intensity. Future investigations of the absorption spectra with temperature are planned, as well as measurement of the fluorescence properties in solution/gel matrix.

Acknowledgements

Financial supports from the German Science foundation (SFB840; project A10), the BayNAT program, and the University of Bayreuth are acknowledged. Fabian Panzer acknowledges financial support by the German Science Foundation DFG through the research training group GRK1640. Ling Peng (MCII, University of Bayreuth) is thanked for the calorimetric measurement. Ottokar Klimm (ACII, University of Bayreuth) is thanked for the measurement of the SEM pictures.

9.6 Supporting Information

Figure 9.10: Magnetic susceptibility temperature product vs. temperature measurement for compound **3** displayed between 50 and 300 K.

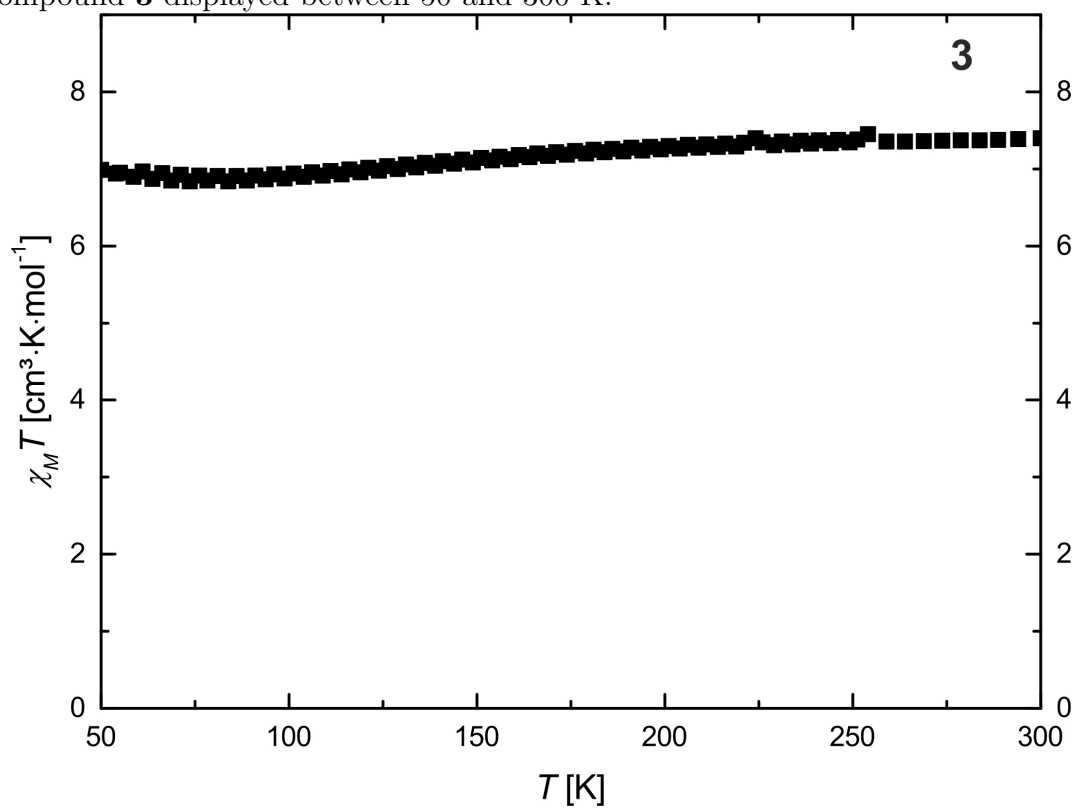


Table 9.3: Crystallographic data of compound **3**.

CCDC	1473427
sum formula	$\text{C}_{62}\text{H}_{64}\text{Fe}_2\text{N}_{10}\text{O}_{16}$
M [$\text{g}\cdot\text{mol}^{-1}$]	1316.93
crystal system	triclinic
space group	$P\bar{1}$
a [\AA]	7.995(4)
b [\AA]	13.598(5)
c [\AA]	14.964(7)
α [$^\circ$]	65.731(3)
β [$^\circ$]	82.036(4)
γ [$^\circ$]	82.580(4)
V [\AA^3]	1463.91(11)
Z	1
ρ [$\text{g}\cdot\text{cm}^{-3}$]	1.494
μ [mm^{-1}]	0.577
crystal size [mm]	$0.182 \times 0.174 \times 0.163$
T [K]	133(2)
λ (MoK α) [\AA]	0.71069
θ -range [$^\circ$]	1.70–27.47
reflns. collected	16292
indep. reflns (R_{int})	6866 (0.0826)
parameters	406
$R(F)$ (all data)	0.0558 (0.0667)
$wR2$	0.1532
$Goof$	0.968

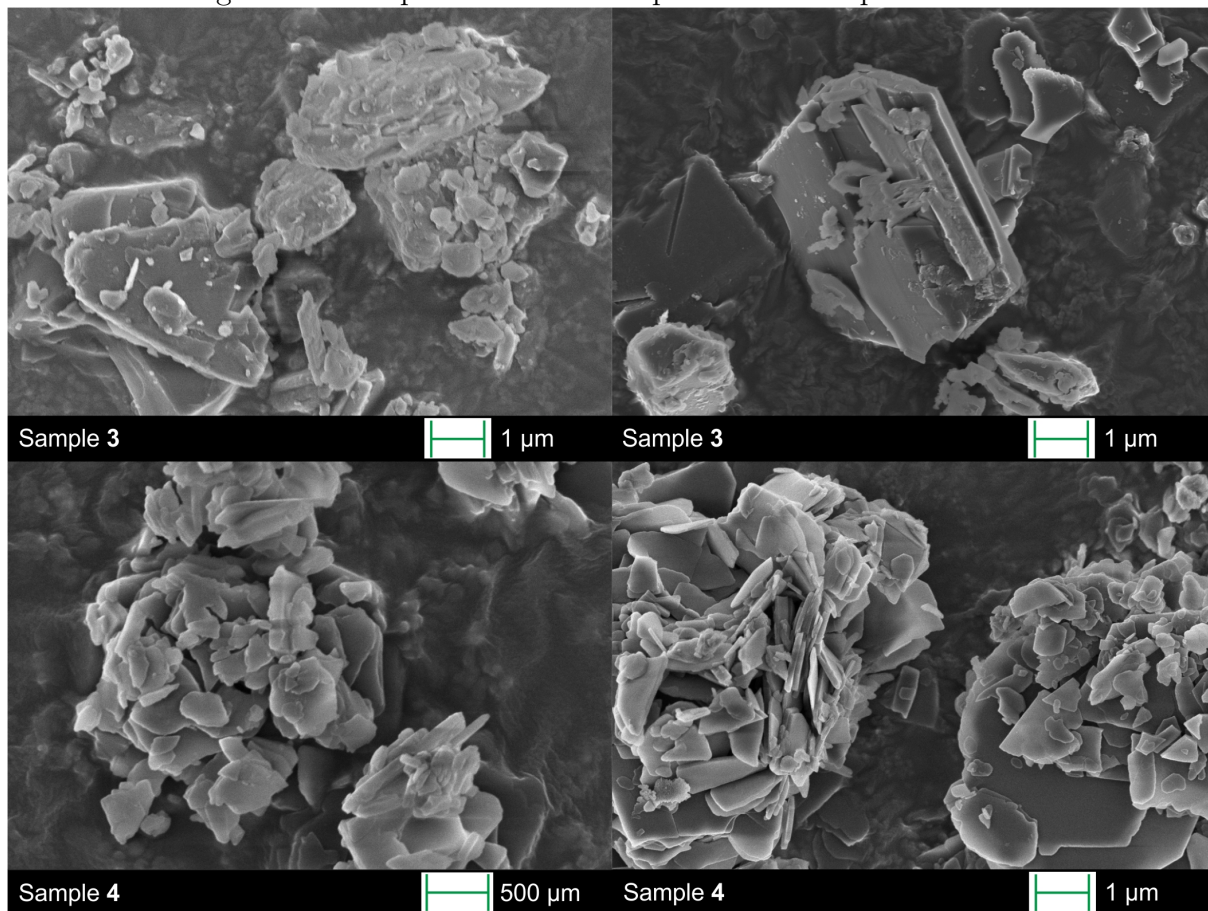
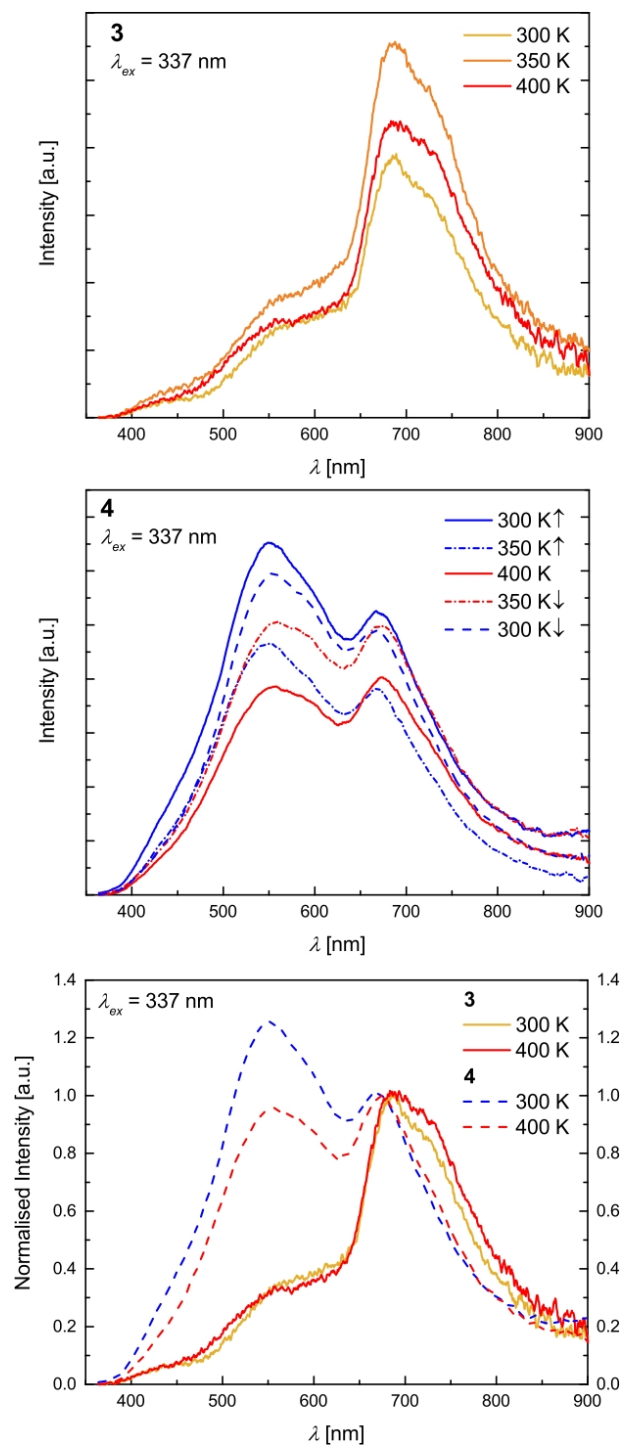
Figure 9.11: Representative SEM pictures of samples **3** and **4**.

Figure 9.12: Temperature-dependent emission spectra of **3** (top & bottom) and **4** (middle & bottom).

References

- [1] M. Halcrow, *Spin-Crossover Materials*, John Wiley & Sons Ltd., Chichester, UK, **2013**.
- [2] P. Gütllich, H. Goodwin, *Spin Crossover in Transition Metal Compounds I-III*, Springer, Berlin, DE, **2004**.
- [3] O. Kahn, *Science* **1998**, *279*, 44–48.
- [4] O. Kahn, C. Jay, J. Krober, R. Claude, F. Groliere, *EP0666561*, **1995**.
- [5] J.-F. Létard, P. Guionneau, L. Goux-Capes, *Spin Crossover in Transition Metal Compounds I-III*, Springer, Berlin, DE, **2004**.
- [6] J. Linares, E. Codjovi, Y. Garcia, *Sensors* **2012**, *12*, 4492–4479.
- [7] C. Lochenie, W. Bauer, A. P. Railliet, S. Schlamp, Y. Garcia, B. Weber, *Inorg. Chem.* **2014**, *53*, 11563–11572.
- [8] B. Weber, W. Bauer, T. Pfaffeneder, M. M. Dîrtu, A. D. Naik, A. Rotaru, Y. Garcia, *Eur. J. Inorg. Chem.* **2011**, 3193–3206.
- [9] B. Weber, W. Bauer, J. Obel, *Angew. Chem. Int. Ed.* **2008**, *47*, 10098–10101.
- [10] S. Schlamp, C. Lochenie, T. Bauer, R. Kempe, B. Weber, *Eur. J. Inorg. Chem.* **2015**, 408–413.
- [11] S. Schlamp, P. Thoma, B. Weber, *Eur. J. Inorg. Chem.* **2012**, 2759–2768.
- [12] W. Bauer, S. Schlamp, B. Weber, *Chem. Commun.* **2012**, *48*, 10222.
- [13] H. L. C. Feltham, C. Johnson, A. B. S. Elliott, K. C. Gordon, M. Albrecht, S. Brooker, *Inorg. Chem.* **2015**, *54*, 2902–2909.
- [14] K. Kuroiwa, T. Arie, S. Sakurai, S. Hayami, T. J. Deming, *J. Mater. Chem. C* **2015**, *3*, 7779–7783.
- [15] M. Nakaya, K. Shimayama, K. Takami, K. Hirata, A. S. Alao, M. Nakamura, L. F. Lindoy, S. Hayami, *Chem. Lett.* **2014**, *43*, 1058–1060.
- [16] J. A. Real, A. B. Gaspar, V. Niel, M. C. Muñoz, *Coord. Chem. Rev.* **2003**, *236*, 121–141.
- [17] C. Lochenie, J. Heinz, M. Milius, B. Weber, *Dalton Trans.* **2015**, *44*, 18065–18077.
- [18] C. Lochenie, A. Gebauer, O. Klimm, F. Puchtler, B. Weber, *New J. Chem.* **2016**, *40*, 4687–4695.
- [19] C. Lochenie, K. G. Wagner, M. Karg, B. Weber, *J. Mater. Chem. C* **2015**, *3*, 7925–7935.

-
- [20] M. Matsuda, K. Kiyoshima, R. Uchida, N. Kinoshita, H. Tajima, *Thin Solid Films* **2013**, *531*, 451–453.
- [21] M. Matsuda, H. Isozaki, H. Tajima, *Chem. Lett.* **2008**, *37*, 374–375.
- [22] M. Matsuda, H. Isozaki, H. Tajima, *Thin Solid Films* **2008**, *517*, 1465–1467.
- [23] L. Salmon, G. Molnár, D. Zitouni, C. Quintero, C. Bergaud, J.-C. Micheau, A. Bousseksou, *J. Mater. Chem.* **2010**, *20*, 5499.
- [24] C.-F. Wang, R.-F. Li, X.-Y. Chen, R.-J. Wei, L.-S. Zheng, J. Tao, *Angew. Chem. Int. Ed.* **2015**, *54*, 1574–1577.
- [25] O. Kraieva, I. Suleimanov, G. Molnár, L. Salmon, A. Bousseksou, *Magnetochemistry* **2016**, *2*, 11.
- [26] H. Matsukizono, K. Kuroiwa, N. Kimizuka, *Chem. Lett.* **2008**, *37*, 446–447.
- [27] Y. Garcia, F. Robert, A. D. Naik, G. Zhou, B. Tinant, K. Robeyns, S. Michotte, L. Piriaux, *J. Am. Chem. Soc.* **2011**, *133*, 15850–15853.
- [28] A. Santoro, L. J. Kershaw Cook, R. Kulmaczewski, S. A. Barrett, O. Cespedes, M. A. Halcrow, *Inorg. Chem.* **2015**, *54*, 682–693.
- [29] M. Hasegawa, F. Renz, T. Hara, Y. Kikuchi, Y. Fukuda, J. Okubo, T. Hoshi, W. Linert, *Chem. Phys.* **2002**, *277*, 21–30.
- [30] L. J. Kershaw Cook, M. A. Halcrow, *Polyhedron* **2015**, *87*, 91–97.
- [31] B. Weber, E. S. Kaps, C. Desplanches, J.-F. Létard, *Eur. J. Inorg. Chem.* **2008**, 2963–2966.
- [32] B. Weber, E. S. Kaps, C. Desplanches, J.-F. Létard, *Eur. J. Inorg. Chem.* **2008**, 4891–4898.
- [33] B. Weber, C. Carbonera, C. Desplanches, J.-F. Létard, *Eur. J. Inorg. Chem.* **2008**, 1589–1598.
- [34] S. Schlamp, K. Dankhoff, B. Weber, *New J. Chem.* **2014**, *38*, 1965–1972.
- [35] K. Dankhoff, C. Lochenie, F. Puchtler, B. Weber, *Eur. J. Inorg. Chem.* **2016**, 2136–2143.
- [36] S. Schlamp, P. Thoma, B. Weber, *Chem. Eur. J.* **2014**, *20*, 6462–6473.
- [37] B. Weber, Jäger, *Eur. J. Inorg. Chem.* **2009**, 465–477.
- [38] B. Weber, *Coord. Chem. Rev.* **2009**, *253*, 2432–2449.
- [39] W. Bauer, M. M. Dîrtu, Y. Garcia, B. Weber, *CrystEngComm* **2012**, *14*, 1229–1231.
- [40] B. Weber, R. Tandon, D. Himsl, *Z. Anorg. Allg. Chem.* **2007**, *633*, 1159–1162.
-

- [41] G. Félix, W. Nicolazzi, L. Salmon, G. Molnár, M. Perrier, G. Maurin, J. Larionova, J. Long, Y. Guari, A. Bousseksou, *Phys. Rev. Let.* **2013**, *110*, 235701.
- [42] H. G. O. Becker, *Organikum. Organisch-Chemisches Grundpraktikum 19th ed.*, Johann Ambrosius Barth, Berlin, DE, **1993**.
- [43] B. Weber, W. Betz, R. and Bauer, S. Schlamp, *Z. Anorg. Allg. Chem.* **2011**, *637*, 102–107.
- [44] A. Altomare, M. C. Burla, M. Camalli, G. L. Cascarano, C. Giavazzo, A. Guagliardi, A. G. G. Moliterni, G. Polidori, R. Spagna, *J. Appl. Crystallogr.* **1999**, *35*, 115–119.
- [45] G. Sheldrick, *Acta Crystallogr., Sect. A* **2008**, *64*, 112–122.
- [46] C. K. Johnson, M. N. Burnett, *ORTEP-III*, **1996**, Oak-Ridge National Laboratory, Oak-Ridge, TN.
- [47] L. Farrugia, *J. Appl. Crystallogr.* **1997**, *30*, 565.
- [48] E. Keller, *Schakal-99*, **1999**, University of Freiburg, Freiburg DE.
- [49] O. Kahn, *Molecular Magnetism*, VCH, New York, N. Y., USA, **1993**.

10. List of Publications

1. C. Lochenie, W. Bauer, S. Schlamp, P. Thoma, B. Weber, *Z. Anorg. Allg. Chem.* **2012**, *638*, 98–102.
"Synthesis and Characterisation of Schiff Base-like Iron(II) Complexes with Imidazole as Axial Ligand"
2. W. Bauer, C. Lochenie, B. Weber, *Dalton Trans.* **2014**, *43*, 1990–1999.
"Synthesis and characterization of 1D iron(II) spin crossover coordination polymers with hysteresis"
3. C. Göbel, T. Palamarciuc, C. Lochenie, B. Weber, *Chem. Asian J.* **2014**, *9*, 2232–2238.
"Synthesis of Microcrystals of the [Fe(L)(bipy)] Spin Crossover Coordination Polymer in a Poly-4-vinylpyridine Matrix"
4. C. Lochenie, S. Schlamp, A. P. Railliet, K. Robeyns, B. Weber, Y. Garcia, *CrytEngComm* **2014**, *16*, 6213–6218.
"Water channels and zipper structures in Schiff base-like Cu(II) and Ni(II) mononuclear complexes"
5. Z. Fang, J. P. Dürholt, M. Kauer, W. Zhang, C. Lochenie, B. Jee, H. B. Albada, N. Metzler-Nolte, A. Pöpl, B. Weber, M. Muhler, Y. Wang, R. Schmid, R. A. Fischer, *J. Am. Chem. Soc.* **2014**, *136*, 9627–9636.
"Structural Complexity in Metal-Organic Frameworks: Simultaneous Modification of Open Metal Sites and Hierarchical Porosity by Systematic Doping with Defective Linkers"
6. C. Lochenie, W. Bauer, A. P. Railliet, S. Schlamp, Y. Garcia, B. Weber, *Inorg.*

-
- Chem.* **2014**, *53*, 11563–11572. "Large Thermal Hysteresis for Iron(II) Spin Crossover Complexes with *N*-(pyrid-4-yl)isonicotinamide"
7. U. Herber, A. Hoffmann, C. Lochenie, B. Weber, S. Herres-Pawlis, *Z. Naturforsch.* **2014**, *69b*, 1206-1214.
"N-Donor Competition in Iron Bis(chelate) Bis(pyrazolyl)pyridinylmethane Complexes"
8. S. Schlamp, C. Lochenie, T. Bauer, R. Kempe, B. Weber, *Eur. J. Inorg. Chem.* **2015**, 408–413.
"Iron(II) Spin-Crossover Complexes with Schiff Base Like Ligands and *N*-Alkyl-imidazoles"
9. S. Schönfeld, C. Lochenie, P. Thoma, B. Weber, *CrystEngComm* **2015**, *17*, 5389–5395.
"1D iron(II) spin crossover coordination polymers with 3,3'-azopyridine – kinetic trapping effects and spin transition above room temperature"
10. D. Adner, M. Korb, C. Lochenie, B. Weber, H. Lang, *Z. Anorg. Allg. Chem.* **2015**, *641*, 1243–1246.
Crystal Structure and Magnetic Properties of a Hexanuclear Copper(II) Carboxylate"
11. C. Lochenie, K. G. Wagner, M. Karg, B. Weber, *J. Mater. Chem. C*, **2015** *3*, 7925–7935.
"Modulation of the ligand-based fluorescence of 3d metal complexes upon spin state change"
12. C. Lochenie, J. Heinz, W. Milius, B. Weber, *Dalton Trans.* **2015**, *44*, 18065–18077.
"Iron(II) spin crossover complexes with diamionaphthalene-based Schiff base-like ligands: mononuclear complexes"
13. C. Schliebe, U. Pfaff, T. Gemming, C. Lochenie, B. Weber, H. Lang, *Eur. J. Inorg. Chem.* **2015**, 3850–3860.
"Si(OCH₂Fc)₄: Synthesis, Electrochemical Behavior, and Twin Polymerization"
-

14. K. Dankhoff, C. Lochenie, F. Puchtler, B. Weber, *Eur. J. Inorg. Chem.* **2016**, 2136–2143.
"Solvent Influence on the Magnetic Properties of Iron(II) Spin-Crossover Coordination Compounds with 4,4'-Dipyridylethyne as Linker"
15. C. Lochenie, A. Gebauer, O. Klimm, F. Puchtler, B. Weber, *New J. Chem.* **2016**, 40, 4687–4695.
"Iron(II) spin crossover complexes with diaminonaphthalene-based Schiff base-like ligands: 1D coordination polymers"

Contributions to national and international conferences

1. C. Lochenie, A.P. Railliet, W. Bauer, K. Robeyns, B. Weber, Y. Garcia: **Poster** "Polymère de coordination FeN_4O_2 à transition de spin : structure cristalline et étude Mössbauer", Groupe Francophone de Spectrométrie Mössbauer 2012, Rouen, France, 23.-24.04.12 — Poster prize.
2. C. Lochenie, A. P. Railliet, S. Schlamp, W. Bauer, K. Robeyns, Y. Garcia, B. Weber: **Poster** "Iron(II) Spin Crossover Polymer: Crystal structure, Mössbauer spectrometry and solvent influence", 9th Koordinationschemietagung, Bayreuth, Germany, 24.-26.02.13.
3. C. Lochenie, B. Weber: **Oral Presentation** "Purposeful design of Schiff base-like ligands for increasing interactions between Fe(II) spin crossover complexes", 10th Koordinationschemietagung, Kaiserslautern, Germany, 02.-04.02.14.
4. C. Lochenie, K. G. Wagner, M. Karg, B. Weber: **Poster** "Modulation of the Ligand-Based Fluorescence of 3d Metal Complexes upon Spin State Change", 1st Olivier Kahn Discussion, Bordeaux, France, 2.-3.07.15.
5. C. Lochenie, K. G. Wagner, M. Karg, B. Weber: **Oral Presentation** "Synergetic effects between spin state change and fluorescent properties of Schiff base-like 3d metal complexes", 13th Mitteldeutsches Anorganiker-Nachwuchssymposium, Chemnitz, Germany, 3.09.15.
6. C. Lochenie, K. G. Wagner, M. Karg, B. Weber: **Oral Presentation and Poster** "Synergetic effects between spin state change and fluorescent properties of Schiff base-like 3d metal complexes", 6th EuCheMS Conference on Nitrogen Ligands, Beaune, France, 13.-17.09.15 — Poster Prize
7. C. Lochenie, K. G. Wagner, M. Karg, B. Weber: **Oral Presentation** "Synergetic effects between spin state change and fluorescent properties of Schiff base-like 3d metal complexes", 12th Koordinationschemietagung, Kiel, Germany, 28.02-01.03.16.
8. K. Dankhoff, C. Lochenie, M. Rothmund, R. Schobert, B. Weber: **Poster** "New

dimeric Cu(II) complexes with tridentate *NNO* Schiff base-like ligands”, 12th Koordinationschemietagung, Kiel, Germany, 28.02-01.03.16.

11. Acknowledgment

First I thank Pr. Dr. Weber for giving me the opportunity to make my Ph.D. in her workgroup, as well as for the support, help, advices, ideas, scientific discussions, and the freedom of research I was given. Her optimism was really helpful in times where the research just do not want to go forward.

I thank my (ex)colleagues Katja Dankhoff, Christoph Göbel, Ottokar Klimm, René Nowak, Stephan Schlamp, and Johannes Weihermüller for the good working atmosphere, for the help they provided when I needed it, and for never letting me procrastinate alone.

I thank the AK Pr. Dr. Kempe for the technical, scientific, and administrative support and the research cooperations we had. This thesis could not have been written without the access to the CHN analysis, NMR, and the X-ray diffractometer. I thank my cooperation partners Pr. Dr. Karg, Pr. Dr. Köhler, Kristina Wagner, Florian Puchtler, Fabian Panzer, and Konstantin Schötz for the fruitful work together. I thank Dr. Lacher for the measurement of the mass spectra, and Thomas Beppler (LOT) for the technical support with the SQUID. I also thank the team of the glass blowing workshop, they made wonderful Schlenk tubes and Schlenk flasks to protect my precious air-sensitive compounds.

This would would not have been possible without the students who worked with me as intern or HiWi: Christian Beck, Konstantin Dieterle, Florian Dresel, Andreas Gebauer, Vitali Gotwich, Franka Gruschwitz, Julia Heinz, Hannah Kurz, Bernadette Maier, Niels Schieschke, Sophie Schönfeld, Michael Schnabel, Sandra Schneider, Dominik Skrybeck, Niklas Weihermüller, Alexander Wöhrle, and Lisa Zappe. Their work made my research go forward, or backward, in both cases I learned a lot.

I thank the SQUID magnetometer for always getting ill, allowing to acquire a deep understanding of the device operation and teaching me it is never too late to learn a bit of electronics.

Finalemment, je remercie ma famille, ainsi qu'Antoine Railliet et mes amis en Belgique, pour leur soutien depuis la Belgique, et pour les bons moments lors de mes visites.

12. Declaration

(Eidesstattliche) Versicherungen und Erklärungen

(§8 S. 2 Nr. 6 PromO)

Hiermit erkläre ich mich damit einverstanden, dass die elektronische Fassung meiner Dissertation unter Wahrung meiner Urheberrechte und des Datenschutzes einer gesonderten Überprüfung hinsichtlich der eigenständigen Anfertigung der Dissertation unterzogen werden kann.

(§8 S. 2 Nr. 8 PromO)

Hiermit erkläre ich eidesstattlich, dass ich die Dissertation selbständig verfasst und keine anderen als die von mir angegebenen Quellen und Hilfsmittel benutzt habe.

(§8 S. 2 Nr. 9 PromO)

Ich habe die Dissertation nicht bereits zur Erlangung eines akademischen Grades anderweitig eingereicht und habe auch nicht bereits diese oder eine gleichartige Doktorprüfung endgültig nicht bestanden.

(§8 S. 8 Nr. 10 PromO)

Hiermit erkläre ich, dass ich keine Hilfe von gewerblichen Promotionsberatern bzw. -vermittlern in Anspruch genommen habe und auch künftig nicht nehmen werde.

.....

Ort, Datum, Unterschrift